Computed tomography phenotyping of perivascular adipose tissue for cardiovascular disease diagnosis and risk stratification

Evangelos K. Oikonomou

The Queen's College
Division of Cardiovascular Medicine,
Radcliffe Department of Medicine,
University of Oxford

A thesis submitted for the degree of
Doctor in Philosophy in Medical Sciences at the University of Oxford

Supervisors:
Professor Charalambos Antoniades, Professor Jemma C. Hopewell

Trinity Term 2020

Table of contents

Acknowledgements

Oxford, May 4, 2019

There are many people I want to thank for their support, advice and mentorship throughout my time in Oxford. First, I would like to acknowledge the State Scholarship Foundation of Greece and the A.G. Leventis Foundation for supporting me in my first years in Oxford. Thank you to the British Heart Foundation and the National Institute for Health Research Oxford Biomedical Research Centre for supporting and funding the research projects that formed the basis of this thesis.

A special thank you to my supervisor and mentor, Professor Charalambos Antoniades, who believed in me, mentored me throughout this project and to whom I am grateful for the scientist I have grown to become. His constant strive for academic excellence is truly inspiring, and I hope to carry this with me in all my future steps as a physician and a scientist. I look forward to working with you on new projects for several years to come.

Thank you to my co-supervisor, Professor Jemma Hopewell, who provided invaluable support as I navigated my path through statistical analyses and my D.Phil. My sincerest thanks also go to Professors Keith Channon and Stefan Neubauer, who have always been a source of insightful feedback on the progress of my project. I also want to thank all our academic collaborators, who have made this project possible by sharing invaluable data from their studies to help us explore our hypotheses. Special thanks to Professors Milind Y. Desai (Cleveland, Ohio, USA), Stephan Achenbach (Erlangen, Germany) and David E. Newby (Edinburgh, U.K.) for kindly sharing their studies and contributing to our work.

To Ms. Sheena Thomas for always being there for early morning, late evening and weekend CT scans, and managing a bank of thousands of coronary CT angiograms. In no special order, thanks to Drs Alexios Antonopoulos, Ioannis Akoumianakis, Christos Kotanidis, Jennifer Mancio, Katherine Thomas, Henry West, Costas Psarros, Fabio Sanna, Maria-Cristina Carena, Hidekazu Kondo, Nadia Akawi and Ms. Laura Herdman for their contributions, scientific support and friendship. You made this journey all the more enjoyable!

To Anna, Caroline, James, KC, Maarten and Sam for all the moments we have shared together. DPhil life is hard but having an amazing group of friends outside work has been an incredible source of support. I will miss all and each one of you.

To Sofia, my best friend and partner. I feel so lucky to have met you. For nine years and counting, you have experienced first-hand all my successes and struggles. I know that I would not have made it without your love and support. I am so proud of you for everything you have achieved, and I look forward to us starting together a new chapter in our careers as medical interns at Yale.

Finally, to my father and mother. There are no words for me to describe my gratitude for everything you have ever done for me. I wish my father had been here to guide me through my failures and celebrate with me my moments of happiness in Oxford. You always taught me how to work hard, and above all, how to be kind to people. As a freshly minted medical graduate back in 2015, experiencing your illness from the patient's side has changed my perspective about medicine. Being a physician and a scientist is a great privilege and I hope to always try my best to improve the lives of the people around me.

Dedication

To my mother

&

to the memory of my father who passed away

one month before I began my journey in Oxford

Abstract

Computed tomography phenotyping of perivascular adipose tissue for cardiovascular disease diagnosis and risk stratification

A thesis submitted for the degree of

Doctor in Philosophy in Medical Sciences at the University of Oxford

Evangelos K. Oikonomou

The Queen's College

Trinity Term 2020

Coronary inflammation is a major driver of cardiovascular disease and has been implicated in all stages of coronary atherosclerosis, from the early formation of coronary lesions to plaque rupture. Far from being an innocent bystander, perivascular adipose tissue (PVAT) is now recognised as a critical regulator of vascular biology. Further to its direct effects on the arterial wall through outside-to-inside paracrine signals mediated by a wide range of adipocytokines, recent evidence suggests that PVAT may also function as a sensor of vascular biology. More specifically, we have shown that coronary inflammation inhibits adipogenesis and triggers lipolysis in the adjacent perivascular adipocytes, resulting in smaller, fat-free adipocytes closer to the diseased artery. These phenotypic changes can now be captured as perivascular attenuation (radiodensity) gradients on coronary computed tomography angiography (CCTA) using a novel metric, the perivascular Fat Attenuation Index (FAI).

My thesis focuses on the technological development of this method of PVAT characterisation (FAI mapping) and its value in improving the cardiac risk stratification of patients undergoing CCTA imaging. First, I demonstrate that perivascular FAI mapping not only detects coronary segments that have a higher likelihood of coronary atherosclerosis progression at five years but can also identify culprit lesions associated with recent acute myocardial infarction. Using longitudinal CCTA imaging, I also show that perivascular FAI exhibits dynamic changes, which reflect the resolution of vascular inflammation and injury around culprit coronary lesions. Next, using two independent cohorts of 3,912 CCTA scans with long-term follow-up, I show that higher perivascular FAI values at baseline are associated with a higher risk of future major adverse cardiac events. Of note, the prognostic value of FAI mapping is incremental to traditional cardiovascular risk factors and the standard interpretation of CCTA scans and remains significant in both patients with and without established coronary artery disease at baseline. Finally, using a radiotranscriptomic, machine learning-guided approach, I develop radiomic signatures that describe adverse fibrotic and microvascular remodelling changes in coronary PVAT, beyond inflammation. As opposed to FAI, these reflect persistent changes in the PVAT structure and offer incremental value for major adverse cardiac event prediction. Taken together, my findings propose that the radiomic phenotyping of coronary PVAT on standard CCTA can maximise the diagnostic and prognostic yield of one of the most commonly used non-invasive imaging modalities in cardiovascular medicine.

List of publications and presentations

Manuscripts contributing to DPhil thesis

- **Oikonomou EK**, Williams MC, Kotanidis CP, Desai MY, Marwan M, Antonopoulos AS, Thomas KE, Thomas S, Akoumianakis I, Fan LM, Kesavan S, Herdman L, Alashi A, Centeno EH, Lyasheva M, Griffin BP, Flamm SD, Shirodaria C, Sabharwal N, Kelion A, Dweck MR, Van Beek EJR, Deanfield J, Hopewell JC, Neubauer S, Channon KM, Achenbach S, Newby DE, Antoniades C. A novel machine learning-derived radiotranscriptomic signature of perivascular fat improves cardiac risk prediction using coronary CT angiography. **Eur Heart J** 2019, Nov 14; 40(43):3529-3543. PMID: 31504423.

- **Oikonomou EK**, Marwan M, Desai MY, Mancio J, Alashi A, Hutt Centeno E, Thomas S, Herdman L, Kotanidis CP, Thomas KE, Griffin BP, Flamm SD, Antonopoulos AS, Shirodaria C, Sabharwal N, Deanfield J, Neubauer S, Hopewell JC, Channon KM, Achenbach S, Antoniades C. Non-invasive detection of coronary inflammation using computed tomography and prediction of residual cardiovascular risk (the CRISP CT study): a post-hoc analysis of prospective outcome data. **Lancet** 2018, Sep 15; 392(10151):929-939. PMID: 30170852.

- Elnabawi YA*, **Oikonomou EK***, Dey AK, Mancio J, Rodante JA, Aksentijevich M, Choi H, Keel A, Erb-Alvarez J, Teague HL, Joshi AA, Playford MP, Lockshin B, Choi AD, Gelfand JM, Chen MY, Bluemke DA, Shirodaria C, Antoniades C, Mehta NN. Association of Biologic Therapy With Coronary Inflammation in Patients With Psoriasis as Assessed by Perivascular Fat Attenuation Index. **JAMA Cardiol** 2019 Jul 31. doi: 10.1001/jamacardio.2019.2589. PMID: 31365032. (*equally contributed)

- **Oikonomou EK**, Antoniades C. The role of adipose tissue in cardiovascular health and disease. **Nat Rev Cardiol** 2019, Feb; 16(2):83-99. PMID: 30287946.

- **Oikonomou EK**, West HW, Antoniades C. Computed Tomography: Assessment of Coronary Inflammation and Other Plaque Features. **Arterioscler Thromb Vasc Biol** 2019, Nov; 39(11):2207-2219. PMID: 31510795.

- **Oikonomou EK**, Siddique M, Antoniades C. Artificial intelligence in cardiovascular computed tomography: radiomics and machine learning for precision phenotyping of cardiovascular disease. Cardiovasc Res. 2020 Feb 24. pii: cvaa021. doi: 10.1093/cvr/cvaa021. [Epub ahead of print]

- Mancio J*, **Oikonomou EK***, Antoniades C. Perivascular adipose tissue and coronary atherosclerosis. **Heart** 2018, Oct; 104(20):1654-1662. PMID: 29853488 (*equally contributed).

- Antonopoulos AS, Sanna F, Sabharwal N, Thomas S, **Oikonomou EK**, Herdman L, Margaritis M, Shirodaria C, Kampoli AM, Akoumianakis I, Petrou M, Sayeed R, Krasopoulos G, Psarros C, Ciccone P, Brophy CM, Digby J, Kelion A, Uberoi R, Anthony S, Alexopoulos N, Tousoulis D, Achenbach S, Neubauer S, Channon KM, Antoniades C. Detecting human coronary inflammation by imaging perivascular fat. **Sci Transl Med** 2017, Jul; 9(398): eaal2658. PMID: 28701474.

- **Oikonomou EK**, Antoniades C. Immunometabolic Regulation of Vascular Redox State: The Role of Adipose Tissue. **Antioxid Redox Signal** 2017, Aug; 29(3): 313-336. PMID: 28657335.

Other published manuscripts during DPhil

- Margaritis M, Sanna F, Lazaros G, Akoumianakis I, Patel S, Antonopoulos AS, Duke C, Herdman L, Psarros C, **Oikonomou EK**, Shirodaria C, Petrou M, Sayeed R, Krasopoulos G, Lee R, Tousoulis D, Channon KM, Antoniades C. Predictive value of telomere length on outcome following acute myocardial infarction: evidence for contrasting effects of vascular vs. blood oxidative stress. **Eur Heart J** 2017, Nov; 38(41): 3094-3104. PMID: 28444175.

- Akoumianakis I, Badi I, Douglas G, Chuaiphichai S, Herdman L, Akawi N, Margaritis M, Antonopoulos AS, **Oikonomou EK**, Psarros C, Galiatsatos N, Tousoulis D, Kardos A, Sayeed R, Krasopoulos G, Petrou M, Schwahn U, Wohlfart P, Tennagels N, Channon KM, Antoniades C. Insulin-induced vascular redox dysregulation in human atherosclerosis is ameliorated by dipeptidyl peptidase 4 inhibition. **Sci Transl Med**. 2020 Apr 29;12(541). pii: eaav8824. doi: 10.1126/scitranslmed.aav8824.

- Antonopoulos AS, Odutayo A, **Oikonomou EK**, Trivella M, Petrou M, Collins GS, Antoniades C; SAFINOUS-CABG (Saphenous Vein Graft Failure—An Outcomes Study in Coronary Artery Bypass Grafting) group. Development of a risk score for early saphenous vein graft failure: An individual patient data meta-analysis. **J Thorac Cardiovasc Surg**. 2019 Aug 26. pii: S0022-5223(19)31640-X. doi: 10.1016/j.jtcvs.2019.07.086. [Epub ahead of print] PMID: 31606176.

- Akoumianakis I, Sanna F, Margaritis M, Badi I, Akawi N, Herdman L, Coutinho P, Fagan H, Antonopoulos AS, **Oikonomou EK**, Thomas S, Chiu AP, Chuaiphichai S, Kotanidis CP, Christodoulides C, Petrou M, Krasopoulos G, Sayeed R, Lv L, Hale A, Naeimi Kararoudi M, McNeill E, Douglas G, George S, Tousoulis D, Channon KM, Antoniades C. Adipose tissue-derived WNT5A regulates vascular redox signaling in obesity via USP17/RAC1-mediated activation of NADPH oxidases. **Sci Transl Med**. 2019 Sep 18;11(510). pii: eaav5055. doi: 10.1126/scitranslmed.aav5055. PMID: 31534019

- **Oikonomou EK**. Clinical and translational science in cardiovascular research: highlights from the American Heart Association Scientific Sessions 2017: Changing view on the concept of cardiovascular risk and blood pressure targets. **Cardiovasc Res** 2018, Jan 1;114(1):e6-e8. PMID: 29202178.

- Toutouzas K, Skoumas J, Koutagiar I, Benetos G, Pianou N, Georgakopoulos A, Galanakos S, Antonopoulos A, Drakopoulou M, **Oikonomou EK**, Kafouris P, Athanasiadis E, Metaxas M, Spyrou G, Pallantza Z, Galiatsatos N, Aggeli C, Antoniades C, Keramida G, Peters AM, Anagnostopoulos CD, Tousoulis D. Vascular inflammation and metabolic activity in hematopoietic organs and liver in familial combined hyperlipidemia and heterozygous familial hypercholesterolemia. **J Clin Lipidol** 2018, Jan; 12(1): 33-43. PMID: 29174439.

- Lazaros G, Antonopoulos AS, **Oikonomou EK**, Vasileiou P, Oikonomou E, Stroumpouli E, Karavidas A, Antoniades C, Tousoulis D. Prognostic implications of epicardial fat volume quantification in acute pericarditis. **Eur J Clin Invest** 2017, Feb; 47(2): 129-136. PMID: 27931089.

- Antonopoulos AS*, **Oikonomou EK***, Antoniades C, Tousoulis D. From the BMI paradox to the obesity paradox: the obesity-mortality association in coronary heart disease. **Obes Rev** 2016, Oct;17(10): 989-1000. PMID: 27405510.

Awards during DPhil period

- Sep 2019: ***ESC Young Investigator Award in Clinical Science*** **(1st prize),** European Society of Cardiology (ESC) Congress 2019 (Paris, France): Oikonomou EK et al. "*Perivascular fat attenuation index stratifies the cardiac risk associated with high-risk plaque features on coronary computed tomography angiography*".

- Mar 2019: ***Radcliffe Department of Medicine (RDM) Graduate Prize***, University of Oxford, U.K. *Annual award to a maximum of three RDM graduate research students on the basis of exceptional achievement in their research.*

- Aug 2018: ***ESC Young Investigator Award in Clinical Science*** **(1st prize),** European Society of Cardiology (ESC) Congress 2018 (Munich, Germany): Oikonomou EK et al. "Computed tomography-based perivascular fat phenotyping identifies unstable coronary lesions and active vascular calcification".

- Jul 2017: ***SCCT Toshiba Young Investigator Award (1st prize)***, Awarded by the Society of Cardiovascular Computer Tomography (SCCT) in its Annual Scientific Meeting (held in Washington D.C.) for the study by Oikonomou EK et al. "*Imaging phenotyping of perivascular adipose tissue using computed tomography detects coronary inflammation in humans*".

Conference abstracts and presentations during DPhil

European Society of Cardiology (ESC) Congress, Paris, France, September 2019

- ***(Oral Presentation)*** **Oikonomou EK**, EK, Marwan M, Mancio J, Kotanidis CK, Thomas KE, Alashi A, Hutt Centeno E, Antonopoulos AS, Shirodaria C, Neubauer S, Channon KM, Achenbach S, Desai MY, Antoniades C. *Perivascular fat attenuation index stratifies the cardiac risk associated with high-risk plaque features on coronary computed tomography angiography*. **Eur Heart J**. 2019; (Supplement). ***This study won the 1st Prize in the Young Investigator Award in Clinical Science/Cardiology category.***

American College of Cardiology (ACC) Scientific Session, New Orleans, LA, March 2019

- Elnabawi Y, **Oikonomou E,** Dey A, Mancio, J, Rodante J, Gelfand J, Chen M, Bluemke D, Shirodaria C, Antoniades C, Mehta N. *Treatment with biologic therapy in psoriasis is associated with a reduction in coronary artery inflammation, assessed by perivascular fat attenuation index.* **J Am Coll Cardiol.** *2019, Mar; 73(9): S1.*

American Heart Association (AHA) Scientific Sessions, Chicago, IL, November 2018

- **Oikonomou EK,** Thomas S, Kesavan S, Fan LM, Antonopoulos AS, Anthony S, Sabharwal N, Kelion A, Shirodaria C, Langrish JP, Lucking AJ, Kharbanda RK, Neubauer S, Channon KM, Antoniades C. *Abstract 13345: Perivascular Fat Phenotyping Predicts Plaque Progression and Allows Detection of Unstable Plaque Using Coronary Computed Tomography Angiography*. **Circulation**. 2018;138: A13345.

- Akoumianakis I, Sanna F, Margaritis M, Akawi N, Herdman L, Coutinho P, Fagan H, Antonopoulos AS, **Oikonomou EK**, Thomas S, Christodoulides C, Karpe F, Petrou P, Krasopoulos G, Sayeed R, Lv L, Hale A, McNeill E, Douglas G, George S, Channon KM, Antoniades C. *Adipose Tissue-Derived Wnt5a as a Novel Link Between Obesity and Vascular Disease.* **Circulation**. 2018;138: A13345.

British Atherosclerosis Society Meeting, Cambridge, UK, September 2018

- **Oikonomou EK,** Thomas S, Kesavan S, Fan LM, Antonopoulos AS, Anthony S, Sabharwal N, Kelion A, Shirodaria C, Langrish JP, Lucking AJ, Kharbanda RK, Neubauer S, Channon KM, Antoniades C. *Perivascular Fat Imaging for Unstable Plaque Detection and Prediction of Coronary Plaque Progression.*

European Society of Cardiology (ESC) Congress, Munich, Germany, August 2018

- ***(Oral Presentation)*** **Oikonomou EK**, Thomas S, Mancio J, Antonopoulos AS, Sabharwal N, Kelion A, Neubauer S, Channon KM, Antoniades C. *Computed tomography-based perivascular fat phenotyping identifies unstable coronary lesions and active vascular calcification*. **Eur Heart J**. 2018;39 (Supplement) 233. ***This study won the 1st Prize in the Young Investigator Award in Clinical Science/Cardiology category.***

- **Oikonomou EK**, Marwan M, Desai MY, Mancio J, Alashi A, Hutt Centeno E, Shirodaria C, Sabharwal N, Deanfield J, Neubauer S, Channon KM, Achenbach S, Antoniades C. *CRISP-CT study - Non-invasive detection of coronary inflammation by computed tomography analysis of pericoronary fat enhances cardiovascular risk prediction in 3912 individuals.* ***This study was selected for presentation in the late-breaking registry results section.***

- Antonopoulos AS, Herdman L, Thomas S, Akoumianakis I, Kotanidis C, Thomas K, **Oikonomou EK**, Psarros K, Sayeed R, Antoniades C. *Metabolically healthy obesity is associated with a distinct epicardial fat phenotype and low myocardial oxidative stress*. **Eur Heart J**. 2018;39 (Supplement) 6.

- Akoumianakis I, Antonopoulos AS, Herdman L, Margaritis M, **Oikonomou EK**, Krasopoulos G, Petrou M, Sayeed R, Channon KM, Antoniades C. *NADPH oxidase activity in internal mammary arteries predicts mortality in patients undergoing coronary bypass surgery.* **Eur Heart J**. 2018;39 (Supplement) 681.

American Heart Association (AHA) Scientific Sessions, Anaheim, CA, November 2017

- Antonopoulos AS, **Oikonomou EK**, Sanna F, Sabharwal N, Thomas S, Herdman L, Margaritis M, Shirodaria C, Kampoli AM, Akoumianakis I, Petrou M, Sayeed R, Krasopoulos G, Psarros C, Ciccone P, Brophy CM, Digby J, Kelion A, Uberoi R, Anthony S, Alexopoulos N, Tousoulis D, Achenbach S, Neubauer S, Channon KM, Antoniades C. *Coronary Inflammation in Humans Drives Spatial Changes of Perivascular Adipose Tissue Composition Detectable by a Novel Computed Tomography-Based Technology*. **Circulation**. 2017;136:A21015.

European Society of Cardiology (ESC) Congress, Barcelona, Spain, August 2017

- ***(Moderated Poster)*** **Oikonomou EK**, Odutayo A, Akoumianakis I, Antonopoulos AS, Thomas S, Herdman L, Trivella M, Collins G, Petrou M, Kardos A, Channon KM, Antoniades C. *Clinical and biological predictors of early vein graft failure: The SAFINOUS-CABG collaborative group*. **Eur Heart J**. *2017;*38:S1 ehx493.P5807.

- Sangha G, **Oikonomou EK**, Antonopoulos AS, Herdman L, Sayeed R, Krasopoulos G, Petrou M, Channon KM, Antoniades C. *Echocardiographic pre-operative early mitral inflow velocity-to-early diastolic strain rate ratio predicts post-operative paroxysmal atrial fibrillation in patients undergoing CABG surgery*. **Eur Heart J**. 2017;38:S1 ehx493.P5243.

- Lazaros G, Antonopoulos A, **Oikonomou EK**, Vasileiou P, Oikonomou E, Stroumpouli E, Karavidas A, Antoniades C, Tousoulis D. *Epicardial fat volume quantification by computed tomography predicts long-term outcome in patients with acute pericarditis*. **Eur Heart J**. 2017;38:S1 ehx493.P6299.

Society of Cardiovascular Computed Tomography (SCCT) Annual Scientific Meeting, Washington D.C., July 2017

- ***(Oral Presentation)*** **Oikonomou EK**, Antonopoulos A, Sanna F, Sabharwal N, Thomas S, Herdman L, Margaritis M, Shirodaria C, Kampoli A, Akoumianakis I, Psarros C, Ciccone P, Kelion A, Tousoulis D, Achenbach S, Neubauer S, Channon K, Antoniades C. *Imaging Phenotyping of Perivascular Adipose Tissue Using Computed*

Tomography Detects Coronary Inflammation in Humans. ***This study was awarded the 2017 Toshiba Young Investigator Award.***

American Heart Association (AHA) Scientific Sessions, New Orleans, LA, November 2016

- ***(Oral Presentation)*** **Oikonomou EK**, Odutayo A, Akoumianakis I, Antonopoulos AS, Thomas S, Herdman H, Trivella M, Collins G, Petrou M, Channon K, Antoniades C. *Abstract 20311: Identifying Biological Predictors of Early Saphenous Vein Graft Failure: A Meta-Analysis of 5134 Patients With Angiographic Follow Up in SAFINOUS-CABG Collaborative Group*. **Circulation**. 2016;134:A20311.

List of figures

List of tables

List of commonly used abbreviations

4-HNE	4-Hydroxy-nonenal
ACEi	Angiotensin-Converting-Enzyme inhibitor
ACS	Acute Coronary Syndrome
AMI	Acute Myocardial Infarction
AMP	Adenosine Monophosphate
ARB	Angiotensin Receptor Blocker
AUC	Area Under the Curve (C-statistic)
BMI	Body Mass Index
BNP	Brain Natriuretic Peptide
CABG	Coronary Artery Bypass Graft
CAD	Coronary Artery Disease
CCB	Calcium Channel Blocker
CCS	(Agatston) Coronary Calcium Score
CCTA	Coronary Computed Tomography Angiography
CD31	Platelet and Endothelial Cell Adhesion Molecule 1 (PECAM1)
CEBPA	CCAAT/Enhancer-Binding Protein Alpha
CI	Confidence Interval
CRISP-CT	Cardiovascular Risk Prediction using Computed Tomography study
CRP	C-Reactive Protein (hsCRP: high-sensitivity CRP)
CT	Computed Tomography
EAT	Epicardial Adipose Tissue
eNOS	Endothelial Nitric Oxide Synthase
FABP4	Fatty Acid-Binding Protein 4
FAI	Fat Attenuation Index
FDG	FluoroDeoxyGlucose
FFR	Fractional Flow Reserve
FRP	Fat Radiomic Profile
GLCM	Gray Level Co-occurrence Matrix
GLDM	Gray Level Dependence Matrix
GLRLM	Gray Level Run Length Matrix
GLSZM	Gray Level Size Zone Matrix
HDL	High-Density Lipoprotein
HR	Hazard Ratio
HU	Hounsfield Unit
IFN-γ	Interferon gamma
IL	Interleukin
LAD	Left Anterior Descending Artery
LCA	Left Coronary Artery
LCX	Left Circumflex artery
LDL	Low-Density Lipoprotein
MRI	Magnetic Resonance Imaging

NADPH	Nicotinamide Adenine Dinucleotide Phosphate
NaF	Sodium Fluoride
NGTDM	Neighbouring Gray Tone Difference Matrix
NICE	National Institute for Health and Care Excellence
NO	Nitric Oxide
NSTEMI	Non-ST-segment Elevation Myocardial Infarction
OR	Odds Ratio
ORFAN	Oxford Risk Factors And Non-invasive imaging study
Ox-IMPACT	Oxford Imaging of Perivascular Adipose Tissue in Acute Coronary Syndromes using Computed Tomography study
OxLDL	Oxidised Low-Density Lipoprotein
PCI	Percutaneous Coronary Intervention
PET	Positron Emission Tomography
PPAR-γ	Peroxisome Proliferator-Activated Receptor gamma
PPIA	Cyclophilin A
PVAT	PeriVascular Adipose Tissue
RBP4	Retinol-Binding Protein 4
RCA	Right Coronary Artery
RNA	RiboNucleic Acid
ROS	Reactive Oxygen Species
SAT	Subcutaneous Adipose Tissue
SCOT-HEART	SCOTtish computed tomography of the HEART trial
STEMI	ST-segment Elevation Myocardial Infarction
TGF-β	Transforming Growth Factor beta
TNF-α	Tumor Necrosis Factor alpha
QALY	Quality-adjusted Life-years
qRT-PCR	Real-Time Quantitative Reverse Transcription Polymerase Chain Reaction
VAT	Visceral Adipose Tissue
VSMC	Vascular Smooth Muscle Cell

1

Chapter 1. Introduction

This introductory chapter provides an overview of current approaches in cardiovascular risk stratification and introduces the concept of the "residual atherosclerotic cardiovascular risk". It also discusses the role of perivascular adipose tissue in cardiovascular disease highlighting its dual role as a regulator and sensor of vascular inflammation and atherosclerosis. Finally, it describes how coronary computed tomography angiography (CCTA) can be used to detect the interactions between the human vasculature and the perivascular adipose tissue. Arterial inflammation is associated with distinct changes in the perivascular adipose tissue, which can be quantified using computed tomography. Detecting such changes may help to identify a residual atherosclerotic risk not detected through traditional screening approaches.

Note: this chapter is based on previously published material [1-4].

1.1. The global burden of cardiovascular disease

While mortality rates for both males and females have been on steady decline since 1979, diseases related to the heart and the circulatory system account for more than a quarter (26%) of the annual number of deaths in the United Kingdom [5]. It is estimated that approximately seven million people are currently living with cardiovascular disease in the United Kingdom alone, with coronary artery disease (CAD) being the most common type. CAD is the major culprit for acute events such as acute coronary syndromes (ACS) and acute myocardial infarction (AMI). As of 2018, it was estimated that 915,000 people in the United Kingdom alone were survivors of a heart attack [5]. Similarly, in the United

States, heart disease remains a leading cause of death in the general population, ahead of cancer, chronic lower respiratory diseases, injuries and stroke [6]. It is estimated that by 2035, more than 130 million adults in the United States will have some kind of cardiovascular disease, thus representing a growing socioeconomic burden. Total costs related to cardiovascular disease are projected to reach $1.1 trillion by 2035 [6]. The rising prevalence and socioeconomic burden of cardiovascular disease has highlighted the need for improved primary and secondary prevention strategies, as well as new approaches for the identification of high-risk individuals. To this end, there is a strong need for novel cardiovascular risk stratification methods which can pave the path towards more personalised and cost-effective practices in cardiovascular medicine.

1.2. Current cardiovascular risk stratification and prevention

1.2.1. Current approaches in cardiovascular disease prevention

Cardiovascular risk stratification in both primary and secondary prevention has traditionally relied on population-based risk factors (e.g. hypertension, hypercholesterolemia) to provide an individualised assessment of a patient's cardiovascular risk [7]. Among patients with no prior evidence of cardiovascular disease, the "pooled cohort equations" are currently recommended to estimate the ten-year risk of atherosclerotic cardiovascular disease based on a patient's age, sex, race, systolic and diastolic blood pressure, total, low- and high-density lipoprotein levels, smoking, diabetes, and treatment with statins, aspirin or antihypertensive medications [7, 8]. These risk estimates can guide subsequent decision-making on the best preventive steps, which include appropriate lifestyle recommendations or initiation of medical therapy. While these equations have been extensively tested and validated, calibration remains a significant concern, as they have often been reported to overestimate an individual's

cardiovascular risk [9]. Incorporating non-invasive imaging techniques enables more reliable phenotyping by describing the actual (observed) presence rather than estimated (predicted) risk of coronary atherosclerosis. For instance, in patients where the need for medical intervention (i.e. statin initiation) remains unclear, current guidelines recommend cardiac computed tomography (CT) imaging for quantification of the Agatston coronary calcium score (CCS) [10]. CCS is a surrogate marker of coronary atherosclerosis that provides a quantitative estimate of the patient-specific calcified plaque burden and therefore an indication of the presence and extent of coronary atherosclerosis [11].

1.2.2. The concept of the "residual atherosclerotic cardiovascular risk"

Until recently, therapeutic options to address an individual's atherosclerotic cardiovascular disease risk had been limited to appropriate lifestyle modifications (i.e. smoking cessation, exercise, diet recommendations), blood pressure-lowering medications, statin and/or antiplatelet therapy and coronary artery revascularisation, where indicated [12, 13]. While these evidence-based strategies have been shown to reduce the future incidence of adverse cardiovascular events, a considerable proportion of patients continue to experience adverse events despite being on optimal therapy. This has led to the notion of the "residual atherosclerotic cardiovascular disease risk", which describes the incidence of adverse cardiovascular events among patients on optimal therapy as dictated by the existing guidelines [14]. Indeed, most guideline-based approaches fail to take into account patient-specific causal pathways that may not be adequately addressed by the "one-size-fits-all" medication regimens often prescribed in the setting of either primary or secondary prevention [14].

In the recent years several landmark clinical trials have revealed a range of conceptually distinct causal pathways in atherosclerosis which can be targeted to mitigate this residual risk (Table 1.1). Let us assume a hypothetical example of a patient with diabetes mellitus, dyslipidemia and elevated circulating high-sensitivity C-reactive protein (hsCRP) levels who presents for a follow-up appointment following a recent AMI event. Further to the traditional recommendations for lifestyle modifications and initiation of a high-intensity statin, beta-blocker, angiotensin-converting enzyme (ACE) inhibitor, aspirin + a P2Y12 inhibitor and appropriate antihyperglycemic therapy (e.g. metformin), current evidence supports the use of ezetimibe or a proprotein convertase subtilisin/kexin type 9 (PCSK9) (residual *hypercholesterolemic* risk) [16, 23], the interleukin-1β-targeting monoclonal antibody canakinumab (residual *inflammatory* risk) [15], a glucagon-like peptide 1 (GLP-1) agonist or a sodium/glucose cotransporter 2 antagonist (residual *hyperglycemic* risk) [19, 20], as well as low-dose rivaroxaban and aspirin after the first twelve months (residual *platelet* or *coagulation* risk) [22].

These observations provide the framework for a revised approach to cardiovascular risk management in the era of "precision medicine". Nevertheless, several unmet needs should be addressed before such approaches are incorporated into everyday clinical practice. Most notably, surrogate markers need to be defined which will enable the longitudinal follow-up of these risk factors and their response to appropriate, targeted

Table 1.1. Sources of residual atherosclerotic cardiovascular disease risk and therapeutics targeting the associated causal pathways (beyond the standard-of-care).

Pathway	Proposed strategy-agent to address this risk [reference]
a) Inflammation	Canakinumab (anti-IL-1β) [15]
b) Hypercholesterolemia	Anti-PCSK9 (e.g. alirocumab, evolocumab) [16, 17]
c) Hypertriglyceridemia	Icosapent ethyl [18]
d) Metabolism	GLP-1 agonists (eg. Liraglutide) [19], SGLT2-inhibitor (e.g. cangliflozin) [20]
e) Coagulation/platelets	Extended dual antiplatelet therapy [21], low-dose rivaroxaban and aspirin [22]

GLP1: Glucagon-like peptide 1; IL: Interleukin; PCSK9: Proprotein convertase subtilisin/kexin type 9; SGLT2: Sodium/glucose co-transporter 2.

interventions [14]. Furthermore, the high cost of some of these medications (e.g. canakinumab) would represent a significant financial burden for national health systems and insurance companies. In a recent healthcare economics analysis, the cost-effectiveness ratio of adding canakinumab to standard of care was estimated at $6.4 million per quality-adjusted life-years (QALY) gained. The investigators concluded that the price would have to be reduced by more than 98% (to $1,150 per year or less) to meet the $100,000 per QALY willingness-to-pay threshold [24]. Moreover, an approach relying on circulating markers (e.g. hsCRP) that may be confounded by any systemic inflammatory process may not be specific enough to guide the deployment of these medications to the patients that are most likely to benefit, further undermining the cost-effectiveness of such interventions.

1.3. Inflammation and atherosclerosis

1.3.1. Inflammatory pathways in atherosclerotic plaque formation and rupture

Among all the different sources of residual atherosclerotic cardiovascular disease risk discussed earlier, inflammation has recently attracted a lot of attention. For several years researchers have focused on cholesterol and lipoproteins as the key regulators of atherosclerotic plaque formation [25]. The demonstration of macrophage markers on several foam cells as well as the existence of small populations of T lymphocytes in the atherosclerotic plaque microenvironment provided some of the first evidence for the role of innate and adaptive immunity in atherosclerosis [26, 27]. Far from being innocent bystanders, T cells in the vascular wall orchestrate a range of pro- and anti-inflammatory responses in the vascular wall. In fact, depending on local stimuli (e.g. oxidative stress, endothelial dysfunction) T cells not only incite (i.e. T helper 1 [Th1] cells) but may also block inflammatory responses (regulatory T cells, Th2 cells) [25, 28].

Cytokines, such as interleukins and chemokines, mediate the complex interplay between leukocytes and the three key cell types of the human atheroma, namely endothelium, smooth muscle and macrophage foam cells [25]. For instance, IL-1 produced by a range of vascular residing cells can induce a pro-inflammatory cascade mediated by the NLRP3 inflammasome (NOD [nucleotide oligomerisation domain]-, LRR [leucine-rich repeat]-, and PYD [pyrin domain]-containing protein 3), which is activated by local danger signals in atherosclerosis, such as oxidised low-density lipoprotein and cholesterol crystals, thus generating a local inflammatory response that triggers plaque development and progression [29]. Th1 cells may further boost this pro-inflammatory milieu through the production of interferon-gamma (IFN-γ), whereas Th2 and Treg cells block local inflammation through the release of IL-17 and transforming growth factor beta (TGF-β) respectively [25, 28]. Macrophages also exhibit a range of phenotypes and responses to e.g. IFN-γ signalling, ranging from the M1, IL-1β-secreting pro-inflammatory to the M2 IL-10-secreting anti-inflammatory phenotype [25]. While both types have been reported in atherosclerotic plaques, the former appear to be enriched in progressing lesions and the latter are predominantly present in regressing lesions [30].

In atherosclerosis, a vicious circle may eventually ensue where inflammation begets inflammation. Local inflammatory stimuli, such as tumour necrosis factor alpha (TNF-α) and IL-1β, further promote immune cell infiltration into the vascular wall through chemotaxis and leucocyte cell adhesion molecule expression on the endothelium and facilitate tissue remodelling through the expression of matrix-degrading metalloproteinases [31]. Inflammation and oxidative stress are also interconnected, with inflammatory cytokines linked to increased production of reactive oxygen species in the atherosclerotic plaque [2]. The generation of oxidised low-density lipoprotein fragments

(ox-LDL) may further activate Th1 cells and boost the production of TNF-α, which in turn activates macrophages, and may also affect the ability of smooth muscle cells to proliferate or produce fibrillary collagen. In the advanced atherosclerotic plaque, the degradation of the extracellular matrix and inflammation-induced cell apoptosis may reduce the mechanical strength of the plaque, making it vulnerable to the force of blood pressure and leading to eventual plaque erosion or rupture. The subsequent exposure of the plaque's thrombogenic inner core induces a cascade of platelet activation and thrombus formation which may partly or completely block flow in the coronary lumen, resulting in an acute coronary syndrome (ACS) [31]. It is therefore evident that vascular inflammation plays a key role in both atherosclerotic plaque formation and rupture.

1.3.2. Detecting and treating the residual inflammatory risk

Our improved understanding of the role of the various, interconnected inflammatory pathways in human atherosclerosis has highlighted the need to develop inflammatory biomarkers that can flag individuals with a higher than normal cardiovascular risk. An ideal biomarker should be both sensitive and specific for the trait of interest, easy to measure (e.g. can be measured non-invasively in the circulating blood), reliable and relatively inexpensive.

Several circulating inflammatory biomarkers have been shown to predict the future incidence of adverse cardiovascular events among apparently healthy individuals. In a prospective study of 27,939 women followed prospectively for a mean of eight years, CRP levels and LDL cholesterol were minimally correlated at baseline (r=0.08), but both were independently associated with a higher incidence of major adverse cardiovascular events during follow-up. Of note, CRP was found to be a stronger predictor than LDL cholesterol and provided incremental prognostic information beyond the Framingham

risk score [32]. Further studies documented a positive association between the circulating levels of other inflammatory markers and future cardiovascular events, including serum amyloid A, soluble intercellular adhesion molecule type 1 (slCAM-1), interleukin-6 and homocysteine. Interestingly, hsCRP remained the strongest univariate predictor of the risk of cardiovascular events [33].

The first evidence for the clinical value of not only detecting but also treating inflammation in cardiovascular disease prevention was provided by the landmark JUPITER trial (Justification for the Use of statins in Primary prevention: An Intervention Trial Evaluating Rosuvastatin), in which investigators allocated 17,802 apparently healthy men and women with LDL levels <130 mg/dL and hsCRP levels ≥2 mg/dL to treatment with rosuvastatin 20mg daily or placebo. Rosuvastatin treatment almost halved the incidence of major cardiovascular events compared to placebo (hazard ratio of 0.56; 95% confidence interval 0.46 to 0.69), thus supporting the inflammatory hypothesis of atherothrombosis and demonstrating the value of addressing both the residual inflammatory and hyperlipidemic risk through the pleiotropic effects associated with statins [34]. More compelling evidence was provided by the more recent CANTOS trial (Canakinumab Antiinflammatory Thrombosis Outcome Study) in which treatment with canakinumab, a therapeutic monoclonal antibody targeting IL-1β, resulted in a significant reduction in cardiovascular events compared to placebo in individuals with previous myocardial infarction and hsCRP levels ≥2 mg/dL [15]. Of note, canakinumab treatment did not affect lipid levels but did result in a significant reduction in hsCRP levels, the magnitude of which was significantly associated with the subsequent clinical benefit [35]. However, as discussed earlier, hsCRP is a non-specific marker of systemic inflammation, that is elevated in response to several pro-inflammatory stimuli, such as

infection or autoimmune diseases [36]. As such, it may not be specific enough to guide the deployment of expensive, targeted therapeutic agents.

1.3.3. Imaging vascular inflammation

Advanced molecular imaging approaches that use targeted molecular probes and radiotracers and hybrid positron emission tomography-computed tomography (PET-CT) imaging may enable a more specific and reliable assessment of arterial inflammation, compared to circulating inflammatory markers such as hsCRP. Over the past few years, several radiotracers have been developed and tested in both pre-clinical and clinical studies, with demonstrated value in identifying inflamed vascular regions and unstable vascular plaques. Perhaps the most extensively studied tracer is ^{18}F-fluorodeoxyglucose (^{18}F-FDG), a glucose analogue whose uptake is analogous to the metabolic rate of inflammatory cells in the presence of inflammation and hypoxia. However, due to spill-over from the metabolically active myocardium its use in the imaging of the coronary tree has been limited, and most of the studies to date have focused on remote vascular sites such as the carotids or the aorta [37]. Newer more specific radiotracers overcome these limitations by targeting pathways or processes specific to the pro-inflammatory environment of the atherosclerotic plaque. For instance, ^{18}F-NaF (sodium fluoride) binds to hydroxyapatite forming in areas of active microcalcification as a result of necrosis or inflammation [38], whereas ^{68}Ga-dotatate has high affinity for the somatostatin SST_2 receptors that are predominantly expressed in pro-inflammatory M1 macrophages in the plaque microenvironment [39]. Both agents have been shown to detect unstable lesions in both the coronary and carotid regions, with higher accuracy than ^{18}F-FDG [38, 39]. However, such molecular imaging approaches are limited by their high cost, limited availability, need for specialised equipment and appropriately trained operators and

analysts, as well as the relatively higher radiation exposure associated with hybrid PET-CT imaging compared to CT imaging alone. As a result, these approaches remain poor candidates to guide primary or secondary prevention strategies and have not been adopted in the clinical setting.

1.4. Imaging coronary artery disease using cardiac computed tomography (CT)

Clinical imaging in CAD remains focused on the detection of significant coronary plaques/lesions that are associated with haemodynamic impairment, thus affecting the delivery of blood, oxygen and nutrients to the downstream myocardium. Given the wide range of diagnostic tests available to clinicians, selection of the appropriate imaging modality relies on a good understanding of the relative strengths and weaknesses of each approach as well as patient-specific information, such as age, gender and nature of symptoms that determine the pre-test likelihood of CAD. In other words, the interpretation of a non-invasive cardiac test follows a Bayesian approach where the test results are interpreted within the context of a patient's background and presentation to generate a post-test probability that will guide further management [40]. Among all routinely available diagnostic tests, coronary CT angiography (CCTA) has the highest sensitivity (95-99%), with a specificity of 64-83% (Table 1.2). In contrast, exercise electrocardiography has a specificity of 85-90%, with a sensitivity of only 45-50% [40]. Therefore, given its non-invasive nature and high sensitivity and negative predictive value, CCTA has traditionally been reserved as a "gatekeeper" test indicated for patients at low pre-test probability of CAD (e.g. 15-65%). However, local expertise, availability as well as patient preference and characteristics also play a role in selecting the optimal modality.

Table 1.2. Sensitivity & specificity of common tests to diagnose coronary artery disease (as summarised by the European Society of Cardiology [40]).

Modality	Sensitivity (%)	Specificity (%)
Exercise electrocardiography	45-50	85-90
Exercise stress echocardiography	80-85	80-88
Exercise stress SPECT	73-92	63-87
Dobutamine stress echocardiography	79-83	82-86
Dobutamine stress MRI	79-88	81-91
Vasodilator stress echocardiography	72-79	92-95
Vasodilator stress SPECT	90-91	75-84
Vasodilator stress MRI	67-94	61-85
Coronary CT angiography (CCTA)	***95-99***	***64-83***
Vasodilator stress PET	81-97	74-91

CT: computed tomography; MRI: magnetic resonance imaging; PET: positron emission tomography; SPECT: single photon emission computed tomography.

1.4.1. Cardiac CT versus functional testing

The clinical benefit associated with the use of CCTA to diagnose stable CAD and guide downstream decision-making has been provided by two large clinical trials, namely PROMISE (Prospective Multicenter Imaging Study for Evaluation of Chest Pain) and SCOT-HEART (SCOTtish computed tomography of the HEART) [41, 42]. PROMISE showed that among symptomatic patients presenting with stable chest pain, initial anatomical assessment with CCTA was associated with fewer catheterisations showing non-obstructive CAD, compared to functional testing [41]. Similarly, SCOT-HEART demonstrated that CCTA use in addition to standard care in patients with anginal chest pain and suspected CAD resulted in a significantly higher certainty of diagnosis of angina due to CAD at 6 weeks, compared to standard care alone, and improved subsequent targeting of diagnostic and medical interventions [42]. Interestingly, while CCTA did not result in a lower incidence of major adverse cardiovascular events compared to functional testing in the PROMISE population (median follow-up of 25 months), the more recent 5-year follow-up data from SCOT-HEART showed a significant reduction in the incidence of myocardial infarction among patients randomised to CCTA [43]. Furthermore, prior evidence from a more acute setting in the Rule Out Myocardial

Ischemia/Infarction by Computer Assisted Tomography (ROMICAT-II) trial, suggests that use of CCTA (compared to standard evaluation) in patients with suspected ACS but without ischemic electrocardiographic changes or an initial positive troponin test leads to significantly shorter length of in-hospital stay and more direct discharges from the emergency department, although at the cost of increased downstream testing and higher radiation exposure [44]. These randomised controlled trials have been instrumental in establishing CCTA as the test-of-choice in many centers when assessing CAD. Notably, in the most recent, updated NICE (National Institute for Health and Care Excellence, United Kingdom) as well as the 2019 European Society of Cardiology guidelines for the management of chronic coronary syndromes, CCTA is now recommended as a first-line diagnostic test for patients with suspected stable, typical or atypical angina, as well as non-anginal chest pain with electrocardiographic changes [45-47].

1.4.2. Quantitative assessment of coronary atherosclerosis using cardiac CT

CCTA traditionally relies on the visual assessment of the coronary anatomy and the detection of macroscopically visible lesions that cause luminal narrowing in the major epicardial coronary vessels of the human heart, using common and widely accepted thresholds (i.e. minimal: <25% stenosis; mild: 25-49% stenosis; moderate: 50-69%; severe: 70-99%; occluded: 100%) [48]. While a dichotomous classification of CAD as "obstructive" versus "non-obstructive" is often used to guide clinical decision-making and downstream management, such a "black-or-white" approach fails to account for between-patient differences in the degree, extent, location and nature of coronary atherosclerosis [49, 50]. Indeed, both the degree of luminal stenosis as well as the location of coronary atherosclerosis and extent of the coronary tree that are affected may determine an individual's future cardiovascular risk. In a cohort of chest pain patients,

coronary plaque severity, global coronary artery plaque extent, coronary artery plaque distribution, presence of left main or left anterior descending artery plaque, and three-vessel coronary artery plaque were all linked to future all-cause mortality risk [50]. To capture this, Min et al. have derived a modified Duke prognostic CAD index that classifies patients in six groups based on the severity and extent of coronary atherosclerosis. Similarly, in a test sample of 17,793 patients and a validation set of 2,506 patients with suspected CAD, the best-performing predictors of all-cause mortality were the number of proximal segments with mixed or calcified plaques and the number of proximal segments with a stenosis >50% [51]. These findings confirmed that both plaque burden and stenosis, particularly in proximal segments, carry incremental prognostic value for future cardiovascular risk prediction. Since the majority of clinical CCTA scans show no evidence of obstructive CAD [41, 42], while a significant percentage of ACS occur in patients with previously angiographically-determined non-obstructive CAD [52], improving cardiovascular risk prediction requires a more comprehensive assessment of coronary atherosclerosis and patient-specific vascular biology.

1.4.3. Coronary calcium on cardiac CT: The Agatston score

One of the main advantages of cardiac CT is the ability to post-process and segment regions of interest in order to calculate a range of quantitative features, thus supplementing the qualitative assessment of luminal stenosis. One of the first and most extensively studied methods is the assessment of coronary artery calcification by means of the Agatston coronary calcium score (CCS). Traditionally obtained through electrocardiogram-gated non-contrast CT scans of the heart, CCS provides a simple and quick indirect assessment of the extent of coronary atherosclerosis by quantifying the volume and relative density of high-attenuation voxels in the heart which correspond to

sites of vascular calcification [53]. Both absolute CCS and a relative increase in CCS over time have been shown to predict incident CAD and adverse cardiac events independently of traditional cardiovascular risk factors [53, 54]. As a result, CCS is recommended in the risk stratification of selected cases where a risk-based treatment approach remains uncertain based on traditional risk factors [7]. Nevertheless, CCS remains an inflexible biomarker that does not regress, and may even increase in response to risk reduction interventions such as statins [55], thus limiting its value in secondary prevention. In addition, it fails to detect low-attenuation, non-calcified plaques that are known to be more prone to rupture compared to calcified lesions in which extensive calcification may be conferring mechanical stability [55, 56].

1.4.4. Identifying the high-risk plaque on cardiac CT

Histological studies have validated coronary wall radiodensity/attenuation as a marker of plaque histological composition (as evaluated by intravascular ultrasound – virtual histology), with calcified plaques corresponding to higher attenuation values (e.g. >465 Hounsfield Units [HU]), compared to fibrotic (e.g. 65-260 HU) and low-attenuation lesions with a necrotic core (e.g. -1-64 HU) [57]. Thus, application of such HU mapping techniques on dedicated analysis platforms allows the detailed characterisation of plaque composition and offers a more individualised insight into the biological profile of a given lesion (Table 1.3). Such measurements may be quantitative (i.e. total/caclficied/non-calcified plaque burden, diameter stenosis, remodelling index) or qualitative features that describe specific plaque attenuation patterns (i.e. low-attenuation plaque, napkin-ring sign and spotty calcification) [58].

Table 1.3. Summary of common CT-derived metrics of coronary atherosclerosis

CT metric	Definition	Meaning	Limitations
Quantitative coronary features			
Degree of luminal stenosis [50]	Percent (%) diameter stenosis compared to a reference proximal/distal segment. When measured in each coronary segment can be used to generate risk scores of CAD extent (e.g. *segment stenosis/involvement score*, *modified Duke Prognostic CAD index* and *CAD-RADS*) [50, 59].	An anatomical index reflecting the degree of luminal stenosis caused by a coronary plaque.	Sensitive to technical artefacts that may lead to over- or under-estimation of the degree of coronary stenosis (e.g. poor opacification, blooming if calcified).
Coronary artery calcium score [11]	Describes the extent of coronary calcification, usually on non-contrast, CT images. Commonly calculated using the Agatston formula that accounts for both the volume and density of calcified lesions.	An established cardiovascular risk score that provides an easy, indirect assessment of the extent of coronary atherosclerosis.	Questionable value in secondary prevention, calcium does not regress in response to risk reduction measures, such as statins.
Non-calcified, calcified, low-attenuation plaque burden [57]	Total non-calcified/calcified/low-attenuation plaque volume/vessel volume (%).	A quantitative volumetric index of plaque burden and composition.	Often not validated across different scanners and parameters.
Qualitative (high-risk) plaque features **[60]**			
Low-attenuation plaque	≥3 regions of interest (0.5-1mm^2) in the plaque with a mean attenuation of <30 HU.	A large, lipid-rich, necrotic core reflecting an extracellular mass in the intima induced by necrosis and apoptosis of lipid-laden foam cells.	Operator-dependent sign.
Spotty calcification	Calcified plaque with <3 mm diameter, length <1.5 times the vessel diameter, and width of the calcification less than two-thirds of the vessel diameter.	Vascular calcification reflecting areas of necrosis, inflammation, osteoblastic metaplasia and hydroxyapatite formation.	Operator-dependent, angle-dependent measurement.
Napkin-ring sign	A ring-like peripheral higher attenuation of the non-calcified portion of the coronary plaque.	A thin fibrotic cap above a lipid-laden, necrotic core.	Subjective, operator-dependent, qualitative sign.
Positive remodelling	A remodelling index >1.1 (ratio of maximum vessel area (or diameter)/proximal vessel area (or diameter)).	Reflects outwards remodelling due to extracellular matrix remodelling (e.g. increased MMP activity).	Operator-dependent, angle-dependent measurement.

CAD: Coronary artery disease; CT: computed tomography; FFR: fractional flow reserve; HU: Hounsfield Units; MMP: matrix metalloproteinase. Reproduced with permission from Oikonomou EK et al. Arterioscler Thromb Vasc Biol. 2019 Sep 12:ATVBAHA119312899. doi: 10.1161/ATVBAHA.119.312899.

For instance, even though CCTA is unable to detect the presence of thin cap fibroatheroma (TCFA), a hallmark of coronary plaque instability, CCTA-derived high-risk plaque features such as positive remodelling (a relative increase in the cross-sectional diameter of a given lesion compared to a proximal, reference segment of 1.1 or higher) and low-attenuation plaque (traditionally defined as a plaque area with mean attenuation <30 HU) can successfully discriminate TCFA from non-TCFA lesions [61], thus identifying unstable coronary lesions that may lead to ACS [62]. Spotty calcification and napkin-ring sign (ring-like peripheral higher attenuation of the non-calcified portion of the coronary plaque) have also been recognised as important high-risk plaque features [63]. These high-risk features are key components of the natural history of atherosclerosis, especially among high-risk populations such as diabetic patients [64], and predict the presence of ACS in patients presenting with acute chest pain [60]. More importantly, they reflect a dynamic biology and have been shown to regress in response to statin treatment [65].

These high-risk plaque features provide a more detailed characterisation of coronary atherosclerosis and are associated with the presence of ACS independent of each other and the degree of luminal stenosis [60]. Vascular wall remodelling in atherosclerosis is the end-result of complex pathways that converge to cell migration and extracellular matrix remodelling, often due to an imbalance in the relative expression and activity of matrix metalloproteinases and their inhibitors in the plaque microenvironment [66]. The resulting outwards vascular remodelling can then be detected on CCTA as a relative increase in vascular diameter around the plaque captured by the remodelling index [60, 61]. Low attenuation plaque on the other hand is associated with a lipid-rich necrotic core, an extracellular mass in the intima induced by necrosis and apoptosis of lipid-laden macrophage foam cells [67]. Such a high-risk plaque phenotype composed of

a thin fibrotic cap above a necrotic core is often described as a "napkin-ring sign" on CCTA, manifesting as a low-attenuation area surrounded by a high-attenuation rim [60, 68]. Finally, spotty calcification identifies inflamed areas of confluent coronary calcification and microcalcification [58, 60]. Vascular calcification represents a local response to an inflammatory microenvironment, with a well-defined link between inflammatory cell infiltration and osteoblastic metaplasia [69].

While high-risk plaque features are a critical component of the assessment of a CCTA scan and their reporting is encouraged by the most up-to-date recommendations of the Society of Cardiovascular Computed Tomography [59], they are only applicable in the presence of visible, advanced atherosclerosis. Therefore, it remains challenging to detect individuals at increased risk of atherosclerosis progression or adverse clinical events among those with no or minimal evidence of CAD on CCTA. A method that would be able to extract functional information on the biological status of the coronary vasculature (e.g. inflammation) from standard CCTA independent of the cross-sectional presence of coronary atherosclerosis would be invaluable in clinical practice.

1.4.5. Identifying the haemodynamically significant plaque on cardiac CT

Computational fluid dynamic modelling can provide tools to assess not only the structural but also haemodynamic significance of coronary plaques through CCTA-derived estimation of the fractional flow reserve (FFR), which represents the ratio of the mean coronary pressure distal to a coronary stenosis to the mean aortic pressure during maximal coronary blood flow [70, 71]. CT-derived FFR (FFR_{CT})-guided management is associated with similar clinical outcomes but significantly lower costs in patients with stable CAD, when compared to the standard-of-care interpretation of cardiac CT scans [72]. For instance, recent evidence suggests that FFR_{CT} can reliably discriminate patients with intermediate-grade stenosis (30-

70%) who would benefit from invasive angiography (FFR_{CT}<0.80) compared to no invasive imaging (FFR_{CT}≥0.80) [73]. However, both high-risk plaque features and FFR_{CT} are only applicable in the presence of macroscopically visible atherosclerosis. Their ability to detect disease only at advanced stages limits their use to secondary prevention and highlights the need for non-invasive imaging modalities that can detect the key processes of early atherosclerosis (i.e. inflammation, cell necrosis or apoptosis) at the earliest stages [74]. Unfortunately, due to limited access to this proprietary technology, FFR_{CT} was not analysed in the scans included in this thesis.

1.5. Adipose tissue and the cardiovascular system

Whereas atherosclerosis is a disease of the vascular wall, its pathogenesis is also under the regulation of remote tissues and organs, such as the adipose tissue [1]. Adipose tissue, or "fat", is a term that describes the anatomical depot of loose connective tissue found in the human body that is composed primarily of adipocytes, as well as a range of stromal cells, including inflammatory cells, fibroblasts, vascular cells and others [75-77]. Adipose tissue has traditionally been implicated in the pathogenesis of obesity, where a positive caloric balance leads to adipocyte hypertrophy (and/or hyperplasia) and therefore an increase in total adipose tissue mass, resulting in a body mass index (BMI) ≥ 30kg/m^2 [78].

1.5.1. Obesity as a risk factor

Adipose tissue expansion and obesity have long been recognised as important risk factors for the pathogenesis of cardiovascular and metabolic disease. In a Mendelian randomisation analysis investigators described positive, causal links between the extent of systemic as well as central obesity with CAD, type 2 diabetes mellitus, stroke, systemic inflammation, dyslipidemia and left ventricular hypertrophy [79]. Further evidence has

been provided by landmark epidemiological studies, such as the Framingham and Dallas Heart Studies, which have linked visceral adipose tissue expansion to a higher incidence of hypertension and cardiovascular disease [80-82]. Interestingly, the association between "obesity" and adverse clinical outcomes becomes less clear when BMI, rather than adipose tissue volume, is used to define obesity. In a meta-analysis that included data from more than 30 million individuals, the association between BMI and total mortality was identified as U- or J-shaped [83]. Further studies in patients with chronic diseases, such as heart failure or metabolic abnormalities, have even demonstrated a paradoxical survival benefit for overweight or obese patients compared to those with normal BMI values <25 kg/m^2 [84, 85]. These observations have resulted in the so-called "obesity paradox", namely the paradoxical survival benefit seen in patients in the higher than normal BMI range compared to their healthy-weight counterparts [86].

When considering the "obesity paradox", one should keep in mind that this is rather a "BMI paradox" and nothing more than an epidemiological observation [86]. It is currently understood that depending on its distribution and anatomical location adipose tissue may exert either atheroprotective (e.g. subcutenous or gluteal adiposity) or pro-atherogenic effects (visceral or ectopic adiposity) [82, 86]. In addition, BMI does not differentiate fat from lean mass and does not account for differences in cardiorespiratory fitness [87, 88]. Moreover, adipose tissue is a rather dynamic organ that responds to systemic and local stimuli, including inflammatory signals in cachexia and chronic disease, such as heart failure or cancer [86, 89]. As such, it is also a sensor of the systemic or local biology, and changes in its volume and composition (such as in cachexia) may be early indicators of worsening health status.

In order to better understand the complex role of adipose tissue in cardiovascular homeostasis and disease, one needs to carefully review the anatomy, distribution,

composition and biological function of adipose tissue and how this changes in response to various exogenous or endogenous stimuli.

1.5.2. Adipose tissue: structure, anatomy and biology

Human adipose tissue is found in several regions and can be divided accordingly based on its anatomical location into two main anatomical depots, namely the visceral adipose tissue (VAT) and the subcutaneous adipose tissue (SAT) depots [82, 90]. Furthermore, VAT can be further separated into intrathoracic or abdominal fat, while intrathoracic VAT can be separated into epicardial (EAT) and pericardial depots depending on its location inside or outside the pericardial layer, respectively [91]. The importance of this classification is dual. First, the association between adipose tissue expansion and incident cardiovascular disease is dependent on the nature of adipose tissue distribution, with abdominal rather than subcutaneous adipose tissue expansion more closely associated with cardiometabolic risk [82]. Second, several transcriptomic and proteomic analyses have revealed distinct biological profiles between these depots [76, 92, 93]. Interestingly, adipose tissue biology appears to vary substantially even within the same anatomical depot. For instance, abdominal SAT carries a transcriptomic signature that more closely resembles that of VAT depots rather than gluteal SAT [94]. Moreover, the transcriptomic profile of EAT, the adipose tissue layer that is located between the visceral layer of the pericardium and the myocardium, varies significantly between its peri-ventricular, peri-atrial and peri-coronary sites [95].

Indeed, at the tissue level, there are remarkable morphological and biological differences between human fat depots [77]. VAT consists of small undifferentiated adipocytes, has a high degree of macrophage infiltration and correlates with insulin resistance, whereas SAT is characterised by smaller and less metabolically active

adipocytes and a rather anti-inflammatory phenotype [77, 96]. Adipocytes can be further classified as white, brown or beige. "White" AT represents the greatest portion of AT in humans and is responsible for energy storage in the form of triglycerides. "Brown" AT is found mainly in young mammals (and as small islets within white AT in adult life), contributing to non-shivering thermogenesis and a favorable metabolic profile [97]. "Beige" or "brite" adipose tissue represents an inducible form of fat that may be found within white AT depots in response to cold exposure or pharmacological (e.g. adrenergic) modulation [98, 99].

While adipocytes occupy most of the volume of an adipose tissue depot, a wide number of different cell types also exist in the stromal fraction of adipose tissue and play an important role in regulating the biological function of the tissue and as well as its remodelling. These range from inflammatory cells [77, 100], pre-adipocytes, fibroblasts, adipose-tissue derived stem cells [101] and vascular cells involved in the adipose tissue microvasculature and lymphatic structures [75, 76].

Most cell types residing in the adipose tissue, including adipocytes, secrete molecules that may travel through autocrine, paracrine, vasocrine or endocrine routes and regulate the biological functions of cells in the same depot or distant tissues and organs. These molecules, collectively known as "adipocytokines" are critical in mediating the involvement of adipose tissue in both homeostasis as well as the pathogenesis of cardiovascular and other diseases [102]. As expected, the secretory profile of adipose tissue is dependent on both the type and location of a given depot, as well as the presence of obesity, insulin resistance, diabetes mellitus and inflammatory stimuli [1, 77]. While a comprehensive review of adipocytokines and their biological properties goes beyond the

scope of this thesis, Table 1.4 provides a brief overview of some of the most extensively studied members of this group. It is evident that the list of adipose tissue-derived bioactive molecules is rather broad, encompassing both adipokines, cytokines [103], micro-ribonucleic acid (miRNAs) molecules [104], gaseous messengers [105], microvesicles [106], as well as reactive oxygen species, antibodies and lipid messengers [1, 107].

1.5.3. Dysfunctional adipose tissue: inflammation, fibrosis & angiogenesis

One of the most remarkable features of adipose tissue is its rapid plasticity. The mass of VAT in mice can double within one week of the initiation of high-fat diet but undergoes

Table 1.4. Representative adipokines and their effects on the cardiovascular system.

Adipose tissue product	Effects on the cardiovascular system[a]	Examples of suggested mechanisms
Activin A	Pro-fibrotic and ↑ IR	• Promotes fibrosis (might be mediated by angiotensin II), which is linked to arrhythmogenicity
Adiponectin	Anti-oxidant, anti-inflammatory, and ↓ IR	• ↓ NF-κB signalling • ↑ AMPK and AKT signalling • ↓ NADPH oxidase activity (↓ $p47^{phox}$/RAC1 translocation) • ↑ eNOS phosphorylation and coupling (↑ BH_4 bioavailability)
Apelin	Pro-oxidant and pro-inflammatory	• ↑ NADPH oxidase activity (↑ subunit expression)
Chemerin	Pro-oxidant and pro-inflammatory	• ↑ eNOS expression, but ↑ eNOS uncoupling
Leptin	Pro-oxidant and other pleiotropic effects	• ↑ NADPH oxidase activity (↑ $p47^{phox}$ activation) • ↑ Mitochondrial ROS generation • ↑ eNOS expression
Omentin-1	Anti-oxidant, anti-inflammatory, and ↓ IR	• ↓ NADPH oxidase activity (↓ $p47^{phox}$ activation) • ↓ TNF-induced VCAM1 expression
Resistin	Pro-oxidant, pro-inflammatory, and ↑ IR	• ↑ NADPH oxidase activity (↑ $p47^{phox}$ activation) • ↓ eNOS expression
Retinol-binding protein-4	Pro-oxidant, pro-inflammatory, ↑IR	• ↑ NF-κB signalling • ↑ NADPH oxidase activity • ↑ Cell-adhesion molecules (such as VCAM1)
Visfatin	Pro-oxidant, (pro-inflammatory)	• ↑ NF-κB signalling • ↑ NADPH oxidase activity • ↑ Cell-adhesion molecules (such as VCAM1)

–, no change. AKT, RAC-alpha serine/threonine-protein kinase; BH4, tetrahydrobiopterin; cGMP: cyclic guanosine monophosphate; DM, diabetes mellitus; eNOS, endothelial nitric oxide synthase; IgM, immunoglobulin M; IR, insulin resistance; NADPH, nicotinamide adenine dinucleotide phosphate; NF-κB: nuclear factor-κB; PAME, palmitic acid methyl ester; PKG: protein kinase G; PVAT: perivascular adipose tissue; ROS, reactive oxygen species; TNF, tumour necrosis factor; VCAM1, vascular cell adhesion molecule 1; VSMC, vascular smooth muscle cell. Reproduced with permission from Oikonomou EK & Antoniades C. **Nat Rev Cardiol**, 2019. 16(2):83-99.

a dramatic reduction within 24-hours of fasting [108]. The ability of adipose tissue to remodel is attributed to a coordinated response orchestrated by the different adipose tissue-residing cells, mainly the adipocytes, immune cells, endothelial cells and fibroblasts [109] (Figure 1.1). In response to excessive caloric intake, adipocytes expand through the intracellular accumulation of triglycerides in the form of lipid droplets. Such rapid, dynamic changes in the tissue microenvironment may surpass the diffusion capacity of oxygen resulting in mild hypoxia and stress signaling responses mediated among others by the hypoxia-inducible factor-1 alpha factor (HIF-1α) [110]. Hypoxia is a key inciting event for the onset of inflammation and is associated with increased production of adipocyte-derived pro-inflammatory mediators, such as IL-6 [109, 111], which may promote the infiltration of adipose tissue with inflammatory cells, mainly macrophages. Hypoxia further promotes angiogenesis through upregulation of genes such as vascular endothelial growth factor (VEGF), while also stimulating extracellular matrix (ECM) remodelling (i.e. collagen and proteoglycan deposition) in order to support adipose tissue expansion [109, 110]. The reciprocal interactions between angiogenesis, ECM remodelling, inflammation and oxidative stress help to sustain this vicious circle of dysfunctional adipose tissue expansion. For instance, macrophages and leukocytes activate endothelial cell proliferation and angiogenesis through the secretion of pro-angiogenic factors [112]. However, prolonged stress signaling may result into local injury, adipocyte death, chronic macrophage infiltration and impaired angiogenesis. While the mechanisms for this are not fully understood, this dysfunctional adipose tissue phenotype

has been associated with obesity, insulin resistance and other conditions that expose adipose tissue to a pro-inflammatory environment [109]. Researchers have traditionally focused on the pathophysiological effects of these phenotypic changes in cardiovascular disease. However, as I will explain later in my thesis, my goal will be to approach this plasticity seen in adipose tissue from a different angle, exploring its potential value as an *in vivo* sensor of local inflammation contributing to cardiovascular disease diagnosis and risk stratification.

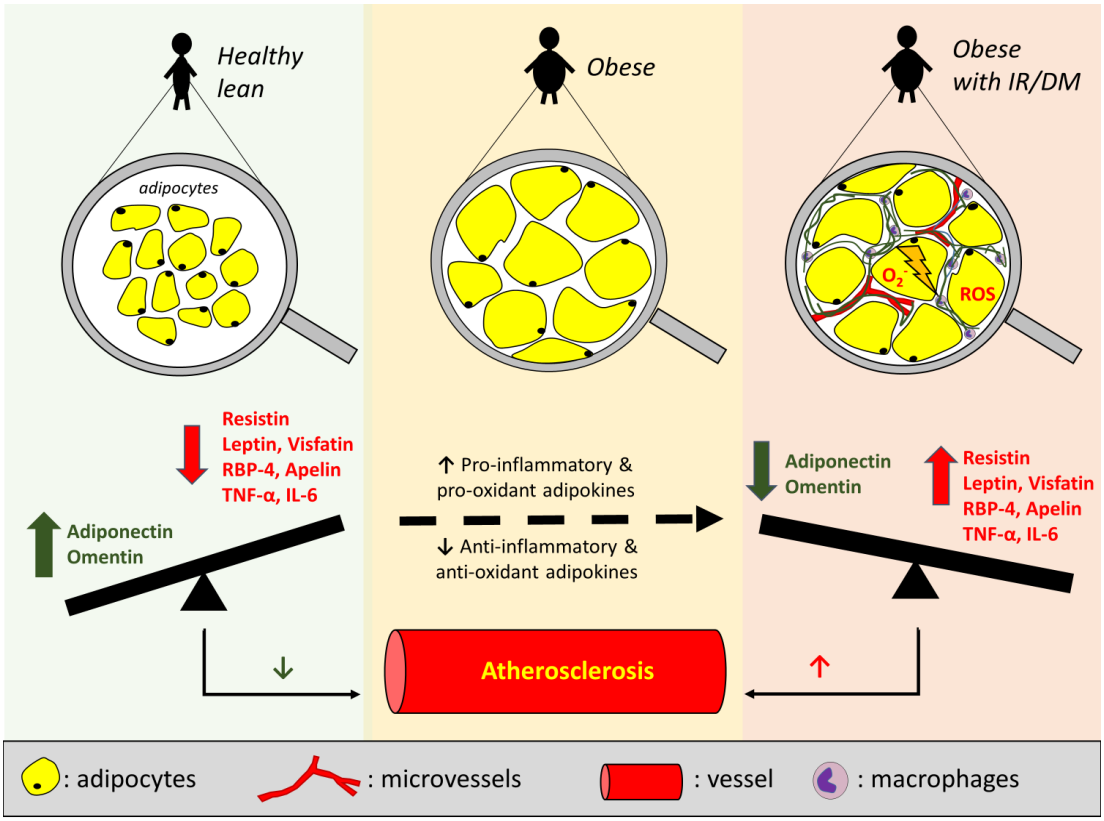

Figure 1.1. Dysfunctional adipose tissue and atherosclerosis. *In the presence of obesity and insulin resistance, adipose tissue undergoes extensive remodelling, characterised by adipocyte hypertrophy, increased oxidative stress, neoangiogenesis and extracellular matrix remodelling (e.g. collagen deposition). At the same time, the secretome of adipose tissue shifts from the production of anti-atherogenic adipocytokines towards the release of molecules with pro-atherogenic and pro-oxidant properties that may diffuse in a paracrine or endocrine manner to the circulation and exert their effects on the vascular wall. DM: diabetes mellitus; IL-6: Interleukin; IR: insulin resistance; RBP4: retinol-binding protein 4; ROS: reactive oxygen species; TNF: tumor necrosis factor. Reproduced with permission from Oikonomou EK & Antoniades C.* ***Antioxid Redox Signal****, 2018. 29(3): p. 313-337.*

1.6. Perivascular adipose tissue and atherosclerosis

1.6.1. Outside-to-inside signaling

While most adipose tissue depots can regulate remote tissues and organs through endocrine signals, perivascular adipose tissue (PVAT) is unique in that its close anatomical proximity to the vascular wall enables direct, paracrine interaction with the adjacent vascular wall [113, 114]. Indeed, PVAT has been implicated in most functions of the vascular wall in health as well as in most steps of the natural history of atherosclerosis, including vascular tone regulation, inflammation, smooth muscle cell migration, endothelial function (or dysfunction) and vascular redox state [1, 115] (Figure 1.2). The ultimate biological effects of PVAT and adipose tissue in general reflect the balance between pro-atherogenic and anti-atherogenic biochemical messengers, which in turn depends on several genetic, environmental (i.e. diet, exercise) and biological triggers (i.e. obesity, inflammation, metabolic syndrome and diabetes).

For instance, in healthy conditions, adipose tissue-derived adiponectin induces vasorelexation through 5' adenosine monophosphate-activated protein kinase (AMPK) or RAC-alpha serine/threonine-protein kinase (AKT)-mediated endothelial nitric oxide synthase (eNOS) phosphorylation [103, 116], whereas adipose tissue-derived hydrogen sulfide (H_2S) activates adenosine triphosphate (ATP)-regulated potassium channels [105]. In mice, PVAT appears to also be involved in the circadian regulation of vascular tone and blood pressure through modulation of local angiotensinogen production [117], and may also contribute to the uptake of the vasoconstrictor noradrenaline [118]. Adiponectin further exerts antioxidant effects both by blocking the membrane translocation of Rac1 and downregulating the expression of the $p22^{phox}$ regulatory subunit of certain NADPH-oxidase isoforms in the vascular wall [103, 119], as well as restoring endothelial nitric oxide synthase (eNOS) coupling [103]. However, in the presence of obesity and metabolic

syndrome, the adipose tissue secretome shifts towards the production of pro-inflammatory and pro-atherogenic adipocytokines, such as visfatin, chemerin and cytokines such as IL-1β. Contrary to adiponectin and its anti-oxidant effects, chemerin promotes eNOS uncoupling and decreases nitric oxide (NO) production in favour of superoxide radicals [120]. Visfatin, TNF-α and IL-1β may promote endothelial cell activation and cell adhesion molecule expression, thus initiating the pro-atherogenic cascade in the vascular

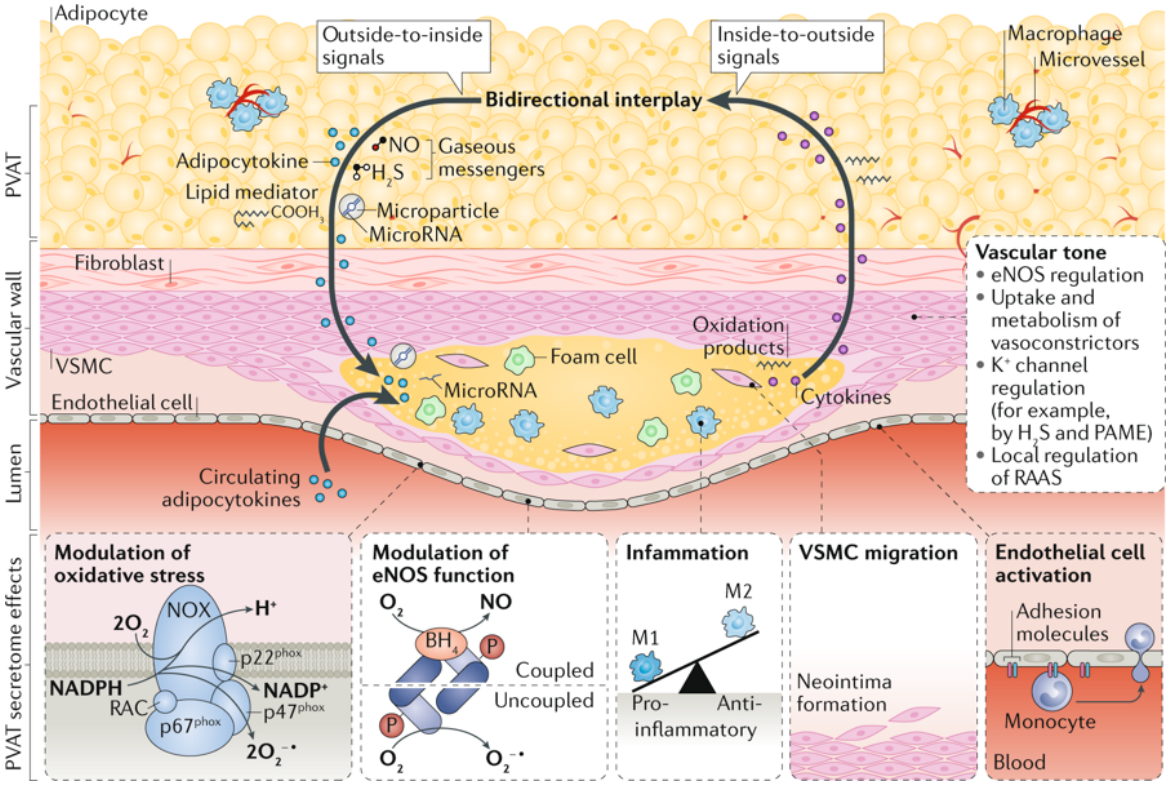

Figure 1.2. Bidirectional paracrine interplay between the vascular wall and perivascular adipose tissue (PVAT). *The adipose tissue releases a range of bioactive products, including adipokines (such as adiponectin, leptin and resistin), chemokines, cytokines, gaseous messengers such as hydrogen sulfide (H_2S) and nitric oxide (NO), fatty acids such as palmitic acid methyl ester (PAME), reactive oxygen species and microparticles molecules to the adjacent vessel. Inside the vascular wall, these molecules have pleiotropic effects on multiple targets and have been involved in the regulation of local redox state (through modulation of NADPH oxidase (NOX) activity and endothelial NO synthase (eNOS) coupling), endothelial function (through regulation of eNOS activity and NO bioavailability), local endothelial cell activation, inflammation (such as the regulation of M1–M2 macrophage polarization), vascular smooth muscle cell (VSMC) migration, neointima formation and vascular tone. In addition to these outside-to-inside signals, vascular inflammation and oxidative stress can also affect the adipose tissue (particularly PVAT) biology in an inside-to-outside manner. Inflammatory signals (such as pro-inflammatory cytokines) or lipid peroxidation products (such as 4-hydroxynonenal) can diffuse to the adjacent PVAT and activate signalling pathways in adipocytes. BH4, tetrahydrobiopterin; RAAS, renin–angiotensin–aldosterone system. Reproduced with permission from Oikonomou EK & Antoniades C.* ***Nat Rev Cardiol****, 2019. 16(2):83-99.*

wall [2, 121]. In conclusion, adipose tissue plays a multi-faceted role in the regulation of vascular biology, which is determined by a patient's overall inflammatory and metabolic profile.

1.6.2. Inside-to-outside signaling

The traditional dogma that adipose tissue affects vascular biology in a unidirectional manner has been challenged by studies describing inside-to-outside signaling pathways from the vascular wall into the surrounding PVAT (Figure 1.2). In one of the earliest examples, an experimental model of vascular injury in mice resulted in TNF-α-mediated upregulation of pro-inflammatory adipocytokines and downregulation of adiponectin expression in the surrounding perivascular fat [122]. Following this, our group described the existence of protective paracrine loops between the vascular redox state and PVAT biology. In the presence of oxidative stress, superoxide and other reactive oxygen species cross-react with lipids in the vascular wall generating lipid-peroxidation products, such as 4-hydroxynonenal (4-HNE) that are able to diffuse into the adjacent PVAT. There 4-HNE can active proliferator-activated receptor-γ (PPARγ) signaling leading to upregulation of adiponectin biosynthesis, an adipokine with well-defined antioxidant effects on vascular redox state [103, 119, 123]. This paracrine loop represents a potential defensive mechanism of the human vasculature against oxidative stress and highlights the critical role of PVAT in regulating vascular homeostasis. Furthermore, a 2018 study using a porcine model of drug-eluting stent-induced coronary vasoconstriction demonstrated localised changes in PVAT inflammation around the stent edges compared to control sites, further supporting close communication links between the vascular wall and its PVAT [124]. Of note, this paracrine interplay is not specific to the vascular wall. Similar interactions have also been described between the myocardial redox state and

adiponectin production in the myocardium [125], whereas adiponectin biosynthesis in remote adipose tissue depots appears to also be regulated by circulating brain natriuretic peptide levels [77].

1.6.3. Perivascular fat as a sensor of coronary inflammation and atherosclerosis

Interestingly, vascular disease is associated with changes in not only the PVAT secretome, but also its composition, as we have recently demonstrated using a series of *in vivo* and *ex vivo* studies [126]. In a proof-of-concept experiment, pre-adipocytes isolated from human peri-aortic adipose tissue were either cultured alone or co-cultured with aortic tissue that had been incubated in the presence or absence of angiotensin-II (AngII). AngII resulted in increased gene expression of the pro-inflammatory markers *TNFA*, *IL6*, *IFNG*. Following a differentiation protocol over nine days, pre-adipocytes cultured in the absence of aortic tissue exhibited a higher degree of differentiation and intracellular lipid accumulation (as quantified by Oli-red-O staining), compared to pre-adipocytes cultured in the presence of inflamed "aortic buttons" (Figure 1.3). In further experiments, human pre-adipocytes exposed to exogenous pro-inflammatory cytokines (IL-6, TNF-α, IFN-γ) exhibited a significantly higher rate of proliferation but lower degree of differentiation (assessed by the relative gene expression of the adipocyte differentiation markers *PPARG*, *CEBPA* & *FABP4*) compared to pre-adipocytes cultured in the absence of pro-inflammatory cytokines.

These ex vivo studies confirmed the dynamic nature of the human adipose tissue, demonstrating that in the presence of exogenous inflammation adipocytes lose their ability to differentiate and mature into large, lipid-laden adipocytes. In accordance with these findings, paired comparisons of adipose tissue biopsies from patients with advanced atherosclerosis undergoing coronary artery bypass grafting (CABG) surgery revealed significantly lower levels of adipocyte differentiation in biopsies obtained from the perivascular area attached to the right coronary artery (RCA) compared to non-

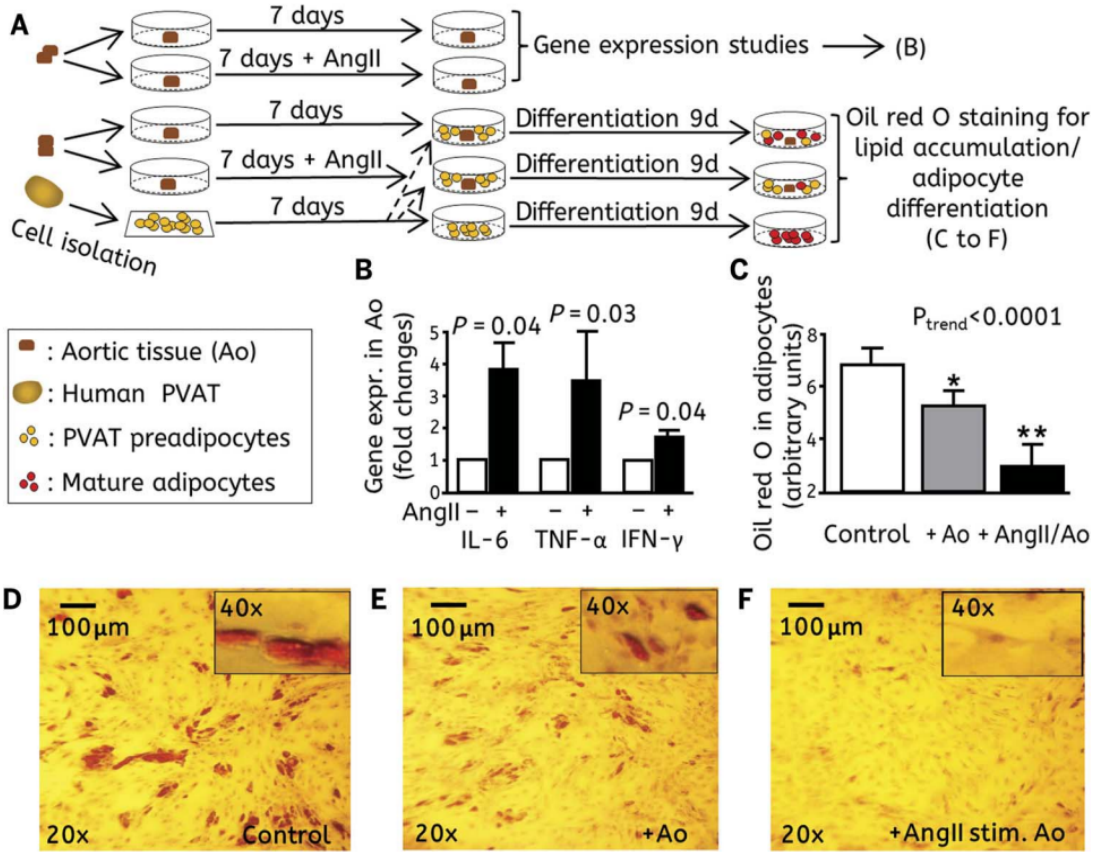

Figure 1.3. Vascular inflammation is associated with impaired pre-adipocyte differentiation. ***(A)*** *Human aortic tissue (Ao) from 15 patients undergoing CABG was harvested and cultured for 7 days ± angiotensin II, which resulted in upregulation of pro-inflammatory cytokine expression* ***(B)****. Preadipocytes isolated from PVAT around the right coronary artery (RCA) were also cultured for this period. After 7 days, the aortic tissue was washed to remove angiotensin II and was cocultured with the preadipocytes before a differentiation time course was induced.* ***(C-F)*** *Quantification of oil red O in preadipocytes (control) or preadipocytes co-incubated with aortic tissue or aortic tissue prestimulated with angiotensin II. Reproduced with permission from Antonopoulos AS et al.* ***Sci Transl Med****., 2017. 9(398).*

perivascular adipose tissue biopsies obtained from the free wall of the right ventricle, approximately 20 mm away from the RCA (Figure 1.4). We therefore hypothesised that this in vivo gradient in adipocyte composition and differentiation could function as a sensor (or a surrogate marker) of coronary inflammation and atherosclerosis. However, since pericoronary adipose tissue biopsies are not a feasible approach in routine clinical practice, we hypothesised that non-invasive imaging characterisation of PVAT could provide the key to the clinical translation and testing of this hypothesis.

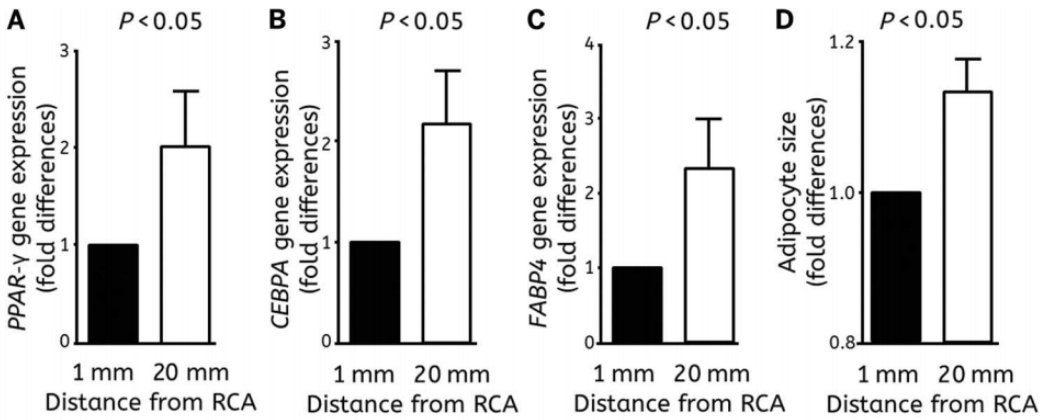

Figure 1.4. Perivascular gradient in perivascular adipose tissue phenotype around the right coronary artery (RCA). (A) *PPAR-g,* ***(B)*** *CEBPA, and* ***(C)*** *CEBPA4 gene expression and* ***(D)*** *adipocyte size in pericoronary adipose tissue samples attached to the RCA and paired samples ~20 mm away from it [n = 6 to 12 pairs for (A) to (D)]. Reproduced with permission from Antonopoulos AS et al.* ***Sci Transl Med****., 2017. 9(398).*

1.7. Imaging perivascular adipose tissue

1.7.1. Imaging phenotyping of adipose tissue composition

Non-invasive imaging modalities enable the direct characterisation of adipose tissue depots in the human body. However, each modality has its own strengths and weaknesses and has found application in different clinical settings (Figure 1.5). In addition, while some modalities are widely used in everyday clinical practice, others remain rather experimental and only used in the context of pre-clinical or small-scale clinical studies. For instance, dual energy X-ray absorptiometry (DEXA) is often used to measure the

total body fat mass based on the body absorption of X-ray beams emitted at distinct energy levels [127]. Despite its ease-of-use and wide availability, DEXA does not allow an accurate and detailed segmentation of specific anatomical adipose tissue depots (e.g. EAT, VAT, SAT or PVAT). Ultrasound on the other hand can be used to measure the two-dimensional thickness of the subcutaneous or gluteal adipose tissue depots [128], whereas transthoracic echocardiography can provide an easy, yet operator-dependent

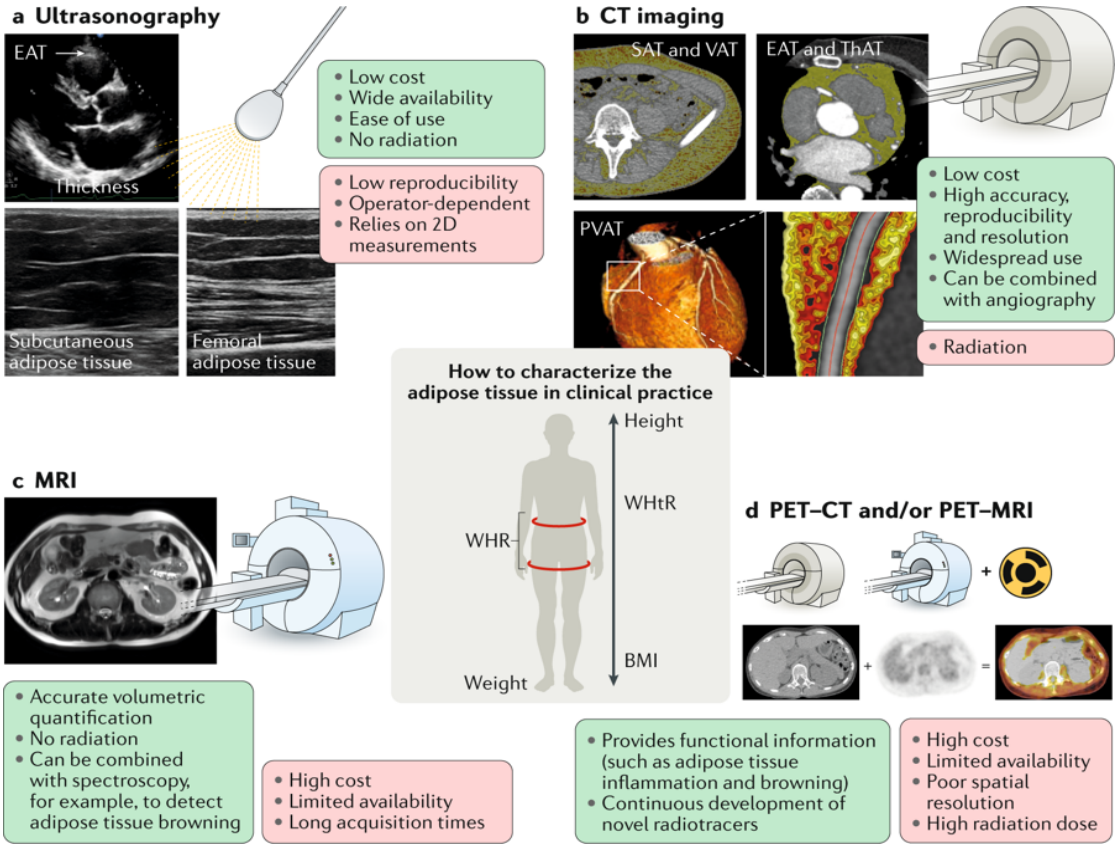

Figure 1.5. Relative advantages and disadvantages of commonly used imaging modalities to characterise the human adipose tissue. *Commonly used anthropometric indices such as the body mass index (BMI) do not capture critical adipose tissue features, such as distribution, biology and overall body fat composition. Alternative anthropometric measurements, such as waist-to-hip ratio (WHR) and waist-to-height ratio (WHtR), are more appropriate obesity indices of cardiometabolic risk than BMI but still do not provide important information on adipose tissue biology and visceral distribution. Several widely used clinical imaging modalities can be employed to provide this information, with each modality having its relative advantages (green boxes) and limitations (red boxes) compared with the others. 2D: two-dimensional; CT: computed tomography; EAT: epicardial adipose tissue; ThAT: thoracic adipose tissue; MRI: magnetic resonance imaging; PET: positron-emission tomography; PVAT: perivascular adipose tissue. SAT: subcutaneous adipose tissue; VAT: visceral adipose tissue. Reproduced with permission from Oikonomou EK & Antoniades C.* ***Nat Rev Cardiol****, 2019. 16(2):83-99.*

estimation of EAT thickness [129]. However, two-dimensional measurements are often poorly associated with three-dimensional volumes and similarly to DEXA, do not allow the segmentation of specific volumes of interest. Magnetic resonance imaging overcomes most of these limitations but is limited by longer acquisition times and limited availability [130].

Computed tomography imaging is one of the most commonly used clinical imaging modalities and enables a detailed characterisation of structures in the human body, powered by its submillimeter spatial resolution and calibrated protocols that rely on the relative attenuation of X-ray beams as they pass through the human body to characterise tissue composition [82]. Using pre-defined and validated attenuation thresholds (i.e. -190 to -30 Hounsfield Units [HU]) several studies have assessed volumetric features of several adipose tissue depots, including SAT, abdominal VAT [82] and EAT [131]. In addition, the quantitative nature of CT (i.e. each voxel is characterised by an attenuation value − Hounsfield Unit that describes its relative radiodensity compared to water) enables an indirect assessment of relative tissue density, therefore adding a qualitative dimension to the volumetric characterisation of adipose tissue depots [132]. More importantly, specific CT protocols that rely on contrast administration for the opacification of the vascular lumen, such as coronary CT angiography, enable the simultaneous assessment of vascular anatomy and segmentation of the perivascular adipose tissue depots [126].

In some cases, the anatomical information provided by CT can be further supplemented by ^{18}F-FDG-PET imaging, which, as described earlier, reflects the metabolic and inflammatory activity of adipose tissue [124, 133, 134]. Of note, high ^{18}F-FDG uptake in coronary PVAT has been linked to the extent of coronary atherosclerosis as well as presence of vasospastic angina in humans [133, 134]. However, PET-CT

imaging has the same limitations that were discussed earlier in this thesis in terms of radiation exposure, clinical availability and costs. In addition, in our experience ^{18}F-FDG-imaging for coronary PVAT assessment is limited by myocardial spill-over which may persist despite strict preparation protocols.

1.7.2. The perivascular Fat Attenuation Index (FAI): basic concepts

Based on the relative strengths and wide clinical applicability of CT, we hypothesised that CCTA would represent an ideal modality to assess both the coronary anatomy while also characterising the phenotype of PVAT. As discussed earlier, CT imaging generates a matrix of standardised CT numbers, commonly known as Hounsfield Units (HU). By definition, a voxel consisting of only water will have a HU value of 0, whereas air corresponds to a HU value of -1000 [135]. From a histological standpoint, adipose tissue consists of adipocytes with varying size or degrees of lipid accumulation and differentiation, as well as a stromal fraction that occupies the inter-adipocyte space, consisting of a network of extracellular matrix proteins, microvessels, inflammatory cells, fibroblasts and others [28]. The plasticity observed in the adipose tissue is attributed to the complex interplay between these entities and their dynamic responses to external stimuli [109]. We have previously shown that in response to pro-inflammatory stimuli pre-adipocytes lose their ability to differentiate and accumulate intra-cellular lipids [126]. Further to the direct effects on adipocyte structure which may take a few days to manifest (as supported by ex vivo studies), inflammation also results in the recruitment of pro-inflammatory cells in the adipose tissue and triggers neoangiogenesis and eventual ECM remodelling [109]. In other words, inflammation is associated with a reduction in the lipid content of adipose tissue (adipocyte content), and a relative increase in the ratio of the inter-adipocyte to intra-adipocyte space. Whereas the former is primarily composed of an

interstitial space composed of ECM, inflammatory cells, fibroblasts and others, the latter is primary composed of lipid/triglyceride droplets. Based on the physics of CT, fat is less radiodense than water/fibrotic tissue and is therefore characterised by lower (negative) HU values. We therefore hypothesised that the dynamic plasticity of AT that manifests as dynamic changes in adipocyte size, lipid content, ECM and vascular remodelling, could be detected at the macroscopic level as a shift in the relative CT attenuation of a given adipose tissue depot.

In previous studies, adipose tissue segmentation had been performed on CT studies using a validated HU range of -190 to -30 HU [136]. Nevertheless, treating this 160 HU-wide range as a homogenous depot fails to take into account the variability that exists between different depots, or between different sites within the same depot. As we have discussed in earlier sections, adipose tissue is characterised by marked heterogeneity and plasticity in its biological profile, including adipocyte size and inflammatory cell infiltration. In order to track this shift in AT composition from a less inflamed (mature, lipid-laden adipocytes [↑lipid/water balance]) towards a more inflamed state (small, lipid poor-adipocytes with inflammatory cell infiltration, ECM remodelling, neoangiogenesis etc [↓lipid/water balance]), we defined the CT-based Fat Attenuation Index (FAI) [126]. FAI was originally defined as the average attenuation of all voxels in a given adipose tissue volume of interest (defined as all voxels with HU values in the -190 to -30 range), and reflects the relative balance between the lipophilic and aqueous component in the adipose tissue [126]. Therefore, an inflammation-induced change in the adipose tissue composition and reduction in adipocyte size/lipid content could potentially be detected

non-invasively as a shift in the mean CT attenuation towards less negative HU values (away from -190 and closer to -30 HU) (Figure 1.6) [126].

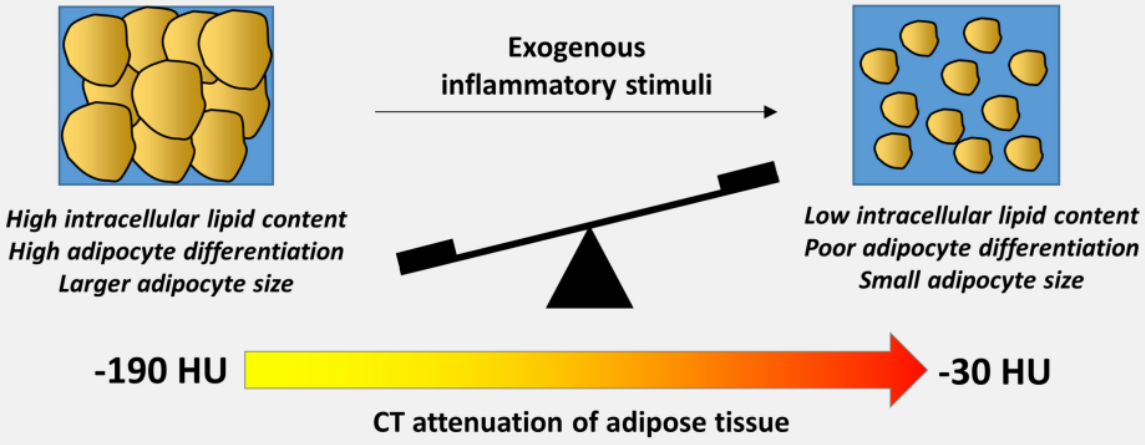

Figure 1.6. Computed tomography-derived adipose tissue attenuation as a marker of adipose tissue composition/phenotype. *In the presence of exogenous inflammatory stimuli, adipocytes lose their ability to differentiate into large, lipid-laden cells (left side) and are instead characterised by decreased cell size, lipid accumulation and poor differentiation status (right side). This correlates with a shift in the composition of AT from a greater lipophilic to a greater aqueous content, which correlates with a gradient in the attenuation of AT on computed tomography (CT) from more negative to less negative Hounsfield Unit (HU) values. Reproduced with permission from Oikonomou EK et al.* ***Heart****, 2018. 104(20): p. 1654-1662.*

1.7.3. The perivascular Fat Attenuation Index (FAI): validation studies

To validate the biological meaning of FAI, we first obtained adipose tissue biopsies from the subcutaneous, thoracic (pericardial) and epicardial depots of 453 patients undergoing cardiac surgery [126]. Ex vivo CT scanning of these biopsies confirmed that in all depots, higher FAI values were inversely associated with adipocyte differentiation (as assessed by the relative expression of *CEBPA* and *FABP4*) as well as adipocyte size. In addition, in a pilot study of 39 volunteers with ^{18}F-FDG PET-CT imaging, I demonstrated that there is a strong positive association between the degree of AT inflammation (assessed by the target-to-background ratio [TBR] of ^{18}F-FDG uptake) and FAI measured on plain CT, suggesting that FAI is a good surrogate marker of AT inflammation (Figure 1.7).

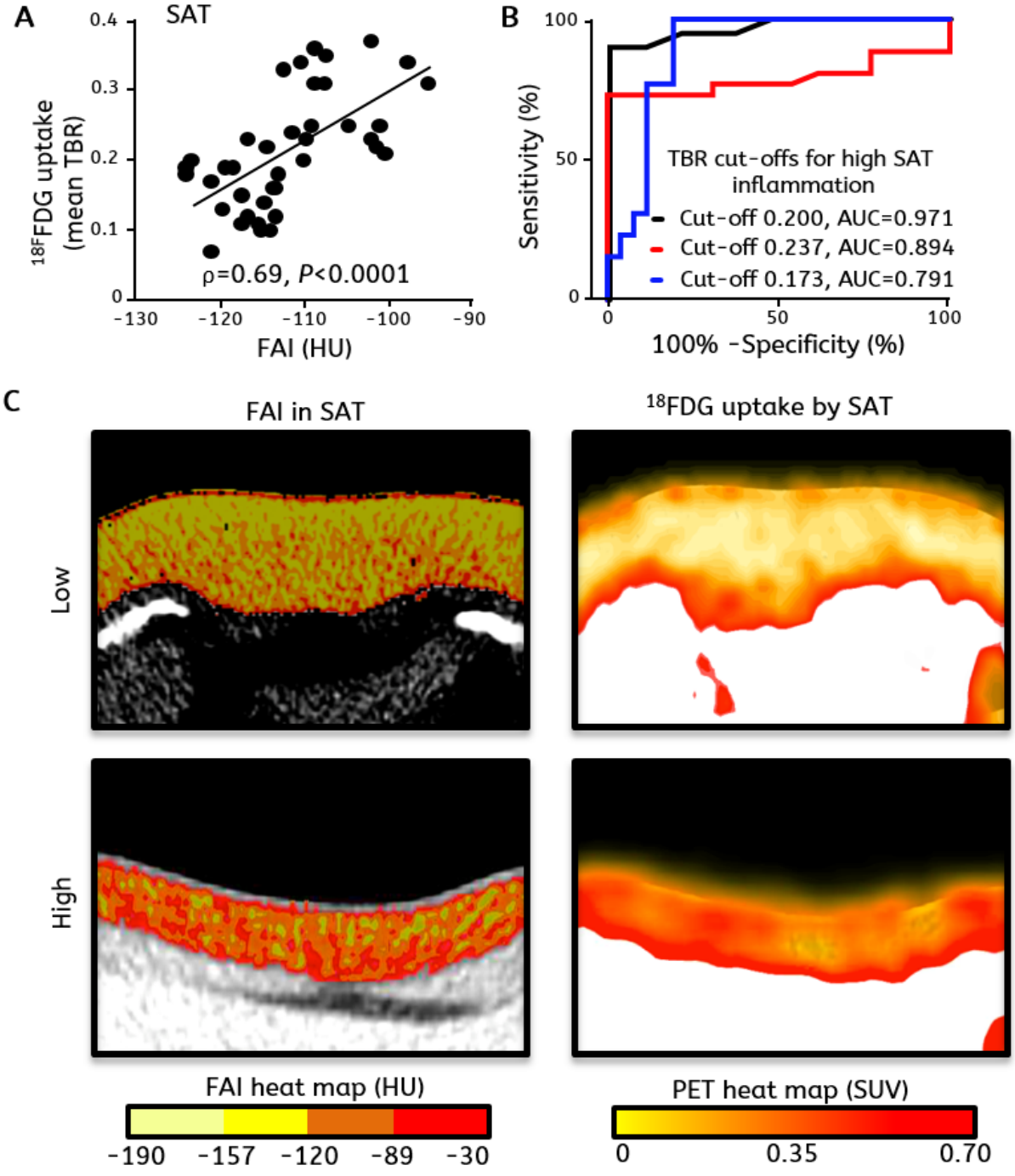

Figure 1.7. Association between adipose tissue inflammation and Fat Attenuation Index (FAI). ***(A)*** *Association between ^{18}F-fluorodeoxyglucose (FDG) uptake of subcutaneous adipose tissue (SAT) by PET/CT [determined as the mean tissue-to-background ratio (TBR)] with FAI of the same tissue (n = 39) and* ***(B)*** *receiver operating characteristic curves for identification of highly inflamed SAT by FAI according to ^{18}F-FDG uptake measured by PET/CT.* ***(C)*** *Representative examples of FAI and 18F-FDG uptake heat maps in SAT. AUC: Area under the curve; HU: Hounsfield Unit; SUV: standardised uptake value. Reproduced with permission from Antonopoulos AS et al.* ***Sci Transl Med****., 2017. 9(398).*

As discussed earlier coronary inflammation is associated with an in vivo gradient in adipose tissue composition phenotype around the coronary vessels. We observed that the expression of adipocyte differentiation markers (*PPARG*, *CEBPA* and *FABP4*) was down-regulated closer to the RCA, whereas there was no difference in the expression of inflammatory mediators and macrophage infiltration or polarisation. Accordingly, perivascular adipocytes were significantly smaller compared to non-perivascular ones [126]. Taken together, these findings suggested that paracrine inflammatory signals originating from the coronary vessels prevent lipid accumulation in the surrounding PVAT, but these effects become less pronounced with increasing distance from the vascular wall.

To examine whether FAI phenotyping could track this in vivo perivascular gradient in PVAT phenotype, we developed a new analysis algorithm that enabled the segmentation of PVAT around a coronary vessel of interest and the analysis of FAI in concentric cylindrical layers around the vascular wall (Figure 1.8). When we applied this perivascular FAI mapping technique around the RCA in a cohort of 273 subjects undergoing CCTA, we observed a progressive decrease in FAI to more negative values with increasing distance from the RCA wall. More importantly, this gradient was more pronounced in patients with CAD versus those without CAD, a finding driven by significantly higher perivascular FAI values in the first few mm away from the coronary wall. Of note, no significant difference was observed in the FAI of the non-perivascular space (20 mm away), suggesting that these morphological changes are confined to PVAT [126]. It should be noted that while FAI phenotyping can be applied around all coronary vessels, the RCA was selected in this proof-of-concept analysis given the absence of major branches, relatively straight course, abundance of epicardial adipose tissue in the right

atrioventricular groove, all of which enabled the reliable definition of PVAT and non-PVAT depots [126].

In summary, coronary atherosclerosis and inflammation are associated with reduced lipid content in the adjacent PVAT, which can be detected non-invasively by quantifying the perivascular FAI on standard CCTA. However, this observation led to a number of questions that formed the main focus of my DPhil thesis. For instance, does FAI phenotyping offer incremental diagnostic and prognostic information beyond simple coronary atherosclerosis assessment? Do the inflammation-induced changes in PVAT as detected by FAI precede the formation of coronary atherosclerosis? Is the presence of

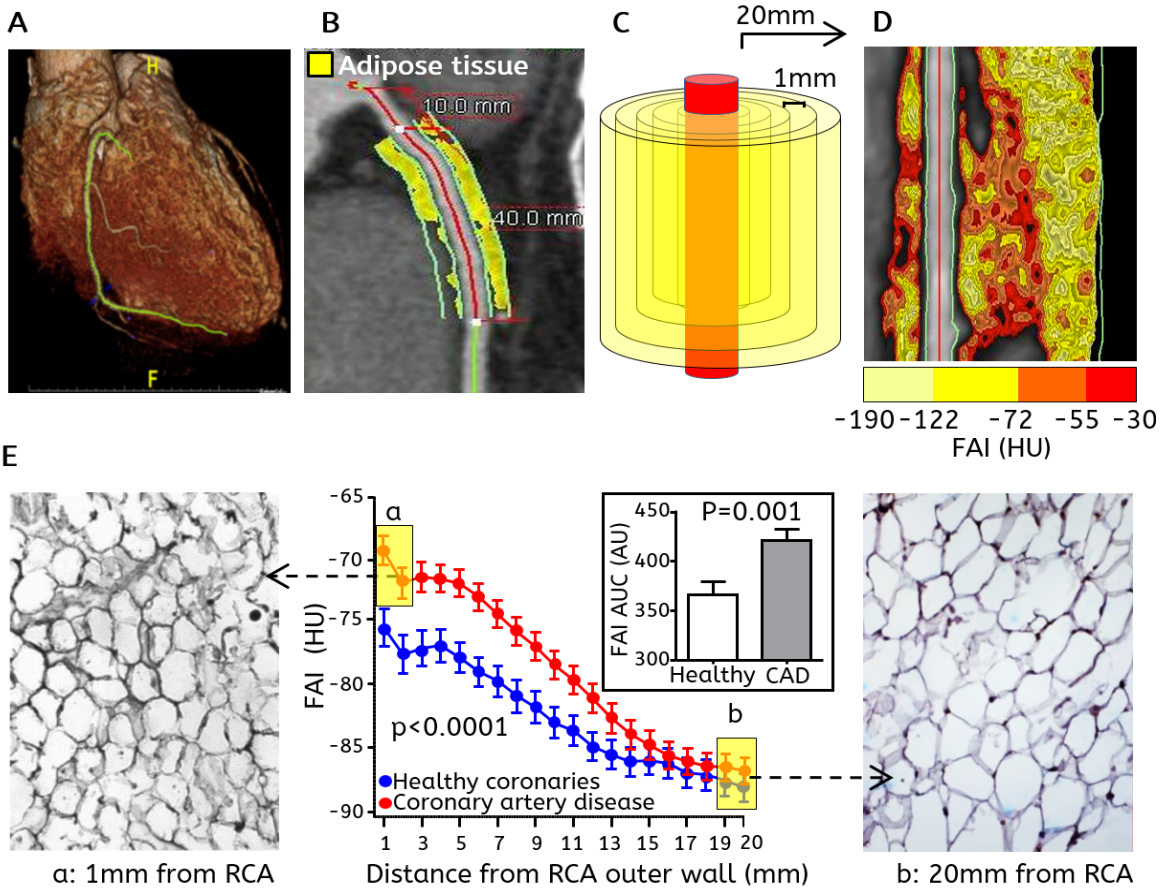

Figure 1.8. Perivascular fat attenuation index detects coronary artery disease (CAD). (A-C) *Fat attenuation index (FAI) for each cylindrical 1-mm-thick layer of perivascular adipose tissue around the right coronary artery (RCA).* ***(D)*** *FAI mapping of PVAT around the RCA.* ***(E)*** *Perivascular FAI and radial distance from the RCA in patients with CAD versus healthy individuals. Reproduced with permission from Antonopoulos AS et al.* ***Sci Transl Med****., 2017. 9(398). AUC: are under the curve; HU: Hounsfield Units.*

unstable, highly inflamed coronary lesions associated with distinct phenotypic changes in the adjacent PVAT? Is it possible to detect these changes non-invasively using CCTA imaging? What is the distribution of perivascular FAI in a typical population referred for CCTA, and what range of values can be classified as normal or abnormal? These questions are explored in Chapters 3 and 4 of this thesis.

1.8. Radiomic applications in adipose tissue characterisation

CT scans are more than plain images; they are data. This notion forms the basis of the field of "Radiomics", a rapidly expanding field of imaging processing that extracts large amounts of quantitative information from imaging data in order to create high-dimensional datasets for data mining [137, 138]. The calculated features, commonly known as radiomic features, range from simple volumetric, shape-related or first order statistics (such as mean or median attenuation), to second and higher-order statistics that describe the texture of a segmented volume and the spatial relationship of voxels with similar or different attenuation values [137, 139]. Such features can identify imaging patterns of significant clinical value that may not be easily recognisable by the naked eye [4, 137].

The main concept in radiomic analysis is that of the radiomic texture. Statistical texture refers to "*the stochastic or random properties of the spatial distribution of gray levels within an image using statistical measures, such as, marginal probabilities*" [138]. As opposed to shape-related or first-order statistics which are derived directly from an attenuation histogram ignoring the distribution of attenuation values in the three-dimensional space, texture statistics (e.g. gray level uniformity or entropy) reflect the unique spatial arrangement of voxels [4, 140]. These second- or higher-order statistics are derived from gray-level intensity matrices, as described in greater detail in Chapter 2.

Originally applied in the field of cancer imaging and tumor segmentation where radiomic features had been found to discriminate malignant from benign lesions [141], radiomic approaches had only found limited application in cardiovascular imaging at the time I started my project. However, they provided a standardised and comprehensive method to identify phenotypic variations in the perivascular fat phenotype around the global coronary tree by encoding spatial information in all dimensions. For example, radiomics enable the assessment of relative changes in fat attenuation in the x, y and z planes (e.g. moving from more proximal to more distal parts of a coronary vessel, as well as radially away from the coronary artery wall). They also possess the ability to capture spatial patterns and discontinuities in the fat structure, which could be linked to other hallmarks of adipose tissue remodelling, including fibrosis and vascular remodelling. This concept is explored in detail in Chapter 5 of this thesis.

1.9. Hypotheses and aims

The principal hypothesis of my doctoral project is that CCTA-based PVAT characterisation and FAI analysis is a promising way to extract information about the inflammatory status of the coronary tree. Therefore, it could be used to improve early cardiovascular disease diagnosis and risk stratification in patients undergoing CCTA as part of their clinical care.

In order to investigate these hypotheses, this thesis aims to:

a) Explore the ability of perivascular FAI analysis to detect unstable, culprit lesions in patients presenting with AMI;
b) Assess the dynamic nature of FAI in tracking longitudinal changes in coronary inflammation following an AMI event;

c) Explore the value of FAI in predicting the future progression of coronary atherosclerosis.

d) Investigate the cross-sectional association of perivascular FAI with markers of CAD presence/severity, CAD extent and traditional cardiometabolic risk factors;

e) Determine the value of FAI in predicting the future incidence of adverse cardiovascular events and whether this is independent of and incremental to traditional risk factors and the standard interpretation of CCTA scans, and finally;

f) Build on the biology behind the FAI and use machine learning-based approaches to generate new imaging biomarkers that can detect the full phenotypic heterogeneity and remodelling seen in PVAT in response to atherogenesis.

2

Chapter 2. General Methods

The present chapter examines the study design, patient populations and general methods used to explore the diagnostic and prognostic value of CCTA-based PVAT phenotyping. First, I present a general overview of the individual studies that were used in this thesis. Next, I discuss the general cardiac CT protocols that were used in these studies and the post-processing and analysis of the obtained images. This includes a description of the workflow in the Oxford Academic Cardiovascular Computed Tomography (OXACCT) core laboratory and the standard operating procedures that have been designed to govern this process. Finally, I describe the method development for the techniques of CT-based perivascular fat characterisation, as well as standard CT analysis techniques, including the assessment of the degree and extent of coronary stenosis, epicardial adipose tissue volume and quantitative coronary plaque burden.

2.1. Study populations included in this thesis

This thesis included six distinct study populations that were used to assess the value of CCTA-based PVAT characterisation in multiple stages of the natural history of coronary atherosclerosis (Figure 2.1). This includes the early formation and progression of coronary plaque burden and calcification, plaque rupture associated with acute coronary syndromes and finally the incidence of hard clinical endpoints, such as cardiac-specific mortality and non-fatal myocardial infarction.

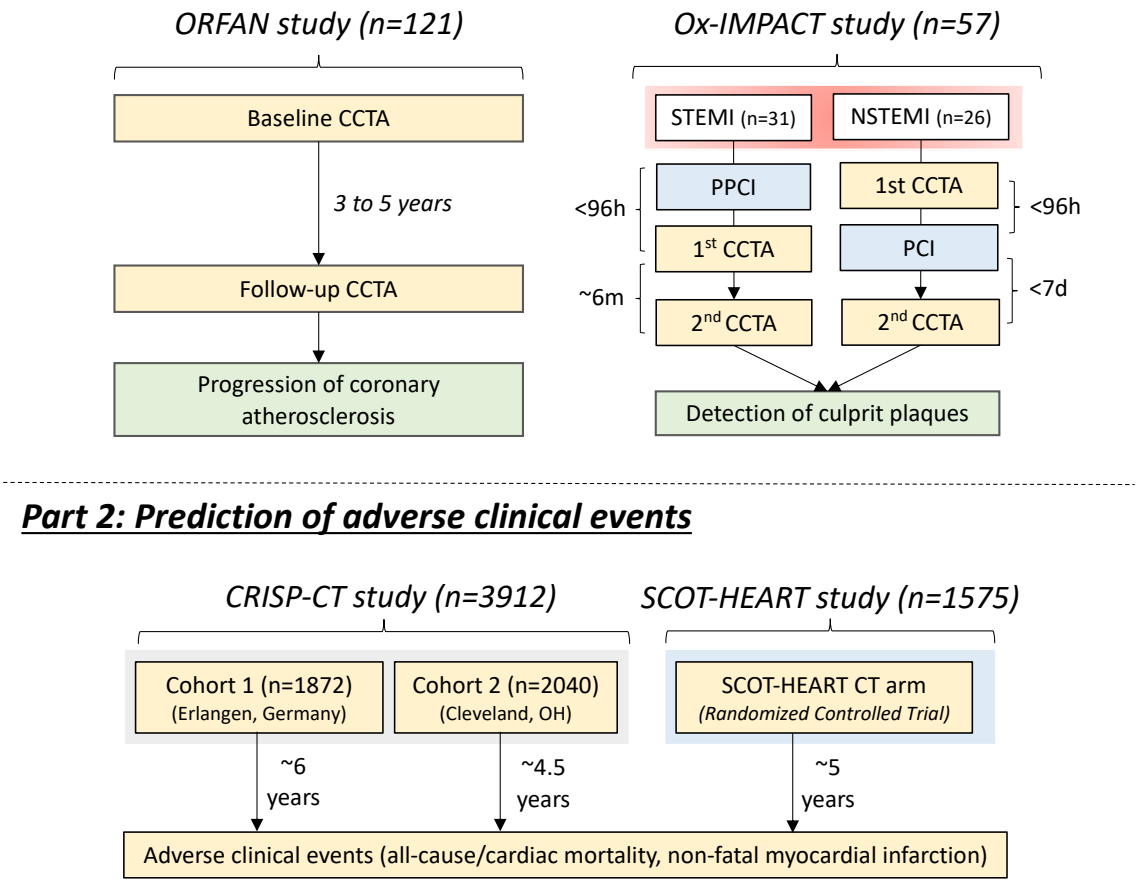

Figure 2.1. Overview of the study design and patient populations included in this thesis. *CCTA: coronary computed tomography angiography; CRISP-CT: Cardiovascular Risk Prediction using Computed Tomography study; CCTA: coronary computed tomography angiography; CT: computed tomography; (N)STEMI: (non)-ST-segment elevation myocardial infarction; ORFAN: Oxford Risk Factors And Non-invasive imaging; Ox-IMPACT: Oxford Imaging of Perivascular adipose tissue in Acute coronary syndromes using Computed Tomography study; (P)PCI: (primary) percutaneous coronary intervention; SCOT-HEART: SCOTtish computed tomography of the HEART trial.*

2.1.1. Coronary atherosclerosis progression: The ORFAN study

The ORFAN-Arm 3 (Oxford Risk Factors And Non-invasive imaging [Oxford Research Ethics Committee C reference 15/SC/0545]) study is a prospective cohort study that recruits patients that have previously undergone clinical CCTA, who are then invited to undergo a follow-up research CCTA scan three to five years later to explore longitudinal changes in the severity and extent of coronary atherosclerosis. A total of 121 patients were recruited to this study arm between April 2016 and July 2018. The records of the Radiology department in the John Radcliffe Hospital (Oxford University Hospitals NHS Foundation Trust, Oxford, United Kingdom) were screened for eligible participants that underwent a CCTA scan in or after 2011 and the patient information leaflet and an invitation letter were sent by post. Participants who agreed to be contacted directly were then scheduled for a follow-up research CCTA scan at the Manor Hospital (Nuffield Health, Oxford, United Kingdom). All males and females aged 18-99 were eligible for inclusion in the study, if willing and able to provide informed consent. Patients were excluded if they had a history of active cancer (diagnosis < 5 years ago or currently undergoing cancer-directed treatment). On the day of the follow-up visit, a brief interview was conducted with the study participants to collect information on demographics, anthropometrics, cardiovascular risk factors and history and active medications. The subsequent CCTA scan was performed according to the local guidelines of the Manor Hospital. However, in order to ensure consistency in technical, acquisition parameters that may confound quantitative CCTA measurements the CT tube voltage was kept consistent between the baseline and the follow-up scan. In addition, given the length of time between the baseline and follow-up scans, it was impossible to use the exact same hardware (CT scanner) in both study visits. However, across the study population the same scanner was used for all baseline visits, with a newer, different scanner used for all

follow-up visits to minimise bias. All images were then transferred to the OXACCT Core Lab for image analysis in a paired manner (baseline and follow-up scans analysed sequentially) in order to explore the association between baseline PVAT characterisation and future changes in coronary atherosclerotic plaque composition and burden.

2.1.2. Unstable lesions in acute coronary syndromes: the Ox-IMPACT study

The Ox-IMPACT (Oxford Imaging of Perivascular adipose tissue in Acute coronary syndromes using CT [Oxford Research Ethics Committee C reference 17/SC/0058]) study is a single-centre, two-arm study that includes patients (males and females, 18 years or older, able to provide informed consent) presenting with ST- or non-ST-segment elevation myocardial infarction (STEMI=Arm 1; NSTEMI=Arm 2) and undergoing invasive angiography with percutaneous coronary intervention in the John Radcliffe Hospital (Oxford University Hospitals NHS Foundation Trust, Oxford, United Kingdom). Exclusion criteria were as follows: inability or unwillingness to consent, pregnant or breast-feeding patients, chronic atrial fibrillation, known advanced hepatic disease, active treatment for cancer, known chronic kidney disease stage IIIB or above (estimated glomerular filtration rate <45 mL/min), haemodynamic instability (blood pressure <90mmHg), documented previous allergy to the contrast agent used for the CCTA, known anaemia (haemoglobin <9 g/dl), involvement in other studies which might have a potential effect on participant health or the study data, and any other medically important factor, as assessed by the medical team or study investigators.

In Arm 1, STEMI patients were approached following the successful deployment of a stent as part of primary percutaneous coronary intervention and were asked to undergo two CCTA scans; the first within 96 hours of presentation prior to their discharge from the hospital and the second within six months of the first scan. In Arm 2,

NSTEMI patients admitted over the weekend or overnight and scheduled for urgent (but not emergent) coronary angiography were asked to undergo a series of research CCTA scans; the first before their invasive coronary angiography and the second within seven days of successful PCI (if performed). Since this was an observational study, no medical or lifestyle recommendations were given, which were left at the discretion of their clinical care team. Once consent was provided, a short interview was conducted with the study participants to collect information on demographics, anthropometrics, cardiovascular risk factors and history, and active medications.

All CCTA scans were performed at the John Radcliffe Hospital using a 64-slice General Electric LightSpeed Ultra CT scanner and stable acquisition parameters across all timepoints for each patient (tube voltage, slice thickness, mAs, pitch, field of view). During each visit, 20 mL of blood were drawn from the intravenous cannula inserted for contrast administration and whole blood, plasma and serum were collected and stored. It was explained to all participants that these CCTA scans were done for research use only and were not used to guide clinical decision-making. Incidental findings (n=1; lung nodules) were managed based on the standardised operating procedures of the OXACCT Core Lab and the University of Oxford. Following successful PCI for a culprit lesion, all patients were started on optimal medical therapy as per the local clinical guidelines (high-dose atorvastatin, dual antiplatelet therapy, angiotensin converting enzyme inhibitor (or angiotensin II receptor blocker) and appropriate beta-blocker therapy (unless contra-indicated or not tolerated). This study design enabled to explore the association between PVAT imaging biomarkers on CCTA and the presence of unstable plaques, as well as their longitudinal changes following a plaque rupture event.

2.1.3. Predicting adverse cardiac events: the CRISP-CT study

To explore the association between CCTA-based PVAT phenotyping and the future incidence of adverse cardiovascular events we designed the CRISP-CT (Cardiovascular RISk Prediction using Computed Tomography) study [142]. This study included two independent, prospective cohorts of individuals undergoing CCTA in two major imaging centres, one in Erlangen, Germany (University of Erlangen-Nurnberg, Germany) and one in Cleveland, Ohio (Cleveland Heart and Vascular Institute). Cohort 1 (Erlangen, Germany) included a total of 1993 consecutive CCTA scans performed between 2005 and 2009 with a median follow-up of 72 (51 to 109) months, whereas Cohort 2 (Cleveland, USA) consisted of 2246 CCTAs performed between 2008 and 2016 with a median follow-up of 54 (4 to 105) months. Patients that were specifically referred for assessment of congenital heart disease/defects were excluded from the cohorts. This clinical design enabled me to explore a) the cross-sectional association of perivascular FAI with traditional cardiovascular risk biomarkers, and b) its prognostic value for hard clinical events, independent of traditional risk factors and standard interpretation of CCTA scans.

2.1.4. Identifying the residual cardiac risk: the SCOT-HEART study

As discussed in the introduction of this thesis, the results of clinical CCTA scans are used to guide downstream management and clinical decision-making. Residual inflammation has been recognised as a major source of residual atherosclerotic risk and a driver of subsequent adverse cardiac events despite "optimal management" [15]. In an effort to understand whether coronary PVAT may function as a sensor and predictor of this residual vascular inflammatory risk, our team collaborated with the SCOT-HEART investigators who kindly granted access to the CCTA arm of the SCOT-HEART study (NCT01149590) [42, 43]. Briefly, SCOT-HEART was a prospective open-label, parallel-

group, multicentre trial, which recruited a total of 4146 patients aged 18–75 years referred for the assessment of suspected angina due to coronary heart disease from 12 cardiology chest pain clinics across Scotland. The study participants were randomly assigned (1:1) to standard care plus CCTA or standard care alone. The full protocol and results of this randomised controlled trial have been previously published and are available to review [42, 43]. Contrary to the CRISP-CT study which was an observational cohort [142], SCOT-HEART was a randomised trial in which CCTA scanning was the intervention of interest [142]. As such, patients were closely followed and management was optimised based on the results of the CCTA scan (antiplatelet and/or statin therapy, revascularisation as appropriate). In this context, the incidence of adverse cardiac events among participants randomised to CCTA assessment represented the *residual* cardiac risk that persisted despite optimal guideline-directed therapy (Figure 2.2). Overall, a total of 1786 available CCTA scans were transferred to the OXACCT

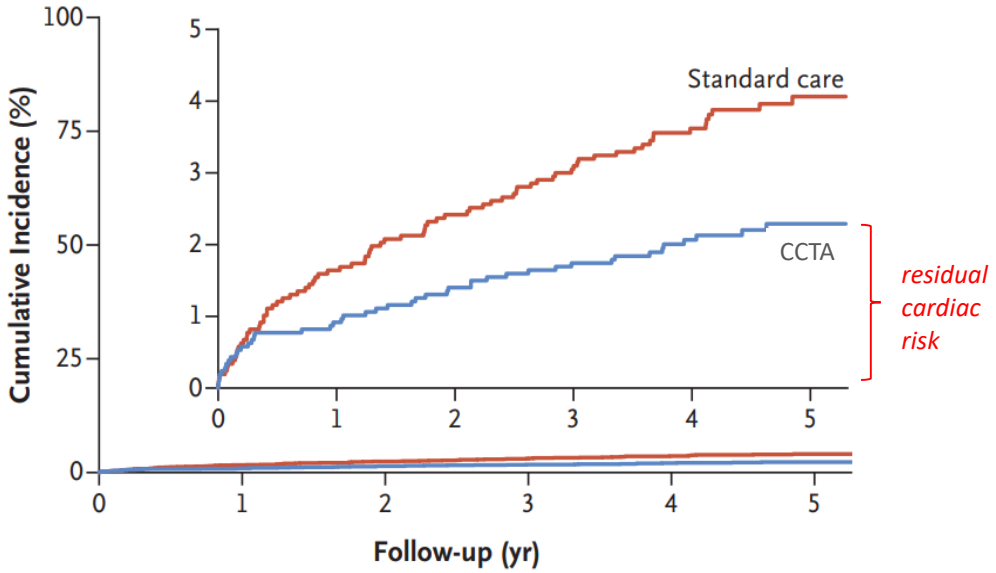

Figure 2.2. Residual cardiac risk in the SCOT-HEART trial. *Kaplan-Meier curves of the cumulative incidence of cardiac mortality and/or non-fatal myocardial infarction in the groups of chest pain patients randomised to either CCTA or standard care. While at five years the CCTA arm had a significantly lower incidence of the composite endpoint compared to the standard care arm, the five-year incidence of adverse cardiac events exceeded 2%. Modified with permission from SCOT-HEART Investigators et al.* ***N Engl J Med****, 2018. 379(10): p. 924-933.*

Core Lab for analysis on dedicated workstations. Using the most recent five-year follow-up outcome data, as reported in reference #[43], I searched for imaging features in the coronary PVAT that are associated with the residual cardiac risk observed in this population.

2.1.5. Biological validation of imaging biomarkers: AdipoRedox study

Finally, in order to understand the biological meaning of different adipose tissue CT imaging biomarkers, I designed a sub-study as part of the Oxford Heart, Vessels & Fat cohort. This included patients undergoing coronary artery bypass grafting surgery that were recruited as part of the AdipoRedox study (Oxford Research Ethics Committee C reference 11/SC/0140) and who agreed to further undergo CCTA. Adipose tissue biopsies were collected intra-operatively from the subcutaneous adipose tissue depot at the incision site. Subsequent gene expression analysis enabled the correlation of the adipose tissue biological profile with its imaging phenotype, as quantified in CCTA. More details on the methods used are presented later in this thesis.

2.2. Coronary computed tomography angiography protocols

This section describes the methodology and standardised operating procedures for the performance of CCTA scans in the aforementioned studies. Since some studies were performed in Oxford (i.e. ORFAN, Ox-IMPACT & AdipoRedox studies) by me and other member of our research team, whereas others were performed in external centers (CRISP-CT and SCOT-HEART studies), a slightly modified protocol was used in each imaging center in accordance with local expertise, hardware and guidelines.

2.2.1. Local research CCTA protocols

John Radcliffe Hospital, Oxford, United Kingdom: Participants in the Ox-IMPACT (*research CCTA* in patients with STEMI or NSTEMI), ORFAN (*clinically-indicated* CCTA *at baseline*) and AdipoRedox studies (*research CCTA* patients undergoing cardiac surgery) underwent CCTA using a 64-slice scanner (General Electric LightSpeed Ultra, General Electric Healthcare) (Figure 2.3). Heart rate was optimised using intravenous injection of beta-blockers to achieve a heart rate of less than 65 beats per minute, unless medically contra-indicated. Sublingual glyceryl-trinitrate (800ug) was also administered to achieve maximum coronary vasodilatation, unless contraindicated or declined by the patient. In the AdipoRedox (but not ORFAN or Ox-IMPACT studies) a non-contrast prospectively ECG triggered axial acquisition CT scan was obtained first (0.35 sec rotation time, 2.5 mm axial slice thickness, 20 mm detector coverage, tube energy of 120 kV and 200 mA) with the carina and the diaphragm used as cranial and caudal landmarks respectively.

Figure 2.3. *The 64-slice General Electric LightSpeed Ultra (General Electric Healthcare) system in the John Radcliffe Hospital, Oxford, United Kingdom.*

Lung field of view was extended to cover the entire thoracic soft tissue (for subcutaneous adipose tissue analysis). In all studies, CCTA was performed following intravenous injection of 60-95ml of iodine-based contrast medium (Niopam 370, BRACCO) at a flow rate rate of 5-7 mL/sec (tube energy of 100 or 120 kVp, axial slice thickness of 0.625 mm, rotation time of 0.35 sec). The selection of these technical parameters was selected based on body type to ensure optimal image quality. Prospective image acquisition was used in most cases by ECG-gating at 75% of cardiac cycle (with additional padding if needed). In the presence of irregular rhythm or high heart rate not responsive to beta blockers, retrospective gating was used as a last resort.

Manor Hospital, Oxford, United Kingdom: Participants in the ORFAN study returning for a follow-up research scan underwent CCTA using a 320-slice scanner (Aquilion ONE, Toshiba Medical Systems) (Figure 2.4). Heart rate was optimised using intravenous injection of beta-blockers to achieve a heart rate of less than 65 beats per minute, unless medically contra-indicated. Sublingual glyceryl-trinitrate (800ug) was also administered to achieve maximum coronary vasodilatation, unless contraindicated or declined by the patient. Between 60 and 80 ml of iodine-based contrast medium (Niopam 370, BRACCO) were given at a flow rate rate of 5-7 mL/sec (tube energy of 100 or 120 kVp, axial slice thickness of 0.50 mm, tube rotation 0.35 sec). A standard CCTA reconstruction algorithm was used to generate a set of images at the 75% phase of the heart cycle as well as the best phase +/- 10% temporal window. Prospective image acquisition was used in most cases by ECG-gating at 75% of cardiac cycle. In the presence of irregular rhythm or high heart rate not responsive to beta blockers, retrospective gating was used as a last resort.

Figure 2.4. *The Toshiba Aquilion ONE computed tomography (CT) scanner in the Manor Hospital, Oxford, United Kingdom.*

2.2.2. External CCTA protocols

Cleveland arm (CRISP-CT study): CCTA scans were performed using either a 256-slice Brilliance iCT scanner (Philips Medical Systems, Best, The Netherlands), a 2 x 128-slice Definition Flash scanner (Siemens Healthcare, Erlangen, Germany) or a 2 x 192-slice Somatom Force CT scanner (Siemens Healthcare, Forchheim, Germany). In patients with heart rate > 60 beats/minute, 5 mg of intravenous metoprolol (with incremental 5 mg doses up to a maximum dose of 30 mg) or intravenous diltiazem (5 mg increments up to 20 mg maximum), if the heart rate remained above 60 beats per minute once the patient was positioned on the CT table. Patients also received 0.3 mg of nitroglycerin sublingually immediately before CCTA and iodinated contrast (Omnipaque 350, General Electric, Milwaukee, USA) was administered at flow rate of 5-6 ml/s.

Erlangen arm (CRISP-CT study): CCTA scans were performed using either a 2 x 64-slice scanner (Definition Flash, Siemens Healthcare, Forchheim, Germany), a 64-slice (Siemens Sensation 64, Siemens Healthcare, Forchheim, Germany) or a 2 x 128-slice scanner (Somatom Definition Flash, Siemens Healthcare, Forchheim, Germany). Oral medication with 100 mg atenolol was administered one hour before CT if heart rate was > 60 beats per minute with additional 5 mg doses of metoprolol intravenously up to a maximum dose of 30 mg, if the heart rate remained above 60 beats per minute once the patient was positioned on the CT table. Patients also received 0.8 mg of nitroglycerine sublingually immediately before CCTA and iodinated contrast (Omnipaque 350, Schering AG, Berlin, Germany) was administered at flow rate of 5-6 ml/s.

SCOT-HEART study: CCTA scans were performed using either two 64 detector row scanners (Brilliance 64, Philips Medical Systems, Netherlands, and Biograph mCT, Siemens, Germany) and one 320 detector row scanner (Aquilion ONE, Toshiba Medical Systems, Japan) at three imaging sites (refs [42, 143]) according to each site's local protocol.

2.3. The Oxford Academic Cardiovascular Computed Tomography (OXACCT) lab

For all research studies included in this thesis, image analysis was performed in the OXACCT Core Lab (Level 6, West Wing, John Radcliffe Hospital, Oxford, U.K., Head: Prof. C. Antoniades). As the lead image analyst for the OXACCT Core Lab, I designed a set of systems and standardised operating procedures to govern the processes relating to image transfer, storage, analysis and data control. In all cases, scans were collected from their source as DICOM (.dcm) files and transferred to the core lab. An exclusive server dedicated to these research studies (The Aquarius Workstation® V.4.4.11-13,

TeraRecon Inc., Foster City, CA, USA) was used to create an accessible library of all research CCTA scans. Access was restricted to authorised users affiliated with the OXACCT core lab and at all stages only anonymised data were used for analysis.

2.4. Quality control of image datasets

The first step in the processing and image analysis of the obtained images was the performance of a quality control check, based on the guidelines of the Society of Cardiovascular Computed Tomography for the interpretation and reporting of CCTA. Based on these recommendations, CCTA should preferably be acquired as isotropic submillimeter 3-dimensional electrocardiography-gated data sets to enable reliable reconstruction of the obtained images and display in various formats [48]. The checklist used for the quality control of the CCTA scans is presented in Table 2.1.

Table 2.1. Technical review and quality assurance of obtained coronary CT angiograms.

Field	Checklist
File format	Are the images stored as DICOM files (or related DICOM-files, e.g. .IMA files)?
Anonymisation	Do the DICOM files contain non-anonymised data?
Date and Time	Does the Study ID, date and time of the scan match what is expected?
CT scanner	Scans should be performed using 64-slice CT scanners or higher
Contrast	Is there adequate opacification of the aortic root? (mean HU of aortic root lumen >200)?
Completeness	Are all slices present?
Image window	Does the window extend from the bifurcation of the pulmonary artery to the apex?
Slice thickness	Was the scan obtained as an isotropic submillimeter 3-dimensional ECG-gated data set?
Tube voltage	Ideally, tube voltage should be set at 120 or 100 kVp.
Motion artefacts	Are there any motion or step artefacts affecting the interpretation of the scan?
Blooming artefacts	Are there artefacts caused by stents/pacemakers leads etc. that affect the interpretation and visualisation of adjacent coronary vessels?

CT: Computed Tomography; ECG: electrocardiogram; HU: Hounsfield Units.

If a CCTA scan was deemed to be of low quality it was excluded from any subsequent analysis. For instance, scans that were performed at tube voltage settings other than 120 or 100 kVp (most commonly used and recommended settings in most centers and scanners) were excluded from inclusion in our studies since most attenuation-based metrics are not adequately validated at these settings [57]. Similarly, CCTA scans with suboptimal opacification of the aortic and coronary artery lumen were excluded since they did not allow an accurate quantitative or qualitative assessment of coronary atherosclerosis burden. Images with missing slices or affected by motion, stair-step or blooming artefacts affecting the region of interest were also excluded from the analysis. Although, exclusion of such suboptimal tests may introduce bias, it should be noted that this is not uncommon in clinical practice. In fact, a substantial percentage of clinical CCTAs are found to be non-diagnostic due to artefacts or suboptimal image acquisition [144]. A representative selection of such artefacts and examples is presented in Figure 2.5.

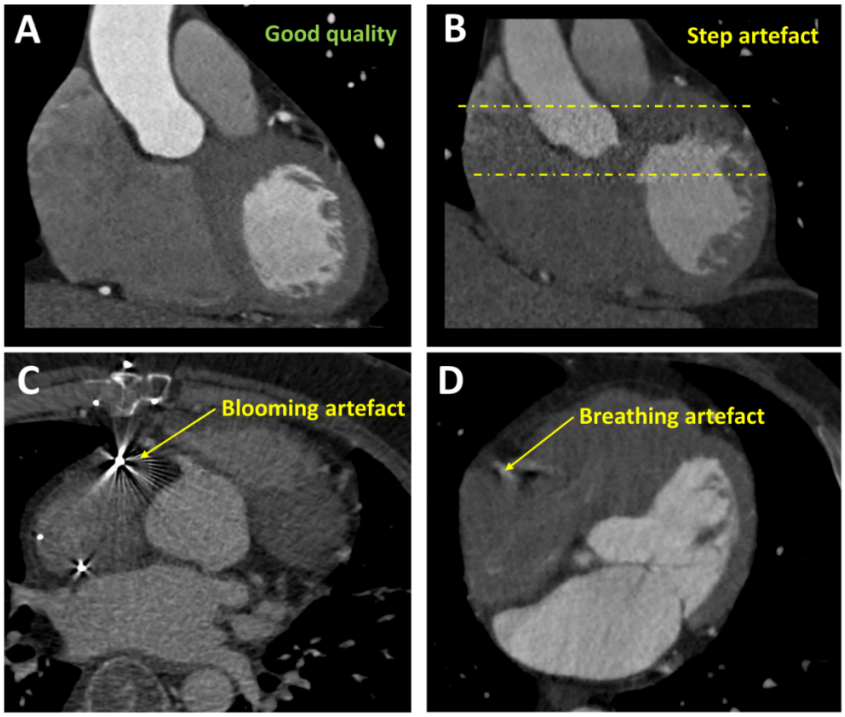

Figure 2.5. Quality control and common image artefacts. (A) *A coronal view of a good quality coronary computed tomography angiogram (CCTA).* ***(B)*** *A stair-step artefact due to the use of a CT scanner that obtains the whole image in three different subset before stitching them together.* ***(C)*** *Blooming artefact due to a pacemaker lead that obscures the right coronary artery.* ***(D)*** *Breathing/motion artefact which results in blurring of the right coronary artery contour.*

2.5. Agatston coronary calcium score (CCS)

When obtained (e.g. Erlangen arm of the CRISP-CT study and SCOT-HEART studies), non-contrast ECG-gated cardiac CT scans were used to a) get a preliminary assessment of cardiac anatomy and presence of coronary or extra-coronary calcification; and b) get a quantitative assessment of coronary calcium by means of the CCS. CCS was computed using commercially-available software (Aquarius Workstation® V.4.4.11-13, TeraRecon Inc., Foster City, CA, USA) using the Agatston method that takes into account the volume as well as density of coronary calcifications (Figure 2.6) [48, 145]. Voxels with attenuation values that exceeded 130 HU on non-contrast CT scans corresponding to calcium were highlighted by the semi-automated software. The reader then scrolled through the axial slices of the cardiac CT scan and reviewed each highlighted area, before circling it and assigning it to a coronary territory (left main, LAD, RCA, LCX). The values for each

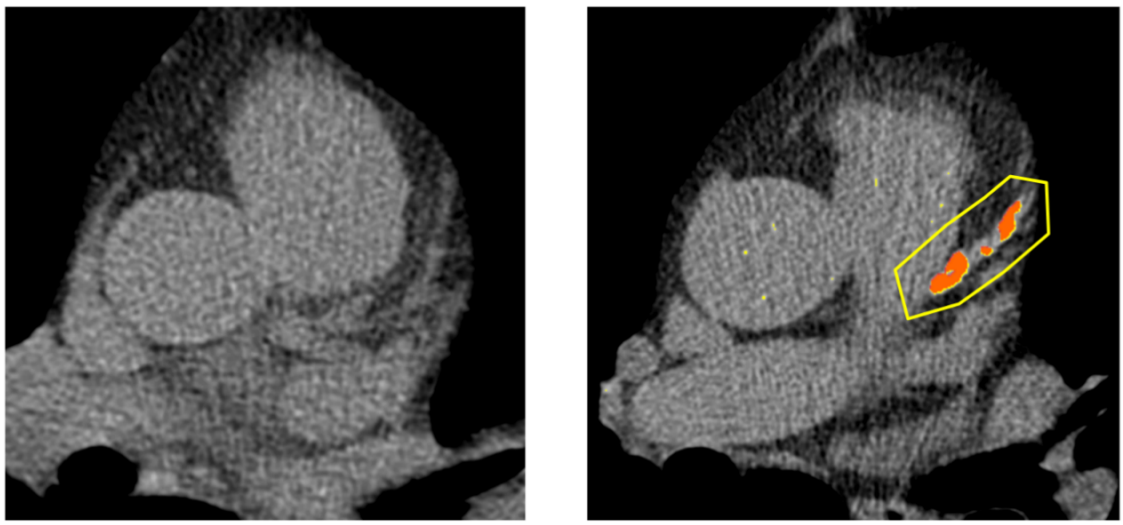

Figure 2.6. Agatston coronary calcium scoring (CCS). *On non-contrast, thick-slice (2.5 to 3 mm axial thickness) cardiac computed tomography scans, voxels in the coronary vessels with Hounsfield Unit (HU) values >130 HU are selected and a score is assigned to each one of them based on their volume and attenuation (higher score assigned for higher attenuation values). The sum of these scores is then computed to produce the total Agatston CCS, a common marker of coronary atherosclerosis which is often used to stratify the cardiac risk of patients and guide the initiation of prevention strategies, such as statin therapy. Left panel: CCS=0; Right panel: CCS>0 with significant calcification in the left anterior descending artery.*

vessel distribution were then summed to generate the Agatston CCS. Extra-coronary calcifications in the aorta, valves, pericardium or myocardium were excluded from the CCS [48, 145].

2.6. Qualitative coronary analysis

Because coronary anatomy can be very complex, motion or calcium-related (e.g. blooming) artefacts are frequent, and coronary lesions are often morphologically subtle, CCTA scans were reviewed on a dedicated cardiac-specific workstation (Aquarius Workstation® V.4.4.11-13, TeraRecon Inc., Foster City, CA, USA) in various, 2- and 3-dimensional reconstruction formats. This included a review of the 2-dimensional image stacks (i.e. axial, sagittal and coronal) as well as multiplanar reformations (MPR) around the tracked centerline of a given coronary vessel. In the presence of heart-rate related artefacts where padding or retrospective gating was performed, alternate times in the cardiac cycle were reviewed to identify the optimal phase for analysis.

2.6.1. Coronary artery stenosis assessment

When reviewing the coronary tree on CCTA, a systematic approach was followed by segmenting the coronary vasculature into 18-segments as recommended by the Society of Cardiovascular Computed Tomography (Figure 2.7) [59]. An initial examination was performed for the course and branching of the main coronary vessels. Then, the lumen and wall of the coronary vessels were examined for the presence of luminal plaque and the maximal percent diameter stenosis was reported. The assessment of stenosis severity was performed using manual measurement tools on the reconstructed images and was used to classify the lesion in one of the pre-defined ranges/groups of stenosis severity. Briefly, mild, moderate and severe coronary stenoses were defined as lesions causing

luminal stenosis 25-49%, 50-69% and ≥70%, respectively [59, 146]. Where mentioned, obstructive CAD was defined as the presence of at least one coronary stenosis ≥50% on coronary computed tomography angiography (CCTA).

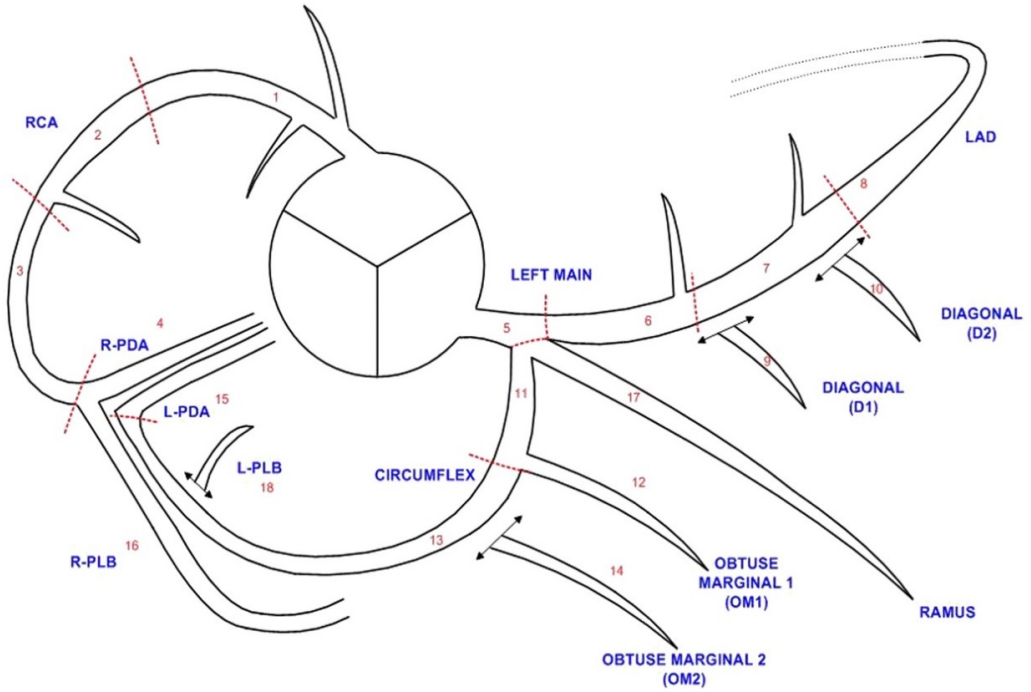

Figure 2.7. Coronary segmentation based on the recommendations of the Society of Cardiovascular Computed Tomography. *1: proximal right coronary artery (RCA); 2: mid RCA; 3: distal RCA; 4: right posterior descending artery (R-PDA); 5: left main coronary artery; 6: proximal left anterior descending (LAD) artery; 7: mid LAD; 8: distal LAD; 9: first diagonal (D1); 10: second diagonal (D2); 11: proximal left circumflex (LCX); 12: obtuse marginal 1 (OM1); 13: distal LCX; 14: obtuse marginal 2 (OM2); 15: left posterior descending artery (L-PDA); 16: right posterolateral branch (R-PLB); 17: ramus intermedius; 18: left posterolateral branch (L-PLB). Reproduced with permission from Leipsic, J., et al.* ***J Cardiovasc Comput Tomogr****, 2014. 8(5): p. 342-58.*

2.6.2. High-risk plaque feature assessment

High-risk plaque features on CCTA were defined based on previous work by Puchner et al [60]. The following four high-risk plaque features were identified and recorded; a) low-attenuation plaque, napkin-ring sign, spotty calcification and low-attenuation plaque (Figure 2.8) [142]. In the CRISP-CT study the analysis was performed by me and other

members of our team, whereas in the SCOT-HEART trial the high-risk plaque features were reported by the study investigators.

Low attenuation plaque was defined as the presence of low CT attenuation in a non-calcified plaque. More specifically, I placed three random region-of-interest measurements (approximately 0.5-1.0 mm^2) in the non-calcified low CT attenuation portion of a given plaque. If the mean CT number within these 3 regions of interest was <30 HU, the patient was identified as having a low-attenuation plaque.

Spotty calcification was defined as the presence of calcified plaque with a diameter <3 mm in any direction, length (extent in the longitudinal direction of the vessel) of the calcium less than 1.5 times the vessel diameter and width (extent of the calcification perpendicular to the longitudinal direction of the vessel) of the calcification <2/3 of the vessel diameter.

Positive remodelling was assessed visually in multi-planar reformatted images reconstructed in long axis and short axis view of the vessel. The remodelling index (RI) was calculated by dividing the cross-sectional lesion diameter by the diameter of a proximal, reference segment and a threshold of 1.1 was used to define positive remodelling.

Finally, *napkin ring sign* was defined as a ring-like peripheral higher attenuation of the non-calcified portion of the coronary plaque [60]. It should be noted that the latter feature is rather operator-dependent and has often been excluded from studies assessing the prognostic role of high-risk plaque features [147]. Nevertheless, in order to ensure a comprehensive assessment of coronary anatomy and in line with the recommendations of the Society of Cardiovascular Computed Tomography [59], it was included in our analysis and models.

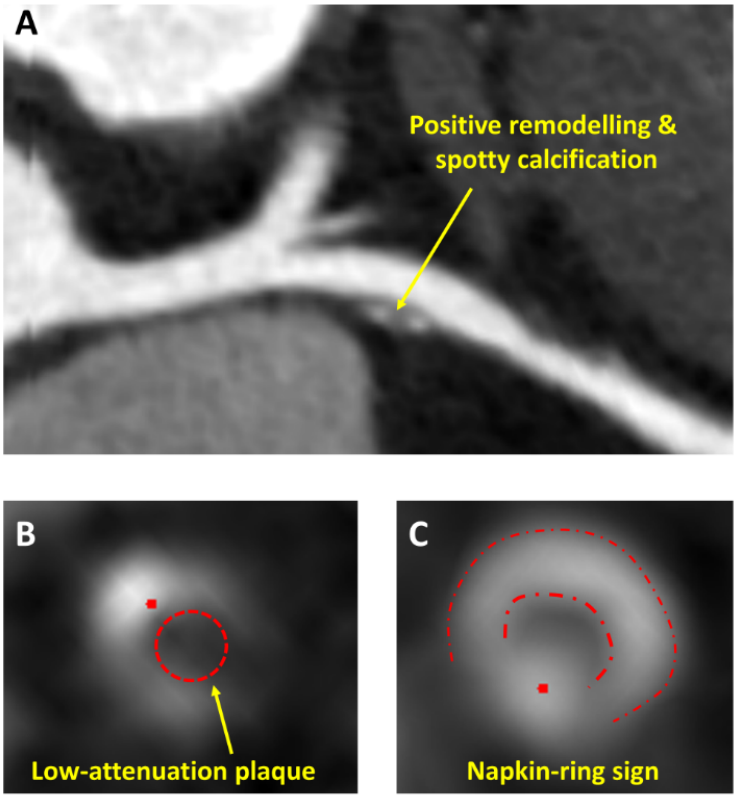

Figure 2.8. Representative images of high-risk plaque features on CCTA. *Panel A demonstrates a coronary plaque with positive remodelling and spotty calcification, panel B shows a lesion with low-attenuation plaque (<30HU), whereas panel C demonstrates a typical "napkin-ring" sign. CCTA: coronary computed tomography angiography; HU: Hounsfield Units.*

2.7. Quantitative coronary plaque analysis

Comprehensive, quantitative coronary plaque burden assessment was performed using commercially available CCTA analysis software (AutoPlaque™, version 2.0, Cedars-Sinai Medical Center, Los Angeles, CA) [148]. First, a region of interest was placed in the aortic root at the level of the left main coronary artery to sample the mean and the distribution of lumen opacification/attenuation in the arterial tree. This enabled the generation of scan specific attenuation thresholds for the definition of different plaque components (i.e. calcified, non-calcified and low-attenuation plaque). Next, the centerline of the coronary vessel was tracked and the coronary segment of interested was identified. A semi-automated plaque analysis algorithm was able to segment the coronary artery wall and calculate the volumes of its calcified and non-calcified plaque components (Figure 2.9). The global total, non-calcified, and calcified plaque burden was calculated for each

vessel or patient by pooling the measurements from all respective coronary segments, and the relative (%) change in plaque burden was calculated as follows: 100*([plaque burden]$_{follow\text{-}up}$-[plaque burden]$_{baseline}$)/[plaque burden]$_{baseline}$.

2.8. Epicardial adipose tissue volume

Adipose tissue depots can be detected on cardiac computed (CT) tomography by applying an attenuation-based segmentation approach, which classifies voxels with attenuation values between -190 and -30 HU as adipose tissue/fat. This basic principle enables a number of different possibilities and functionalities in the non-invasive characterisation of adipose tissue quality and quantity.

Epicardial adipose tissue volume is a well-established cardiometabolic risk factor that provides a direct assessment of visceral adiposity, as opposed to anthropometric indices such as BMI. Several observational studies have described a positive association between the degree of epicardial obesity and the presence of coronary calcification, CAD,

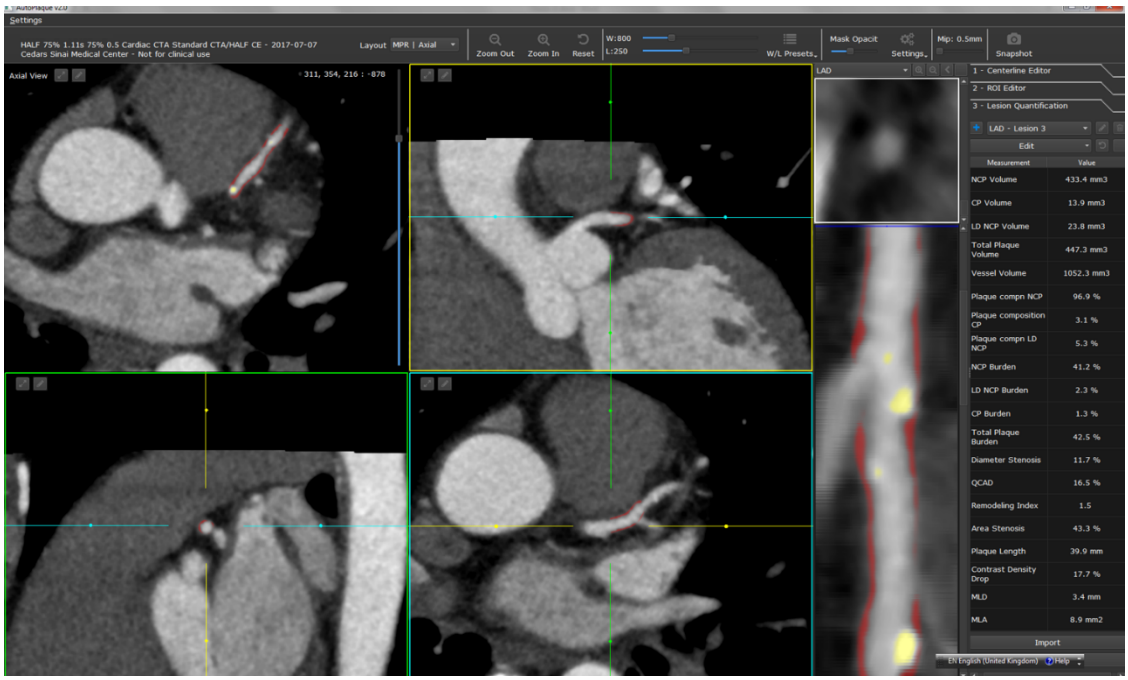

Figure 2.9. *The AutoPlaque™, version 2.0, Cedars-Sinai Medical Center, Los Angeles, CA.*

as well as the future incidence of adverse cardiac events [149]. The volume of epicardial adipose tissue can be measured on cardiac CT scans by selecting all adipose tissue-containing voxels (-190 to -30 HU) which are found between the pericardium and the myocardial surface. This analysis was performed in a semi-automated manner by tracking the contour of the pericardium from the level of the pulmonary artery bifurcation to the apex of the heart at the most caudal end (Figure 2.10) (Aquarius Workstation® V.4.4.11-13, TeraRecon Inc., Foster City, CA, USA). [142].

2.9. Perivascular adipose tissue characterisation: the Fat Attenuation Index

While the epicardial adipose tissue volume provides a volumetric assessment of visceral obesity, it fails to provide information on the paracrine interactions between coronary artery wall inflammation and its adjacent PVAT [126]. As discussed in the Introduction section, inflammation is associated with structural changes in PVAT composition that are instead detected through standardised analysis of PVAT attenuation by means of the Fat Attenuation Index. As shown in Figure 1.8, perivascular fat attenuation around the coronary vessels follows a gradient from higher towards lower attenuation values with increasing distance from the vascular wall. Unfortunately, there is no clear definition of coronary PVAT in the literature, since there is no visible anatomical barrier that separates the non-perivascular sites of epicardial adipose tissue (e.g. those attached to the free wall of the right ventricle) from the perivascular ones. In order to provide a standardised definition, I defined coronary PVAT as any fat-containing voxel (attenuation between -190 and -30 HU) within a radial distance from the outer vessel wall that is equal to the diameter of the respective/adjacent vessel. This approach is based on the following rationale and hypotheses:

- In previous biological validation studies (discussed earlier in the introduction section of this thesis) we have characterised adipose tissue gene expression patterns and demonstrated direct links between adipose tissue inflammation and weighted CT attenuation metrics independent of adipose tissue volume [126].
- The effects of coronary atherosclerosis are more pronounced in the PVAT that is directly adjacent to the coronary vessel wall. As previously shown [126], differences in PVAT attenuation between CAD and healthy patients disappear with increasing distance from the coronary wall.
- On the other hand, limiting the analysis to the first 1-mm layer of perivascular space could magnify any potential confounding role of partial voluming due to

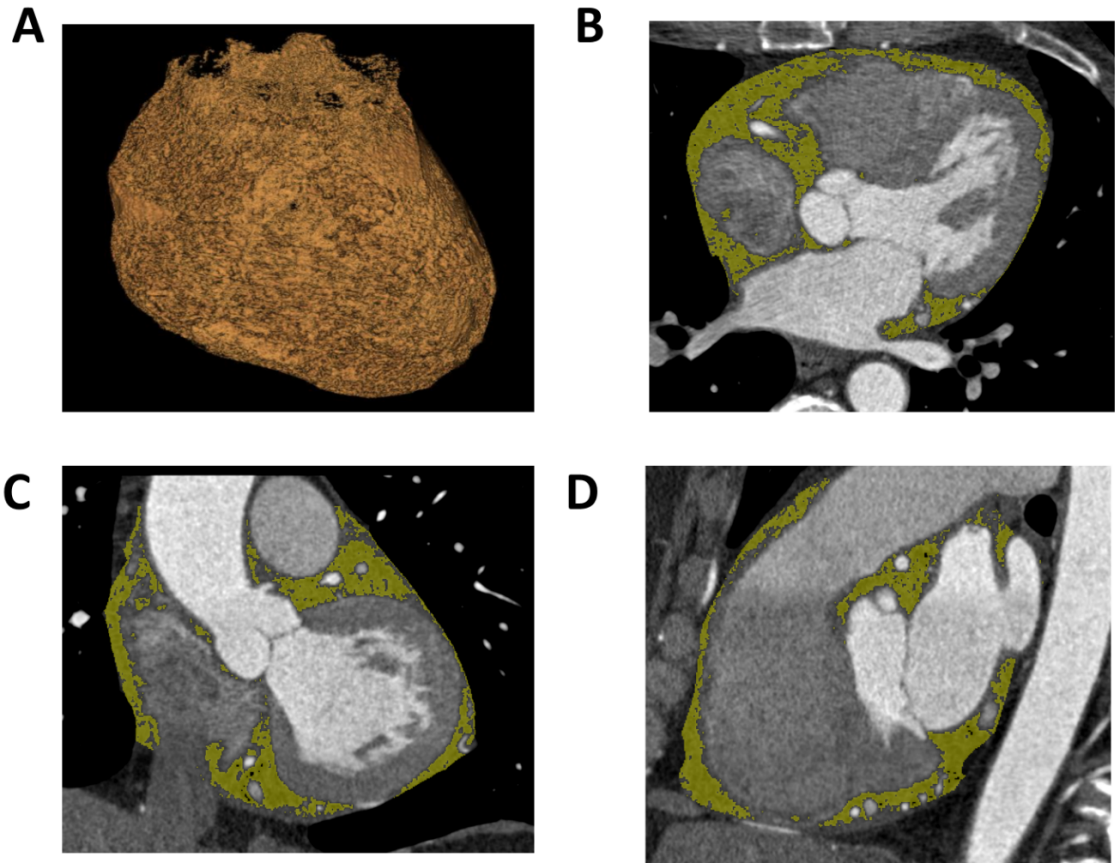

Figure 2.10. Segmentation of the epicardial adipose tissue volume. *(A) Three-dimensional reconstruction of the epicardial adipose tissue volume following segmentation of the pericardium and attenuation-based selection of all adipose tissue voxels (between -190 and -30 Hounsfield Units). (B) Axial, (C) coronal, and (D) sagittal views of the epicardial adipose tissue voxels which have been highlighted with yellow color.*

coronary calcifications. By expanding the volume of interest beyond that first 1 mm, one ensures that the contribution of partial voluming from the vessel wall to the PVAT attenuation signal remains negligible. Since the volume of a cylinder is proportional to the square of its radius, the contribution of the first 1-mm layer becomes less important.

- Several transcriptomic studies have revealed significant differences in the biological profile of peri-atrial, peri-coronary and peri-ventricular epicardial adipose tissue [95]. As a result, in order to ensure that changes in PVAT attenuation are predominantly driven by the coronary vessels rather than other neighbouring structures, the analysis had to be confined to the direct perivascular space.
- Limiting the analysis to a radial distance equal to the diameter of the adjacent vessel also enabled the expansion of the analysis to all three major epicardial coronary vessels and their branches, since there is minimal overlap between the PVAT of neighbouring coronary branches.
- Since coronary vessels vary a lot in their geometry, a definition that accounts for variations in vessel diameter was needed so that the final results are indexed for differences in coronary vessel size.
- This definition also allows the flexible application of the perivascular Fat Attenuation Index tool in different vascular beds. In other words, perivascular FAI can be computed around any coronary vessel, segment or lesion.

Following the early observations from our team regarding the potential use of coronary PVAT attenuation as a marker of coronary inflammation, I designed a standardised analysis protocol for the calculation of perivascular FAI. An important

requirement is that prior to perivascular FAI mapping all the quality control checks for a CCTA scans are satisfied (as outlined in section 2.4). For instance, slice thickness higher than 1 mm may lead to substantial partial voluming between PVAT and the coronary wall. If all requirements are satisfied then a pre-defined workflow is applied using a dedicated analysis tool that was first incorporated into the Aquarius Workstation® platform (Figure 2.11):

i. Any coronary segment can be selected for analysis and a semi-automated plaque segmentation tool is applied. This identifies the outer and inner border of the coronary vessel wall for that segment. Further manual optimisation of the contours may be performed.
ii. For a given coronary segment I defined its respective perivascular fat as the adipose tissue within a radial distance from the outer vessel wall equal to the diameter of the vessel. Application of an attenuation filter in this perivascular space then selects all fat-containing voxels in the -190 to -30 HU range. Once segmented, this volume represents the PVAT (perivascular adipose tissue) for that segment.
iii. Perivascular FAI is ascertained by quantifying the mean weighted perivascular fat attenuation after adjustment for technical parameters, based on the attenuation histogram of perivascular fat within the range −190 HU to −30 HU.
iv. Similar to findings of previous validation studies [126], technical (tube voltage, lumen attenuation) and anatomical (vessel diameter) parameters are all weakly associated with perivascular fat attenuation, accounting for roughly 5% of its variation (see also Chapter 4).

v. To adjust for differences in attenuation between scans done at different tube voltages, the perivascular adipose tissue fat attenuation index (FAI) for scans performed at 100 kVp is divided by a conversion factor of 1.11485 to be comparable to scans performed at 120 kVp, as previously validated [150].

vi. Given the standardised nature of the perivascular FAI analysis, the intra- and inter-observer agreement for the analysis were found to be excellent (intra-class correlation coefficient: 0.987 [P<0.0001] and 0.980 [P<0.0001] respectively) [142].

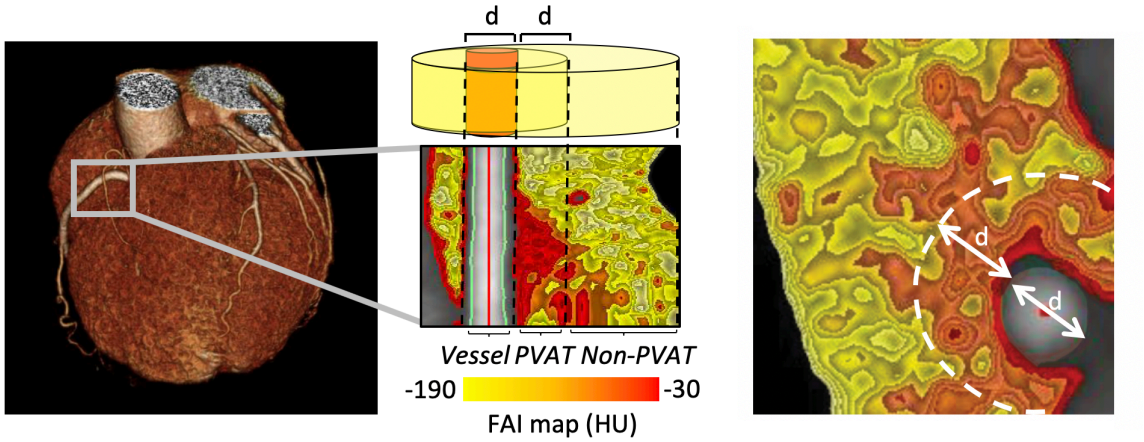

Figure 2.11. Method for perivascular Fat Attenuation Index characterisation. *First, the centerline of the vessel is extracted and then the segment of interest is identified and segmented in a semi-automated way with manual optimisation of the inner and outer vessel borders. Next, the volume of interest is expanded to include the perivascular space within a radial distance (d) from the outer wall equal to the diameter of the adjacent vessel. The perivascular FAI is then ascertained by quantifying the mean weighted perivascular fat attenuation after adjustment for technical parameters, based on the attenuation histogram of perivascular fat within the range −190 HU to −30 HU (Hounsfield Units). Reproduced with permission from Oikonomou EK et al.* ***Lancet*** *2018, Sep 15;392(10151):929-939.*

2.10. Radiomic texture phenotyping

2.10.1. Radiomic feature extraction

The first step in radiomic analysis is the segmentation of the volume of interest, whether that is a tumor or an adipose tissue depot. This is performed using standard manual or attenuation-based segmentation methods. Next, the attenuation values present in the

volume of interest are discretised into bins of a given size/HU range. The selection of the range and number of bins for discretisation relies a) on the range of HU present in the original volume of interest; and b) the signal/noise ratio. For example, for an adipose tissue segmentation with HU values in the range of -190 to -30 HU (160 HU-wide range), voxels can be discretised into two bins (each with a range of 90 HU), four bins (each with a range of 40 HU), or even 160 bins with a range of a single HU value. Evidently, the latter approach introduces a lot of mathematic complexity in the computation of radiomic features. Treating HU values of -167 and -168 HU as significantly different decreases the signal-to-noise ratio of radiomic measurements by introducing potential noise. On the other hand, using just two bins leads to loss of potentially useful information since HU values of -89 and -30 fall into the same bin. Once the volume has been segmented and discretised into bins, the next step involves the generation of the mathematical matrices (i, j) [138, 139, 151] (Figure 2.12).

Gray level co-occurrence matrix (GLCM): First described by Haralick et al in 1973 [152], GLCMs are second-order statistics, which means that they examine the relationship between *two* voxels. For a given angle (e.g. 0, 90, 180 or 270 degrees) a GLCM (i, j) matrix is calculated by computing the number of times a value j occurs to the right (or bottom, left, top) of value i (Figure 2.12). To compute rotationally invariant results, the transpose is added to the raw GLCM and the absolute values are then substituted by the frequency values. Using this normalised GLCM, multiple metrics can be calculated as described in the Appendix. For instance, GLCM entropy will increase in the presence of multiple types of gray-level transitions in a volume. On the other hand, correlation assesses the linear dependence between adjacent voxels throughout a given volume, which is inversely

proportional to an image's contrast (i.e. think of checkerboard with alternating black and white squares/voxels resulting in low correlation and high contrast) [138, 139, 151].

Gray level run-length matrix (GLRLM): Contrary to second-order statistics, higher-order statistics examine the spatial relationship between *three or more* voxels. The easiest concept within this group is that of GLRLM matrices, as proposed by Galloway, which assesses how many voxels are next to each other with same value. In the GLRLM matrix, the

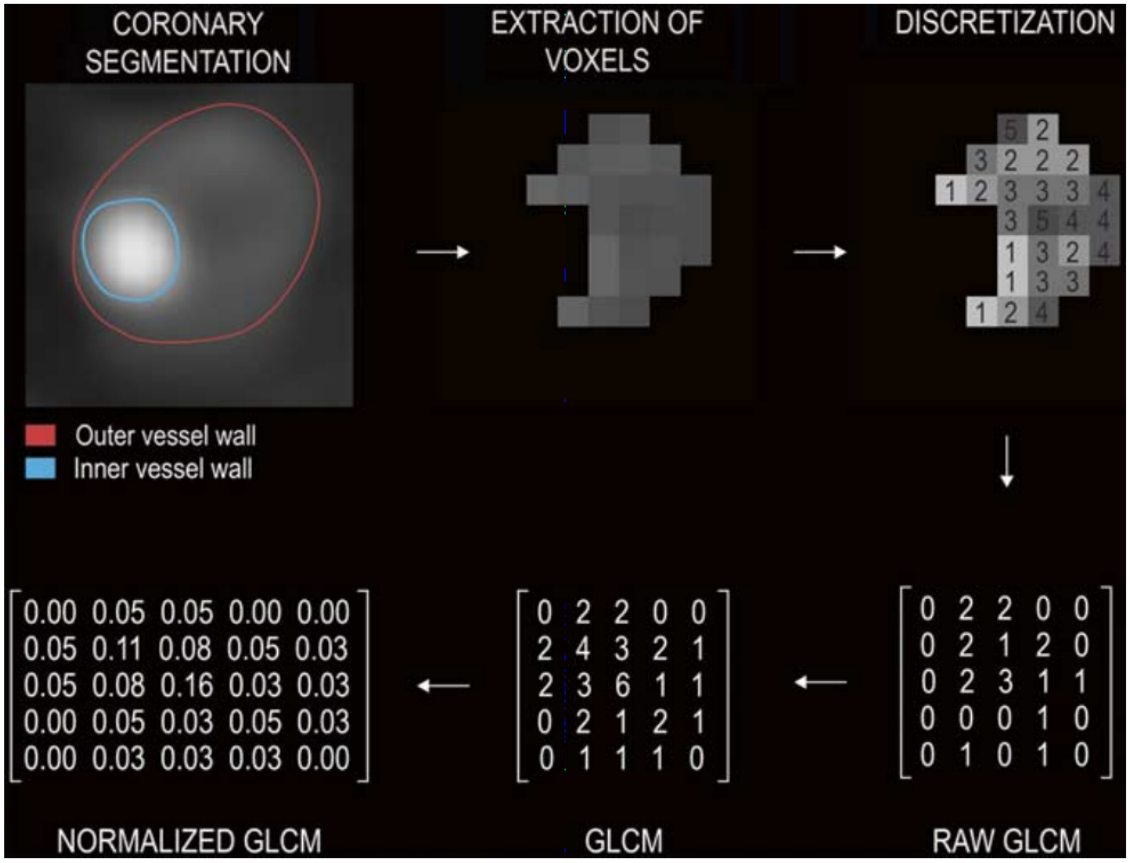

Figure 2.12. Creating a gray level co-occurrence matrix. *This example demonstrates the generation of a gray level co-occurrence matrix (GLCM) for a segmented coronary plaque. First, the voxels of interest are extracted (based on manual or attenuation-based segmentation) and are then discretised into n different value groups, known as "bins". For a given direction and distance (e.g. distance 1 voxel and angle 0 degrees) we calculate the number of times a value j is found to the right of value i. This number is then inserted into the ith row and jth column of the raw matrix. In order to ensure symmetry, the transpose is added to the raw matrix. Each number is then substituted by its frequency in order to generate a normalised GLCM. In order to ensure rotationally invariant results, the same process is repeated in all directions and then the averaged GLCM is computed and used to generate GLCM-derived radiomic features. Reproduced with permission from Kolossvary, M., et al.* ***J Thorac Imaging****, 2018.* ***33****(1): p. 26-34.*

rows refer to the attenuation values (bins) and the columns the run lengths. For instance an element in the *i*th row and *j*th column describes the number of times in the volume that *i* value voxels are next to each other *j* times. Similarly to GLCM, GLRLM are calculated in all directions and then normalised. Based on the definitions used to calculate the individual features in this group (Appendix & Figure 2.13), different weightings can be applied to short versus long runs and high versus low gray level values, thus describing different attenuation/texture patterns in the volume of interest [138, 139, 151].

Neighbouring gray tone/level different matrix (NGTDM): The neighbouring gray tone/level different matrix is a one-dimensional matrix, where each gray level entry in the matrix (defined as *gt*) is the sum of the differences between all the voxels with gray-level value *gt*

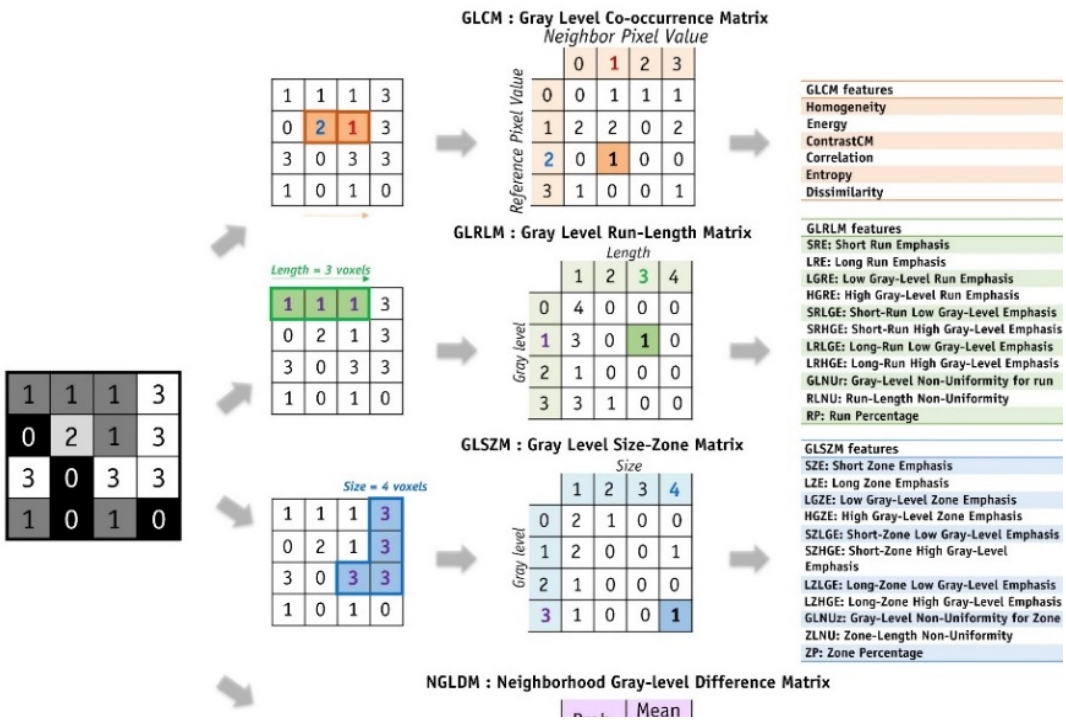

Figure 2.13. Radiomic characterization of textural features. *For a given volume of interest, histogram-based first-order features only reflect the voxel attenuation distribution. Different texture patterns (same number of voxels with similar attenuation values but different location) may still have identical histogram and therefore similar first-order statistics, such as mean attenuation, skewness, kurtosis. These differences can instead be described using higher-order features derived from texture matrices that reflect the unique spatial arrangement of voxels. Reproduced with permission from Reuze, S., et al.* ***Int J Radiat Oncol Biol Phys****, 2018. 102(4): p. 1117-1142.*

and the mean gray-level value of its neighbourhood (as described in the Appendix & Figure 2.13). This enables the calculation of radiomic features that described the visual properties of an image, such as coarseness, contrast, busyness, complexity and strength. These metrics are close to the visual interpretation of texture by humans. For instance, coarseness is a quantitative metric that reflects the difference in the radiodensity levels of neighbouring regions, whereas strength has even been associated with the visual aesthetics of an image, with higher texture strength linked to more attractive images to the human observer [138, 139, 151].

Gray level size zone matrix (GLSZM): Using different approaches and matrices more features can be defined. For instance, gray level size zone matrices (GLSZM) are similar to GLRLMs but instead of focusing on one-dimensional lengths, they focus on two-/three-dimensional zones of connected voxels (Appendix & Figure 2.13) [138, 139, 151].

Gray level dependence matrix (GLDM): Finally, a gray level dependency is defined as the number of connected voxels within distance *d* that are dependent on the center voxel. A neighbouring voxel with gray level *j* is considered dependent on center voxel with gray level *i* if $|i-j| \leq \alpha$ *(usually d=1 and a=0)*. Thus, in a GLDM, the $(i,j)^{th}$ element refers to the number of times a voxel with gray level *i* with *j* dependent voxels in its neighbourhood appears in image (Appendix & Figure 2.13).

Shape-related features: Contrary to attenuation or texture-based radiomic features, shape features describe the dimensions, shape, surface, volume and other geometric features of a segment volume of interest. As such, they are independent of the attenuation values and

derived from simple euclidean geometric analysis of a segmentation's shape (Appendix & Figure 2.13).

Wavelet transformations: Radiomic features can be calculated using both the original images as well as mathematical transformations of the original data. An image can be transformed from the original spatial domain into the frequency domain without any information loss. Rather than assigning radiodensity values to spatial (x, y, z) coordinates, the frequency domain describes the pattern and rate at which attenuation changes along spatial directions. Wavelet transforms can transform an image into the frequency domain by retaining spatial information. They rely on a window function, where the window width reflects both the spatial resolution (localisation precision) and frequency resolution (global image features). Wavelet transformation decomposes the data into high and low-frequency components (narrow and wide window respectively) (Figure 2.14). At high frequency (shorter time intervals), the wavelets can capture discontinuities, ruptures and singularities in the original data. At low frequency (longer time intervals), the wavelet characterises the coarse structure of the data to identify the long-term trends. Thus, the wavelet analysis allows extraction of hidden and significant temporal features of the original data, while improving the signal-to-noise ratio of imaging studies [153, 154]. High- and low-frequency wavelet transformations can be applied in all directions (x, y, z) resulting in eight additional datasets: HHH, HLL, HHL, HLH, LLL, LHH, LHL and LLH. Attenuation and texture-based metrics can be calculated for all of these wavelet transformations. However, since they are independent of gray level intensities, shape-related statistics are consistent across all wavelet transformations and the original CT image and are therefore calculated only once.

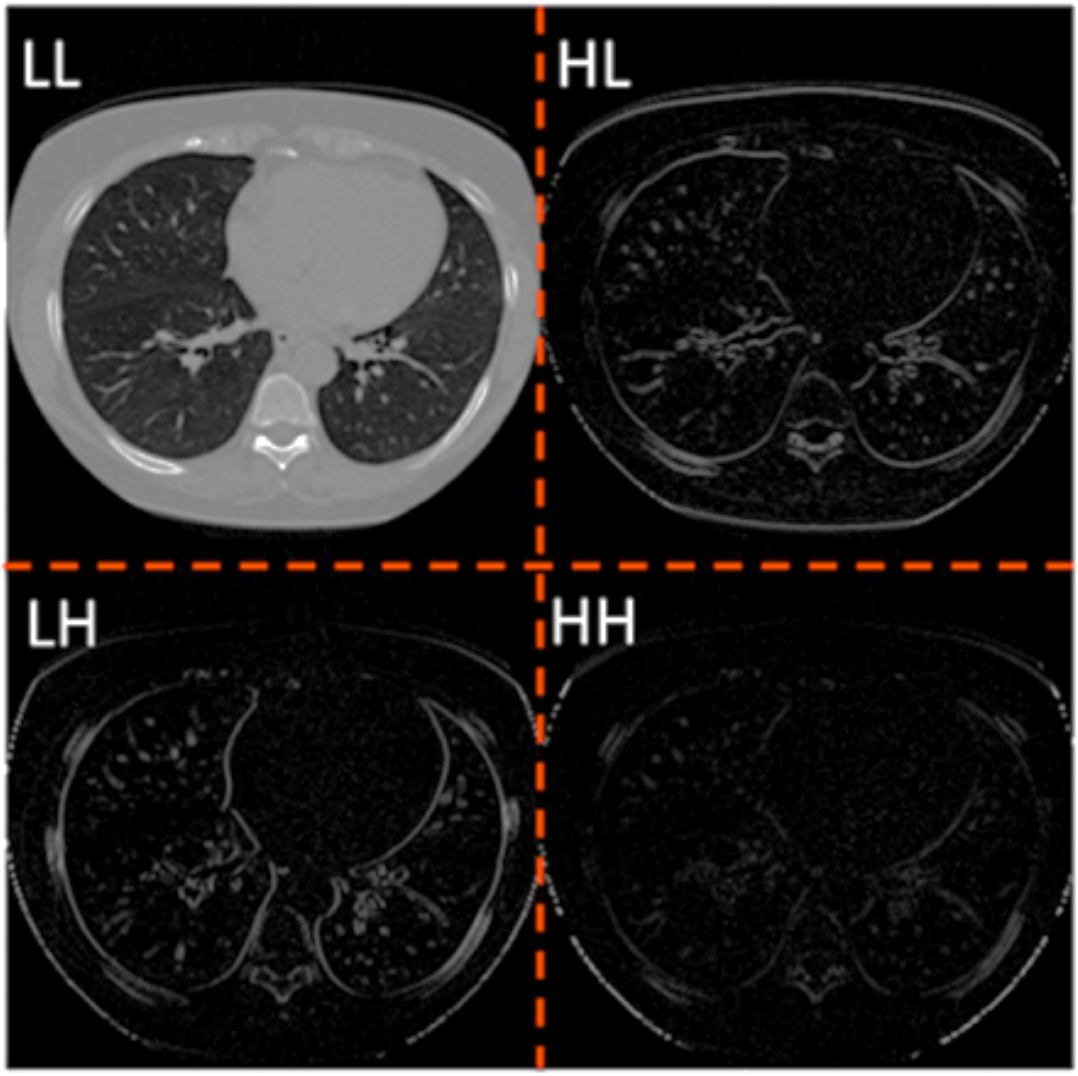

Figure 2.14. Wavelet decomposition of an axial slice from computed tomography scan. *Four wavelet transformation of the original image using high- (H) and low- (L) frequency wavelet filters along the x and y axis. In this example of a patient with lung nodules, wavelet transformations may help to distinguish true nodules from normal parenchymatous injuries or other tissues. Reproduced with permission from Orozco M et al.* ***BioMedical Engineering OnLine*** *(2015) 14:9.*

2.10.1. Human adipose tissue radiomic phenotyping

Based on the aforementioned principles, I created an algorithm/process that enables the comprehensive radiomic phenotyping of adipose tissue using computed tomography. As explained later, a radiomic approach that detects changes in the texture of perivascular adipose tissue may help uncover further high-risk patterns related to adverse PVAT fibrotic and vascular remodelling. Using the open source-software 3D Slicer (v.4.9.0-

2017-12-18 r26813) [155] (Figure 2.15), I first load the CCTA scan of interest and perform manual segmentation of the volume of interest by manually drawing around its contours and selecting all voxels in the -190 to -30 Hounsfield Unit (HU) range. For each unique AT segmentation, a total of 843 radiomic features can be calculated, ranging from shape-related to first- and higher-order (texture) statistics (Table 2.2 and Appendix Tables A1-A7), using the SlicerRadiomics extension which incorporates the Pyradiomics library into 3D Slicer [151]. Shape-related and first-order radiomic features were calculated using the raw HU values of the segmented PVAT. For calculation of texture features (Gray Level Co-occurrence Matrix [GLCM], Gray Level Dependence Matrix [GLDM], Gray Level Run-Length Matrix [GLRLM], Gray Level Size Zone Matrix [GLSZM], and Neighbouring Gray Tone Difference Matrix [NGTDM]), adipose tissue voxels are discretised into 16 bins of equal width (width of ten HU), to reduce noise while allowing a sufficient resolution to detect biologically significant spatial changes in PVAT attenuation. Discretisation into 16 bins has been previously recommended as the optimal approach to increase the signal-to-noise ratio of images for radiomic analysis [139, 156]. To enforce

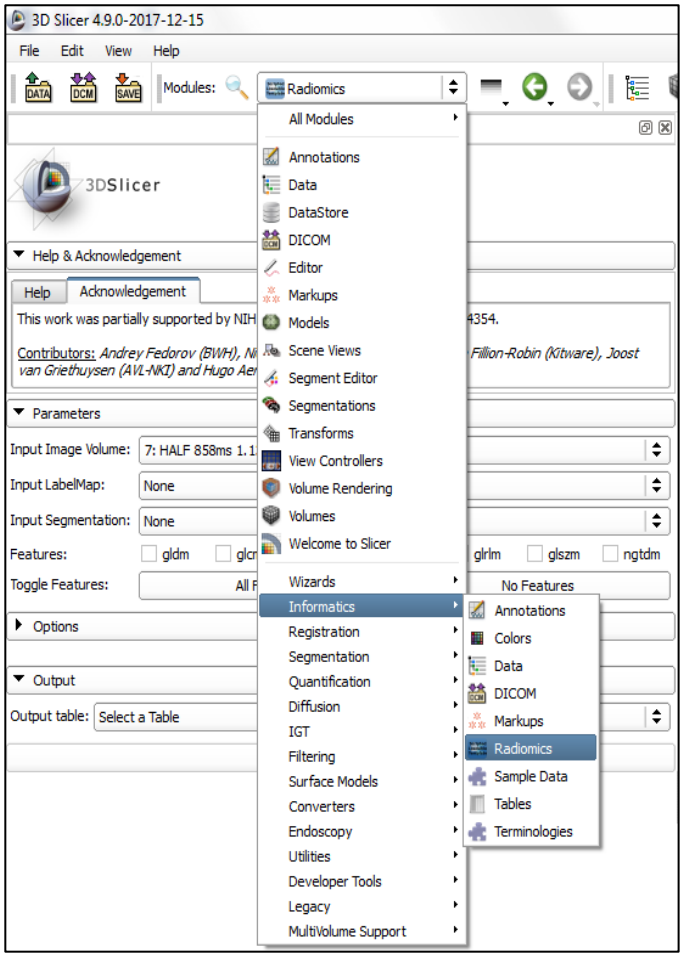

Figure 2.15. *The 3D Slicer open software with the Pyradiomics library extension.*

symmetrical, rotationally-invariant results, texture statistics (GLCM etc.) were calculated in all directions and then averaged, as previously described [139]. First order and texture-based statistics were also calculated for three-dimensional wavelet transformations of the original image resulting in eight additional sets of radiomic features [153]. More details on the segmentation methodology and its application in CCTA scans for the radiomic texture phenotyping of coronary PVAT are presented in the respective Results chapters.

Table 2.2. Breakdown of measured Radiomic features.

	Original	Wavelets transformations (n=8)	All
First order	18	144	162
Shape-related	15	-	15
GLCM	23	184	207
GLDM	14	112	126
GLRLM	16	128	144
GLSZM	16	128	144
NGTDM	5	40	45
Total	107	736	843

GLCM: gray level co-occurrence matrix; GLDM: gray level dependence matrix; GLRLM: gray level run length matrix; GLSZM: gray level size zone matrix; NGTDM: neighbouring gray tone dependence matrix; PVAT: perivascular adipose tissue.

2.11. Personal contribution

The methods for the analysis of perivascular FAI were originally developed by my supervisor Prof. Charalambos Antoniades together with Dr. Alexios Antonopoulos (patent application PCT/GB2015/052359) and were further refined and standardised by me (patent application PCT/GB2017/053262). The inception and methods for the comprehensive *radiomic* phenotyping of pericoronary fat were developed by me under the guidance of Prof. Charalambos Antoniades (patent application GB2018/18049.7). In the Ox-IMPACT study, I designed the study protocol, applied for approval from the research ethics committee, recruited the patients, performed the research CCTA scans with the help of Ms. Sheena Thomas (research radiographer, OXACCT core lab), as well as all image and statistical analyses. In the ORFAN study, I designed the sub-study exploring

imaging biomarkers of coronary atherosclerosis progression and performed all image and statistical analyses. In the CRISP-CT studies, I performed all perivascular image analyses in the Erlangen sub-arm. However, given the time-consuming nature of the perivascular fat analysis algorithms the completion of this study would not have been possible without the contribution of Drs. Christos Kotanidis, Katharine Thomas, Jennifer Mancio and Ms. Sheena Thomas and Laura Herdman who performed perivascular and epicardial fat analyses in the Cleveland sub-arm of the CRISP-CT and SCOT-HEART studies under my guidance. Radiomic and statistical analyses, including machine learning analyses and training of the random forest classifier in the CRISP-CT and SCOT-HEART studies were done by me. The recruitment of patients and processing of adipose tissue samples in the Adiporedox study was done by Drs Ioannis Akoumianakis and Christos Kotanidis. In this substudy, I performed the radiomic phenotyping of subcutaneous adipose tissue and identified the genes to be tested in proof-of-concept analyses.

3

Chapter 3. Perivascular fat attenuation & coronary atherosclerosis progression

Parts of this chapter were presented in the European Society of Cardiology Congress 2018 (Munich, Germany) in the abstract: Oikonomou EK et al. "Computed tomography-based perivascular fat phenotyping identifies unstable coronary lesions and active vascular calcification" (Eur Heart J. 2018;39 Suppl. 233), which won the Young Investigator Award in Clinical Cardiology.

3.1. Introduction

This chapter examines the association between non-invasive PVAT characterisation using CCTA-derived perivascular FAI mapping and the natural history of coronary artery disease in the adjacent vascular segments. More specifically, the main objective of this study was to explore the ability of perivascular FAI to identify coronary segments that are more likely to exhibit atherosclerotic plaque progression in the future, as well as detect unstable coronary lesions that are associated with plaque rupture and linked to acute myocardial infarction (AMI) events [157]. Although often presented as distinct stages of CAD, coronary atherosclerosis initiation, progression and ultimately plaque rupture represent sequential phases of a continuum, which is mediated by the same pathophysiological mechanisms, including inflammation, oxidative stress, cell migration and matrix remodelling [158]. As discussed in the introduction of this thesis, vascular inflammation is causally involved in all these steps and is a well-established prognostic marker and therapeutic target in both primary and secondary cardiovascular disease prevention and risk stratification [15, 32, 35].

CCTA provides an optimal tool to simultaneously assess the presence, extent and composition of coronary atherosclerosis using extensively validated, quantitative, attenuation-based mapping methods [57]. More importantly, the addition of the perivascular FAI mapping algorithm can now supplement this traditional, "anatomical" approach with a functional assessment of the coronary inflammatory burden, potentially enabling a more individualised assessment of the future patient- or vessel-specific atherosclerotic risk [126].

In this chapter, I hypothesised that perivascular FAI mapping in patients undergoing CCTA can: i) predict the future progression of coronary atherosclerosis independently of traditional risk factors; ii) identify unstable, culprit lesions that are associated with acute myocardial infarction as opposed to stable lesions, and; iii) detect longitudinal changes in coronary inflammation following plaque rupture associated with an index AMI event.

3.2. Methods

To address the aforementioned hypotheses, I used data from the ORFAN and Ox-IMPACT studies, which have been previously described in Sections 2.1.1 and 2.1.2.

3.2.1. ORFAN arm design

Briefly, the Oxford Risk Factors and Non-invasive imaging (ORFAN) study recruited a total of 121 patients that agreed to undergo a follow-up research CCTA within three to five years after a baseline, clinical CCTA scan (Figure 3.1). All eligible patients (see section 2.1.1) from the hospital CCTA records were approached in order to create a patient sample representative of a real-life CCTA cohort. Patients who underwent coronary artery bypass grafting (CABG) surgery (n=25) were included in the study but excluded

from the analysis of this sub-study. Likewise, patients with suboptimal image quality (step or motion artefacts) in the baseline or follow-up scan that precluded a reliable, quantitative analysis of coronary atherosclerotic burden (n=3) were excluded from analysis. This resulted in a study dataset of 93 patients with paired CCTA scans performed a median of 4.2 years (Interquartile range: 3.8-4.4 years) apart. The baseline demographics of the 93 patients included in this study arm are presented in Table 3.1.

Perivascular FAI mapping using the tools described in sections 2.9-2.10 and quantitative plaque analysis using the Autoplaque 2.0 software (section 2.7) were performed around the following three coronary sections: i) proximal, mid and distal RCA (corresponding to the SCCT segments #1-3); ii) left main and proximal to mid left anterior descending arteries (SCCT segments #5-7), and; iii) proximal left circumflex artery (SCCT segment #11) (see Figure 2.7 for a description of the SCCT anatomical

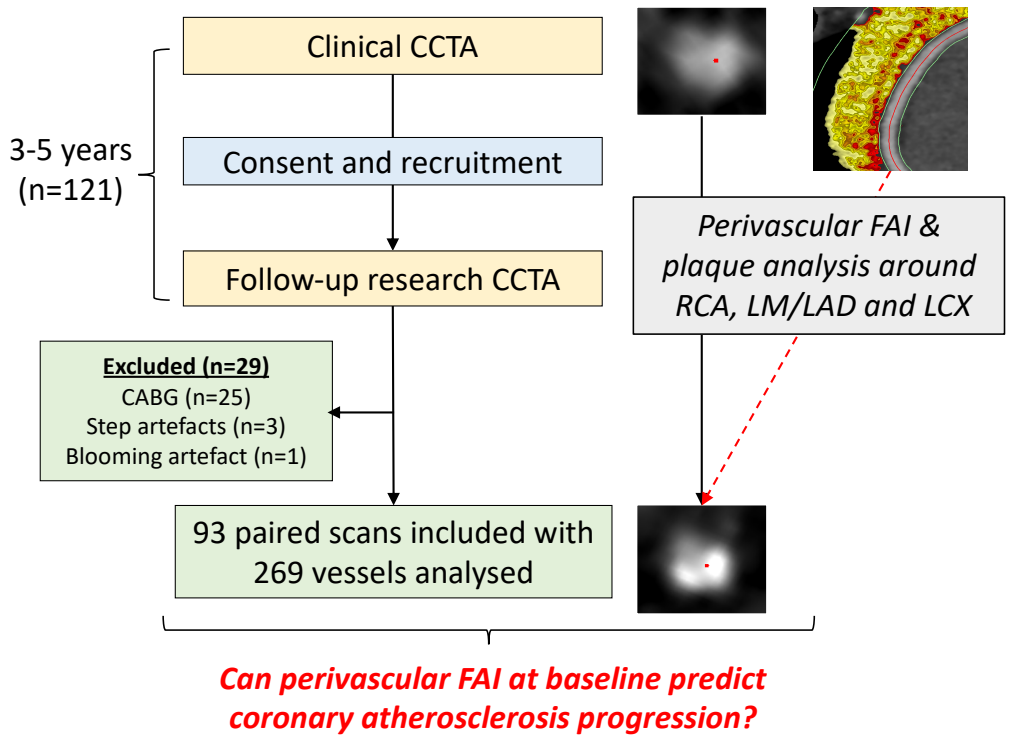

***Figure 3.1. ORFAN study design**. CABG: coronary artery bypass grafting; CCTA: coronary computed tomography angiography; FAI: fat attenuation index; LAD: left anterior descending artery; LCX: left circumflex; LM: left main coronary artery; RCA: right coronary artery.*

classification). More distal coronary segments were not analysed given their small caliber which precludes a reliable assessment of coronary atherosclerotic burden and composition. Indeed, for vessels with a diameter of <2 mm, quantitative plaque analysis is not reliable given the presence of a significant partial volume effect [159]. Whereas perivascular FAI mapping was performed only at baseline, quantitative plaque analysis was performed at both timepoints to calculate the relative change in coronary atherosclerosis. This included the presence and burden of coronary calcified plaque (defined as the volume of calcified plaque relative to the total vessel wall volume), as well as the total and non-calcified plaque burden (defined as the volume of total or non-calcified plaque relative to the total vessel wall volume, respectively). The segmentation of the coronary plaque burden in different sub-types (calcified versus non-calcified) was

Table 3.1. ORFAN population demographics

Total number	**93 (100)**
Age (years)	62 [53-69]
Body Mass Index (kg/m^2)	26.9 [23.2-30.1]
Male sex (n, %)	51 (54.8)
Hypertension (n, %)	32 (34.8)
Hypercholesterolaemia (n, %)	27 (29.3)
Diabetes mellitus (n, %)	13 (14.0)
Smoking	
Active (n, %)	4 (4.3)
Past (n, %)	33 (35.5)
Medication	
Beta-blocker (n, %)	25 (28.7)
Statin (n, %)	37 (43.0)
Antiplatelet (n, %)	21 (24.4)
ACEi or ARB (n, %)	28 (32.6)
Tube voltage (n, %)	
120 kVp	43 (46.2)
100 kVp	47 (50.5)

ACEi: angiotensin-converting enzyme inhibitor; ARB: angiotensin-II-receptor blocker; P values derived from Pearson's Chi-square test for categorical variables and Mann-Whitney for continuous variables. Categorical variables are presented as numbers (percentages), while continuous variables are summarised as median [25th-75th percentile].

performed according to scan-specific thresholds defined by the software based on scan-specific characteristics such as the degree of coronary lumen opacification [148].

Perivascular FAI was defined as the weighted mean attenuation of all adipose tissue-containing voxels (-190 to -30 HU) in the perivascular space, corresponding to a radial distance from the outer vascular wall equal to the mean diameter of the adjacent vessel, as previously described (section 2.9) [126].

3.2.2. Ox-IMPACT arm design

The Ox-IMPACT study included 57 patients presenting with AMI (n=31 with STEMI [Arm 1]; and n=26 with NSTEMI [Arm 2]). A total of 22 patients with stable CAD undergoing CCTA were used as the control group (defined as patients with past PCI > 6 months ago and no recent symptoms or evidence of ACS) (Figure 3.2).

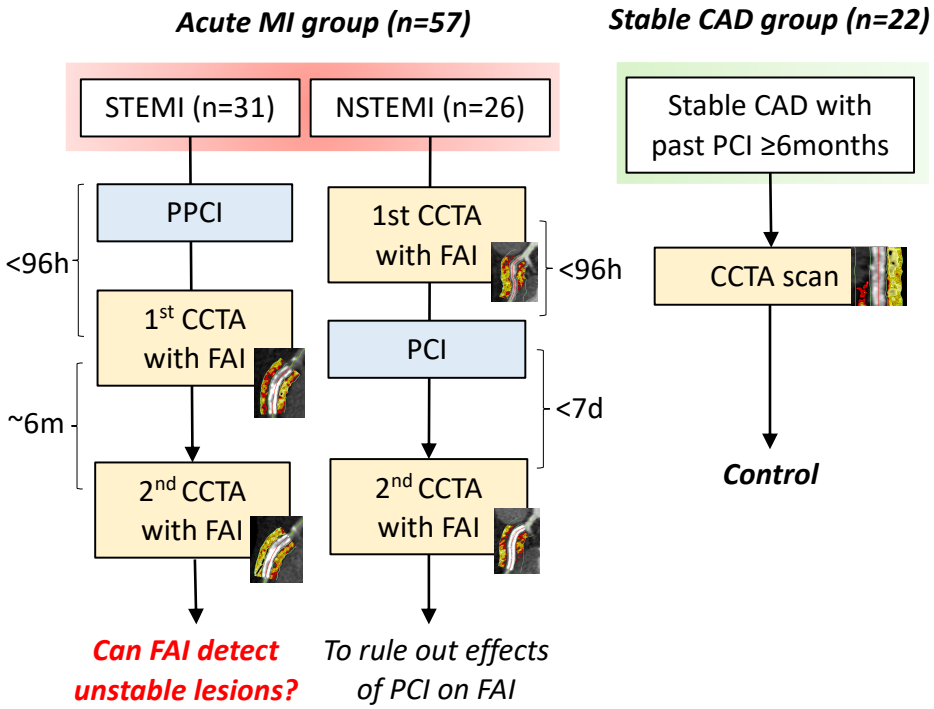

***Figure 3.2. Ox-IMPACT study design**. CAD: coronary artery disease; (C)CT(A): (coronary) computed tomography (angiography); FAI: fat attenuation index; (N)(STE)MI: (non)-(ST-segment elevation) myocardial infarction; (P)PCI: (primary) percutaneous coronary intervention.*

In the STEMI arm, patients underwent a research CCTA scan within 96 hours of admission. A subgroup of 15 STEMI patients also completed a six-month follow-up CCTA visit. This paired analysis enabled a longitudinal assessment of changes in perivascular FAI mapping around the culprit coronary lesion, following optimal medical therapy.

In the NSTEMI arm, patients presenting with suspected NSTEMI first underwent a research CCTA scan within 96 hours of admission and prior to the performance of urgent coronary angiography. Out of the n=26 enrolled patients initially classified as NSTEMI cases, four (15.4%) had no evidence of obstructive CAD, four (15.4%) had extensive, multi-vessel CAD with no detectable culprit lesion (and were referred for CABG surgery), whereas another four (15.4%) has in-stent restenosis. Of the remaining ten NSTEMI cases where a new culprit lesion was identified and treated with PCI, seven patients were able to return within seven days of the index event to undergo a second CCTA scan. The aim of this was to assess whether stenting may be confounding the association between culprit lesions and PVAT changes detected by perivascular FAI mapping. The baseline demographics of the patients included in this study arm are presented in Table 3.2.

Perivascular FAI mapping in all cases was performed as described in section 2.9. Lesions were localised based on the invasive coronary angiogram and the presence of a coronary stent, and their length was split in tertiles to allow a comparison between lesions of different length. Proximal and distal 5mm-long reference segments were also analysed to provide a reference for FAI comparison along the same vessel. The operator was not blinded to the timepoint of CCTA assessment, however all scans were analysed in a paired manner to enable an accurate co-registration of baseline and follow-up CCTA

scans and the selection of matched segments (of same length and diameter) in both scans (for all patients with two CCTA scans performed at different timepoints).

Table 3.2. Ox-IMPACT demographics for the final study population

		AMI	Stable CAD	P value
Total n		38	22	
Age (years)		56 [51-65]	59 [46, 65]	0.66
Sex (female)		32 (84.2%)	17 (77.3%)	0.51
Hypertension		13 (34.2%)	16 (72.7%)	0.007
Hypercholesterolaemia		13 (34.2%)	17 (77.3%)	0.003
Diabetes mellitus		3 (7.9%)	6 (27.3%)	0.06
Smoking				0.07
	Former	20 (52.6%)	6 (27.3%)	
	Active	7 (18.4%)	2 (9.1%)	
Body Mass Index (kg/m^2)		26.4 [23.7-31.7]	28.9 [27.6, 32.1]	0.046
Medications at baseline				
Antiplatelet		38 (100%)	20 (90.9%)	0.13
Beta-blocker		35 (92.1%)	17 (77.3%)	0.13
ACEi/ARBs		34 (89.5%)	14 (63.6%)	0.001
Statin		37 (97.4%)	19 (86.4%)	0.14

ACEi: angiotensin-converting enzyme inhibitor; ARB: angiotensin-II-receptor blocker; P values derived from Pearson's Chi-square test for categorical variables and Mann-Whitney for continuous variables. Categorical variables are presented as numbers (percentages), while continuous variables are summarised as median [25th-75th percentile].

3.2.3. Statistical analysis

Continuous variables are presented as median [interquartile range], whereas categorical variables are summarised as numbers (%, percentages). Comparisons of continuous and categorical variables between two independent groups were performed using the non-parametric Mann-Whitney and Pearson's χ^2 (or Fisher's exact) tests, respectively.

In the ORFAN arm, the association between vessel-specific total and non-calcified plaque progression (dependent variable: [100*(burden$_{\text{follow-up}}$-burden$_{\text{baseline}}$) /burden$_{\text{baseline}}$]%) and perivascular FAI at baseline was assessed in a multiple linear regression model, further adjusted for age, sex, body mass index, hypertension, hypercholesterolaemia, diabetes mellitus, smoking, EAT volume, CT tube voltage, total

plaque burden at baseline, vessel location and statin/antiplatelet therapy with clustering at the patient level. For calcium progression a similar *logistic* regression model was applied with calcified plaque progression (delta[Calcified plaque burden]>0 vs 0) as the dependent variable given the presence of several 0 (zero) values at both baseline and follow-up.

In the Ox-IMPACT arm, the difference in perivascular FAI along a given coronary lesion between different groups (e.g. culprit lesions in AMI patients, non-culprit lesions in AMI patients, and stable lesions in stable CAD patients) was assessed using a repeated measures two-way analysis of variance test with a distance (x) group interaction. Comparison of pre-specified, single coronary segments at different timepoints (e.g. before and after PCI) was performed using a non-parametric Wilcoxon-signed-rank test.

In all cases, α was set at 0.05 and tests were two-tailed. Statistical analyses were performed using Stata/MP 14.0 (StataCorp. 2015. Stata Statistical Software: Release 14. College Station, TX: StataCorp LP) and GraphPad Prism version 7.0 for Windows (GraphPad Software, La Jolla California USA, www.graphpad.com).

3.3. Results

3.3.1. Perivascular FAI and progression of coronary atherosclerosis

In the ORFAN arm, a total of 269 (out of 279, 96.4%) vessels (RCA, LM/LAD and LCX) in 93 patients were analysed at both baseline and follow-up. In the remaining ten vessels, quantitative plaque analysis could not be performed due to technical artefacts that affected the segmentation and volumetric characterisation of the arterial wall. The median percent change in total plaque burden was 15.4% [IQR: -2.9& – 44.7%], whereas a total of 73 vessels (27.1%) showed evidence of coronary calcium progression. Median

perivascular FAI around the 269 analysed coronary segments was -75.3 HU [IQR: -80.6 - -70.50 HU].

Adjusted regression modelling showed that higher perivascular FAI values at baseline were significantly associated with a higher risk of coronary calcium progression at follow-up, independent of age, sex, traditional risk factors, total plaque burden at baseline and epicardial adipose tissue volume (Table 3.3). More specifically, for every 10 HU increase in baseline perivascular FAI, there was a 61% higher adjusted risk of coronary calcium progression in the adjacent coronary vessel at follow-up (Figure 3.3).

Table 3.3. Perivascular FAI and progression of coronary calcification

Independent variable		Odds Ratio (95% CI)
Perivascular FAI (per SD)		1.61 (1.06 – 2.44), P=0.025
Age (years)		1.04 (0.97 – 1.12), P=0.28
Male sex		3.43 (1.20 – 9.80), P=0.021
Body Mass Index (kg/m^2)		1.04 (0.92 – 1.18), P=0.49
Hypertension		1.79 (0.78 – 4.11), P=0.17
Hypercholesterolaemia		0.54 (0.24 – 1.20), P=0.13
Diabetes mellitus		0.50 (0.15 – 1.64), P=0.25
Smoking (*never*: ref.):	*active*	0.99 (0.22 – 4.43), P=0.99
	past	0.89 (0.39 – 2.03), P=0.79
EAT volume (cm^3)		1.00 (0.99 – 1.02), P=0.72

EAT: epicardial adipose tissue volume; FAI: fat attenuation index; SD: standard deviation. Model adjusted for tube voltage, total plaque burden at baseline, coronary vessel location (right coronary, left anterior descending and left circumflex artery), use of antiplatelet or statin therapies, and clustered at the patient level.

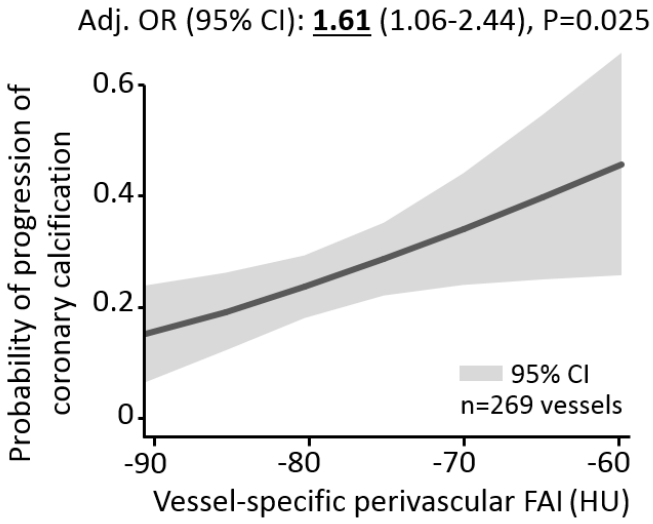

Figure 3.3. Perivascular FAI mapping and coronary calcium progression. *An adjusted, fitted regression line showing the association between higher perivascular FAI at baseline and a higher risk of coronary calcification progression in the adjacent vessel. CI: confidence interval; FAI: fat attenuation index; HU: Hounsfield Unit; OR: odds ratio. *OR is presented per 10 HU increments in FAI.*

On the other hand, no significant association was found between baseline perivascular FAI and the percent change in total or non-calcified plaque burden (Tables 3.4 and 3.5).

Table 3.4. Perivascular FAI and progression of total plaque burden

Independent variable		β coefficient (95% CI), P value
Perivascular FAI (per SD)		0.74 (-6.77 – 8.24), P=0.85
Age (years)		-0.31 (-1.28 – 0.66), P=0.53
Male sex		-0.40 (-15.03 – 14.22), P=0.96
Body Mass Index (kg/m^2)		0.53 (-1.05 – 2.10), P=0.51
Hypertension		3.66 (-10.51 – 17.83), P=0.61
Hypercholesterolaemia		-9.17 (-24.03 – 5.68), P=0.22
Diabetes mellitus		-7.23 (-29.27 – 14.80), P=0.52
Smoking (*never*: ref.):	*active*	-4.06 (-28.33 – 20.20), P=0.74
	past	5.54 (-7.99 – 19.06), P=0.42
EAT volume (cm^3)		-0.02 (-0.24 – 0.20), P=0.86

EAT: epicardial adipose tissue volume; FAI: fat attenuation index; SD: standard deviation. Model adjusted for tube voltage, total plaque burden at baseline, coronary vessel location (right coronary, left anterior descending and left circumflex artery), use of antiplatelet or statin therapies, and clustered at the patient level.

Table 3.5. Perivascular FAI and progression of non-calcified plaque burden

Independent variable		β coefficient (95% CI), P value
Perivascular FAI (per SD)		0.78 (-6.75 – 8.32), P=0.84
Age (years)		-0.29 (-1.24 – 0.66), P=0.55
Male sex		-2.33 (-17.02 – 12.37), P=0.75
Body Mass Index (kg/m^2)		0.59 (-0.93 – 2.12), P=0.44
Hypertension		2.17 (-12.06 – 16.39), P=0.76
Hypercholesterolaemia		-9.63 (-24.68 – 5.41), P=0.21
Diabetes mellitus		-10.46 (-31.09 – 10.18), P=0.32
Smoking (*never*: ref.):	*active*	-4.10 (-28.21 – 20.00), P=0.74
	past	5.60 (-8.27 – 19.47), P=0.42
EAT volume (cm^3)		-0.03 (-0.24 – 0.19), P=0.81

EAT: epicardial adipose tissue volume; FAI: fat attenuation index; SD: standard deviation. Model adjusted for tube voltage, total plaque burden at baseline, coronary vessel location (right coronary, left anterior descending and left circumflex artery), use of antiplatelet or statin therapies, and clustered at the patient level.

3.3.2. Perivascular FAI and unstable coronary lesions

In the Ox-IMPACT arm, perivascular FAI mapping was characterised by a significant increase in perivascular FAI around culprit lesions in STEMI patients scanned <96 hours of admission (n=31 lesions in 31 patients), compared to non-culprit (previously treated) lesions from STEMI patients (n=9) or stable lesions from the stable CAD group (n=25 lesion in 22 patients) (Figures 3.4 & 3.5). This difference was driven predominantly by an increase in perivascular FAI around the middle lesion tertile compared to the proximal reference segment, whereas perivascular FAI decreased when moving away from the lesion towards proximal or distal "healthy" reference segments (Figure 3.5).

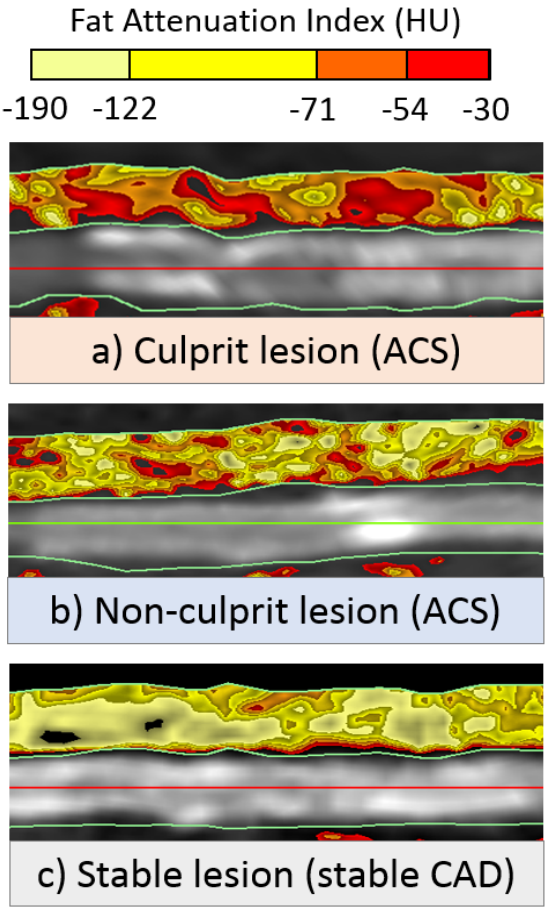

Figure 3.4. Perivascular FAI mapping in acute myocardial infarction versus stable disease. *Perivascular FAI mapping (with corresponding color map) around a culprit lesion from an ACS patient **(A)**, a non-culprit lesion from an ACS patient **(B)**, and stable lesion from a patient with stable CAD **(C)**, demonstrating higher FAI values around the recently ruptured and stented plaque compared to stable, "control" lesions. ACS: acute coronary syndrome; CAD: coronary artery disease; FAI: fat attenuation index; HU: Hounsfield Unit.*

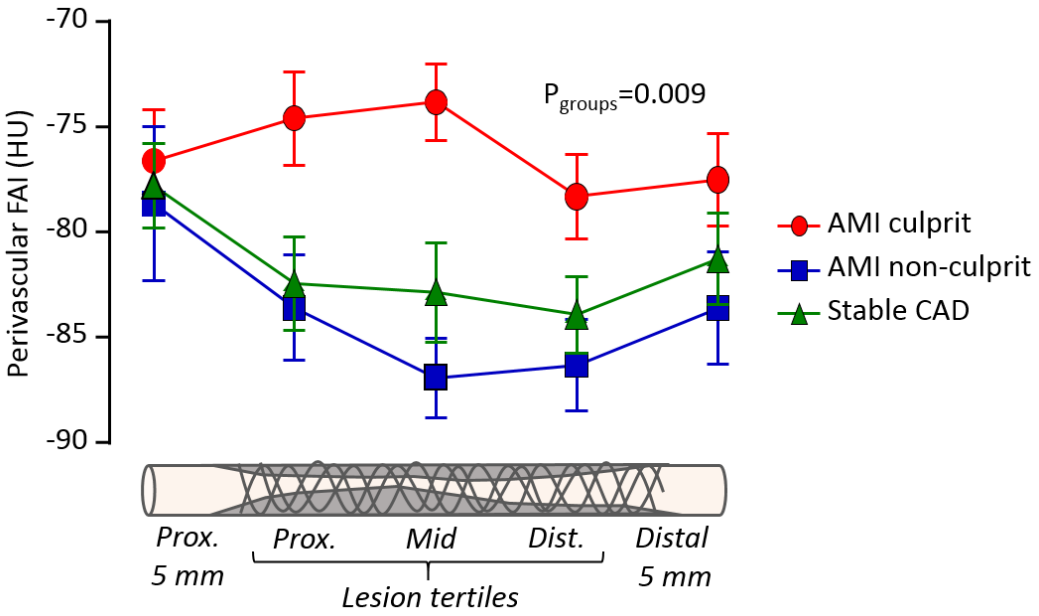

Figure 3.5. Perivascular FAI around unstable versus stable coronary lesions. *Perivascular FAI mapping revealed a significant increase in perivascular FAI around culprit lesions from ACS patients (red circle, n=31), compared to non-culprit lesion from ACS patients (blue square, n=9), and stable lesions patients with stable CAD (green triangle, n=25). ACS: acute coronary syndrome; CAD: coronary artery disease; FAI: fat attenuation index; HU: Hounsfield Unit.*

To assess the dynamic nature of this observation, a subgroup of 13 STEMI returned for a follow-up research CCTA scan six months following the index event. A repeat FAI mapping analysis around the same culprit lesion revealed a significant decrease in the perivascular FAI values compared to the baseline scan, a shift that was mainly observed in the PVAT directly adjacent to the treated lesion, but not seen around proximal or distal reference segments (Figure 3.6).

Finally, to explore whether the observed association between perivascular FAI and plaque rupture may be confounded by PCI and stent placement, a subgroup of NSTEMI patients agreed to undergo CCTA both before and within seven days of coronary angiography with PCI. Perivascular FAI mapping was performed around the treated lesions at both timepoints and demonstrated no significant changes around the treated lesion or a proximal 5mm-long reference segment (Figure 3.7).

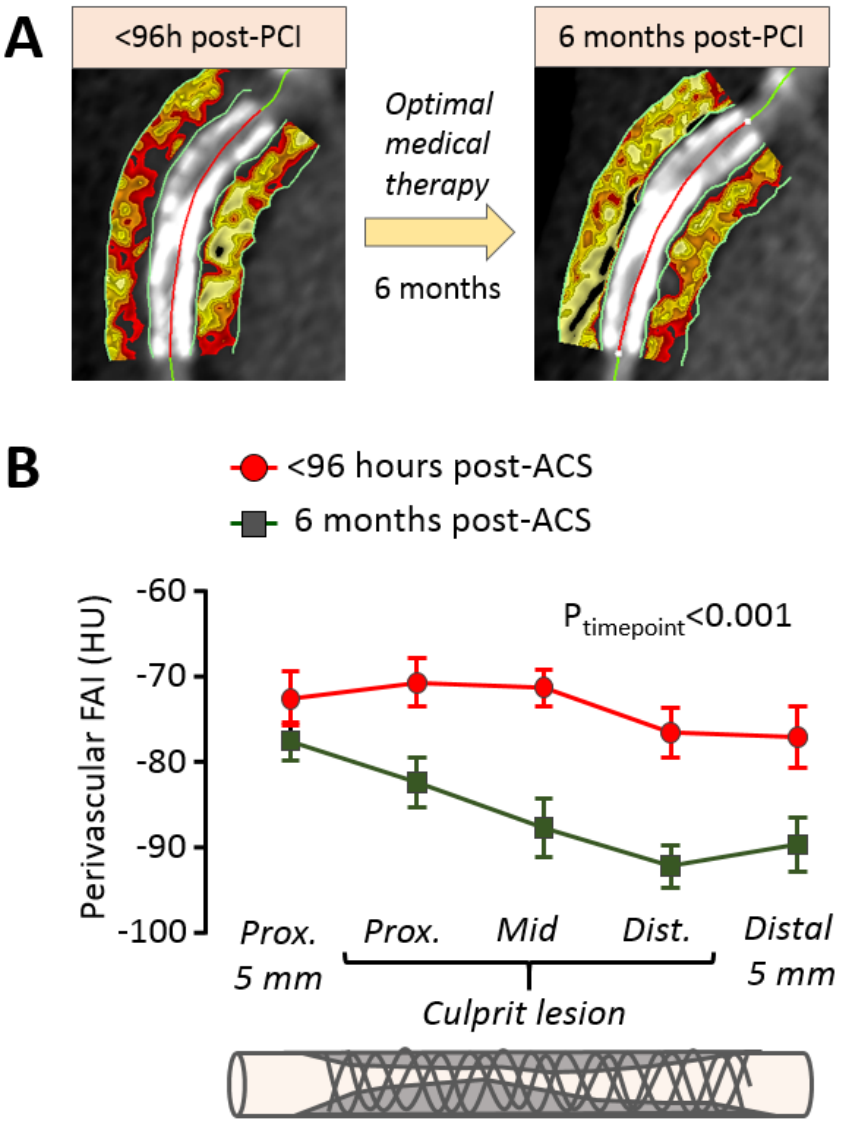

Figure 3.6. Longitudinal changes in perivascular FAI following acute myocardial infarction. ***(A)*** *Perivascular FAI mapping (with corresponding color map, as in Figure 3.4) around a culprit lesion from a STEMI patient scanned within 96 hours of admission* ***(left)****, and six months later* ***(right)****.* ***(B)*** *Follow-up scans at six months (n=13 pairs) show a significant decrease in perivascular FAI around the culprit lesion, but not proximal or distal reference segments in STEMI patients. ACS: acute coronary syndrome; FAI: fat attenuation index; HU: Hounsfield Unit; pPCI: primary percutaneous coronary intervention.*

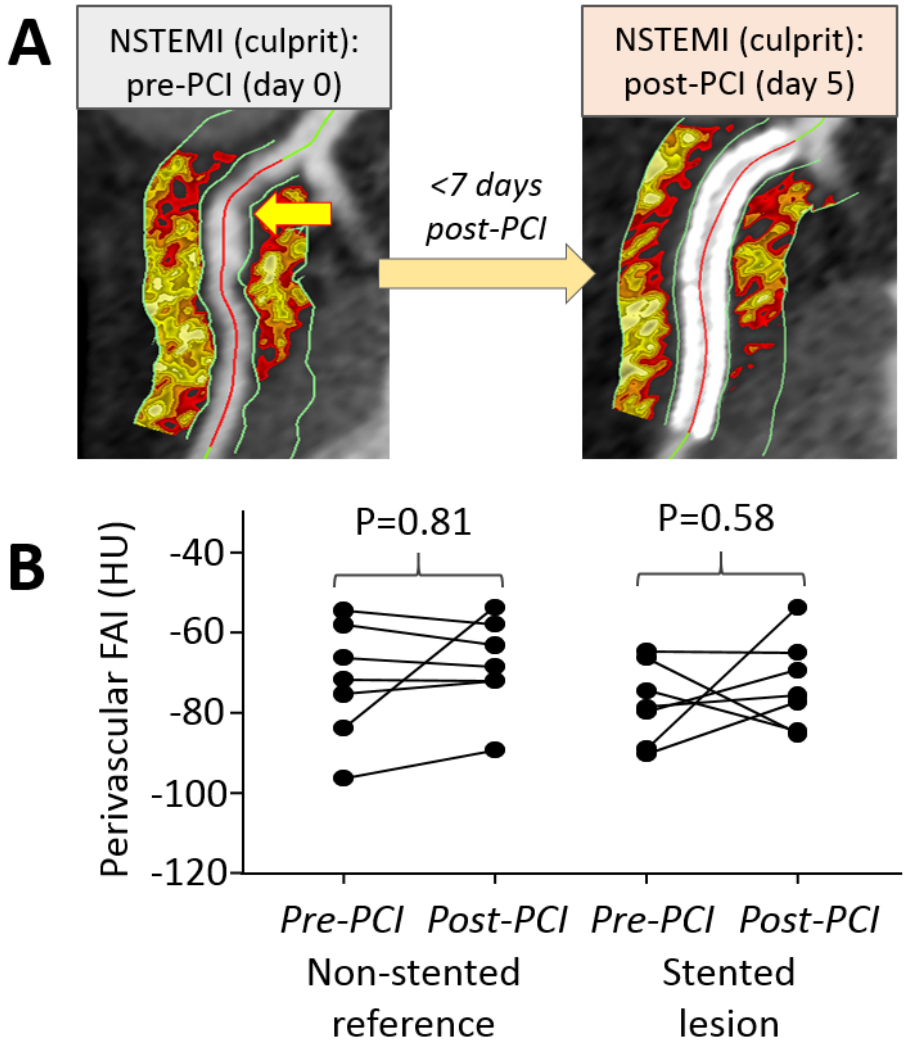

Figure 3.7. Perivascular FAI pre- and post-coronary stenting. (A) *Perivascular FAI mapping (with corresponding color map, as in Figure 3.4) around a culprit lesion from a NSTEMI patient scanned prior to PCI* ***(left)****, and within seven days of the procedure* ***(right)****. **(B)** Paired comparisons of perivascular FAI before and after PCI around a 5mm-long reference segment proximal to the treated lesion* ***(left)*** *and the culprit lesion* ***(right)*** *(n=7 pairs) show no significant changes in perivascular FAI following PCI. FAI: fat attenuation index; HU: Hounsfield Unit; NS: non-significant; NSTEMI: non-ST-segment elevation myocardial infarction. PCI: percutaneous coronary intervention.*

3.4. Discussion

In summary, in this chapter and using two independent studies comprising a total of 266 CCTA scans in 153 individuals, I have demonstrated that:

a. Higher perivascular FAI values are independently associated with a higher risk of coronary calcification progression in the adjacent coronary vessel.
b. Culprit lesions in patients with AMI are associated with increased perivascular FAI values compared to reference stable lesions from the same patients, or stable lesions from patients with stable CAD.
c. Perivascular FAI is a dynamic imaging biomarker and appears to decrease around the culprit lesions at six months following the index AMI event.
d. These changes in PVAT phenotype detected by perivascular FAI mapping are not significantly associated with PCI and stent placement.

These findings highlight an interesting association between atherosclerotic disease activity and PVAT composition and support the diagnostic and prognostic value of perivascular FAI mapping in a range of clinical scenarios.

3.4.1. Perivascular FAI as a potential marker of coronary calcification

My findings suggest that perivascular FAI is a risk factor for future vascular calcification. This observation is supported by further evidence in the literature that support a close association between inflammatory cell infiltration and osteoblastic metaplasia in the vascular wall [38, 69]. Joshi et al. have compared atherosclerotic vascular calcification, a pathognomonic feature of atherosclerosis, to the formation of caseating granulomata in tuberculosis [38]. In both cases, a localised, controlled response to an intense, chronic pro-inflammatory environment contributes to the local formation of hydroxyapatite, the main component of coronary calcifications. Hydroxyapatite crystals are deposited during

the early phases of vascular mineralisation, and subsequently "*nucleate, propagate and mineralise the extracellular matrix*" [38, 160]. The resulting areas of coronary calcium can then be detecting using cardiac CT and both their presence, as well as accumulation rate, are independent predictors of adverse cardiac events [11, 53, 54]. Nevertheless, cardiac CT can only detect areas of macro-calcification, which may take months to years to become detectable [38]. Instead, PET-CT imaging with ^{18}F-NaF (sodium fluoride) relies on the ability of fluoride ions to be incorporated into forming hydroxyapatite crystals by ion exchange with hydroxyl groups found on the surface of the crystals. Since the surface-to-volume ratio for a crystal or sphere is higher at lower volume/sizes, this phenomenon is more prominent at the earliest stages of mineralisation (i.e. micro-calcification). In a prospective clinical trial, ^{18}F-NaF PET-CT imaging was able to identify ruptured lesions in AMI patients, as well as high-risk plaques in patients with stable CAD. Nevertheless, the investigators reported no significant differences between culprit and non-culprit lesions in ^{18}F-FDG uptake, which was commonly affected by myocardial uptake and often not discernible [38].

After we presented our findings, Kwiecinski et al. published a study of 41 patients that underwent both ^{18}F-NaF PET and CCTA imaging. Lesions with increased ^{18}F-NaF had significantly higher peri-coronary adipose tissue radiodensity, compared to lesions without ^{18}F-NaF uptake (median radiodensity of -73 HU [IQR -79 to -68] versus -86 HU [IQR -94 to -80], P<0.001) (Figure 3.8) [161]. On adjusted regression analysis, only the presence of low-attenuation plaque on CCTA and peri-coronary adipose tissue radiodensity were significantly and independently associated with increased ^{18}F-NaF uptake [161]. Therefore, high PVAT radiodensity could represent an additional high-risk plaque feature on CCTA which reflects the local coronary inflammatory burden, which is in turn associated with active micro-calcification. Rather than using PET-CT imaging,

an expensive imaging test with limited availability and higher radiation exposure, CCTA-based perivascular fat phenotyping could provide an alternative way of characterising coronary inflammation using a widely used and available imaging modality.

Interestingly, our study showed no association between perivascular FAI and quantitative progression of total or non-calcified plaque burden. One possible reason for this may be the limited statistical power to detect a significant difference. Contrary to coronary calcium which is easily discernible, the accurate volumetric quantification of minor non-calcified plaques is dependent on the technical quality of the scan, lumen opacification and partial voluming, all of which introduce noise into the volumetric assessment of the non-calcified plaque [162]. Furthermore, while some studies suggest

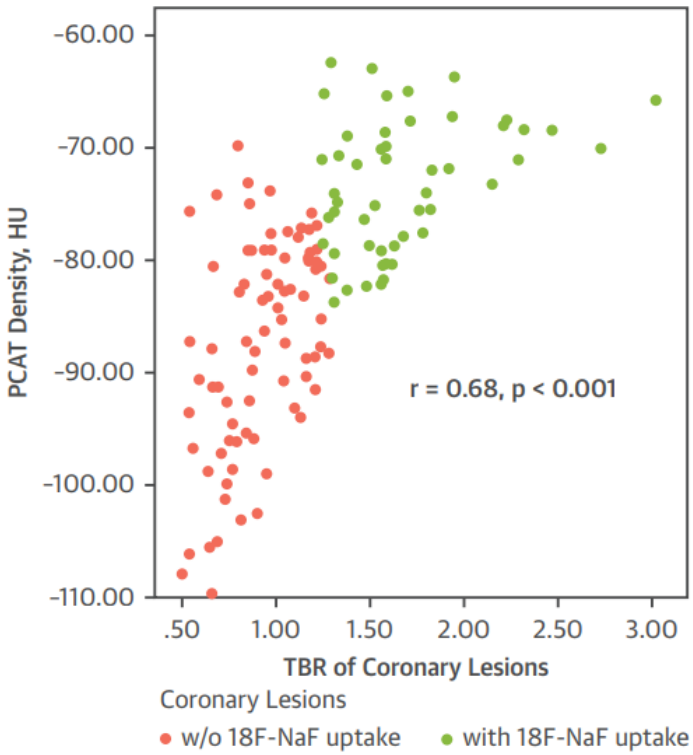

Figure 3.8. Pericoronary adipose tissue (PCAT) radiodensity and coronary inflammation. *A scatter plot demonstrating a strong, positive correlation between PCAT CT radiodensity and ^{18}F-NaF (sodium fluoride) uptake from the adjacent coronary lesion on PET-CT. These findings lend further support to the role of perivascular fat attenuation as a surrogate marker of coronary inflammation. Reproduced with permission from Kwiecinski et al.* ***JACC Imaging****. 2019. HU: Hounsfield Units; TBR: target to background ratio.*

that calcified plaques may be more stable than non-calcified ones [163], perivascular FAI mapping rather detects ongoing coronary calcification that is likely to result in areas macro-calcifications a few years later. Whereas macro-calcifications may confer mechanical stability, active areas of micro-calcification reflect an intense pro-inflammatory environment that renders the coronary plaque susceptible to mechanical stress, erosion and rupture [38].

3.4.2. Perivascular FAI as a marker of unstable coronary lesions

Mathematic modelling studies have shown that micro-calcification at the surface of thin-cap fibro-atheroma can enhance the mechanical stress to the plaque, thus contributing to plaque instability, rupture and acute coronary syndromes [38]. In addition, plaque erosion, rupture and thrombosis are all associated with activation of pro-inflammatory pathways and accumulation of inflammatory cells in the coronary injury site [31]. In the Ox-IMPACT study, I demonstrated that culprit lesions in AMI patients are associated with a localised, increase in perivascular FAI, compared to stable lesions from the same patients or stable lesions from patients with stable CAD. These findings, first reported by our group, have subsequently been replicated by other independent investigators. In a brief report of a retrospective analysis of 19 ACS patients and 16 stable CAD controls, Goeller et al. confirmed that pericoronary fat attenuation on CCTA is increased around culprit lesions compared to non-culprit lesions of patients with ACS and the lesions of matched controls [164]. Interestingly, an independent group of investigators have also detected macroscopic changes in pericoronary fat phenotype around areas of intense coronary injury, such as around sites of coronary artery dissection. Such areas of increased fat attenuation, described as “perivascular fat stranding”, may indicate a local response of perivascular fat to exogenous inflammatory signals, and have also been

reported in other conditions, such as in abdominal CT scans around inflamed areas (e.g. inflammatory bowel disease) [165]. While perivascular FAI may be a marker of ruptured coronary plaques, it remains unclear whether this is an epiphenomenon and the result of plaque injury, or whether perivascular FAI precedes plaque rupture. However, given that coronary inflammation is actively involved in all stages of coronary atherosclerosis [166], it may be hard to discriminate between these stages. In addition, my findings suggest that the observed effects may be independent of any coronary injury induced by PCI and coronary stent placement. However, since all patients received drug-eluting coronary stents, the local release of anti-inflammatory agents from the stent may exert anti-inflammatory effects over six months resulting in a localised decrease in perivascular FAI. Indeed, such a pattern was observed in both stable CAD patients as well as in AMI patients at their six-month follow-up visit.

3.4.3. The dynamic nature of perivascular FAI

Follow-up of AMI patients demonstrated a significant decrease in perivascular FAI measured around culprit lesions following the index event, which was more pronounced in areas adjacent to the treated lesion. These observations are of significant importance, since they highlight the dynamic biology detected by perivascular FAI mapping and its ability to track longitudinal changes in coronary inflammatory burden. In contrast, coronary calcium is known to be an inflexible biomarker that does not regress and may even increase in response to risk reduction measures, such as statin initiation, thus losing its value in secondary prevention.

More recent evidence from an ongoing collaboration with Prof. Nehal Mehta's group at the National Heart, Lung, and Blood Institute (NHLBI), National Institutes of Health (Bethesda, MD, USA), further supports the dynamic nature of perivascular FAI. In this study, a total of 134 patients with a documented diagnosis of psoriasis underwent paired CCTA scans before and after the initiation of local or systemic treatment. Psoriasis is a chronic inflammatory disease that affects the skin, joints but also the cardiovascular system, and has been linked to an increased cardiovascular risk compared to the general population [167]. While treatment with local agents was not associated with a change in perivascular FAI at 1 year, treatment with systemic anti-inflammatory medications (i.e.

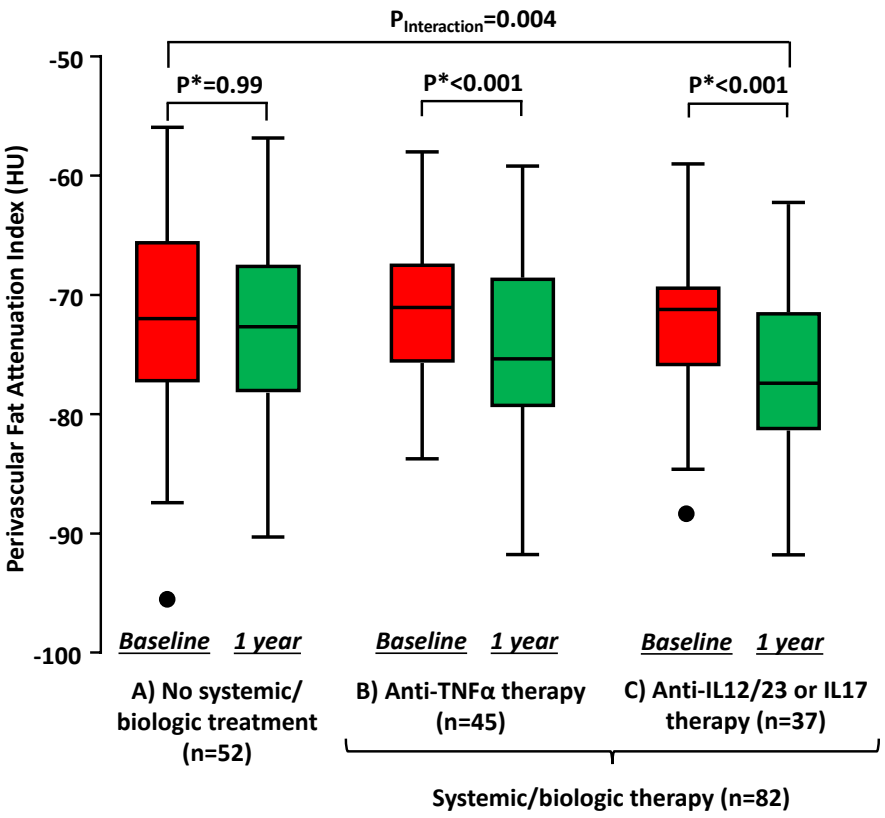

Figure 3.9. Dynamic changes in perivascular FAI following one year of anti-inflammatory treatment in patients with psoriasis. *A total of 134 patients with a documented diagnosis of psoriasis underwent paired CCTA scans before and after the initiation of local or systemic treatment. While treatment with local agents was not associated with a change in perivascular FAI at 1 year, treatment with systemic anti-inflammatory medications (i.e. methotrexate, anti-TNF-a and anti-IL12/23 & anti-IL-17 novel biologics) was associated with a significant reduction in perivascular FAI. FAI: fat attenuation index; IL: interleukin; TNF-a: tumor necrosis factor alpha. Based on the conference. P values derived from Wilcoxon signed-rank test. Full results presented in: Elnabawi Y, Oikonomou EK et al.* ***JAMA Cardiol****. 2019;4(9):885-891.*

methotrexate, anti-TNF-a and anti-IL12/23 & anti-IL-17 novel biologics) was associated with a significant reduction in perivascular FAI [168]. Therefore, FAI appears to be a reversible biomarker that relies on the ability of adipocytes to sense exogenous inflammatory stimuli and respond accordingly.

3.5. Conclusion

Taken together, my results suggest that increased perivascular FAI is a CCTA-based imaging biomarker of coronary inflammation and a vessel-specific risk factor for progression of coronary calcification. In addition, perivascular FAI mapping is able to detect culprit coronary lesions in AMI patients, discriminating these from stable plaques, and may track longitudinal changes in coronary inflammation following an AMI index event or treatment with anti-inflammatory agents. Of note, the studies presented in this chapter relied on soft endpoints and outcome measures (e.g. coronary calcium progression), underlining the need for large-scale cohort studies which would explore the independent association between perivascular FAI mapping and hard clinical endpoints, such as cardiac mortality and myocardial infarction.

4

Chapter 4. Perivascular fat attenuation & future cardiac risk prediction

This chapter is based on the manuscript by: Oikonomou EK et al. "Non-invasive detection of coronary inflammation using computed tomography and prediction of residual cardiovascular risk (the CRISP CT study): a post-hoc analysis of prospective outcome data". Lancet 2018, Sep 15;392(10151):929-939 (ref [142]). The authors have retained copyright of the material, published under a CC BY 4.0 license.

4.1. Introduction

As described in the Introduction of this thesis, CCTA is a sensitive and widely used, non-invasive imaging modality for diagnosing CAD [41, 42] and recent clinical guidelines have expanded its use as a first-line diagnostic tool in the management of chest pain of recent onset, suggestive of typical/atypical angina or non-anginal chest pain with electrocardiographic changes [45]. However, CCTA focuses predominantly on the identification of anatomically significant coronary artery stenoses which are only found in <50% of all patients referred for this test [41, 42]. Importantly, the majority of acute coronary syndromes is caused by unstable but non-obstructive atherosclerotic plaques [52], which cannot be easily identified by CCTA or other non-invasive diagnostic tests detecting coronary luminal stenosis or stress-induced myocardial ischemia [67, 169].

Vascular inflammation is a driver of coronary atherosclerotic plaque formation, and a characteristic feature of atherosclerotic plaque rupture, leading to acute coronary syndromes including myocardial infarction [170]. The causal role of inflammation in vascular disease pathogenesis has recently been documented by the CANTOS (Canakinumab Antiinflammatory Thrombosis Outcome Study) trial [171], which

demonstrated that specific targeting of residual inflammatory risk improves clinical outcomes. However, there is no readily available non-invasive method to quantify the inflammatory status of coronary vessels and/or atherosclerotic plaques, and measurement of circulating biomarkers, such as high sensitivity C-reactive protein, is not specific for coronary plaque inflammation [172]. The coronary calcium score (CCS), derived from non-contrast cardiac CT, is a well-established marker for cardiac risk prediction [11], but it does not change in response to cardiovascular risk reduction strategies [173], and therefore its value in secondary prevention is limited. Detection of coronary micro-calcification and inflammation using ^{18}F-NaF PET-CT, as described in the previous chapter, is promising [38], but is currently limited by clinical availability, and its prognostic value has not been validated in large cohorts [174].

There is a pressing unmet need for newer, non-invasive and cost-effective methods to detect coronary inflammation in clinical practice, to allow precision medicine to guide personalised risk reduction strategies in primary and secondary prevention [157, 175]. In this chapter, I hypothesised that, by quantifying coronary artery inflammation, CCTA-based perivascular FAI mapping may be able to predict adverse events, independent of the degree of coronary stenosis or any other factor taken into account in the risk stratification of individuals undergoing CCTA. Integration of perivascular FAI into current risk prediction models may significantly improve discrimination for adverse cardiac events and may lead to significant cardiac risk re-classification in patients undergoing routine, clinically-indicated CCTA, thus identifying high risk subjects who may benefit from more aggressive therapeutic strategies.

4.2. Methods

4.2.1. Study design

This chapter is based on the Cardiovascular Risk Prediction using Computed Tomography (CRISP-CT) study. CRISP-CT was a post-hoc analysis of prospectively collected data from two independent cohorts of patients undergoing clinically-indicated CCTA (as described in section 2.1.3). The two cohorts were analysed in an independent manner and were used as derivation and validation sets to test the prognostic value of perivascular FAI mapping for future adverse cardiac events.

In the derivation cohort, 1872 out of 1993 consecutive patients (1178 [62.9%] males, 62 [17-89] years old) who underwent clinically-indicated CCTA between 2005 and 2009 at the Erlangen University Hospital (Erlangen, Germany) were included in the study. Median patient follow-up time was 72 (51 to 109) months post-CCTA. A subgroup of 1415 patients further underwent non-contrast cardiac computed tomography (CT) to assess the extent of coronary calcification by the Agatston coronary calcium score (CCS) score, in line with local clinical practice [7, 12, 176, 177].

In the validation cohort, 2040 out of 2246 consecutive patients that underwent CCTA at Cleveland Clinic, Cleveland, Ohio, between 2008-2016 (1126 [55.2%] males, 53 [range: 19-87] years old), were followed up for a median of 54 (range: 4 to 105) months. In order to create a study population reflective of the real-life patient population undergoing diagnostic CCTA, all consecutive patients (aged 16 years or older) were included in the study, unless they were specifically referred for assessment of congenital heart disease. The primary objective was to evaluate the predictive value of perivascular FAI for the two primary endpoints of all-cause and cardiac mortality. The research protocol was approved by local institutional review boards with waiver of individual

informed consent. The study flowchart and baseline characteristics of the study populations are presented in Figure 4.1 and Table 4.1 respectively.

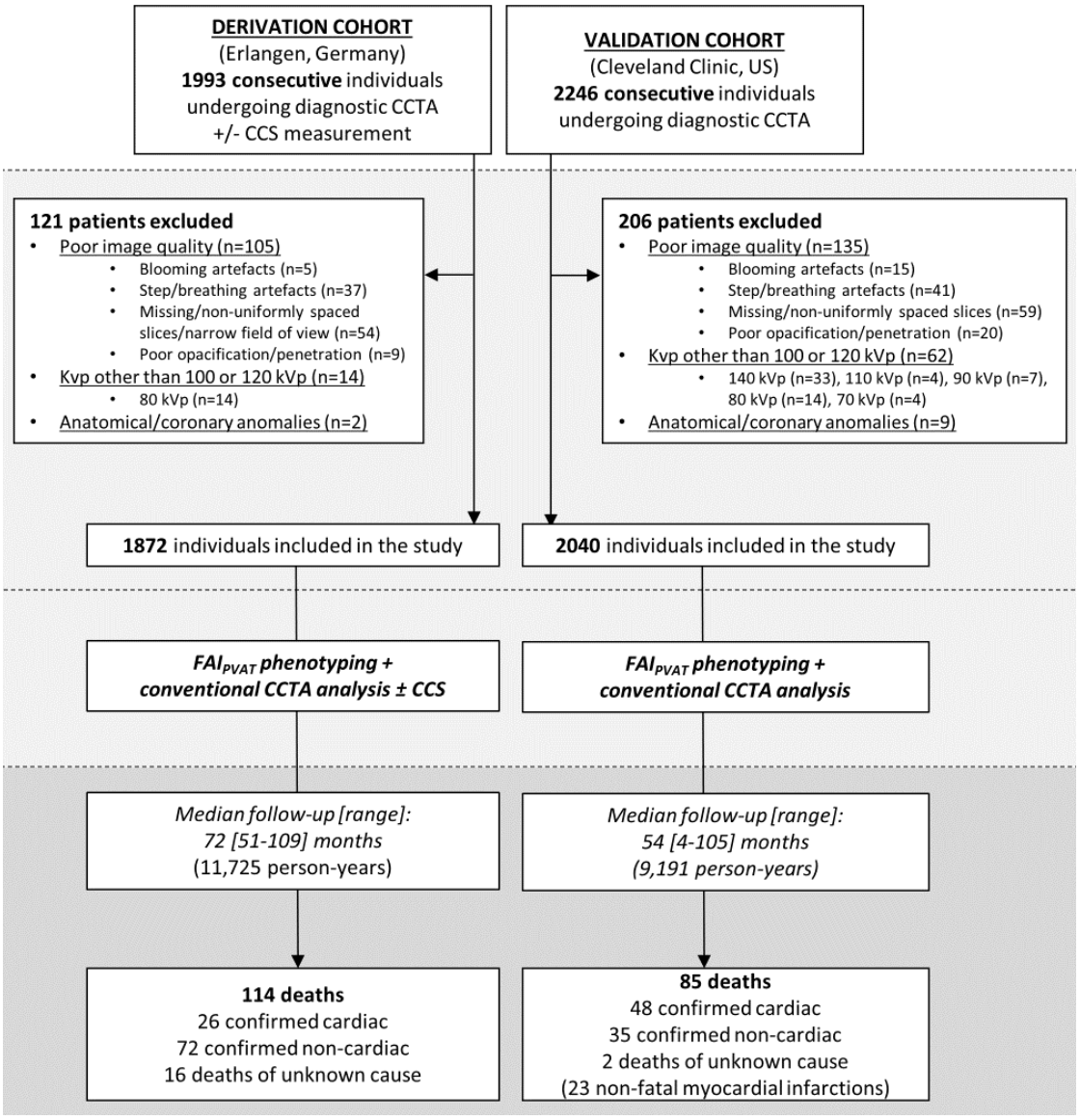

Figure 4.1. CRISP-CT Study design and flowchart. *CCS: Agatston coronary calcium score; CCTA: coronary computed tomography angiography; CRISP-CT: cardiovascular risk prediction using computed tomography (study); FAI_{PVAT}: fat attenuation index of the perivascular adipose tissue. Reproduced with permission from Oikonomou EK et al.* ***Lancet*** *2018, Sep 15;392(10151):929-939.*

Table 4.1. Cohort demographics and clinical characteristics.

	Derivation	Validation	P value
Number of subjects in the original cohorts	1993	2246	-
Eligible subjects included in the study, n (%)	1872 (100)	2040 (100)	-
Age in years (median [range])	62 [17-89]	53 [19-87]	<0.001
Male sex, n (%)	1178 (62.9)	1126 (55.2)	<0.001
Risk factors* (n, valid %)			
Hypertension	1068 (62.0)	949 (46.5)	<0.001
Hypercholesterolaemia	930 (54.7)	1126 (55.2)	0.78
Diabetes Mellitus	215 (12.4)	219 (10.7)	0.11
Smoking	221 (12.8)	465 (22.8)	<0.001
Medications at baseline** (n, valid %)			
Antiplatelets (aspirin/clopidogrel/ticagrelor)	606 (37.6)	987 (48.4)	<0.001
Statins	557 (34.6)	813 (39.9)	0.001
ACEi or ARBs	696 (43.1)	599 (29.4)	<0.001
Beta-blockers	721 (44.8)	303 (14.9)	<0.001
Cardiac CT parameters and results			
CT scanner type, n (%)			
2 x 64 Definition Flash (Siemens Healthcare)	1482 (79.2)	-	
1 x 64 Sensation 64 (Siemens Healthcare)	339 (18.1)	-	
2 x 128 Definition Flash (Siemens Healthcare)	71 (2.7)	221 (10.8)	<0.001
1 x 256 Brilliance iCT (Philips Healthcare)	-	1777 (87.1)	
2 x 192 Somatom Force (Siemens Healthcare)	-	42 (2.1)	
Tube voltage, n (%)			
100 kVp	415 (22.2)	673 (33.0)	<0.001
120 kVp	1457 (77.8)	1367 (67.0)	
Total CCS score, n (%)			
<300	1153 (61.6)	N/A	
≥300	262 (14.0)	N/A	-
N/A	457 (24.4)	N/A	
Coronary Artery Disease: maximal stenosis, n (%)			
None to mild (<25%)	673 (36.0)	1033 (50.6)	
Mild (25-49%)	732 (39.0)	721 (35.4)	<0.001
Moderate (50-69%)	226 (12.1)	196 (9.6)	
Severe (≥70%)	241 (12.9)	90 (4.4)	
Prospective follow-up			
Duration in months (median [follow-up])	72 [51-109]	53.8 [4-105]	<0.001
All-cause mortality, n (%)	114 (6.1)	85 (4.2)	-
Confirmed cardiac	26 (1.4)	48 (2.4)	
Confirmed non-cardiac	72 (3.8)	35 (1.7)	

Values presented as median [range] or number (percentages, %); maximum missingness in the derivation cohort: *9.2%, **13.9%; ACEi: Angiotensin-Converting Enzyme inhibitors; ARBs: Angiotensin-II-Receptor Blockers; CAD: coronary artery disease; CCS: Coronary Calcium Score; CT: Computed Tomography. N/A: not available/applicable. P values are derived from Mann-Whitney U-test (continuous variables) and Pearson's chi-square test (categorical variables) comparisons between the two cohorts.

4.2.2. Data collection, definitions and outcome assessment

Data collection: In both cohorts, outcome data were assembled through search of medical records, and querying of local/national databases by local investigators not involved in subsequent image/data analysis. Clinical data and demographics were recorded prospectively in the electronic medical records at the time of the initial clinical encounter and manually extracted for the current study. The beginning of follow-up was considered as the date of the CCTA scan. The primary endpoints of the study were the occurrence of all-cause and cardiac mortality. In the validation cohort, additional data on myocardial infarction events during follow-up (ST-segment elevation or non-ST segment elevation) were retrieved through search of electronic health records.

Endpoint definitions: For the purpose of this study, we followed the guidelines of the ACC/AHA (American College of Cardiology/American Heart Association) [178] and the Academic Research Consortium for definition of the cause of death [179]. Cardiac mortality was defined as any death due to proximate cardiac causes (e.g. myocardial infarction, low-output heart failure, fatal arrhythmia). Deaths fulfilling the criteria of sudden cardiac death were also included in this group [178, 179]. Any death not covered by the previous definition, such as death caused by malignancy, accident, infection, sepsis, renal failure, suicide or other non-cardiac vascular causes such as stroke or pulmonary embolism was classified as non-cardiac [178, 179]. Deaths where information on the exact cause could not be collected with certainty were classified as "deaths of unknown cause" at the discretion of the local site investigators.

Event adjudication: Adjudication of events and the exact cause of death was performed internally within each site by local study investigators not involved in subsequent image

or statistical analysis, through chart review, inspection of the death certificate and/or telephone follow-up and/or verification with a family member. For the classification of the cause of death, study investigators followed the guidelines of the ACC/AHA [178] and the Academic Research Consortium [179], as described above.

Risk factors: In regression models, hypertension was defined based on the presence of a documented diagnosis or treatment with an antihypertensive regimen, according to the relevant clinical guidelines [180]. Similar criteria were applied for the definition of hypercholesterolemia and diabetes mellitus [10, 181].

Pre-test probability of coronary artery disease (CAD): I calculated the pre-test probability of CAD in the included study population by using the updated formula of the CAD Consortium, using all available clinical variables (age, sex, hypertension, hypercholesterolaemia, diabetes mellitus, smoking, atypical/typical angina) and assuming a high-prevalence geographical setting [182].

4.2.3. CCTA protocol and analysis

The indications for CCTA as well as the presenting symptoms are summarised in Table 4.2. In both cohorts, the majority of patients had a low-to-mid pre-test probability of CAD (median [interquartile range] of 30.4% [15.4%-50.4%] in the derivation versus 21.5% [9.3%-38.7%] in the validation cohort, P<0.001). The detailed CCTA protocols and the image analysis methodology, including CCS calculation from non-contrast CT images, CAD assessment, high-risk plaque definitions has been previously described in chapter 2 (sections 2.2.2. and 2.3-2.9).

Table 4.2. Presenting symptoms and indications for CCTA in the study population.

	Derivation cohort	Validation cohort
Total number included, n (%)	1872 (100)	2040 (100)
Pre-test likelihood of CAD (%)*	30.4 [15.4-50.4]	21.5 [9.3-38.7]
Indications for CCTA referral, n (%)		
Assessment for CAD/coronary anatomy	1790 (95.6)	1761 (86.4)
Other non-coronary indications	82 (4.4)	279 (13.6)
Symptoms prior to CCTA, n (valid %)		
Chest pain	768 (43.4)	1184 (58.0)
Dyspnoea	193 (10.8)	452 (22.2)
Palpitations	240 (13.5)	225 (11.0)

CAD: coronary artery disease; CCTA: coronary computed tomography angiography; IQR: interquartile range. Valid % refers to the study population with known symptoms, after excluding individuals with undocumented symptoms. *median [IQR]

Briefly, all reconstructed images were transferred to a processing workstation (Aquarius Workstation® V.4.4.11-13, TeraRecon Inc., Foster City, CA, USA). All scans were reviewed based on their quality. Scans were excluded from inclusion in the study in the presence of severe artefacts, missing slices, coronary abnormalities or if done at tube voltage other than 100 or 120 kVp, where perivascular FAI has been validated [126, 150]. To adjust for differences in mean attenuation between scans done at different tube voltages, the perivascular adipose tissue fat attenuation index (FAI) for scans performed at 100 kVp was divided by a conversion factor of 1.11485 to be comparable to scans performed at 120 kVp, as previously validated [126, 150]. Tube voltage was also included as a factor in all relevant multiple regression models. Scans performed at different tube voltage settings were excluded, since the perivascular FAI analysis methodology has not been validated yet at these settings. Scans performed at 140, 110, 90 and 70 kVp were only present in the Cleveland cohort, accounting for just 2.1% (48/2246) of the total number of scans. Similarly, scans performed at 80 kVp accounted for 0.7% (14/1993) and 0.6% (14/2246) of the total number of CCTA scans in the Erlangen, and Cleveland cohorts respectively. In the latter cohort, all 80 kVp scans were performed in 2016

suggesting a possible change in clinical practice, which could introduce a bias compared to older cases from within the same cohort.

4.2.4. Perivascular FAI mapping

The proximal 40mm-long segments of all three major epicardial coronary vessels (right coronary artery [RCA], left anterior descending artery [LAD] and left circumflex artery [LCx]) were traced and respective PVAT was defined as the adipose tissue within a radial distance from the outer vessel wall equal to the diameter of the vessel, as previously described and validated [126]. To avoid the effects of the aortic wall, the most proximal 10 mm of the RCA were excluded and analysis was performed in the proximal 10-50 mm of the vessel, as previously described [126]. In the LAD and LCX, analysis was performed in the proximal 40 mm of each vessel (Figure 4.2). The left main coronary artery was not analysed because it is of variable length and may be absent. Perivascular FAI was determined by measuring the average PVAT attenuation based on the attenuation histogram of PVAT within the -30 to -190 HU window, as previously described in chapter 2 (section 2.9) [126] Similar to our previous validation studies [126] technical (tube voltage, lumen attenuation) and anatomical parameters (vessel diameter) were all weakly associated with perivascular FAI, explaining only ~5% of its variation (R^2=0.05, p<0.001 in a multivariable model [Figure 4.3]). Intra-observer and inter-observer agreement for perivascular FAI was excellent (intra-class correlation coefficient: 0.987 [P<0.001] and 0.980 [P<0.001] respectively), as previously reported (section 2.9).

4.2.5. Statistical analysis

Continuous variables are presented as mean ± standard deviation or median [range], as appropriate. Categorical variables between two or more groups were compared using a Pearson's Chi-square test, whereas continuous variables between groups were compared by a Student's t-test or Mann-Whitney U test (for two groups, as appropriate) and analysis of variance (ANOVA) (for three groups). Correlations between continuous variables were tested by either Pearson's r (including the coefficient of determination R^2) or Spearman's rank correlation coefficient, as appropriate. The association between perivascular FAI

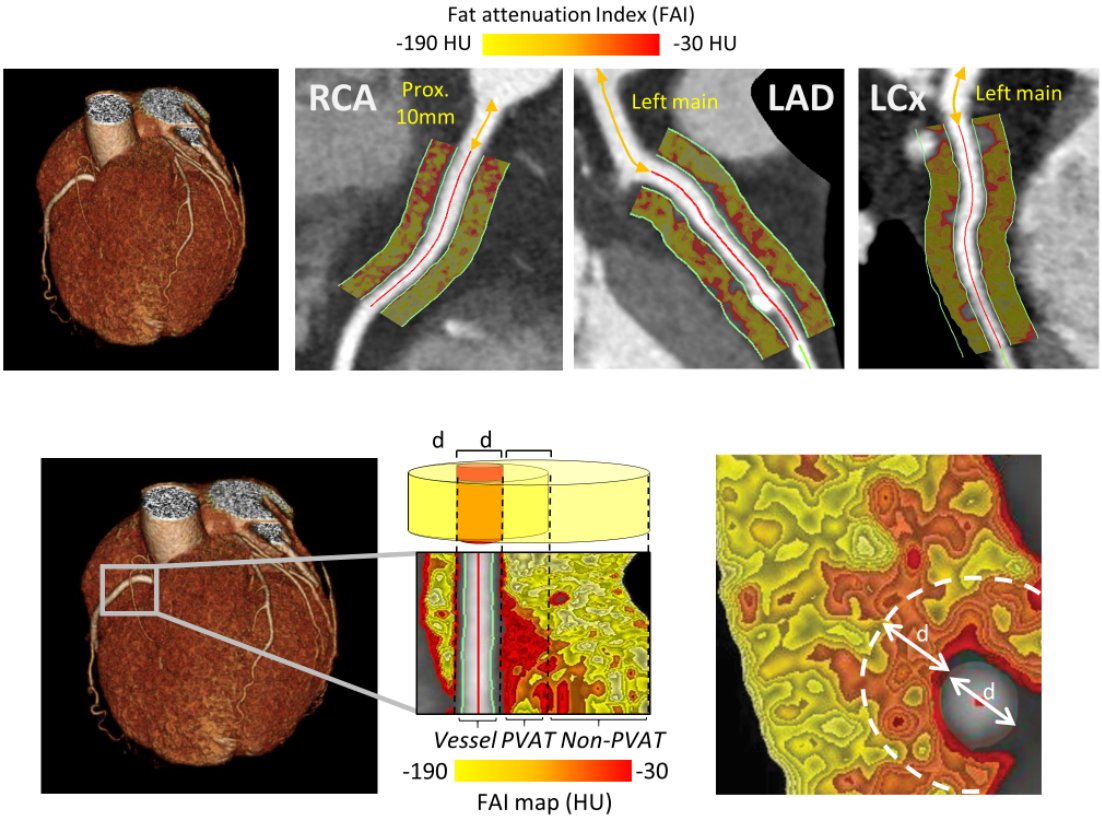

Figure 4.2. Pericoronary FAI analysis around the major epicardial coronary vessels. (Upper panel) *Pericoronary FAI mapping of the proximal segments of all major three epicardial coronary vessels (right coronary artery [RCA], left anterior descending artery [LAD] and left circumflex artery [LCx]) with corresponding FAI color maps.* ***(Lower panel)*** *Definition of perivascular FAI as the average attenuation of fat voxels within a radial distance from the outer vessel wall that is equal to the diameter of the adjacent vessel. FAI: fat attenuation index; HU: Hounsfield Units; LAD: left anterior descending artery; LCx: left circumflex; PVAT: perivascular adipose tissue; RCA: right coronary artery. Reproduced with permission from Oikonomou EK et al.* ***Lancet*** *2018, Sep 15;392(10151):929-939.*

and technical/anatomical variables was tested in multivariable linear regression models. Where information on categorical risk factors was missing, a third group was created (yes/no/unknown, maximum degree of missingness: 13.9%). The prognostic value of FAI_{PVAT} for all-cause, cardiac or non-cardiac mortality was assessed using multivariable Cox regression models, while unadjusted Kaplan-Meier curves were also plotted and are graphically presented. CCS values were log-transformed before inclusion in regression models (ln[CCS+1]). Fractional polynomials were used to model non-linear relationships of perivascular FAI with time-to-mortality in Cox regression models and the best-fitting

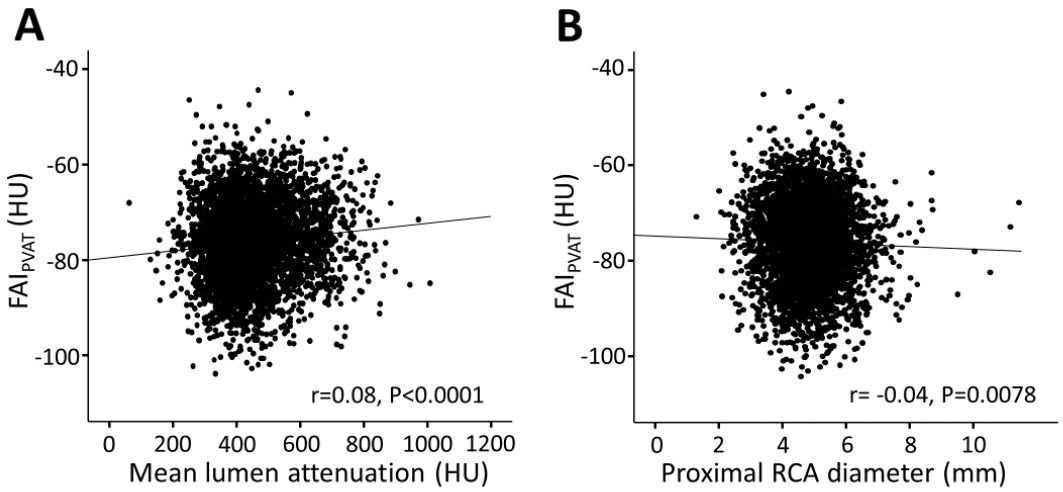

C **Association of FAI_{PVAT} with technical/anatomical parameters.**

Multiple linear regression model [Dependent variable: FAI_{PVAT} (HU)]				
Independent variables	**Unstandardised coefficient**	**Standardised coefficient**	**P value**	**R^2 of the model**
Lumen attenuation (HU)	0.007	0.10	<0.0001	
RCA diameter (mm)	-0.253	-0.026	0.10	0.05
Tube voltage (120 vs 100 kVp)	-5.315	-0.278	<0.0001	

FAI_{PVAT}: fat attenuation index of the perivascular adipose tissue; HU: Hounsfield Units; RCA: right coronary artery.

Figure 4.3. Association of perivascular FAI with technical and anatomical parameters. (A) *Bivariate association between FAI_{PVAT} and mean lumen attenuation in the aortic root.* ***(B)*** *Bivariate association between FAI_{PVAT} and average diameter of the proximal RCA.* ***(C)*** *Multiple linear regression model with FAIPVAT as the dependent variable and mean lumen attenuation, vessel diameter and tube voltage as the independent predictors. FAI_{PVAT}: fat attenuation index of the perivascular adipose tissue; HU; Hounsfield Units; RCA: right coronary artery. Reproduced with permission from Oikonomou EK et al.* ***Lancet*** *2018, Sep 15;392(10151):929-939.*

fractional polynomial models are graphically presented. An optimal cut-off point was selected for perivascular FAI by identifying the cut-off value that maximises Youden's J statistic (sum of sensitivity and specificity) on time-dependent receiver operating characteristic curve (ROC) analysis for cardiac mortality to ensure an optimal balance between sensitivity and specificity in our models. The prognostic value of perivascular FAI (as a dichotomous variable) was then tested in multivariable Cox regression analysis after adjustment for age, sex, hypertension, hypercholesterolaemia, diabetes mellitus, smoking, epicardial obesity (measured as total epicardial adipose tissue volume), tube voltage, modified Duke Prognostic CAD Index and number of high-risk plaque features. The improvement in model performance/discrimination and risk classification by adding perivascular FAI in a baseline model consisting of traditional risk factors was assessed by a) comparing the C-statistic (Area under the Curve) of the two nested models (from time-dependent ROC analysis), b) a likelihood-ratio test (in Cox regression models), and c) the integrated discrimination improvement (IDI), and net reclassification improvement (NRI) indices for censored data. Bootstrapping with 200 replications was used to calculate 95% confidence intervals for AUC, NRI, and IDI [183]. All models were independently tested in the two cohorts of the study. Heterogeneity in further subgroup analyses was assessed using the I^2 statistic. Statistical analyses were performed using Stata v14.0 (Stata Corp Inc., College Station, Texas) and R version 3.4.0 (packages: survival, survIDINRI, timeROC, survminer and nricens). All tests were two-sided and α was set at 0.05.

4.3. Results

4.3.1. CCTA results and follow-up

In the derivation cohort, among the 1993 subjects who underwent CCTA, 121 scans (6.1%) were excluded from the analysis due to technical considerations (Figure 4.1).

Similarly, in the validation cohort, 206 (9.2%) out of 2246 CCTA scans were excluded from analysis. A detailed break-down of CCTA findings is presented in Table 4.3. During follow-up, 114 deaths were recorded in the derivation cohort (26 confirmed cardiac, 72 confirmed non-cardiac and 16 of unknown cause). In the validation cohort, 48 out of 85 hs were classified as cardiac, 35 as non-cardiac and 2 as deaths of unknown cause.

4.3.2. Perivascular FAI, all-cause and cardiac mortality

FAI measured around the proximal RCA was strongly associated with FAI measured around the proximal LAD and LCx (Figure 4.4). In both cohorts, higher FAI values in the PVAT of all three coronary vessels were associated with a significantly higher adjusted risk of all-cause mortality, while peri-RCA and peri-LAD FAI (but not peri-LCx) were also significantly associated with the prospective cardiac mortality risk (Figure 4.5). The non-significant association of peri-LCx FAI with cardiac mortality could reflect the

Table 4.3. Break-down of CCTA findings in the derivation and validation cohorts.

	Derivation cohort	Validation cohort
Subjects included in the study, n (%)	**1872 (100)**	**2040 (100)**
Total CCS score, n (%)		
0	526 (28.1)	-
1-99	444 (23.7)	-
100-299	183 (9.8)	-
≥300	262 (14.0)	-
Not performed	457 (24.4)	100.0
Coronary Artery Disease: maximal stenosis, n (%)		
None to mild (<30%)	673 (36.0)	1033 (50.6)
Mild (30-50%)	732 (39.0)	721 (35.4)
Moderate (50-70%)	226 (12.1)	196 (9.6)
Severe (≥70%)	241 (12.9)	90 (4.4)
High-risk plaque features, n (%)		
Any	465 (24.8)	458 (22.5)
Spotty calcification	417 (22.3)	407 (20.0)
Low-attenuation plaque	84 (4.5)	64 (3.1)
Positive remodelling	72 (3.9)	126 (6.2)
Napkin-ring sign	51 (2.7)	55 (2.7)

CAD: coronary artery disease; CCTA: coronary computed tomography angiography; CCS: Agatston coronary calcium score; LAD: left anterior descending artery.

predominant localisation of culprit coronary lesions in the RCA and LAD [184]. Given the statistical collinearity between perivascular FAI measurements around the RCA and

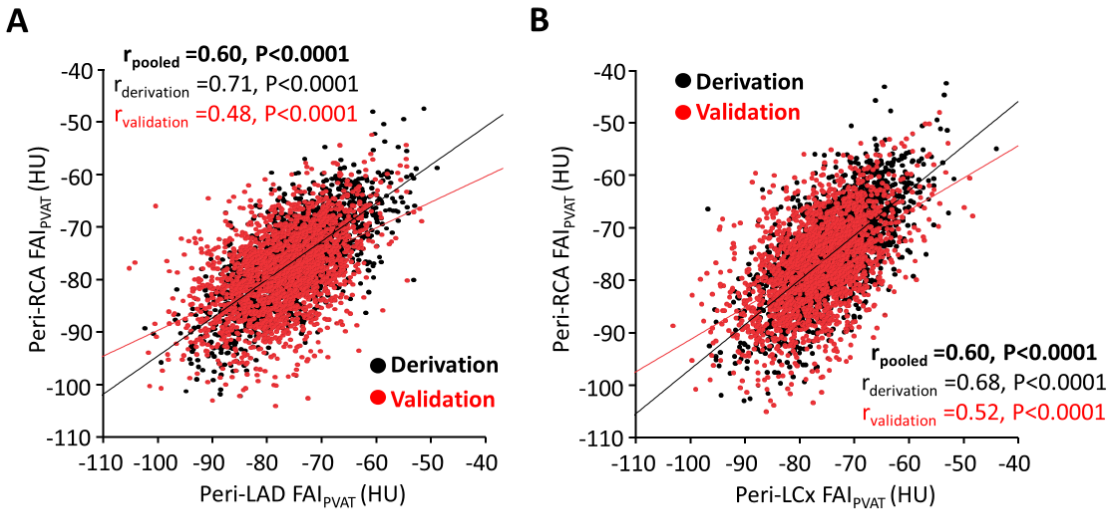

Figure 4.4. Bivariate associations of perivascular FAI measured around the three major epicardial coronary vessels. *Correlation between FAI_{PVAT} values measured around the RCA and LAD/LCx. FAI_{PVAT}: fat attenuation index of the perivascular adipose tissue; HU: Hounsfield Units; LAD: left anterior descending artery; LCx: left circumflex; RCA: right coronary artery. Reproduced with permission from Oikonomou EK et al.* ***Lancet*** *2018, Sep 15;392(10151):929-939.*

Perivascular FAI around the three major coronary arteries and mortality risk in the two cohorts

Pericoronary FAI	Cohort	All-cause mortality (adj. HR [95%CI])*	Cardiac mortality (adj. HR [95%CI])*
RCA (per 1SD increments)	*Derivation*	1.49 (1.20-1.85), P<0.001	2.15 (1.33-3.48), P=0.002
	Validation	1.84 (1.45-2.33), P<0.001	2.06 (1.50-2.83), P<0.001
LAD (per 1SD increments)	*Derivation*	1.78 (1.42-2.23), P<0.001	2.61 (1.60-4.27), P<0.001
	Validation	1.77 (1.39-2.27), P<0.001	1.81 (1.29-2.55), P<0.001
LCX (per 1SD increments)	*Derivation*	1.37 (1.10-1.70), P=0.005	1.32 (0.83-2.08), P=0.24
	Validation	1.47 (1.16-1.86), P=0.002	1.29 (0.93-1.79), P=0.13

*Adjusted for age, sex, hypertension, hypercholesterolemia, diabetes, smoking status, epicardial adipose tissue volume, extent of CAD disease (Duke Prognostic CAD Index), number of high-risk plaque features and tube voltage.
CAD: coronary artery disease; CI: confidence interval; FAI_{PVAT}: fat attenuation index of the perivascular adipose tissue; HR: hazard ratio; LAD: left anterior descending artery; LCX: left circumflex; RCA: right coronary artery; SD: standard deviation.

Figure 4.5. Perivascular FAI analysis around the major epicardial coronary vessels and adverse events. *Adjusted Hazard Ratios for all-cause and cardiac mortality for pericoronary FAI around the RCA, LAD and LCx (expressed per 1 SD increments). CAD: coronary artery disease; CI: confidence interval; FAI: fat attenuation index; HU: Hounsfield Units; LAD: left anterior descending artery; LCx: left circumflex; RCA: right coronary artery; SD: standard deviation. Reproduced with permission from Oikonomou EK et al.* ***Lancet*** *2018, Sep 15;392(10151):929-939.*

LAD, analysis was subsequently restricted to the proximal RCA (henceforth referred to simply as perivascular FAI/FAI_{PVAT}), which has been linked in our previous work to the overall coronary inflammatory and atherosclerotic status [126].

Perivascular FAI was normally distributed around a mean (SD) of -75.1 (8.6) HU in the derivation and -77.0 (8.5) HU in the validation cohorts. Of note, FAI was not associated with either CCS on non-contrast CT or local calcium burden in the adjacent vascular segment (P=0.86 and 0.18 respectively, Figure 4.6). Adjusted fractional polynomial modeling revealed the presence of a J-shaped relationship between FAI_{PVAT} and the prospective risk of all-cause and cardiac mortality in both cohorts (Figure 4.7).

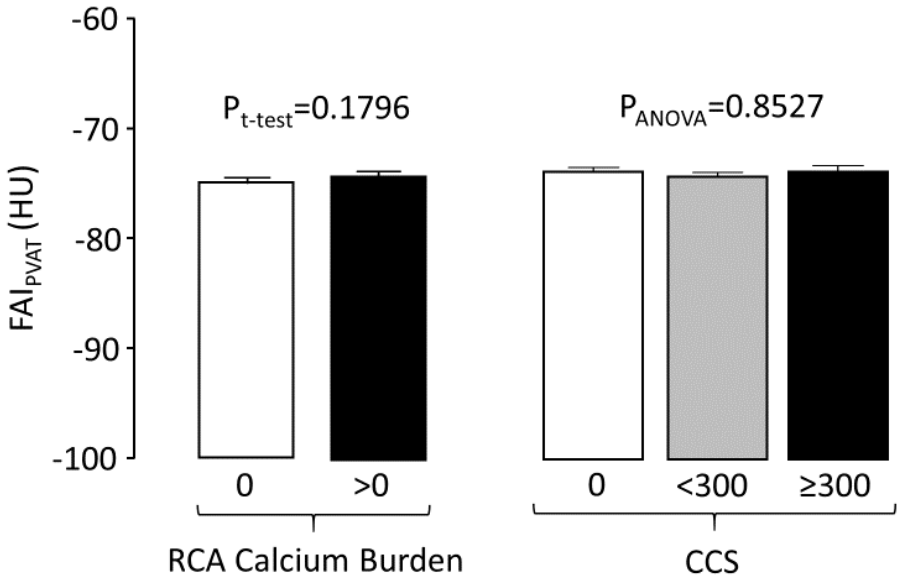

Figure 4.6. Association of perivascular FAI with local and global coronary calcium. *In the Erlangen cohort, FAI_{PVAT} was independent of coronary calcium, measured either in the whole coronary tree on non-contrast images (Agatston coronary calcium score, CCS) or in the adjacent vascular segment on contrast CCTA images (calcium burden of the RCA). ANOVA: analysis of variance; CCS: Agatston coronary calcium score; CCTA: coronary computed tomography angiography; FAI_{PVAT}: fat attenuation index of the perivascular adipose tissue; RCA: right coronary artery. Reproduced with permission from Oikonomou EK et al.* ***Lancet*** *2018, Sep 15;392(10151):929-939.*

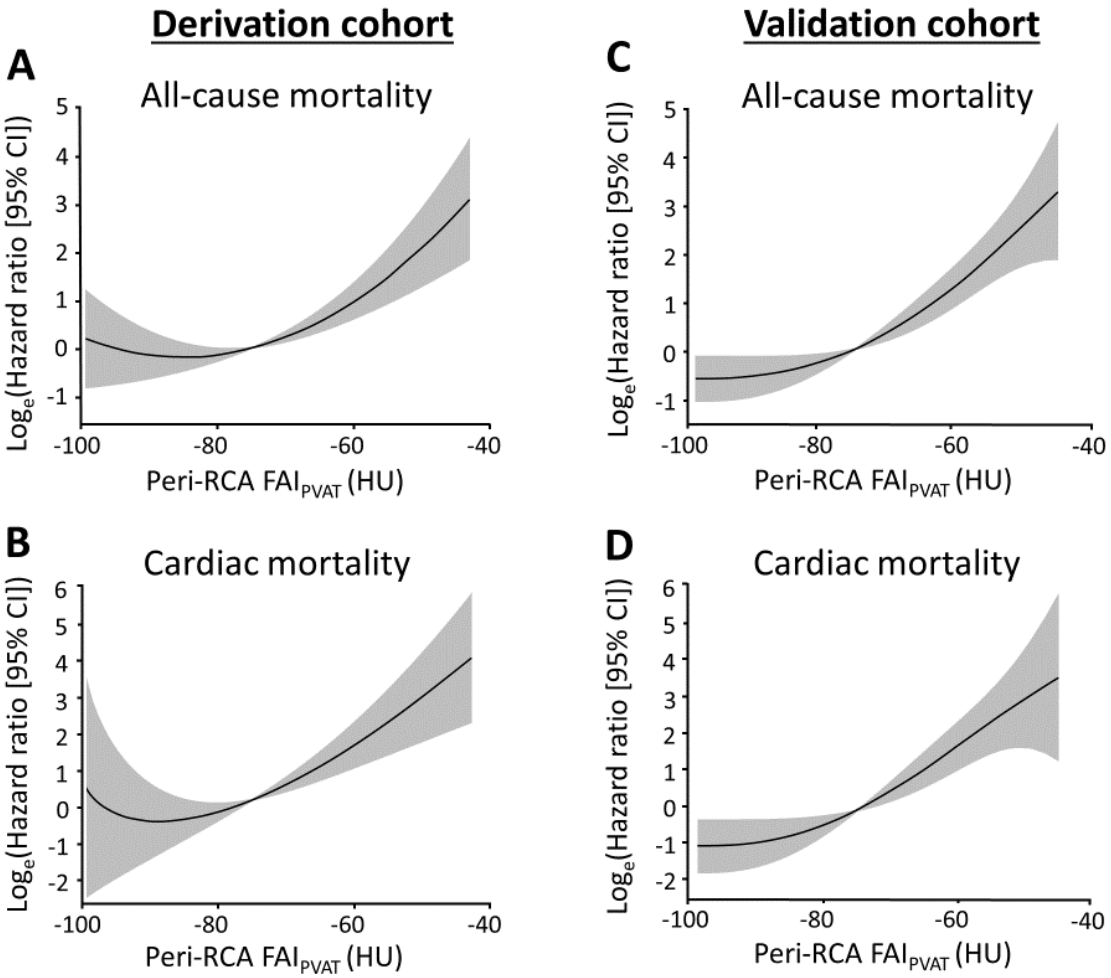

Figure 4.7. Fractional polynomial models to assess non-linear associations between perivascular FAI and mortality risk. *(A, B) Best fitting fractional polynomials for FAI_{PVAT} as a predictor of all-cause and cardiac mortality, in the Erlangen (A, B) and Cleveland cohorts (C, D), respectively. All models demonstrate a J-shaped association between FAI_{PVAT} at baseline and prospective mortality risk. Models are adjusted for age, sex, tube voltage, and epicardial adipose tissue volume. CI: confidence interval; FAI_{PVAT}: Fat Attenuation Index of Perivascular Adipose Tissue; HU: Hounsfield Units. Reproduced with permission from Oikonomou EK et al.* ***Lancet*** *2018, Sep 15;392(10151):929-939.*

Based on this observation and in order to generate distinct clinical risk groups, the study population was dichotomised in a high versus low FAI group, based on an optimal cut-off of -70.1 HU (specificity 85.0%, sensitivity 67.7%, negative predictive value 99.5%, positive predictive value 5.9%, calculated at the median follow-up interval of 72 months), as defined in the derivation cohort (Figure 4.8 & Table 4.4).

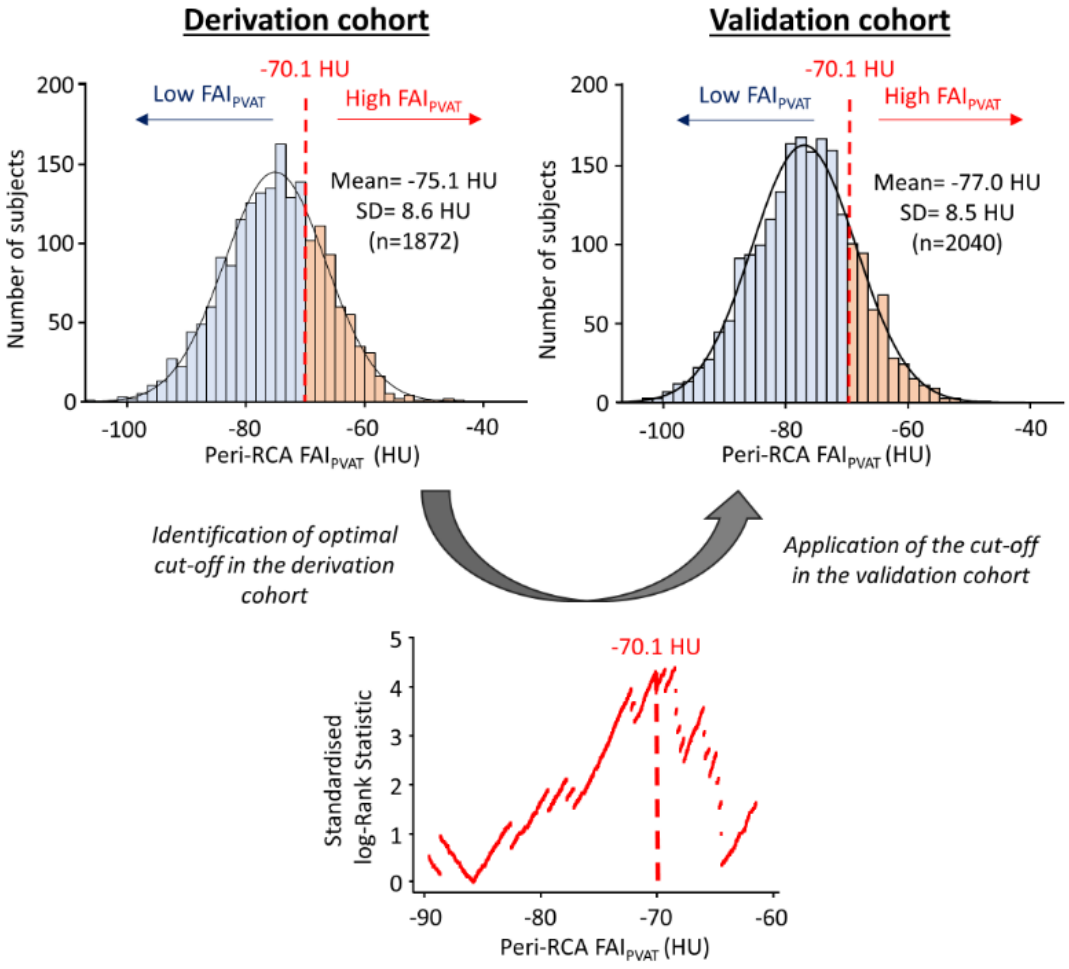

Figure 4.8. Identifying an optimal cutoff for perivascular FAI as a prognostic biomarker. *An optimal cutoff was selected in the derivation cohort, by identifying the perivascular FAI value (around the reference segment of the proximal right coronary artery) that maximised the Youden's J index (sum of sensitivity and specificity) in time-dependent receiver operating characteristic curves for the primary endpoint of cardiac mortality at t_0=6 years (72 months, corresponding to the median follow-up interval in this cohort). The derived cutoff was subsequently applied in both the derivation cohort and the validation cohort in order to validate its prognostic value for cardiac mortality. FAI_{PVAT}: fat attenuation index of the perivascular adipose tissue; HU: Hounsfield Units; RCA: right coronary artery. Reproduced with permission from Oikonomou EK et al.* ***Lancet*** *2018, Sep 15;392(10151):929-939.*

Table 4.4. Sensitivity and specificity of different perivascular FAI cut-offs for prediction of cardiac mortality in the derivation cohort.

Perivascular FAI cutoff (HU)	Specificity	Sensitivity
-66	92.7	40.1
-68	89.0	44.0
-70	85.1	63.7
-70.1	**85.0**	**67.7**
-72	79.4	71.7
-74	70.8	75.6
-76	60.4	75.6
-78	52.2	83.4
-80	41.8	87.3
-82	32.8	87.3
-84	24.3	91.3
-86	17.3	91.3

Specificity and sensitivity presented at different cutoffs of FAI_{PVAT} (per increments of 2 HU in the range of -66 to -86 HU, including the optimal cut-off of -70.1 HU as identified by the Youden's J index (maximal sum of sensitivity and specificity) in the derivation cohort. All presented at t_0=6 years (median follow-up). FAI: fat attenuation index; HU: Hounsfield Units.

In the same cohort, following multivariable adjustment for age, sex, risk factors, tube voltage, modified Duke Prognostic CAD index, and number of high-risk plaque features, high perivascular FAI (≥ vs < -70.1 HU) was associated with a two-fold and nine-fold higher prospective risk of all-cause and cardiac mortality respectively (Figure 4.9). Of note, high perivascular FAI was not significantly associated with non-cardiac mortality (adjusted HR [95% CI]: 1.66 [0.95-2.90], P=0.07). Importantly, in a subgroup of patients where CCS was measured (n=1415, 75.6%), perivascular FAI retained its predictive value for both endpoints following additional adjustment for CCS (adjusted HR [95% CI]: 2.03 [1.17-3.52], P=0.0122 for all-cause and 12.83 [2.76-59.56], P=0.0011 for cardiac mortality). These findings were subsequently validated in the validation cohort, where perivascular FAI values ≥-70.1HU (specificity 81.6%, sensitivity 52.9%, negative predictive value 98.5%, positive predictive value 7.0%), were linked to an adjusted HR [95%CI] of 3.69 [2.26-6.02], P<0.0001 and 5.62 [2.90-10.88], P<0.0001) for all-cause and cardiac mortality respectively (Figure 4.9).

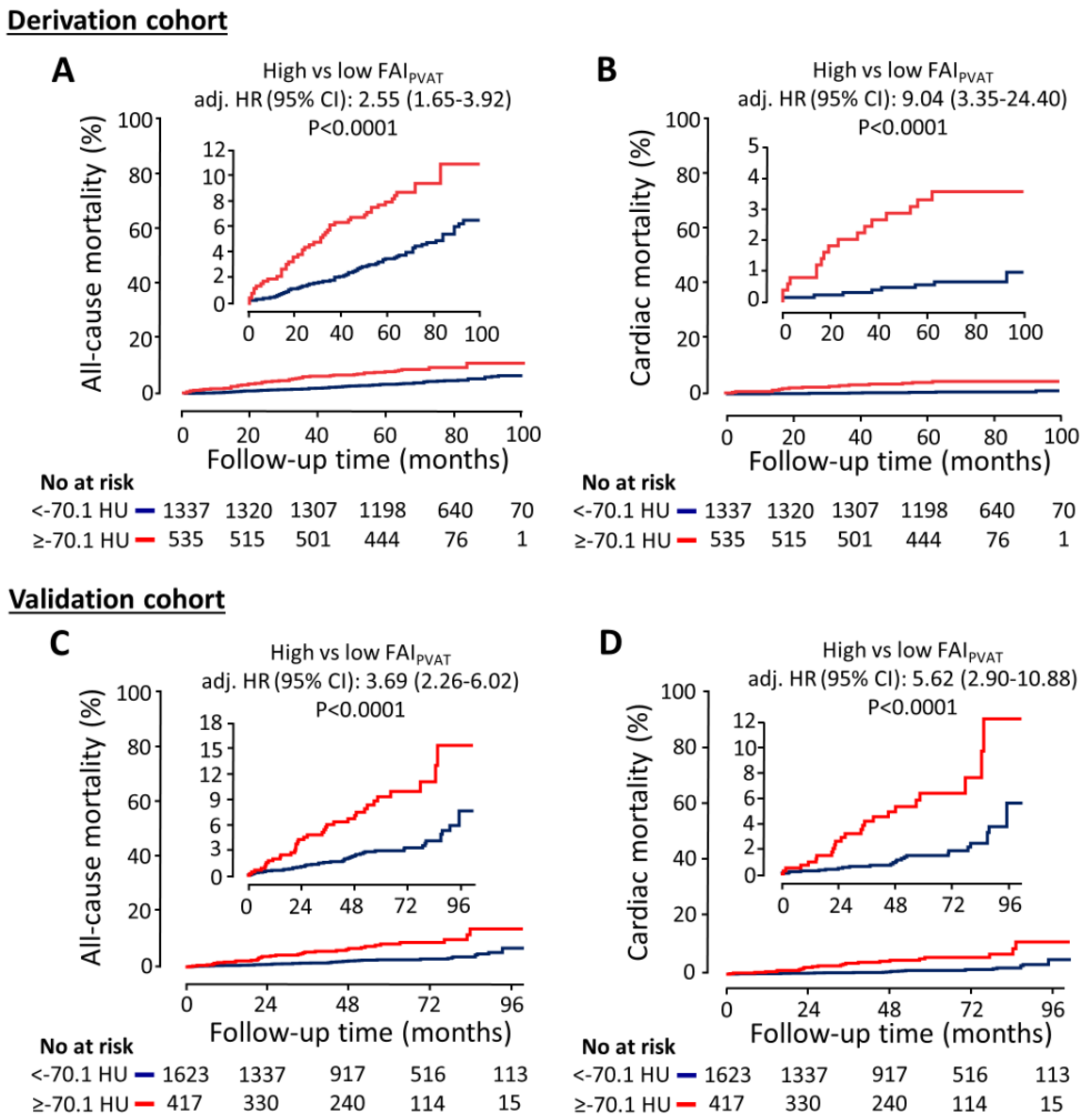

Figure 4.9. High perivascular FAI and future mortality. (A-D) *Unadjusted Kaplan-Meier and adjusted Hazard Ratios for high versus low FAI$_{PVAT}$ (≥ vs < -70.1 HU) for the primary endpoints of all-cause and cardiac mortality, in the derivation and validation cohorts. Multivariable models are adjusted for age, sex, hypertension, hypercholesterolaemia, diabetes mellitus, smoker status, epicardial adipose tissue volume, tube voltage, extent of CAD (Duke Prognostic CAD index) and number of high-risk plaque features. CAD: Coronary Artery Disease; CCS: Coronary Calcium Score; CI: Confidence Interval; FAI$_{PVAT}$: Fat Attenuation Index of Perivascular Adipose Tissue; HR: Hazard Ratio; HU: Hounsfield units, PVAT: Perivascular Adipose Tissue. Reproduced with permission from Oikonomou EK et al.* ***Lancet*** *2018, Sep 15;392(10151):929-939.*

4.3.3. Incremental value of perivascular FAI beyond traditional risk factors

Inclusion of high perivascular FAI (≥-70.1HU) significantly improved the discriminatory value of a CCTA-based risk prediction model that included age, sex, cardiovascular risk factors (hypertension, hypercholesterolaemia, diabetes, smoking, epicardial obesity), extent of CAD (modified Duke Prognostic CAD Index) and number of high-risk plaque features for both all-cause and cardiac mortality (Figure 4.10). Furthermore, perivascular FAI significantly improved all-cause and cardiac mortality risk stratification in both study populations, contributing to significant net reclassification improvement (Table 4.5), driven primarily by a significant reduction in the estimated risk for non-events, highlighting the high specificity and negative predictive value of the method and proposed cutoff. Interestingly, among patients without events the change in the estimated risk following FAI–based risk stratification was not significantly different among individuals with versus without CAD (Derivation cohort: P=0.09 and 0.72, Validation cohort: P=0.68 and 0.40 for all-cause and cardiac mortality respectively).

Table 4.5. Improvement in discrimination and risk reclassification for all-cause and cardiac mortality using perivascular FAI* beyond a current risk prediction model

Cohort	Model performance	Discrimination	Risk Reclassification				
	Change in χ^2, $P_{LR\text{-}test}$	IDI (95% CI)	Events		Non-events		NRI (95% CI)
			Risk Up	Risk Down	Risk Up	Risk Down	
Cardiac mortality							
Derivation	20.29 (P<0.001)	0.038 (0.000-0.174)	0.64	0.36	0.17	0.83	0.94 (0.07-1.34)
Validation	25.30 (P<0.001)	0.032 (0.001-0.090)	0.56	0.44	0.20	0.80	0.72 (0.34-1.07)
All-cause mortality							
Derivation	16.54 (P<0.001)	0.017 (0.003-0.052)	0.48	0.52	0.19	0.81	0.58 (0.35-0.77)
Validation	25.60 (P<0.001)	0.030 (0.008-0.068)	0.51	0.49	0.21	0.79	0.60 (0.30-0.86)

Baseline model (current state-of-the-art or Model 1): age, sex, hypertension, hypercholesterolaemia, diabetes mellitus, active smoker status, epicardial adipose tissue volume, modified Duke Prognostic Coronary Artery Disease Index (reference: Group 1; mild or no disease) and number of high-risk plaque features; **New model (Model 2):** Model 1 + high FAI_{PVAT}. CI: confidence interval; FAI: Fat Attenuation Index of Perivascular Adipose Tissue; IDI: integrated discrimination improvement; LR: Likelihood Ratio; NRI: Net Reclassification Improvement index. *Perivascular FAI (≥-70.1 HU vs <-70.1 HU). IDI and NRI are calculated at t_o=6 years.

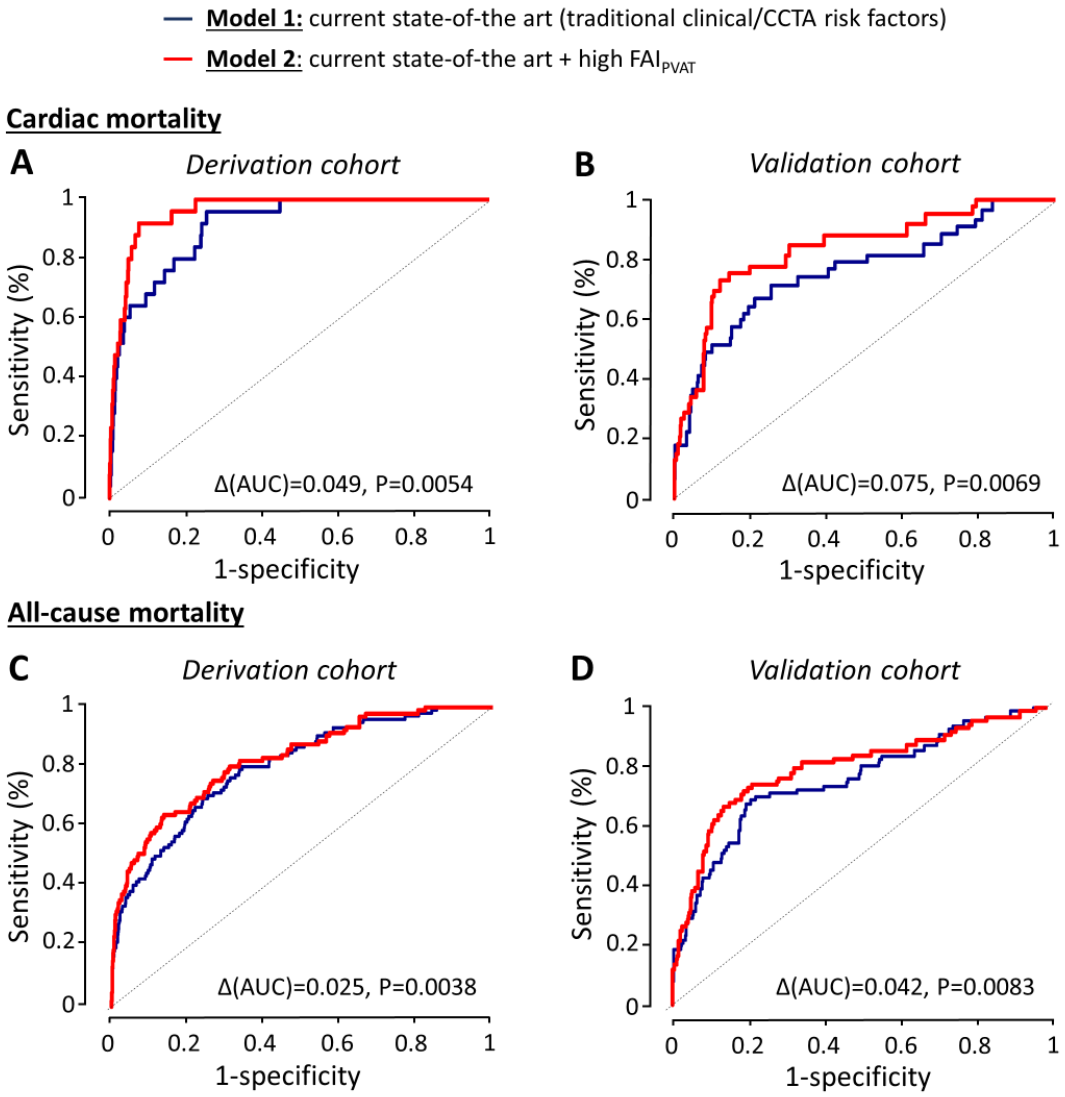

Figure 4.10. Incremental prognostic value of perivascular FAI beyond current CCTA-based risk stratification. *Model 1 represents the current-state-of-the-art in risk assessment and consisted of age, sex, risk factors (hypertension, hypercholesterolaemia, diabetes mellitus, smoker status, epicardial adipose tissue volume), modified Duke Prognostic CAD index and number of high-risk plaque features on CCTA, while Model 2 was constructed by incorporating high FAI_{PVAT} (≥ vs < -70.1 HU) into Model 1. Comparison of time-dependent ROC curves (at t_0=6 years) and respective AUC of the two nested Models 1 & 2 (before, and after the addition of FAI) for discrimination of cardiac **(A-B)** and all-cause mortality **(C-D)** in the derivation and validation cohorts. For cardiac mortality, in the derivation cohort **(A)**, the AUC increased from 0.913 (95% CI: 0.867-0.958) to 0.962 (95% CI: 0.940-0.983) ($P_{\Delta AUC}$=0.0054), whereas in the Cleveland cohort **(B)**, the AUC increased from 0.763 (95% CI: 0.669-0.858) to 0.838 (95% CI: 0.764-0.912) ($P_{\Delta AUC}$=0.0069). For all-cause mortality, in the derivation cohort **(C)**, the AUC increased from 0.800 (95% CI: 0.752-0.848) to 0.825 (95% CI: 0.778-0.872) ($P_{\Delta AUC}$=0.0038), whereas in the validation cohort **(D)**, the AUC increased from 0.755 (95% CI: 0.686-0.823) to 0.797 (95% CI: 0.731-0.863) ($P_{\Delta AUC}$=0.0083). AUC: area under the curve; CAD: coronary artery disease; CCTA: coronary computed tomography angiography; CI: confidence interval; FAI_{PVAT}: fat attenuation index of the perivascular adipose tissue; ROC: receiver operating characteristic. Reproduced with permission from Oikonomou EK et al.* ***Lancet*** *2018, Sep 15;392(10151):929-939.*

Of note, in the subgroup of individuals in the derivation cohort with available CCS, FAI added significant incremental value in risk prediction beyond an enhanced model that included CCS in addition to the previously mentioned risk factors (χ^2=5.95, $P_{LR\text{-}test}$=0.0147 for all-cause and χ^2=10.71, $P_{LR\text{-}test}$=0.0011 for cardiac mortality).

4.3.4. Perivascular FAI in primary and secondary prevention

To evaluate the performance of perivascular FAI in both primary and secondary prevention, subgroup analysis was performed according to the CCS score [7, 10], presence of obstructive CAD, modifed Duke Prognostic CAD Index [50], and presence of high-risk plaque features [60]. Perivascular FAI retained its positive association with both all-cause and cardiac mortality in all subgroups, with no evidence of significant heterogeneity between the subgroups (Figure 4.11). The Cleveland cohort provided information on different ethnic groups and, in a post-hoc analysis, the positive association of high perivascular FAI with adverse events was also found to be consistent across ethnicities (heterogeneity: I^2=0%, P=0.97 for all-cause and P=0.60 for cardiac mortality) (Figure 4.12). In further subgroup analysis, the association between high perivascular FAI and mortality risk was found to be independent of the indications for CCTA referral, presenting symptoms (chest pain) (Figure 4.13) or post-CCTA recommendations (Figure 4.14). However, among individuals who received a recommendation to initiate treatment with statins and/or aspirin post-CCTA, FAI (measured before deployment of the new treatment) was no longer significantly predictive of cardiac mortality (adj. HR [95% CI]: 2.85 [0.44-18.49], P=0.25). In contrast, among those who did not receive any recommendations for change of management post-CCTA, the predictive value of high FAI for cardiac mortality was retained (adj. HR [95% CI]: 18.71 [2.01-174.04], P=0.01).

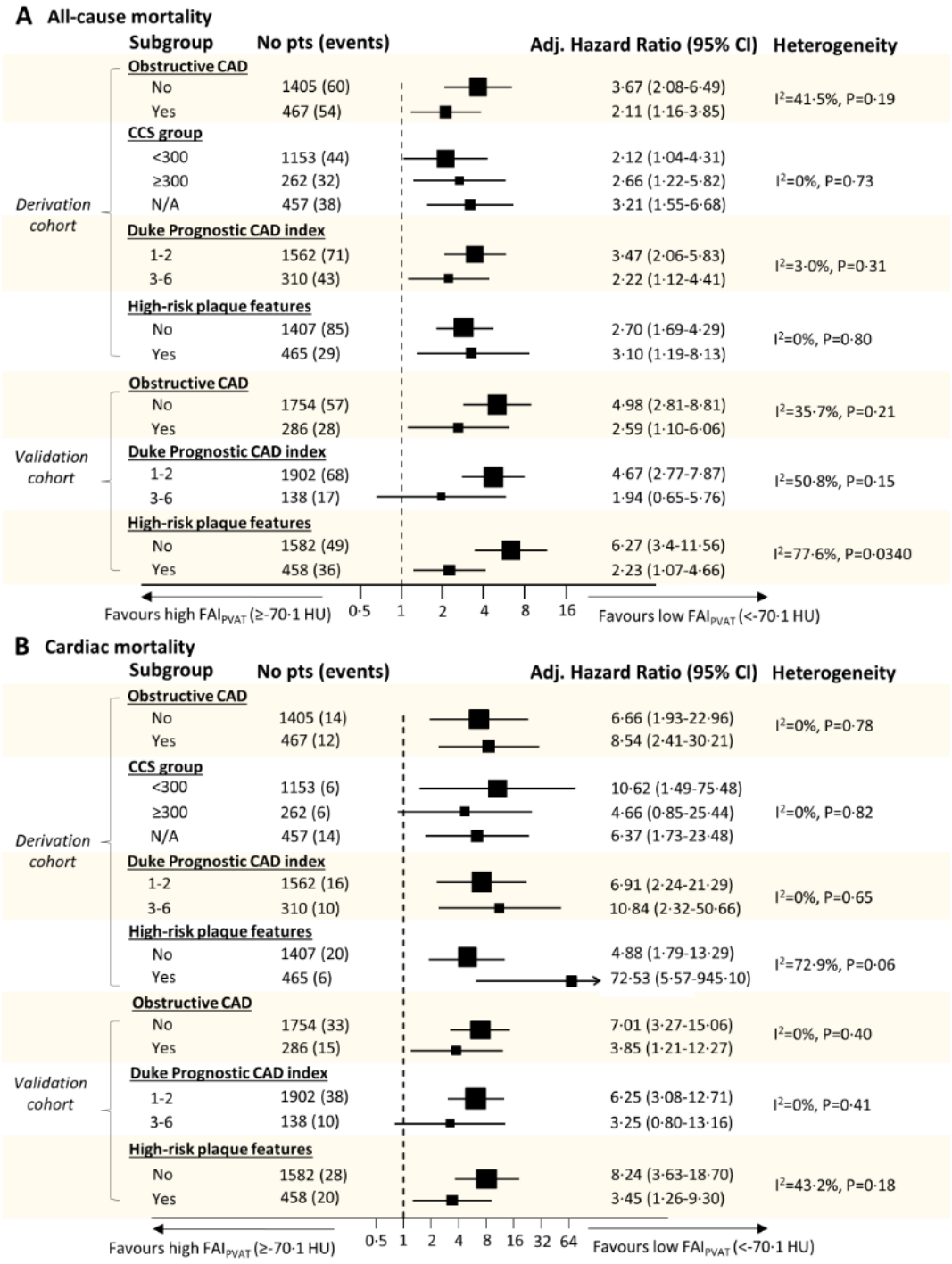

Figure 4.11. Subgroup analysis of the prognostic value of perivascular FAI in patients with and without coronary artery disease. *Adjusted Hazard Ratios for high perivascular FAI (≥ vs < -70.1 HU) as a prognostic biomarker of all-cause* ***(A)*** *and cardiac* ***(B)*** *mortality. Subgroup analysis is stratified by:* ***i.*** *the presence of obstructive CAD;* ***ii.*** *the extent of coronary calcification (measured on non-contrast CT scans in the derivation cohort only);* ***iii.*** *the extent of CAD (assessed by the modified Duke Prognostic CAD Index) and* ***iv.*** *the presence of high-risk plaque features on CCTA. Hazard Ratios are adjusted for age, sex and epicardial adipose tissue volume. CAD: coronary artery disease; CCTA: coronary computed tomography angiography; CI: confidence interval; FAI_{PVAT}: fat attenuation index of perivascular adipose tissue; HU: Hounsfield Units; pts: patients. Reproduced with permission from Oikonomou EK et al.* ***Lancet*** *2018, Sep 15;392(10151):929-939.*

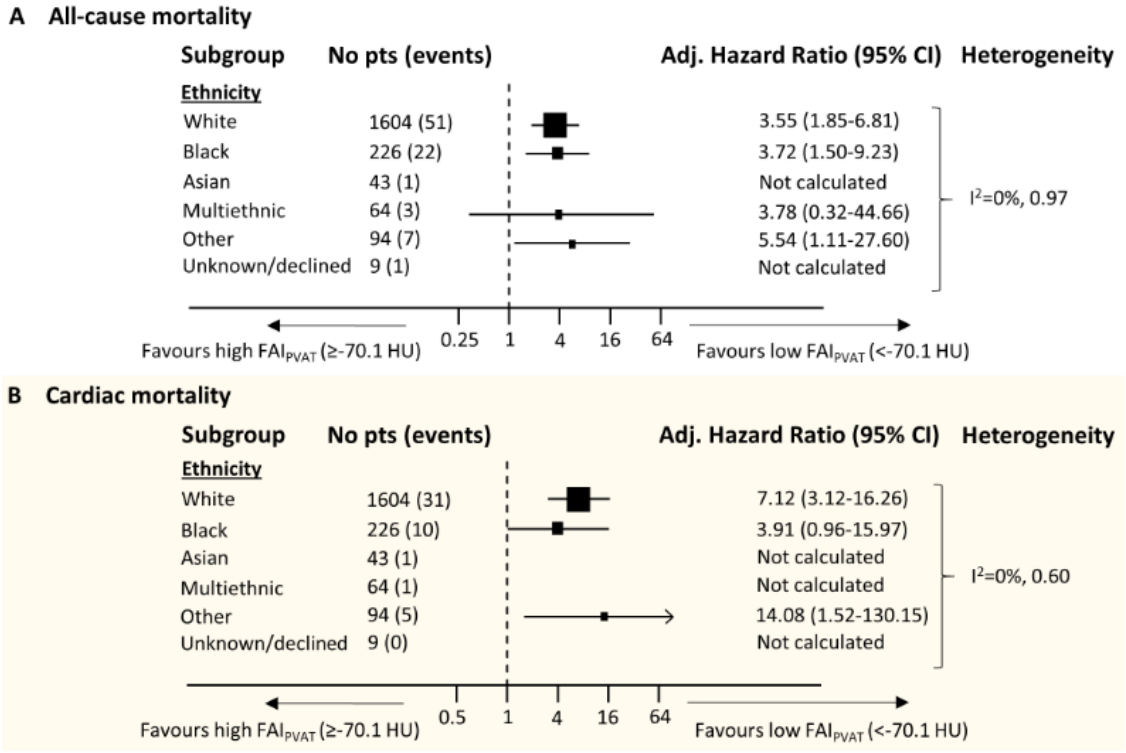

Figure 4.12. Subgroup analysis of the predictive value of perivascular FAI by ethnicity. *In a post-hoc analysis of data collected from the validation cohort, the positive association between perivascular FAI (FAI_{PVAT}) and all-cause (A) or cardiac mortality (B) was found to be independent of the ethnic background of the included study population (no between-group heterogeneity). Models adjusted for age, sex and epicardial adipose tissue volume. CI: confidence interval; FAI_{PVAT}: fat attenuation index of perivascular adipose tissue; HU: Hounsfield Units; pts: patients. Reproduced with permission from Oikonomou EK et al.* ***Lancet*** *2018, Sep 15;392(10151):929-939.*

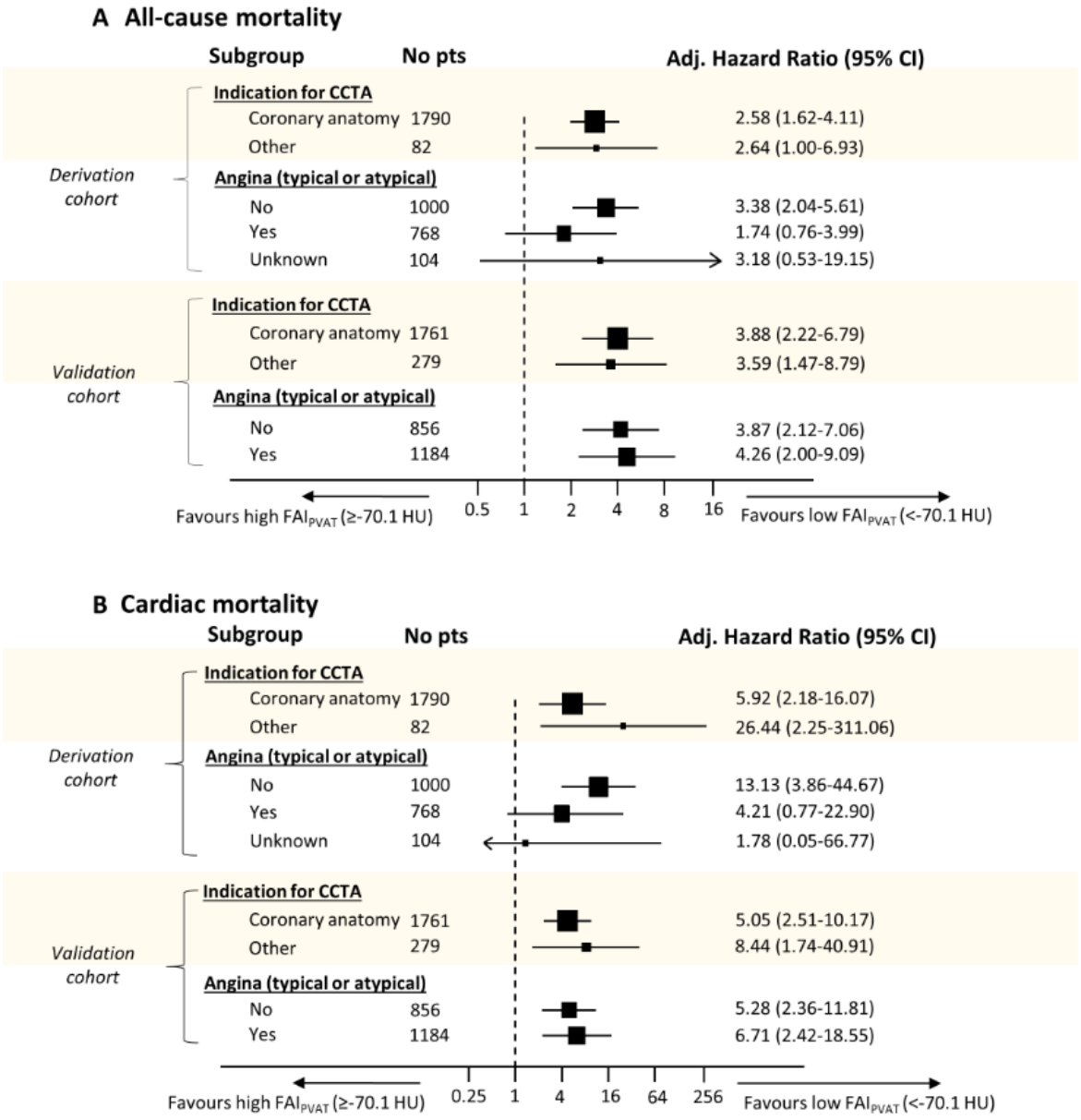

Figure 4.13. Subgroup analysis of the predictive value of perivascular FAI by indication for CCTA and presenting symptoms. *To explore whether different indications for CCTA or different presenting symptoms may affect the predictive value of perivascular FAI for all-cause (A) and cardiac mortality (B), subgroup analysis was performed using adjusted Cox regression models (adjusted for age, sex and epicardial adipose tissue volume) stratified by: i. the indications for CCTA referral (grouped in coronary versus non-coronary indications) and ii. presenting symptoms (presence versus absence of chest pain/angina). Perivascular FAI (FAI_{PVAT}) retained its positive association with the prospective risk of both all-cause and cardiac mortality in both cohorts, with no evidence of heterogeneity between different indications for CCTA or presenting symptoms (I^2<20% and P>0.05 for all between-subgroup comparisons). This supports the predictive value of FAI_{PVAT} as a risk biomarker in a wide range of patients referred for CCTA. CCTA: coronary computed tomography angiography; CI: confidence interval; FAI_{PVAT}: fat attenuation index of perivascular adipose tissue; HU: Hounsfield Units; pts: patients. Reproduced with permission from Oikonomou EK et al.* ***Lancet*** *2018, Sep 15;392(10151):929-939.*

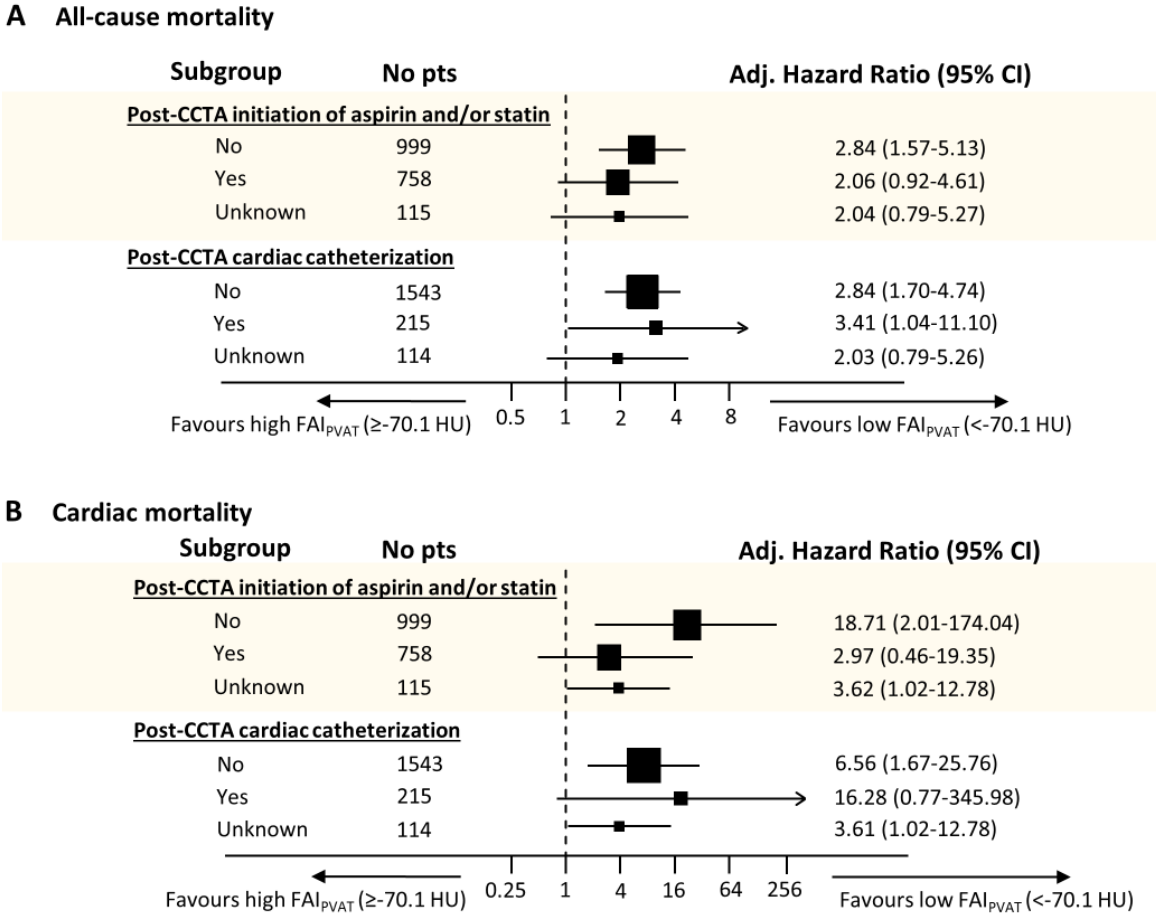

Figure 4.14. Subgroup analysis of the predictive value of perivascular FAI based on post-CCTA changes in medical management. *To explore whether different recommendations post-CCTA may have affected the predictive value of perivascular FAI for all-cause* ***(A)*** *and cardiac mortality* ***(B)****, subgroup analysis was performed in the derivation cohort using adjusted Cox regression models (adjusted for age, sex and epicardial adipose tissue volume) stratified by the following post-CCTA recommendations: i. treatment with statin and/or aspirin; and ii. referral for cardiac catheterization. FAI retained its positive association with the prospective risk of both all-cause* ***(A)*** *and cardiac mortality* ***(B)*** *in all subgroups. Nevertheless, it is worth highlighting that FAI was strongly associated with cardiac mortality events in patients that did not receive recommendations for treatment with statins or aspirin, while the association in the group that did receive such recommendations was non-significant. This may suggest a role for perivascular FAI in guiding the deployment of secondary prevention measures in patients that do not qualify for medical treatment based on conventional CCTA analysis and highlights a significant room for improvement in current clinical practice. CCTA: coronary computed tomography angiography; CI: confidence interval; FAI_{PVAT}: fat attenuation index of perivascular adipose tissue; HU: Hounsfield Units; pts: patients. Reproduced with permission from Oikonomou EK et al.* ***Lancet*** *2018, Sep 15;392(10151):929-939.*

4.3.5. Perivascular FAI versus perivascular fat volume

I then explored whether pericoronary fat volume may offer complementary information beyond perivascular FAI. To this end, I quantified perivascular adipose tissue volume in the perivascular space (as defined for the perivascular FAI analysis). When included in a multivariable model, perivascular fat volume was not associated with the risk of all-cause or cardiac mortality in either of the two cohorts, while perivascular FAI remained a strong, independent predictor of events in both the derivation and validation datasets (Table 4.6). It should be noted that epicardial adipose tissue volume (a well-established surrogate marker of obesity and cardiometabolic risk) was already included in all models and the predictive value of perivascular FAI is already corrected for epicardial adipose tissue volume.

Table 4.6. Association of perivascular FAI and fat volume with mortality

	Derivation cohort HR (95% CI), P value	Validation cohort HR (95% CI), P value
All-cause mortality:		
Perivascular FAI	2.22 (1.42-3.48), P=0<001	3.58 (2.13-6.01), P<0.0001
Perivascular fat volume	0.80 (0.63-1.00), P=0.050	0.95 (0.72-1.25), P=0.73
Cardiac mortality:		
Perivascular FAI	7.14 (2.60-19.59), P<0.001	5.00 (2.47-10.13), P<0.001
Perivascular fat volume	0.63 (0.37-1.09), P=0.10	0.84 (0.58-1.23), P=0.37

CI: confidence interval; EAT: epicardial adipose tissue; FAI: fat attenuation index of the perivascular adipose tissue; HR: hazard ratio; HU: Hounsfield Units; PVAT: perivascular adipose tissue; SD: standard deviation. Models adjusted for age, sex, hypertension, hypercholesterolaemia, diabetes mellitus, smoking, tube voltage, Duke Prognostic Coronary Artery Disease index, and number of high-risk plaque features, and epicardial adipose tissue volume. HR for FAI ≥ vs < -70.1 HU and for Perivascular fat volume per 1 SD.

4.3.6. Perivascular FAI and acute myocardial infarction

Availability of information on prospective AMI events in the validation cohort allowed us to further test the prognostic role of perivascular FAI for this secondary endpoint in a post-hoc analysis. Following multivariable adjustment, high FAI values (≥vs<-70.1HU) were linked to an increased risk of AMI (n=23 reported events, adj.HR [95% CI]: 5.08 [1.89-13.61], P=0.001) (Figure 4.15), suggesting a link between abnormal FAI and plaque instability.

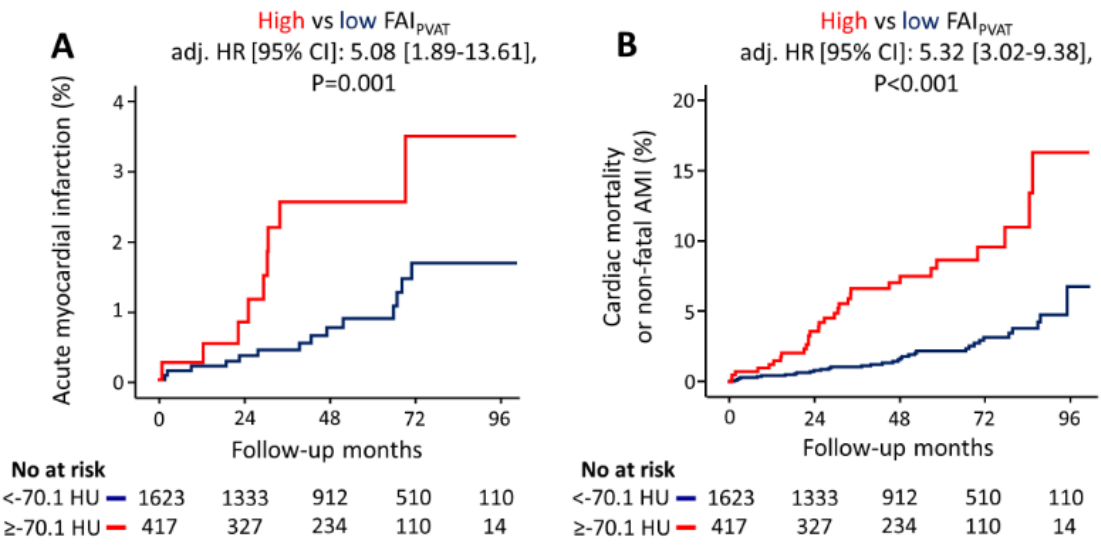

Figure 4.15. Predictive value of perivascular FAI for acute myocardial infarction events. *In the validation (Cleveland) cohort, additional prospective follow-up information on the secondary outcome of acute myocardial infarction (AMI) events, revealed a significant higher risk of AMI in patients with high versus low FAI$_{PVAT}$ values at baseline (≥ versus < -70.1HU). Following multivariable adjustment for age, sex, risk factors (hypertension, hypercholesterolaemia, diabetes mellitus, smoker status, epicardial adipose tissue volume), tube voltage, extent of CAD (assessed by the modified Duke Prognostic CAD Index), and number of high-risk plaque features on CCTA, those in the high FAI$_{PVAT}$ group had a five-fold higher risk of suffering an AMI event (A, n=23 events) or a major adverse cardiac event (MACE) (B, n=65 events), defined as the composite endpoint of non-fatal myocardial infarction and cardiac mortality. AMI: acute myocardial infarction; CAD: Coronary Artery Disease; CCTA: coronary computed tomography angiography; CI: Confidence Interval; FAI$_{PVAT}$: Fat Attenuation Index of Perivascular Adipose Tissue; HR: Hazard Ratio; HU: Hounsfield units. Reproduced with permission from Oikonomou EK et al.* ***Lancet*** *2018, Sep 15;392(10151):929-939.*

4.3.7. Perivascular FAI and the high-risk plaque phenotype

Finally, to further assess the ability of perivascular FAI mapping to stratify the cardiac risk associated with HRP on CCTA, I performed a pooled analysis of the two cohorts (n=3912 individuals). The global prevalence of HRP and increased FAI (≥-70.1 HU) was 23.6% (n=923) and 24.3% (n=952) respectively. Over a median follow-up of 5.6 years (25^{th}-75^{th} percentile: 4.0-7.0 years), 91 cardiac deaths or non-fatal myocardial infarction events were recorded. Patients with both HRP features and high FAI (FAI+/HRP+) had a 6.3-fold higher adjusted risk of MACE compared to those with neither of these risk features (HRP-/FAI-) (Figure 4.16). Furthermore, patients without HRP features but with high FAI (HRP-/FAI+) had a 4.9-fold higher adjusted risk of MACE compared to the reference (HRP-/FAI-) group. Among low perivascular FAI patients, there was no significant difference between HRP- and HRP+ subgroups (P=0.87).

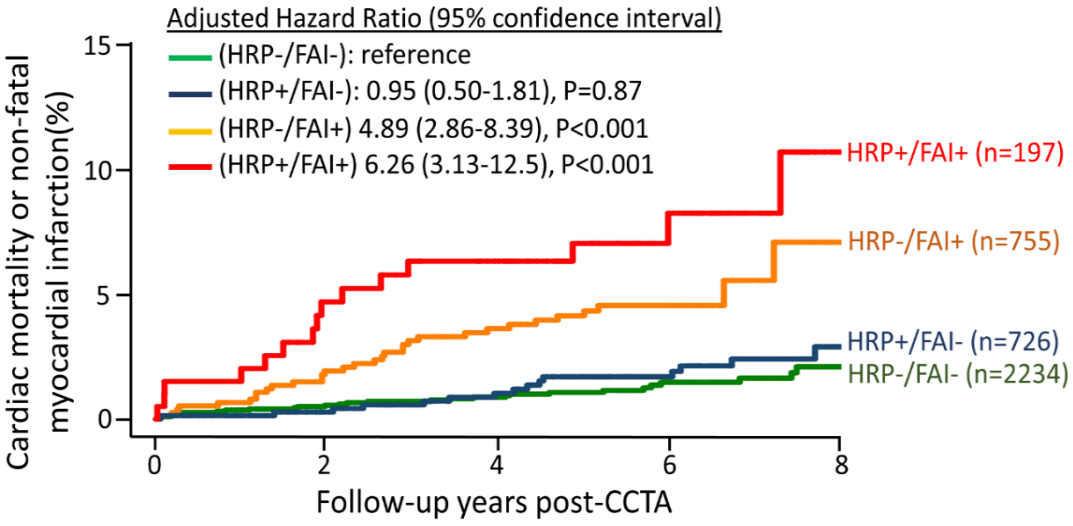

Figure 4.16. Major adverse cardiac events in the presence or absence of high-risk plaque features (HRP+/-) and/or high perivascular FAI (FAI+/-). *Kaplan-Meier curves with adjusted hazard ratios (adjusted for age, sex, CAD, and epicardial obesity) for the pooled CRISP-CT study. HRP features were defined as the presence of ≥1 of the following: positive remodelling, low-attenuation plaque, spotty calcification or napkin-ring sign. CCTA: coronary computed tomography angiography; FAI: perivascular fat attenuation index; HRP: high-risk plaque.*

4.3.8. Prognostic value of regional perivascular FAI assessment

Finally, using the complete dataset of the CRISP-CT study, I explored whether perivascular FAI mapping around the right and left coronary territories can provide independent prognostic information for future cardiac risk. Using the *pooled* data (n=3912 individual CCTA scans), I observed that both higher peri-RCA and peri-LAD FAI values were independently associated with a higher adjusted risk of cardiac mortality (≥50% stenosis) (adjusted Hazard Ratio [95% confidence interval] of 1.75 [1.29-2.39], P<0.001 & 1.52 [1.12-2.07], P=0.008 per 1SD [standard deviation] increments, respectively) (Figure 4.17). These results highlight the existence of regional variability in perivascular FAI mapping and the need for a comprehensive assessment of the whole coronary tree in order to better characterise the coronary inflammatory burden of each patient.

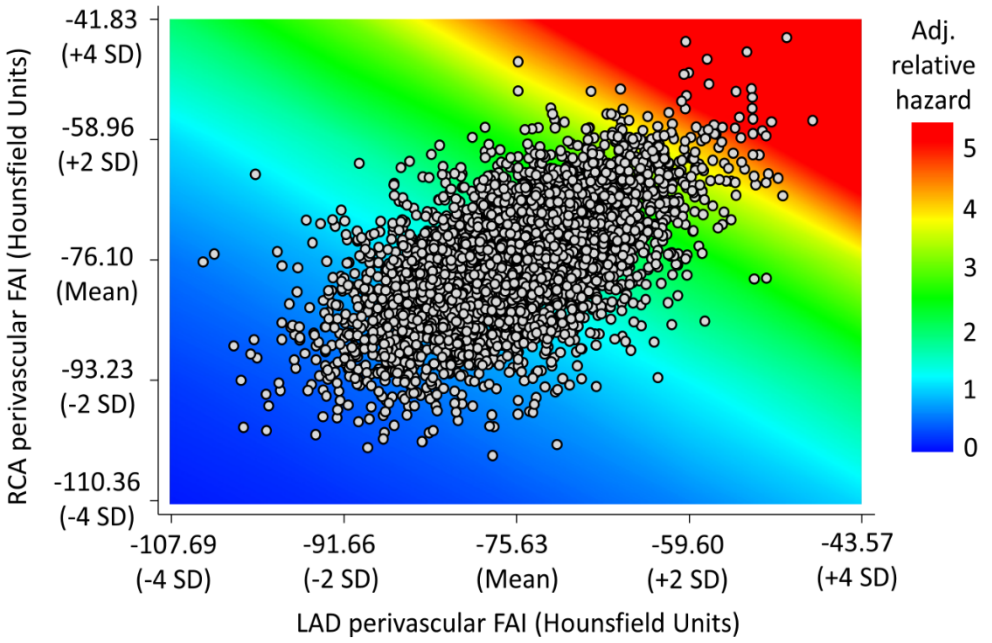

Figure 4.17. Two-way contour plot showing the interaction between peri-LAD and peri-RCA perivascular FAI for prediction of cardiac mortality. *FAI: Fat Attenuation Index; LAD: left anterior descending artery; RCA: right coronary artery; SD: standard deviation.*

4.3.9. A dynamic nomogram application for perivascular FAI

In an attempt to demonstrate the potential use of a FAI-guided risk stratification approach, I then created an automated application using R ("DynNom" package) that calculates an individualised cardiac risk based on a patient's clinical profile and FAI mapping profile. This dynamic nomogram relies on the Cox regression models derived from the CRISP-CT study and can be used to provide a more personalised prediction incorporating both the baseline clinical risk factors, as well as the extent of CAD (assessed by the modified Duke prognostic CAD index) as well as perivascular FAI values measured around the RCA and the LAD (Figure 4.18).

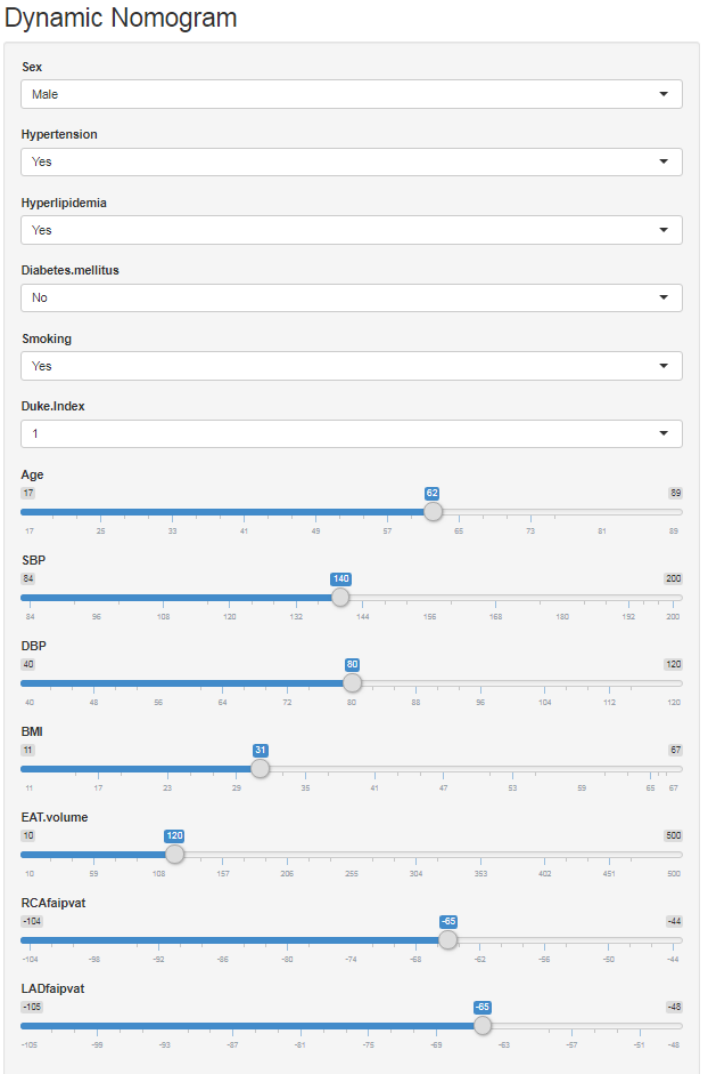

Figure 4.18. Dynamic nomogram for FAI-guided cardiac risk stratification. *A dynamic nomogram that incorporates perivascular FAI (Fat Attenuation Index) for a more individualised cardiac risk prediction.*

In a hypothetical example, I calculate the estimated hazard curve for major adverse cardiac events in a 62-year-old obese smoker male (BMI of 31 kg/m^2) with hypertension, hypercholesterolaemia, minimal non-obstructive coronary atherosclerosis, a systolic and diastolic blood pressure of 140 and 80 mmHg respectively using three different levels of coronary FAI:

a) Perivascular FAI of -65 HU around both the LAD and RCA (black line)

b) Perivascular FAI of -75 HU around both the LAD and RCA (red line)

c) Perivascular FAI of -85 HU around both the LAD and RCA (green line)

The hazard plots for these three different scenarios are summarised in Figure 4.19, showcasing how, despite the same risk factor profile, differences in perivascular FAI can be used to get a more individualised assessment of the future cardiac risk for a given patient.

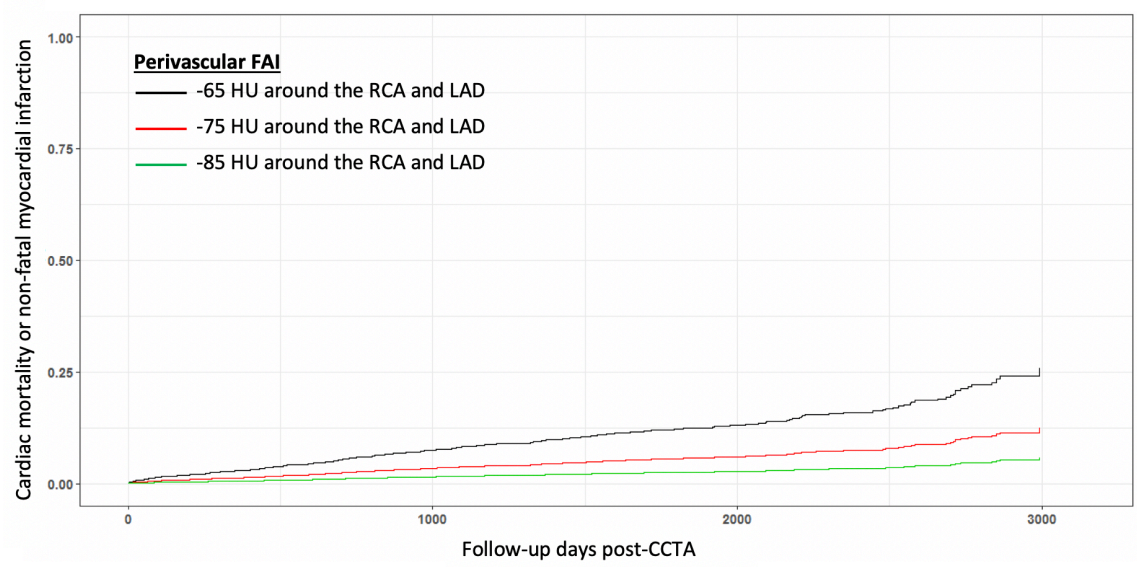

Figure 4.19. Cumulative hazard plots at different perivascular FAI levels. *Estimated hazard curves for major adverse cardiac events in a hypothetical 62 year-old obese, smoker male (BMI of 31 kg/m^2) with hypertension, hypercholesterolaemia, minimal non-obstructive coronary atherosclerosis, a systolic and diastolic blood pressure of 140 and 80 mmHg respectively using three different levels of coronary FAI: a) Perivascular FAI of -65 HU around both the LAD and RCA (black line); b) Perivascular FAI of -75 HU around both the LAD and RCA (red line); and c) Perivascular FAI of -85 HU around both the LAD and RCA (green line). CCTA: coronary computed tomography angiography; FAI: fat attenuation index; HU: Hounsfield Units; LAD: left anterior descending artery; RCA: right coronary artery.*

4.4. Discussion

In this chapter, having used data from a post-hoc analysis of 3,912 CCTA scans from two independent real-life CCTA cohorts with long-term follow-up, I have demonstrated that the perivascular FAI, a non-invasive imaging biomarker of coronary inflammation derived from CCTA [126], predicts all-cause and cardiac mortality over and above clinical risk factors and the current state-of-the-art interpretation of CCTA. By quantifying the residual inflammatory risk, FAI leads to significant risk re-stratification in both primary and secondary prevention, dissociating risk prediction from the strict anatomical severity of coronary stenosis or the degree of myocardial ischaemia. These findings are validated in two large and different "real-life" prospective cohorts of patients undergoing clinically-indicated CCTA in Europe and the United States. Integrating perivascular FAI mapping in modern CCTA interpretation will facilitate identification of individuals at risk of future cardiac death, before structural changes of the coronary wall are visible, and will also flag "vulnerable" patients with inflamed coronary atheroma, who might be candidates for more intensive interventions.

4.4.1. Wide-scale application of perivascular FAI: feasibility and clinical value

One of the major strengths of this study is the first large-scale application of perivascular FAI mapping in the scans from two independent and substantially different prospective cohorts of 1872 and 2040 individuals who underwent clinical CCTA and were subsequently followed up for a median period of 6 and 4.5 years respectively. Despite using a range of scans performed at different timepoints and using different CT hardware and protocols, we were able to apply our perivascular FAI mapping algorithm in the vast majority of the clinically interpretable scans. This demonstrates the feasibility of our

method and its potential applicability in a range of acquisition settings and clinical imaging protocols.

4.4.2. Perivascular FAI in a range of clinical settings and presentations

Of note, the clinical indication for CCTA was based on local clinical practice, which differed between the two cohorts, as evidenced by the significantly different clinical and medication profile of the two populations. This provided the opportunity to measure FAI in subjects with a broad range of cardiovascular risk factors and extent of CAD, scanned in a variety of hardware and during different time periods. Traditional risk factors performed less well in the derivation versus the validation cohort for prediction of mortality, possibly due to a more aggressive pharmacological management of risk factors in the Cleveland cohort. Despite these differences, I demonstrate that perivascular FAI ≥ 70.1 HU is a strong predictor of all-cause and cardiac mortality in both cohorts, over and above clinical risk factors, extent of CAD, number of high-risk plaque features, epicardial adipose tissue volume and CCS [7, 12, 177]. Importantly, perivascular FAI performed equally well as a risk stratification tool among individuals with low or high CCS, independently of the presence of CAD. Individuals without CAD, who form the vast majority of individuals undergoing clinical CCTA worldwide, may benefit from early, targeted deployment of more aggressive measures of primary prevention. Indeed, I present evidence that the residual inflammatory risk identified by perivascular FAI might be modifiable by intensive medical treatment, calling for future randomised clinical trials to document this initial observation. Finally, by identifying the patients with CAD who still have unstable atherosclerotic plaques despite optimum treatment, perivascular FAI can guide future clinical trials evaluating targeted treatments with modern anti-inflammatory agents, making their use affordable in modern healthcare systems. A

theoretical framework for the implementation of FAI in clinical practice based on data from the CRISP-CT study is presented in Figure 4.20.

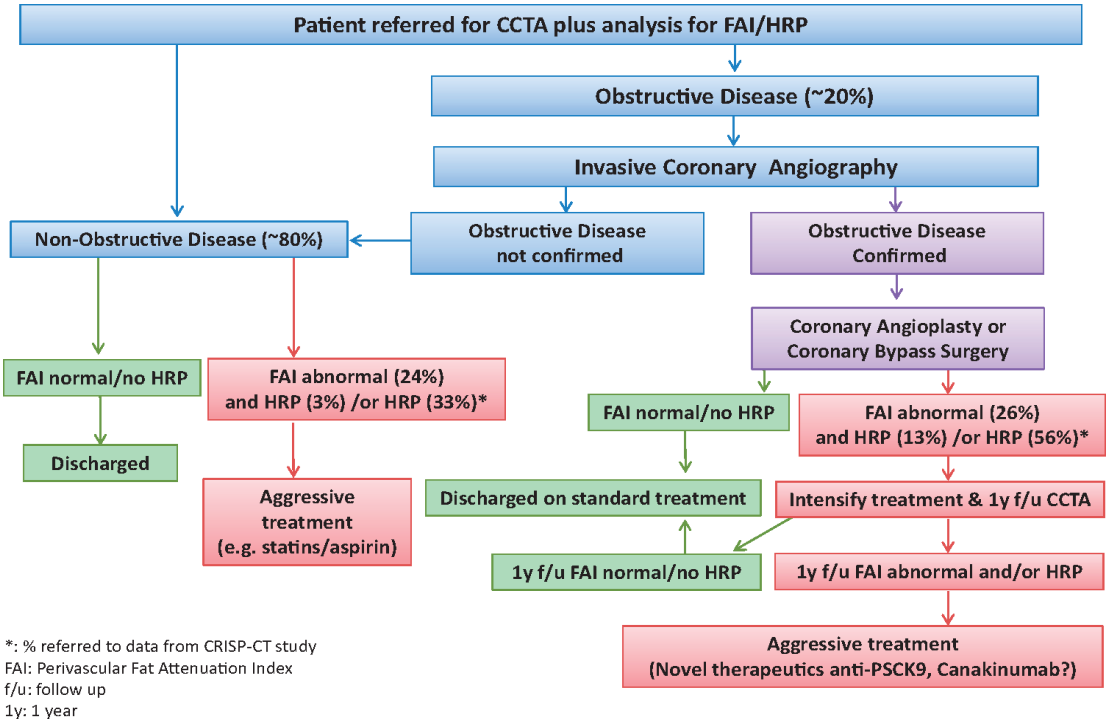

Figure 4.20. A theoretical framework for the implementation of FAI in clinical practice. *Vision for implementing fat attenuation index (FAI) and high-risk plaque features (HRP) in clinical practice. CAD: coronary artery disease; CV: cardiovascular; OMT: optimal medical treatment; anti-PCSK9: pro-protein convertase subtilisin/kexin type 9 inhibitors. Figure reproduced with permission from Antoniades et al.* ***Eur Heart J****. 2019 Jul 16. pii: ehz474. doi: 10.1093/eurheartj/ehz474).*

4.4.3. Exploring the regional variability of perivascular FAI

Notably, in a post-hoc analysis of the pooled dataset from both cohorts included in the CRISP-CT study revealed that higher perivascular FAI values around the RCA and LAD are independently associated with the future risk of cardiac death. This finding only became evident in a post-hoc and not pre-specified analysis of the pooled dataset. However, it supports some interesting hypotheses regarding the existence of regional variability in the perivascular fat phenotype that needs to be taken into account and may

carry incremental diagnostic and prognostic value. While such a task may be challenging for the human brain, artificial intelligence and machine learning approaches can provide the necessary tools to facilitate a more comprehensive, global assessment of the perivascular fat "radiomic profile" and its clinical significance.

4.4.4. Study limitations

This study was not without limitations. The relatively low number of fatal events may limit the statistical power for some subgroup analyses, but this was overcome by the large effect sizes on the primary endpoints. In addition, while the spatial resolution of CT on a 128-slice scanner may get to a theoretical voxel size of 0.35mm^2, this is limited by coronary artery motion [185]. However, the definition of PVAT as the fat within a radial distance equal to the diameter of the vessel (based on previous histological and biological observations) [126] exceeds the spatial resolution of CCTA, allowing for a valid assessment of the perivascular space. Furthermore, while the present study supports the use of perivascular FAI mapping in symptomatic cohorts, its value in asymptomatic cohorts remains unclear. Therefore, FAI is not intended to generate new indications for CCTA but it is proposed as an additional readout in standard CCTA performed under the current clinical indications.

It should also be noted that the semi-automated algorithm applied in this study required ~30-45 minutes for a comprehensive FAI mapping analysis per patient. The time-consuming nature of this analysis that relies on careful segmentation of the coronary vasculature is one of the main limitations of this technique with regards to its potential application in everyday clinical practice. Nevertheless, efforts are currently underway to automate this process and generate tools that can be integrated into CCTA analysis

workstations to streamline the workflow and provide a FAI mapping report within a few seconds.

4.5. Conclusion

In this chapter, I have demonstrated that perivascular FAI predicts all-cause and cardiac mortality over and above current risk stratification tools, including coronary calcium and state-of-the-art assessment of CCTA. These findings are supported by the analysis of more than 3900 patients with long-term follow-up, from two different and diverse centers in Europe and the United States. Integration of perivascular FAI mapping into standard clinical CCTA reporting has the potential to advance CCTA from a method that is used to exclude anatomical CAD into a dynamic cardiac risk stratification tool, applicable even in the absence of coronary plaques and/or significant calcification. This was the first study to highlight PVAT as a host of prognostic biomarkers in cardiovascular disease, suggesting that more comprehensive approaches that capture the full phenotypic and biologic heterogeneity of PVAT (expansion, obesity, remodelling) may provide further value in cardiovascular disease diagnosis and risk stratification.

5

Chapter 5. Radiomic phenotyping of adverse pericoronary fat remodelling

This chapter is based on the manuscript by: Oikonomou EK et al. "A novel machine learning-derived radiotranscriptomic signature of perivascular fat improves cardiac risk prediction using coronary CT angiography". Eur Heart J 2019, Nov 14; 40(43):3529-3543. PMID: 31504423 [186].

5.1. Introduction

Optimal medical therapy and clinical risk factor management do not always prevent acute coronary syndromes, resulting in the concept of the "residual atherosclerotic risk", a major factor driving uncertainty in risk stratification and targeting of healthcare interventions (also discussed in section 1.2.2) [171]. Vascular inflammation in particular is recognised as a major contributor to both atherosclerotic plaque formation and destabilisation [25, 171].

In the previous chapter [142], I demonstrated that perivascular FAI mapping, a CCTA-based tool that quantifies the changes associated with coronary inflammation in the adjacent PVAT, can predict all-cause and cardiac mortality with incremental value beyond traditional risk factors. Interestingly, the predictive value of FAI was attenuated among patients who initiated treatment with aspirin and statin therapy after CCTA, suggesting that the risk identified by this biomarker may be modifiable. However, chronic atherosclerosis and vascular inflammation may also be related to further structural changes in the adjacent adipose tissue, including fibrosis and vascularity [1, 109]. An imaging biomarker detecting these changes in PVAT composition could have important

clinical implications for CAD diagnosis and treatment by supplementing the inflammatory burden detected by FAI.

Advances in computational radiomic approaches and machine learning now enable the extraction of large amounts of quantitative information from imaging data using specific data-characterisation algorithms, thus identifying imaging patterns of significant clinical value that cannot be recognised by a human reader [137]. Linking such imaging patterns to underlying tissue biology and gene expression status in a "radiotranscriptomic" approach could lead to a more individualised assessment of disease activity in patients undergoing CCTA.

In the present chapter, inspired by similar approaches in the field of cancer imaging [154], I hypothesised that comprehensive CCTA-based radiomic phenotyping of coronary PVAT may reveal new biomarkers of adverse remodelling in response to coronary inflammation and atherosclerosis. Such a global approach could integrate perivascular FAI with volumetric features of epicardial adipose tissue (EAT) expansion, as well as radiomic texture patterns associated with pro-fibrotic or vascular adipose tissue remodelling, thus providing a more detailed assessment of a patient's cardiovascular risk.

5.2. Methods

This chapter is based on a multi-arm study which included data from the CRISP-CT (section 2.1.3), SCOT-HEART (section 2.1.4), ORFAN (section 2.1.1), AdipoRedox (section 2.1.5) as well as Ox-IMPACT (section 2.1.2) studies.

5.2.1. Study design

The patient demographics and relevant clinical characteristics for each arm are presented in the Tables 5.1-5.4.

Arm 1: To understand how fibrosis and vascularity of adipose tissue are visualised using CT, 167 patients (Table 5.1) scheduled to undergo cardiac surgery underwent CCTA and biopsies of subcutaneous adipose tissue (ScAT) were obtained during surgery. The CT radiomic profile of subcutaneous adipose composition was quantified and, using a radiotranscriptomic approach, was subsequently linked to the expression of genes characterising inflammation (e.g. tumor necrosis factor a-*TNFA*), fibrosis (e.g. *COL1A1*) and vascularity (e.g. *CD31*) within the visualised tissue. This (remote) depot was selected for radiotranscriptomic analysis, given that its radiomic attenuation and texture is influenced by inflammatory signals generated within the tissue, unlike depots such as epicardial or perivascular fat where inflammatory signals may originate from the adjacent vessels in a paracrine manner [103, 119, 126].

Arm 2: To train and subsequently validate a radiomic signature of global coronary PVAT that identifies individuals at increased risk for major adverse cardiac events (MACE), and compare it with the radiotranscriptomic signatures of inflammation, fibrosis and vascularity, I designed a case-control study of patients with a MACE (defined as the composite endpoint of cardiac mortality and non-fatal myocardial infarction) within five years of a CCTA scan versus matched controls who had no cardiac event during the same follow-up period (Table 5.2). Eligible cases were retrieved from the prospectively collected data of the CRISP-CT study (n=3912) [142], as well as the CCTA arm of the SCOT-HEART trial (n=1786 available CCTA scans) [42, 143]. One-to-one matching was performed for the cohorts, including age, gender, CT scanner used and tube voltage, whereas a nearest matching approach was used for traditional cardiovascular risk factors (hypertension, hypercholesterolemia, diabetes mellitus, smoking), BMI, EAT volume and baseline medications. The pooling of three distinct CCTA cohorts with variable hardware

and CCTA protocols was performed to facilitate the discovery of radiomic patterns that are less likely to be confounded by scanner- or center-specific variables and are more likely to be generalisable and valid across different centers and CT scanner types. The final radiomic profile of the high-risk coronary PVAT, as defined based on a machine learning algorithm, was defined as the Fat Radiomic Profile (FRP).

Table 5.1. Clinical characteristics of the Arm 1 population.

		N (%) or median [25th-75th percentile]
Total number		**167**
Age (years)		67 [59-74]
Body Mass Index (kg/m^2)		27.9 [25.2-31.1]
Female sex (n, %)		27 (16.2)
Hypertension (n, %)		123 (73.7)
Hypercholesterolemia (n, %)		147 (88.0)
Diabetes mellitus (n, %)		40 (24.0)
Smoking (n, %)		11 (6.6)
Systolic BP (mmHg)		133 [118-144]
Diastolic BP (mmHg)		70 [63-80]
Total cholesterol (mg/dL)		126 [107-148]
High-density lipoprotein (HDL, mg/dL)		32 [27-38]
Medications		
Beta-blocker (n, %)		128 (76.6)
Statin (n, %)		147 (88.0)
Antiplatelet (n, %)		155 (92.8)
Calcium Channel Blocker (n, %)		48 (28.7)
ACEi or ARB (n, %)		110 (65.9)
CAD presence (n, %)		167 (100)
Tube voltage (n, %)	*120 kVp*	167 (100)

ACEi: angiotensin-converting enzyme inhibitor; ARB: angiotensin-II-receptor blocker; BP: blood pressure; CAD: coronary artery disease.

Table 5.2. Clinical characteristics of the Arm 2 population.

	5-year MACE group	No-MACE group	P value
Total number	**101**	**101**	
Cohort			1.000
CRISP-CT (n=3912)	73 (72.3)	73 (72.3)	
SCOT-HEART (n=1575)	28 (27.7)	28 (27.7)	
Age (years)	64 [55, 72]	62 [53, 70]	0.531
Body Mass Index (kg/m^2)*	27.3 [25.1-32.2]	27.7 [24.5-32.3]	0.932
Female sex	34 (33.7)	34 (33.7)	1.000
Hypertension (n, %)	67 (66.3)	62 (61.4)	0.485
Hypercholesterolemia (n, %)	40 (39.6)	40 (39.6)	0.936
Diabetes mellitus (n, %)	19 (18.8)	15 (14.9)	0.550
Smoking (n, %)	31 (30.7)	25 (24.8)	0.448
Systolic BP (mmHg)*	132 [120-141]	136 [120-145]	0.297
Diastolic BP (mmHg)*	76 [69-82]	78.5 [70-84]	0.374
Total Cholesterol (mg/dL)*	172 [140-216]	205 [169-236]	0.008
High-density lipoprotein (mg/dL)*	45 [37-53]	46 [37-61]	0.265
Epicardial adipose tissue volume (cm^3)	96 [68-125]	94 [69-122]	0.420
Medications			
Beta-blocker (n, %)	38 (37.6)	36 (35.6)	0.291
Statin (n, %)	52 (51.5)	40 (39.6)	0.197
Antiplatelets (n, %)	62 (61.4)	54 (53.5)	0.165
Calcium Channel Blocker (n, %)	22 (21.8)	20 (19.8)	0.705
ACEi or ARB (n, %)	37 (36.6)	37 (36.6)	0.766
CAD presence and severity (n, %)			0.011
No	14 (13.9)	31 (30.7)	
Mild non-obstructive (<50%)	38 (37.6)	40 (39.6)	
Moderate non-obstructive (50-69%)	23 (22.8)	13 (12.9)	
Obstructive (≥70%)	26 (25.7)	17 (16.8)	
Tube voltage (n, %)			1.000
120 kVp	69 (68.3)	69 (68.3)	
100 kVp	32 (31.7)	32 (31.7)	
Five-year clinical events			
Cardiac mortality (n, %)	61 (60.4)	-	-
Non-fatal acute myocardial infarction (n, %)	40 (39.6)	-	-

ACEi: angiotensin-converting enzyme inhibitor; ARB: angiotensin-II-receptor blocker; BP: blood pressure; CAD: coronary artery disease; FAI: fat attenuation index; HU: Hounsfield Units; LCA: left coronary artery; MACE: major adverse cardiac event; RCA: right coronary artery. P values derived from Pearson's Chi-square test for categorical variables and Mann-Whitney for continuous variables. *Degree of missingness: 28.7% for Total Cholesterol, 39.1% for HDL, 21.8% for SBP/DBP, and 12.9% for BMI. Categorical variables are presented as numbers (percentages), while continuous variables are summarised as median [25th-75th percentile].

Arm 3: To explore the prognostic value of the radiomic signature derived and validated in Arm 2, the Fat Radiomic Profile (FRP) was applied to the CCTA arm of the SCOT-HEART trial, a population in which CCTA (as well as non-contrast cardiac CT for Agatston coronary calcium scoring [CCS]) was used to guide changes in clinical care. The aim was to explore whether this radiomic signature could add value in cardiac risk prediction over and above traditional risk factors and detect a residual risk not modified by subsequent interventions. The study population consisted of 1786 patients (SCOT-HEART, NCT01149590) with images available for analysis. Scans performed at tube voltage settings other than 100 or 120 kVp, and scans with missing slices, beam hardening or step artifacts were excluded from the analysis (n=211), resulting in a study dataset of 1575 individual CCTA scans (Table 5.3). The median follow-up period was 4.8 years (interquartile range: 4.2 to 5.7 years), and adverse cardiac events, including death, non-fatal acute myocardial infarction (AMI) and revascularisation events were recorded as described previously [42, 143].

Arm 4: To compare the ability of FRP to track changes in acute vascular inflammation related to AMI in comparison to FAI, a total of 44 AMI patients underwent CCTA within 96 hours of presentation and after six event-free months, as part of a prospective study aiming to assess the association between vulnerable plaques and pericoronary fat radiomic features (Ox-IMPACT study). A total of 44 patients with stable CAD matched for age, gender, hypertension, hypercholesterolemia, diabetes mellitus, smoking, body mass index (BMI), epicardial adipose tissue volume and medications were selected as the control group (ORFAN study) (Table 5.4).

Table 5.3. Clinical characteristics of the Arm 3 (SCOT-HEART) population.

	N (%) or median [25th-75th percentile]
Total number	**1575**
Age (years)	58 [51, 65]
Body Mass Index (kg/m^2)	28.7 [25.7, 32.4]
Female sex (n, %)	687 (43.6)
Hypertension (n, %)	539 (34.2)
Diabetes mellitus (n, %)	176 (11.2)
Smoking (n, %)	302 (19.8)
Systolic Blood Pressure (SBP, mmHg)*	140 [126, 152]
Diastolic Blood Pressure (DBP, mmHg)*	80 [76, 90]
Total cholesterol (mg/dL)*	208 [174, 239]
High-density lipoprotein (HDL, mg/dL)*	50 [42, 59]
CAD presence and severity	
No	571 (36.3)
Mild non-obstructive (<50%)	336 (21.3)
Moderate non-obstructive (50-69%)	275 (17.5)
Obstructive (≥70%)	393 (25.0)
High-risk plaque (HRP) feature presence	
Any	610 (38.7)
Spotty calcification	264 (16.8)
Low-attenuation plaque	148 (9.4)
Positive remodelling	527 (33.5)
Napkin-ring sign	70 (4.4)
Medications	
Beta-blocker (n, %)	580 (36.3)
Statin (n, %)	701 (44.5)
Antiplatelet (n, %)	870 (55.2)
Calcium Channel Blocker (n, %)	150 (9.5)
ACEi or ARB (n, %)	256 (16.3)
Tube voltage (n, %)	
100 kVp	758 (48.1)
120 kVp	817 (51.9)
Follow-up and clinical events	
Follow-up duration (years)	4.82 [4.18-5.72]
Deaths, n	33
Confirmed cardiac deaths, n	1
Non-fatal Acute Myocardial Infarction events, n	33
Cardiac death or non-fatal AMI (MACE), n	34
Late revascularisation (≥6 weeks)**, n	176
MACE or late revascularisation, n	188

ACEi: angiotensin-converting enzyme inhibitor; AMI: acute myocardial infarction; ARB: angiotensin-II-receptor blocker; CAD: coronary artery disease; FAI: fat attenuation index; HDL: high-density lipoprotein; HU: Hounsfield Units; LCA: left coronary artery; MACE: major adverse cardiac event; RCA: right coronary artery; SCOT-HEART: Scottish COmputed Tomography of the HEART trial. P values derived from Pearson's Chi-square test for categorical variables and Mann-Whitney for continuous variables. *Degree of missingness: Systolic blood pressure = 0.8%, Total cholesterol = 7.4%, HDL =28.1%. **All revascularisation events were percutaneous coronary intervention.

Table 5.4. Clinical characteristics of Arm 4.

	Stable CAD	AMI	P value
Total number	**44**	**44**	**-**
Age (years)	62 [51-70]	62 [53-72]	0.363
BMI (kg/m^2)	27.8 [24.3-31.0]	26.8 [24.1-31.9]	0.867
Male sex (n, %)	28 (63.6)	37 (84.1)	0.052
Hypertension (n, %)	17 (38.6)	25 (56.8)	0.135
Hypercholesterolemia (n, %)	16 (36.4)	25 (56.8)	0.087
Diabetes mellitus (n, %)	5 (11.4)	8 (18.2)	0.548
Smoking			0.300
Active (n, %)	2 (4.5)	3 (6.8)	
Past (n, %)	22 (50.0)	28 (63.6)	
Medications			
Beta-blocker (n, %)	10 (22.7)	8 (18.2)	0.792
Statin (n, %)	15 (34.1)	15 (34.1)	1.000
Antiplatelet (n, %)	11 (25.0)	10 (22.7)	1.000
CCB (n, %)	5 (11.4)	8 (18.2)	0.548
ACEi or ARB (n, %)	15 (34.1)	12 (27.3)	0.644
Tube voltage (n, %)			0.145
120 kVp	34 (77.3)	40 (90.9)	
100 kVp	10 (22.7)	4 (9.1)	
FRP (AU)	0.45 [0.42-0.49]	0.55 [0.49-0.63]	<0.001

ACEi: angiotensin-converting enzyme inhibitor; ARB: angiotensin-II-receptor blocker; AU: arbitrary units; BMI: body mass index; CCB: calcium-channel blocker; FRP: Fat Radiomic Profile. P values derived from Pearson's Chi-square test for categorical variables and Mann-Whitney for continuous variables. Categorical variables are presented as numbers (percentages), while continuous variables are summarised as median [25th-75th percentile].

5.2.2. CCTA protocol, data collection and definitions

The detailed CCTA protocols for image acquisition have been previously presented in section 2.2 (CCTA protocol) as well as in published studies [42, 126, 142, 143]. The process for data collection and definitions of risk factors and endpoints are described in section 4.2.2 of this thesis as well as in the published manuscripts of the original studies [42, 126, 142, 143].

5.2.3. Radiomic analysis

The general concept and methods behind radiomic phenotyping of adipose tissue using CT are described in section 2.10 of this thesis. Briefly, all images were first anonymised locally and subsequently transferred to the Oxford Academic Cardiovascular Computed Tomography (OXACCT) core lab (Oxford, United Kingdom) for analysis on a dedicated workstation, where I led the analysis, blinded to population demographics and outcomes. Subcutaneous adipose tissue (Arm 1) was segmented on three consecutive axial slices at the caudal end of the sternum (xiphoid process) by selecting all subcutaneous voxels in the -190 to -30 Hounsfield Unit (HU) range. Coronary PVAT (Arms 2 to 4) was defined as all voxels in the Hounsfield Unit range of -190 to -30 Hounsfield Units (HU) located within a radial distance from the outer vessel wall equal to the diameter of the respective vessel, as previously described [142]. PVAT segmentation was manually performed around the proximal to distal right coronary artery (RCA) (anatomical segments #1, 2 and 3 based on the American Heart Association anatomical classification) and the combined left main and proximal to mid left anterior descending artery (LAD) (segments #5, 6, 7) (Figure 5.1) [187]. The left circumflex artery was not analysed given its variable anatomy and small caliber, as already described in the chapter 4 [142]. Calculation of radiomic features was performed using 3D Slicer (v.4.9.0-2017-12-18 r26813), as described in section 2.10 and Appendix 3. [155]. For each unique AT segmentation, a total of 843 radiomic features were calculated, ranging from shape-related to first- and higher-order (texture) statistics (Appendix Tables 1-8), using the SlicerRadiomics extension which incorporates the Pyradiomics library into 3D Slicer [151].

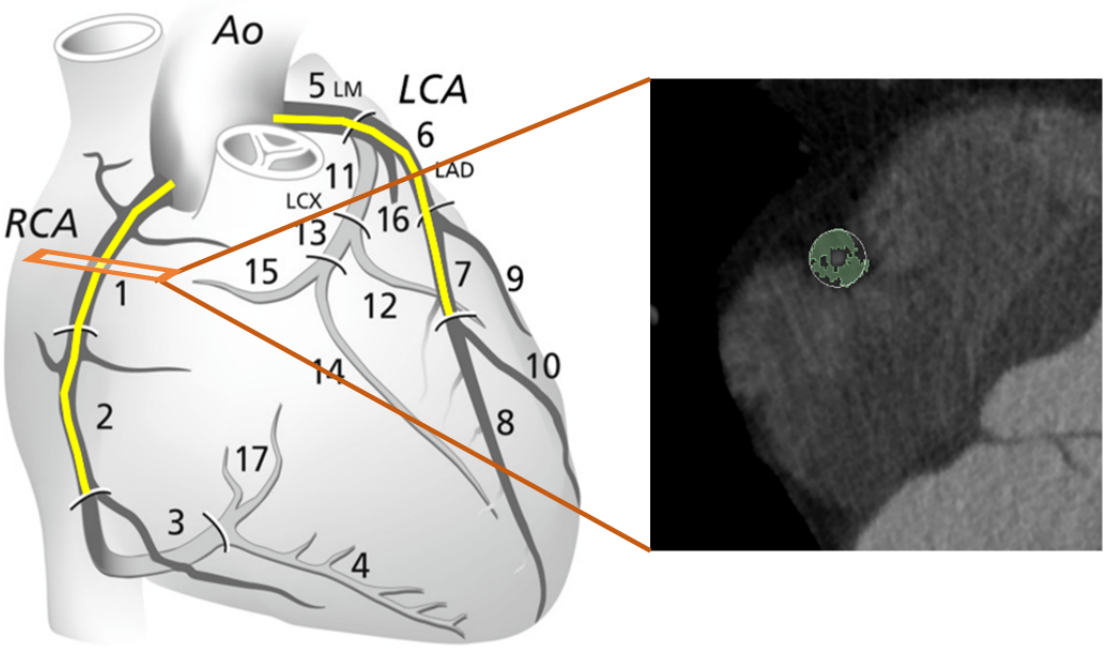

Figure 5.1. Global pericoronary adipose tissue segmentation for radiomic characterisation. *PVAT segmentation was manually performed around the proximal to distal right coronary artery (RCA) (anatomical segments #1, 2 and 3 based on the American Heart Association anatomical classification) and the combined left main and proximal to mid left anterior descending artery (LCA: left coronary artery) (segments #5, 6, 7). The left circumflex artery was not analysed given its variable anatomy and small caliber, as already described in the Chapter 4.*

5.2.4. Subcutaneous AT collection, RNA isolation and gene expression analysis

In the AdipoRedox study (Arm 1 of this chapter), subcutaneous adipose tissue specimens were collected during surgery, and stored in TRI reagent (Sigma, catalogue number T9424) at -80oC until thawed for RNA isolation. Total RNA was isolated by a phenol to chloroform (1:5 ratio) separation protocol followed by a magnetic beads-based RNA purification method on a KingFischer magnetic particle processor (Thermo Fischer Scientific), using the MagMAX mirVana total RNA isolation kit (Thermo Fischer Scientific, Catalogue Number A27828). RNA concentration and integrity were assessed spectrophotometrically on NanoDrop ND-1000. For reverse transcription of RNA to cDNA we used the SuperScript VILO mastermix (Thermo Fischer Scientific) adhering

to manufacturer's instructions and extending the cDNA synthesis step to two hours at 60oC on a Veriti thermal cycler (ABI).

Quantitative real-time polymerase chain reaction (PCR) was performed on a QuantStudio 7 flex real-time PCR system (Thermo Fischer Scientific) perusing TaqMan chemistry, in accordance with the standard universal TaqMan protocol, as indicated by the manufacturer. Using a starting mass of 5ng of cDNA, all samples were run in duplicates, and data was analysed by the Pfaffl method (you can use this as reference here). Cyclophilin A (*PPIA*) was used as the housekeeping gene for all human adipose tissue samples. TaqMan probes IDs are as follows: *PPIA*: Hs99999904 m1; *PECAM1* (*CD31*): Hs01065279 m1; *TNF*: Hs01065279 m1; *COL1A1*: Hs00164004 m1. Sample collection, RNA isolation and PCR experiments were performed by Drs. Marios Margaritis, Ioannis Akoumianakis and Christos Kotanidis, whereas I identified the genes to be tested in this proof-of-concept analysis. The selection of these genes was based on previous studies that have used *COL1A1 [188]*, *CD31 [189],* and *TNFA [126, 190]* as markers of adipose tissue fibrosis, vascularity and inflammation, respectively.

5.2.5. Statistical analysis

Participant demographics are summarised as numbers (percentages) or median [25^{th}-75^{th} percentile] for categorical and continuous variables respectively (unless specified otherwise). Between-group comparisons were performed using Pearson's χ^2 or Fisher's exact test for categorical variables, and Mann-Whitney's test for continuous variables.

In Arm 1, the strength of association between 825 attenuation- & texture-based radiomic features of AT and the relative gene expression of *TNFA, COL1A1* and *CD31* in respective adipose tissue biopsies was summarised using Manhattan plots ($-\log_{10}$[p values] of the Spearman's rho coefficients). Bonferroni correction was applied by dividing the

significance level of α=0.05 by the number of components that described 99.5% of the radiomic variation, as described elsewhere [191]. In order to assess the incremental value of texture analysis for description of adipose tissue biology, stepwise multivariable linear regression models were built with gene expression as the dependent variable and age, sex, body mass index, hypertension, dyslipidemia and diabetes mellitus (block 1), followed by the addition of mean attenuation (block 2), and the three top principal components of the AT "radiome" (block 3, F level cutoff of 0.05 and 0.10 for inclusion/exclusion in the model). Gene expression profiles were log-transformed prior to inclusion in the models. The F-metric and F-test were used to assess the improvement in model performance at each step.

In Arm 2, only features with an inter-observer intra-class correlation coefficient (ICC) $\geq$ 0.9 were included in all subsequent analyses (n=15 scans analysed by two independent analysts). Correlation plots (using the non-parametric Spearman's rank correlation coefficient) and a heatmap depicting the variance of the Z-score-transformed individual radiomic features across the SCOT-HEART population are graphically presented. Further hierarchical clustering of the individual radiomic features was performed using the squared Euclidean distance and the Ward method.

To address the multi-dimensionality and possible redundancy of the radiomic dataset, the amount of pairwise correlations was reduced at the level of $|\text{rho}| \geq 0.9$ using the *findCorrelation* function of the *caret* package in R. In short, the absolute values of all pairwise correlations were considered. If two variables were highly correlated ($|\text{rho}| \geq 0.9$), the function looked at the mean absolute correlation of each variable and removed the variable with the largest mean absolute correlation. In an initial assessment of the dataset, a Manhattan plot was created based on the value of each radiomic feature in discriminating the MACE from the non-MACE cases (graphical representation of the

negative logarithm [$\log_{10}$] of the P value from univariable receiver operating characteristic curve [ROC] analysis). Subsequently, the nested case-control study in Study 2 was randomly split in a training (80%) and testing set (20%), ensuring an equal representation of events and non-events in both splits. A random forest method was selected to train a model to discriminate 5-year MACE from no MACE, since it enables modelling of non-linear relationships, can train on small datasets, is less sensitive to outliers and has been previously used in patient-specific predictive modelling [192]. In my analysis (as shown later) random forests outperformed alternative methods, such as generalized linear models, naïve Bayesian models, bagging conditional inference regression trees, support vector machines, k-nearest neighbours, and classification and regression trees. All radiomic features were centered and scaled prior to inclusion in the models. The optimal number of features in the model was estimated using a recursive feature elimination approach (with 4, 8, 16, 32, 64, 128, 256 and maximum number of features) and based on the model's accuracy on repeated five-fold cross validation (three repeats). Following internal validation, the model was further validated by measuring the C-statistic in the remaining (validation) dataset. The final product of the random forest algorithm (namely the probability of belonging to the MACE versus no MACE group) was defined as the fat radiomic profile (FRP). The biological meaning of the most important constituent features of FRP was assessed by presenting the significance level of association with adipose tissue fibrosis (*COL1A1* relative expression), inflammation (*TNFA* relative expression) and vascularity (*CD31* relative expression), as assessed in Study 1.

FRP was subsequently quantified in the entire SCOT-HEART cohort (Arm 3). An optimal cut-off point was selected to define high- versus low-risk groups by identifying the value that maximises the log-rank statistic for MACE. Its predictive value for i) MACE; ii) a composite endpoint of MACE and late revascularisation (revascularisation

≥6 weeks post-CCTA; corresponding to the timepoint for assessment of the certainty of coronary heart disease diagnosis in the SCOT-HEART trial [42]), and iii) non-cardiac mortality was then assessed in both univariable Kaplan-Meier curves and Cox regression models adjusted for age, sex, systolic blood pressure, diabetes mellitus, body mass index, smoking status, presence of coronary artery disease (≥50% stenosis), total cholesterol and high-density lipoprotein levels as well as Agatston CCS (log[CCS+1]), high-risk plaque features (as defined in section 2.6.2) and CT scanner used. The incremental value of FRP for prediction of MACE beyond a baseline model consisting of the aforementioned factors was assessed by comparing the time-dependent ROC curves of the two nested models (traditional risk factors ± FRP) at five years post-CCTA.

In Arm 4, the distribution of FRP between AMI and matched stable CAD patients was compared using the non-parametric Mann-Whitney test. The changes in FAI or FRP between baseline and follow-up were assessed using a paired, non-parametric Wilcoxon signed-rank test.

Statistical analyses were performed in the R environment (R version 3.4 and R Studio version 1.1.453) and using IBM SPSS Statistics for Windows (Version 22.0. IBM Corp. Released 2013. Armonk, NY). All tests were two-sided and α was set at 0.05, unless specified otherwise.

5.3. Results

5.3.1. Adipose tissue radiomic phenotype as a marker of adipose remodelling

Radiotranscriptomic analysis of human adipose tissue revealed that mean attenuation (a first-order statistic which forms the basis of the Fat Attenuation Index) was the best-performing metric for detection of adipose tissue inflammation, as assessed by the relative expression of tumour necrosis factor alpha (*TNFA*; Figure 5.2A). However, higher order

statistics reflecting the radiomic texture of adipose tissue on CT imaging had comparable or even higher accuracy than mean attenuation (Figures 5.2B-C) in detecting fibrosis and vascularity, as assessed by the relative expression of *COL1A1* (collagen type 1 alpha 1 chain) and the endothelial-marker *CD31* (platelet-endothelial cell adhesion molecule-1). In multivariable analysis, inclusion of the first three principal components of the adipose tissue "radiome" (Figure 5.2D) improved the value of a model including clinical risk factors and mean attenuation to detect adipose tissue fibrosis and vascularity, but not inflammation (Figure 5.3).

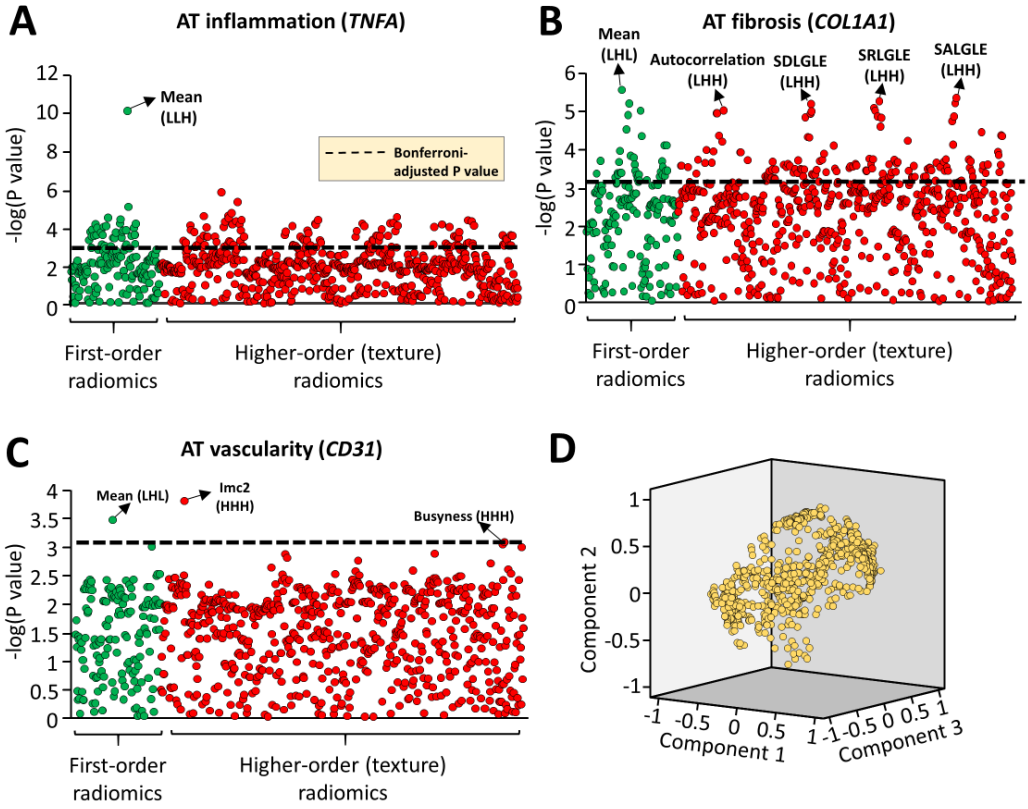

Figure 5.2. Radiomic phenotyping to detect biological hallmarks of dysfunctional adipose tissue. ***(A-C)*** *Manhattan plots presenting the strength of association (-log$_{10}$[P value] of Spearman's rho) between adipose tissue radiomic features and the relative gene expression of TNFA (inflammation), COL1A1 (fibrosis) and CD31 (endothelial marker, vascularity). Radiomic features were split into two groups, consisting of first-order statistics (green color, derived from simple attenuation histogram analysis) or higher-order statistics (red color, reflecting the radiomic texture and spatial interrelation of voxels). The dotted line represents the Bonferroni-adjusted significance level (α=0.00068).* ***(D)*** *Component plot of the three principal components of the adipose tissue radiome. L/H: low/high wavelet transformation; SALGLE: small area low gray level emphasis; SDLGLE: small dependence low gray level emphasis; SRHGLE: Short Run Low Gray Level Emphasis. *Relative gene expression was calculated using cyclophilin A (PPIA) as the housekeeping gene. Reproduced with permission from Oikonomou EK et al.* ***Eur Heart J****. 2019. doi: 10.1093/eurheartj/ehz592.*

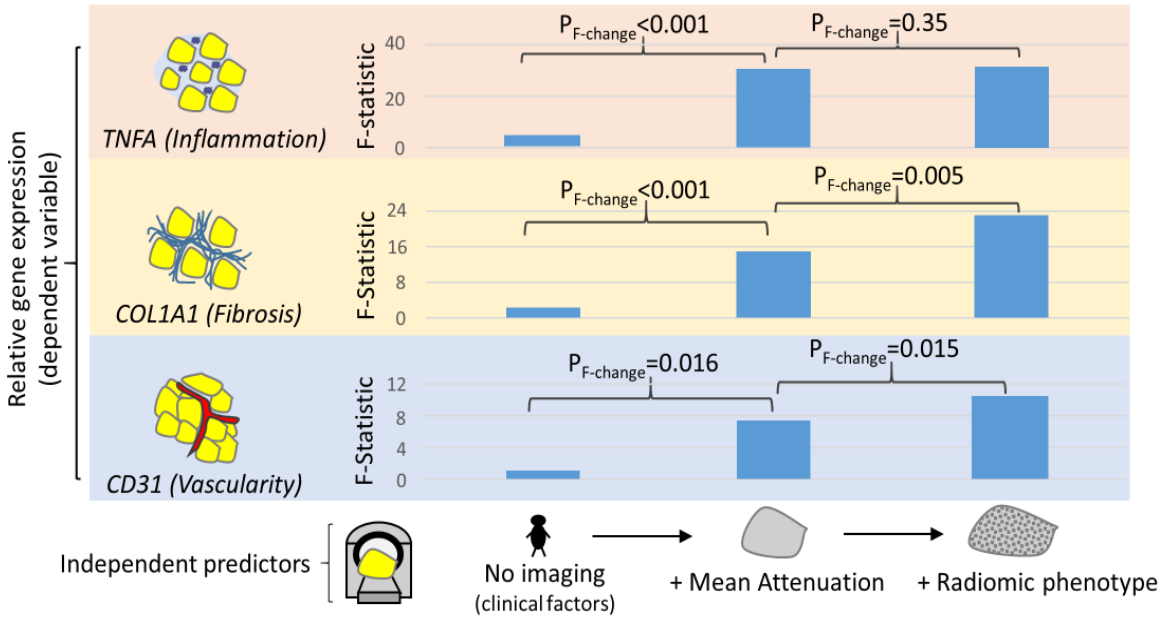

Figure 5.3. Radiomic phenotyping improves detection of adipose tissue remodelling features. *Comparison of nested linear regression models with relative gene expression as the dependent variable and i) clinical risk factors alone (Model 1: age, sex, hypertension, hypercholesterolaemia, diabetes mellitus, body mass index); ii) Model 1 + Mean Attenuation (Model 2); and iii) Model 2 + PVAT radiome (first three principal components, as shown in Figure 5.2D) as the independent predictors. The F statistic at each step is presented and compared to the previous step using the F test. Imc: Informational measure of correlation 2; *Relative gene expression was calculated using cyclophilin A (PPIA) as the housekeeping gene. Reproduced with permission from Oikonomou EK et al.* ***Eur Heart J****. 2019. doi: 10.1093/eurheartj/ehz592.*

5.3.2. A radiomic signature for adverse pericoronary fat remodelling

Radiomic phenotyping of coronary PVAT around the RCA and LCA produced a total of 1686 radiomic features Figure 5.4A. Stability analysis identified 1391 (82.0%) features with an ICC≥0.9 (Figure 5.5). A correlation plot with further hierarchical clustering of these stable 1391 radiomic features in 1575 SCOT-HEART patients revealed distinct clusters of highly correlated features (Figure 5.4B), with notable variance across the cohort population (Figure 5.4C).

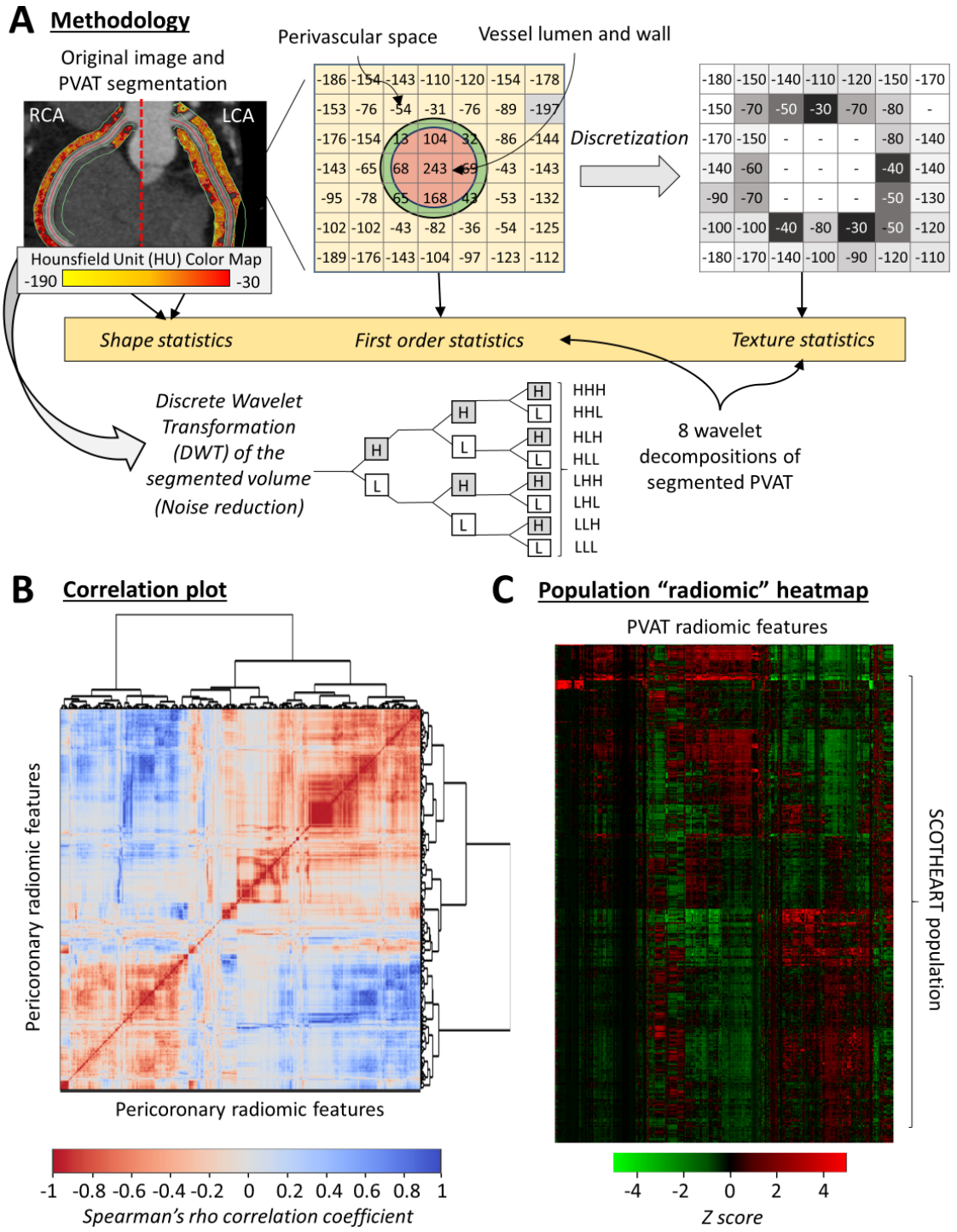

Figure 5.4. Radiomic phenotyping of coronary perivascular adipose tissue (PVAT). (A) *The PVAT of the right and left coronary arteries (left main and proximal to mid left anterior descending artery) was segmented and used to calculate a number of shape-, attenuation- and texture-related statistics. Attenuation values were discretised into 16 bins of equal 10 Hounsfield Unit-width to compute texture statistics, whereas additional wavelet transformation with a high- or low-filter was applied in the x, y and z plane.* ***(B)*** *Correlation plot of all 1391 stable radiomic features in the SCOT-HEART population (n=1575 patients), with hierarchical clustering revealing distinct clusters of radiomic variance.* ***(C)*** *Heatmap of scaled radiomic features in the SCOT-HEART population revealing between-patient variance across the cohort. H: high filter; L: low filter; LCA: left coronary artery; PVAT: perivascular adipose tissue; RCA: right coronary artery. Reproduced with permission from Oikonomou EK et al.* ***Eur Heart J****. 2019. doi: 10.1093/eurheartj/ehz592.*

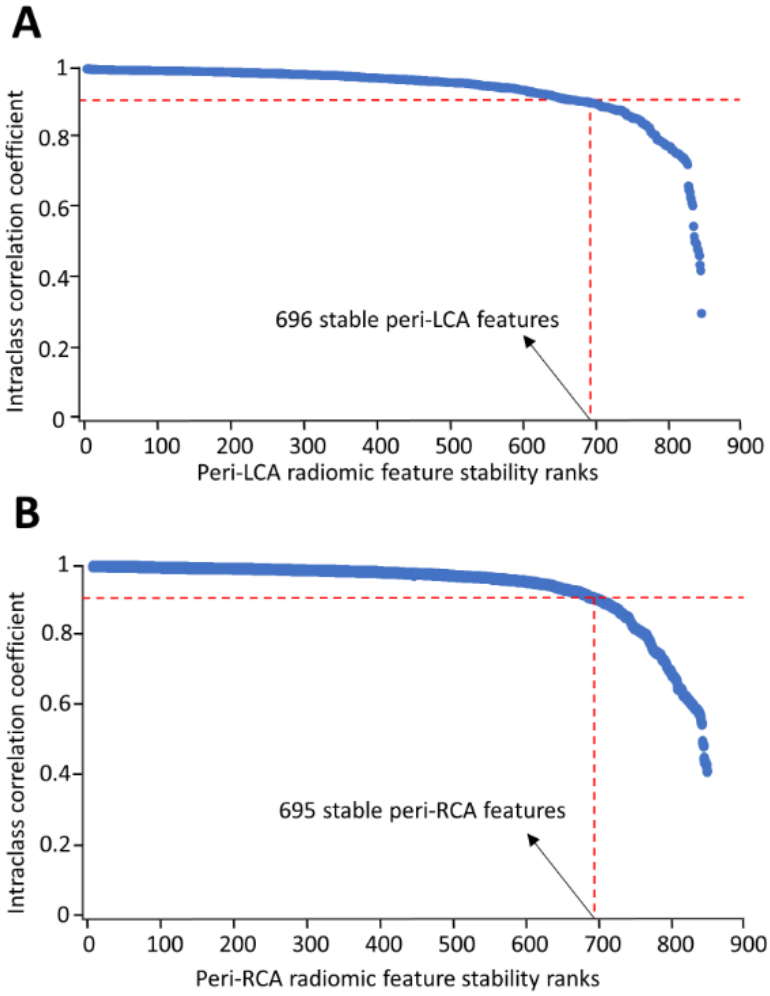

Figure 5.5. Stability analysis of coronary perivascular adipose tissue radiomic features. *Plot of the inter-observer intraclass correlation coefficient of all 843 radiomic features measured around the right (RCA)* ***(A)*** *and left coronary arteries (LCA)* ***(B)****. Radiomic features are ranked on descending order based on their ICC. A total of 696 and 695 radiomic features were found to have an ICC equal to or greater than 0.90 on inter-observer analysis around the RCA and LCA respectively and were subsequently selected for inclusion in further analyses. Reproduced with permission from Oikonomou EK et al.* ***Eur Heart J****. 2019. doi: 10.1093/eurheartj/ehz592.*

MACE cases (101 events within five years of CCTA) and 101 matched controls with MACE-free five-year follow-up (Table 5.2) were retrieved from the CRISP-CT and SCOT-HEART studies, and a case-control study was designed to identify the presence of a distinct radiomic signature that is independently associated with cardiac risk (Figure 5.6A). The two groups were well-matched for age, traditional cardiovascular risk factors, systemic or epicardial obesity, CT scanning parameters (Table 5.2). In univariable ROC

analysis, a total of 22 (1.6%), 86 (6.2%) and 241 (17.3%) radiomic features were found to discriminate MACE from non-MACE cases ($P<0.001$, $P<0.01$ and $P<0.05$ respectively) (Figure 5.6B). In order to identify a combined radiomic signature that combines the diagnostic value of all these features, the study population was randomly split into a training (80%) and a validation set (20%). Reduction of pairwise correlations at the level of $|\text{Spearman's rho}|\geq 0.9$ resulted in 335 independent features. Recursive feature elimination with a random forest algorithm and repeated five-fold cross-validation showed a plateau in the accuracy of the trained model with a selection of 64 features (Figure 5.7 & Figure 5.8). Following three rounds of repeated five-fold cross-validation in order to validate the best-performing model internally and avoid overfitting, the discriminatory value of the model was confirmed in the remaining validation set (AUC 0.778 [95% CI 0.622-0.926]) (Figure 5.6C-D).

While perivascular FAI alone was able to discriminate MACE from the matched non-MACE cases in all subpopulations (AUC of 0.70 [95% CI: 0.61-0.78] in CRISP-CT and 0.67 [95% CI: 0.53-0.81] in the SCOT-HEART cases), the fully trained radiomic model provided incremental discriminatory value beyond perivascular FAI in both populations ($P<0.001$ for all paired comparisons of AUC in each cohort).

To understand the biological interpretation of FRP, I then searched for the overlap between the radiotranscriptomic signatures for adipose tissue inflammation, fibrosis and vascularity and the features included in the FRP (Figure 5.6E). Notably, FRP consists of a range of PVAT radiomic features that are differentially associated with either inflammation, fibrosis and vascularity or any combination of these hallmarks of dysfunctional adipose tissue.

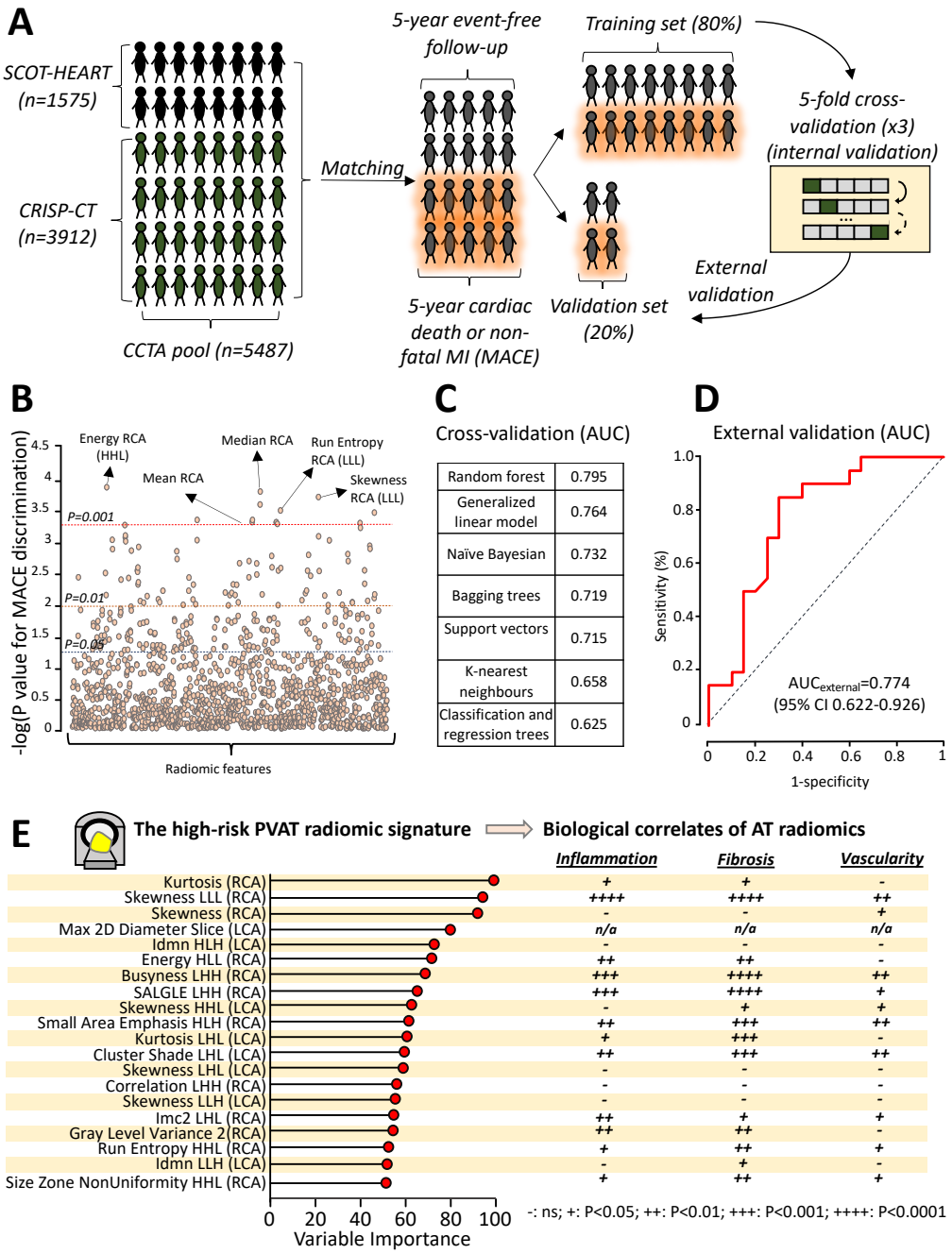

Figure 5.6. Identifying the high-risk PVAT radiomic signature. (A) *Cases of individuals that suffered a major adverse cardiac event (MACE; cardiac death or non-fatal myocardial infarction) within five years of their CCTA scan and matched controls were selected from three independent cohorts and randomly split in a training and a testing set (80 vs 20%), to train and test a random forest model to discriminate MACE from non-MACE cases.* ***(B)*** *A forest plot of the discriminatory value of each radiomic feature in univariable analysis.* ***(C)*** *Internal cross-validation performance (AUC_{max}) of different machine learning algorithms for discrimination of MACE.* ***(D)*** *External validation of the best-performing random forest algorithm (20% of the initial sample).* ***(E)*** *Variable importance of the top 20 radiomic features of the final random forest model and corresponding strength of association with adipose tissue inflammation, fibrosis and vascularity, as assessed in Study 1 (++++ for P<0.0001; +++ for P<0.001. ++ for P <0.01, + for P<0.05 and – if P≥0.05). AUC: area under the curve; CI: confidence interval; H: high filter; L: low filter; LCA: left coronary artery; MACE: major adverse cardiac events; MI: myocardial infarction; RCA: right coronary artery. Radiomic feature abbreviations and definitions are explained in the Appendix section 3. Reproduced with permission from Oikonomou EK et al.* ***Eur Heart J****. 2019. doi: 10.1093/eurheartj/ehz592.*

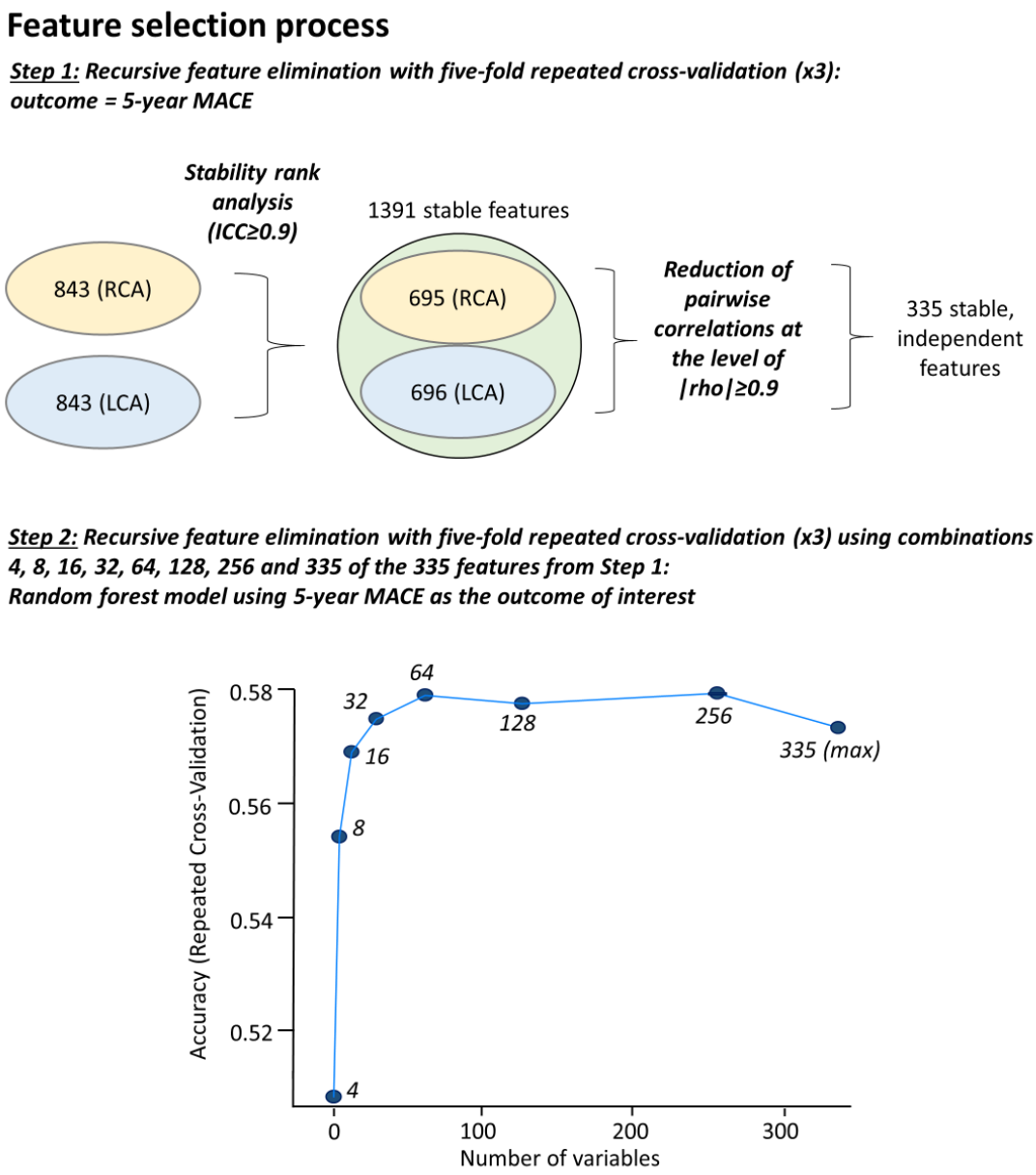

Figure 5.7. Radiomic feature selection process. *A total of 1391 out of 1686 (82.0%) features were found to be stable following intra-observer analysis, as defined by an intraclass correlation coefficient (ICC) of ≥0.9. Further reduction of pairwise correlations at the level of |rho|≥0.9 resulted in 335 independent features. Next, recursive feature elimination with a random forest algorithm and repeated five-fold cross-validation showed a plateau in the accuracy of the trained model with a maximal number of 64 selected features. LCA: left coronary artery; MACE: major adverse cardiac events; RCA: right coronary artery. Reproduced with permission from Oikonomou EK et al.* ***Eur Heart J****. 2019. doi: 10.1093/eurheartj/ehz592.*

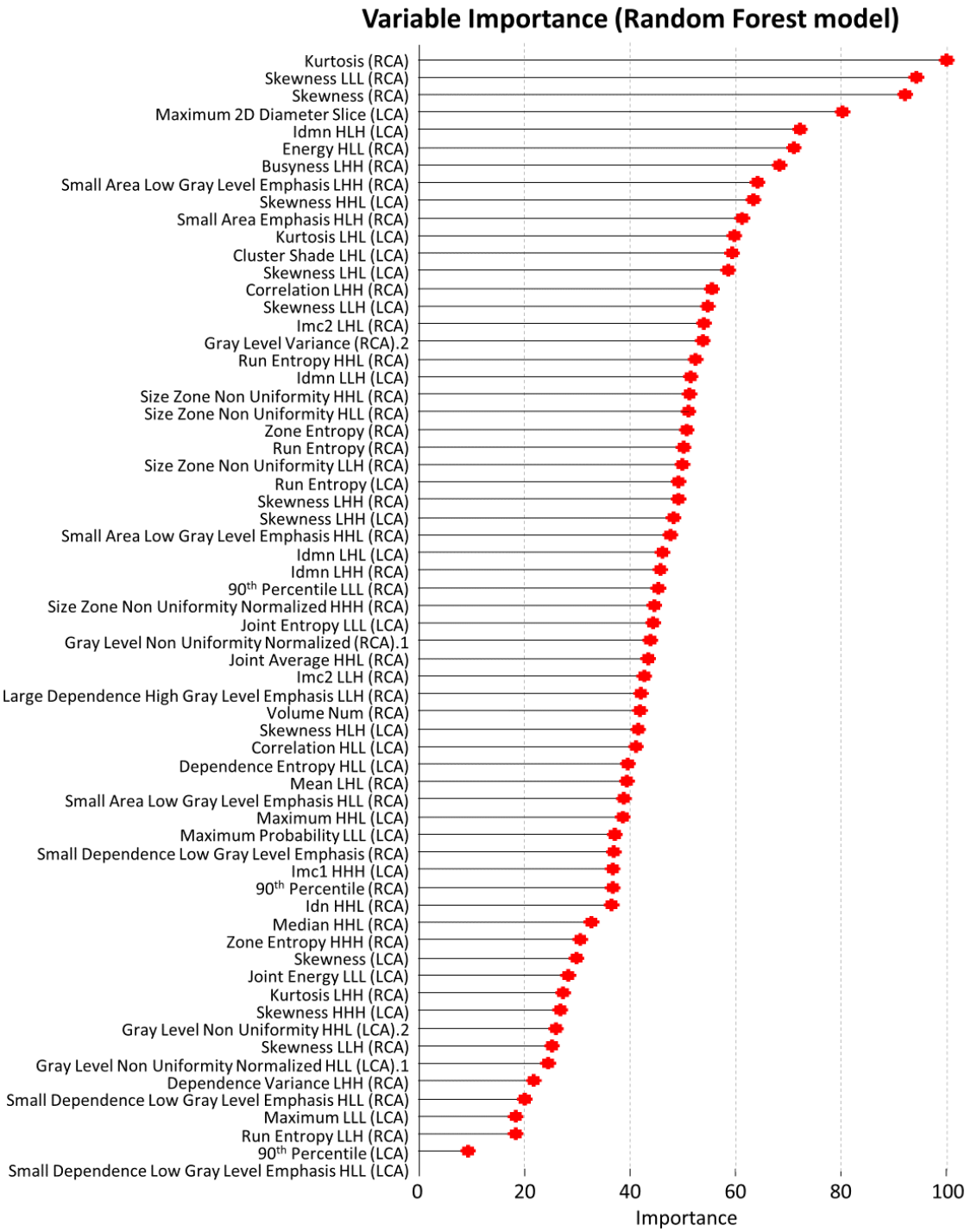

Figure 5.8. Variable importance in the final random forest model. *A graphical representation of the relative variable importance of the 64 selected radiomic features in the final random forest model for MACE discrimination. H: high wavelet filter; L: low wavelet filter; MACE: major adverse cardiac events. Radiomic feature abbreviations and definitions are explained in the Appendix section 3. Reproduced with permission from Oikonomou EK et al.* ***Eur Heart J****. 2019. doi: 10.1093/eurheartj/ehz592.*

5.3.3. Exploring the prognostic value of the Fat Radiomic Profile

I next characterised FRP in the 1575 eligible CCTA scans from the SCOT-HEART study, in order to explore its prognostic value for detecting adverse events. Over a median follow-up period of 4.8 (25^{th}-75^{th} percentile: 4.2 to 5.7) years, one confirmed cardiac death, 33 non-fatal AMI events, 176 late revascularisation events and 32 non-cardiac death events were recorded (Table 5.3). FRP was positively associated with the adjusted risk of MACE (per 0.01 increments: adj. HR 1.12 [95% CI 1.08-1.15], P<0.0001). For an optimal cut-off point of 0.63 (Figure 5.9) individuals with FRP ≥ versus <0.63 (FRP+ vs FRP-) had a 10.8-fold higher risk of MACE, after adjustment for age, sex, SBP, total cholesterol, HDL, diabetes mellitus, smoking, BMI, obstructive disease, scanner type, presence of high-risk plaque features, and calcium score (Figure 5.10A). Of note, FRP was not related to the presence of HRP features (Rho=0.004, P=0.87), and correlated very weakly with calcium score (rho=0.07, p=0.007). FRP+/HRP+ individuals had a 43-fold higher risk of MACE compared to the FRP-/HRP- participants, after adjustment for age, sex, SBP, total cholesterol, HDL, diabetes mellitus, smoking, BMI, and scanner type (Figure 5.10B). FRP significantly improved the predictive value of a traditional model consisting of age, sex, systolic blood pressure, diabetes mellitus, body mass index, smoking status, presence of coronary artery disease (≥50% stenosis), total cholesterol, high-density lipoprotein levels, scanner type, presence of HRP, as well as Agatston CCS (log[CCS+1]) (Figure 5.10C). In further analyses, FRP did not predict non-cardiac mortality (Figure 5.10D) but remained an independent predictor of a composite endpoint of MACE or late coronary revascularisation (≥ six weeks post-CCTA) (Figure 5.10E-F) confirming the cardiac-specific nature of the biomarker.

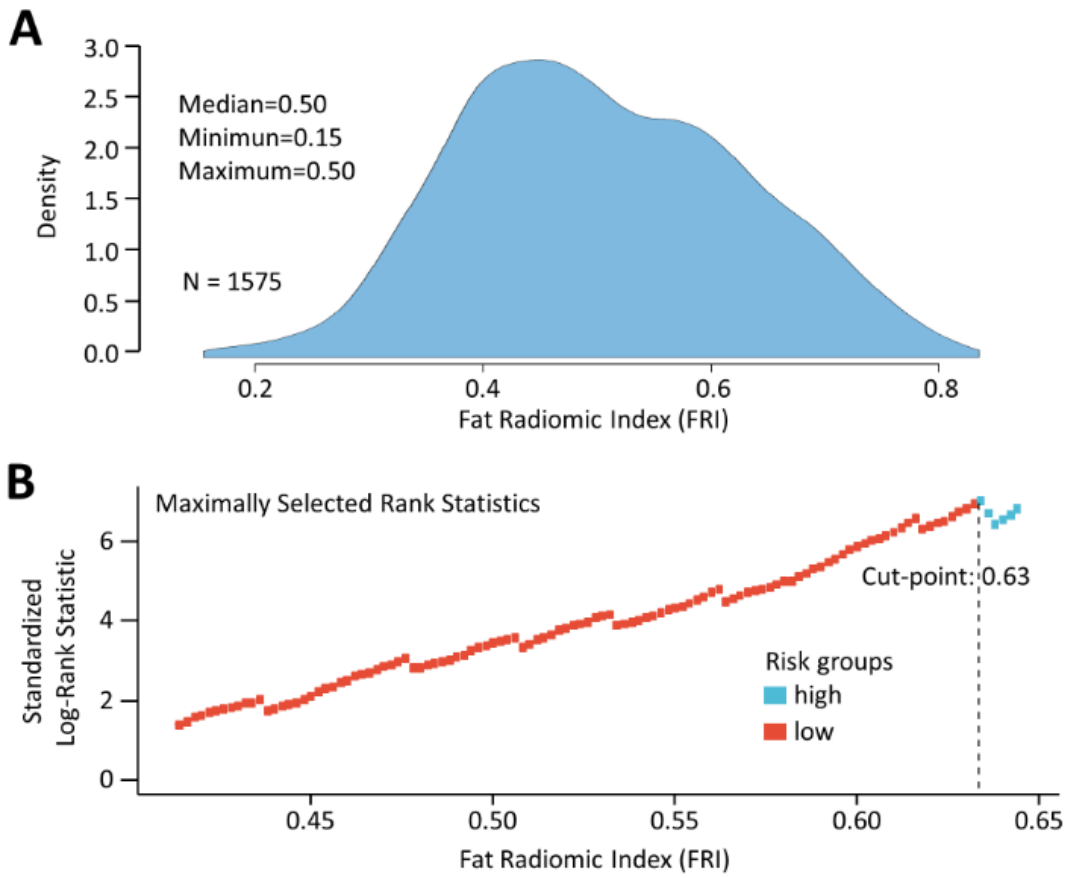

Figure 5.9. Identifying the optimal cut-off for the perivascular fat radiomic profile (FRP). ***(A)*** *Density plot describing the distribution of FRP in the SCOT-HEART population (n=1575 individuals).* ***(B)*** *Plot of the standardised log-rank statistic for prediction of major adverse cardiac events versus different cut-off points for FRP, showing optimal discrimination for a cut-off point of 0.63. FRP: fat radiomic profile. Reproduced with permission from Oikonomou EK et al.* ***Eur Heart J****. 2019. doi: 10.1093/eurheartj/ehz592.*

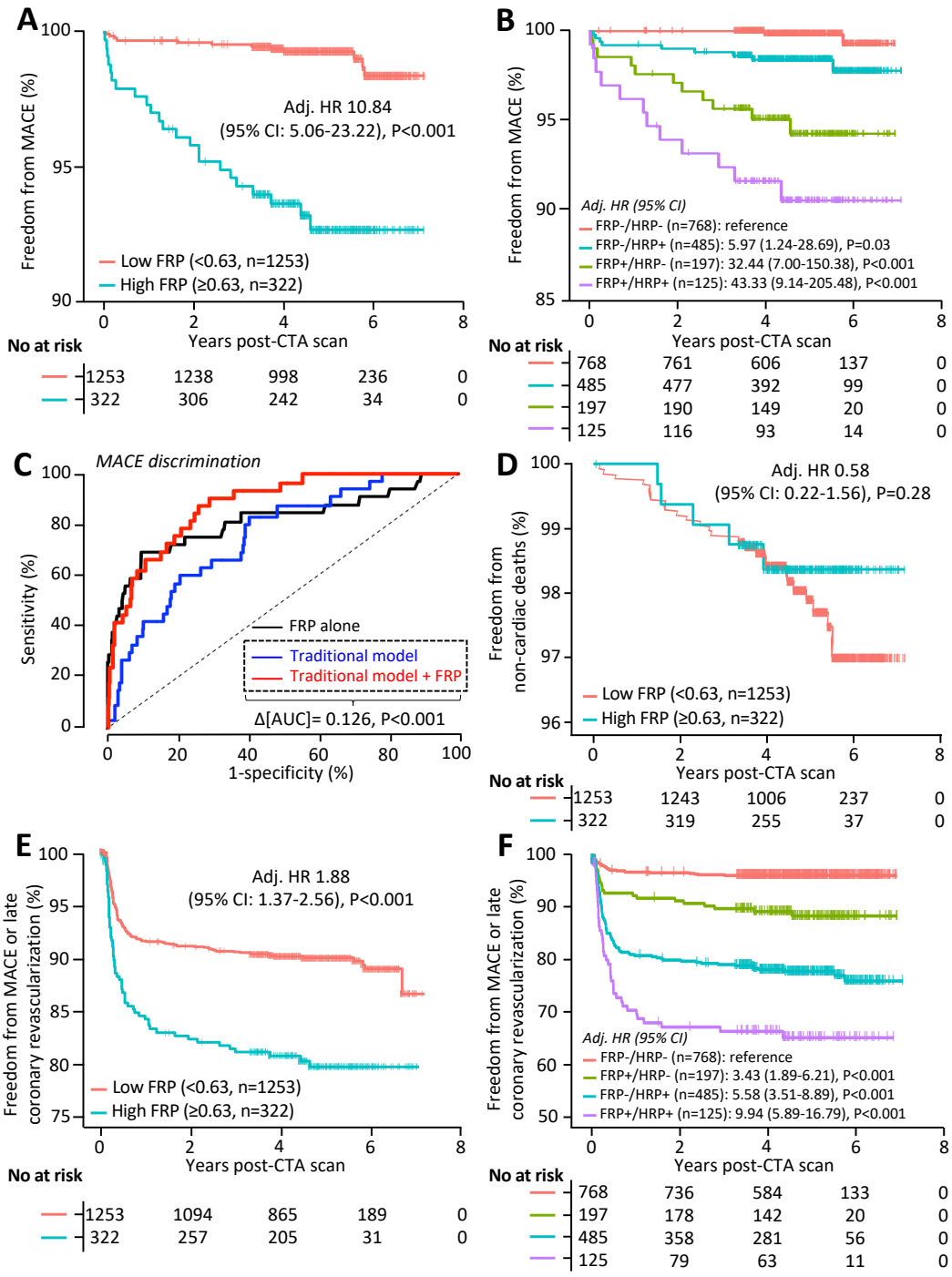

Figure 5.10. Prognostic value of the pericoronary Fat Radiomic Profile (FRP). (A-B) *Kaplan-Meier curves and adjusted hazard ratios for MACE across strata of Fat Radiomic Profile (≥0.63 [FRP+] versus 0.63 [FRP-]) and high-risk plaque (HRP) features.* ***(C)*** *Time-dependent receiver operating characteristic curves (t=5 years post-CCTA) for two nested prediction models consisting of age, sex, systolic blood pressure, diabetes mellitus, body mass index, smoking status, presence of coronary artery disease (≥50% stenosis), total cholesterol, high-density lipoprotein levels, scanner type, presence of HRP, as well as Agatston CCS (log[CCS+1]) with (AUC: 0.880) or without FRP (AUC: 0.754). FRP alone is represented by the black line (AUC 0.79).* ***(D)*** *Kaplan-Meier curves and adjusted hazard ratios for non-cardiac mortality, as well as a composite endpoint of MACE and/or late revascularization* ***(E-F)*** *across strata of FRP and HRP features. AUC: area under the curve; CI: confidence interval; CCS: coronary calcium score; CCTA: coronary computed tomography angiography; FRP: fat radiomic profile; HR: hazard ratio; HRP: high-risk plaque feature; MACE: major adverse cardiac events. Reproduced with permission from Oikonomou EK et al.* ***Eur Heart J****. 2019. doi: 10.1093/eurheartj/ehz592.*

5.3.4. Fat Radiomic Profile in acute myocardial infarction

Radiomic phenotyping of 44 AMI patients scanned within 96 hours of admission and 44 matched controls undergoing clinical CCTA for stable CAD revealed higher FRP values in the AMI versus the control group (Figure 5.11A), despite no differences in demographics, clinical risk factors or medications (Table 5.4). Finally, in a subgroup of 16 patients who underwent sequential CCTA scanning within 96 hours of admission and six months later, no changes were observed in FRP (Figure 5.11B). In contrast, perivascular FAI (as quantified in chapter 4) changed dynamically at 6 months (Figure 5.11C).

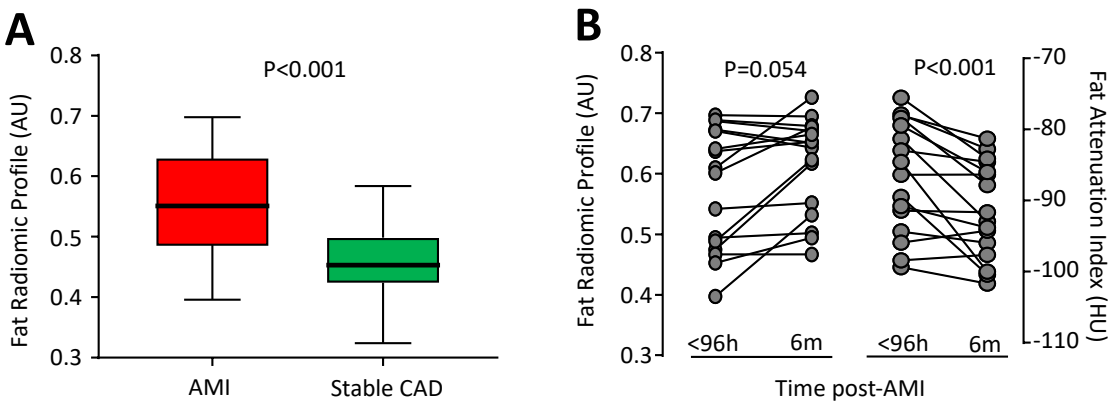

Figure 5.11. Pericoronary Fat Radiomic Profile (FRP) in acute myocardial infarction (AMI). *(A) Tukey box-plot of FRP values in patients scanned within 96 hours of AMI and matched controls undergoing clinical CCTA for stable CAD (n=44 per group). (B) FRP and perivascular FAI in AMI patients scanned within 96 hours of admission and six months later (n=16 per group). FAI: Fat Attenuation Index. AMI: acute myocardial infarction; AU: arbitrary units; CAD: coronary artery disease; HU: Hounsfield Units; P values derived from Mann-Whitney test (A) and Wilcoxon-signed rank test (B). Reproduced with permission from Oikonomou EK et al.* ***Eur Heart J****. 2019. doi: 10.1093/eurheartj/ehz592.*

5.4. Discussion

The development and validation of the perivascular Fat Attenuation Index (FAI), a CCTA-derived biomarker of coronary inflammation based on quantification of PVAT attenuation shifts, highlighted the potential for complementary imaging biomarkers that

can describe the full phenotypic heterogeneity of PVAT composition and remodelling and its clinical importance. Using a "radiotranscriptomic" approach, I have now demonstrated that specific texture patterns within the radiomic profile of PVAT describe fibrosis and vascularity, possibly reflecting permanent changes in adipose tissue induced by chronic coronary inflammation [109]. Following this discovery, I employed a machine learning approach to build a new radiomic signature of high-risk PVAT around the coronary arteries, namely the perivascular Fat Radiomic Profile (FRP) that relies on detection of such changes to identify individuals at increased cardiac risk. FRP was then validated in the SCOT-HEART cohort, where it demonstrated striking prognostic value for MACE. This study suggests that FRP captures the adverse remodelling of PVAT in response to atherosclerosis and the cumulative effects of coronary inflammation over time. As opposed to FAI, which changes dynamically and can be used to prospectively monitor responsiveness to risk reduction measures, FRP detects a residual risk not confounded by concomitant medications or other acute processes.

5.4.1. Developing Radiotranscriptomic Signatures of Adipose Remodelling

Imaging studies in oncology have shown that specific shape- and texture-related patterns generate tumor phenotypes that are independently linked to the underlying tumor biology and to clinical prognosis [154]. Such patterns, often derived from complex mathematic formulae, are invisible to the naked eye of experienced radiologists and clinicians [139]. Radiomic approaches map these qualitative imaging features and generate a number of quantitative variables that describe the imaged structure. In a recent study, Kolossvary et al. showed that radiomic features can reliably identify plaques with the high-risk plaque feature napkin-ring sign, the identification of which normally relies on a qualitative

assessment of plaque anatomy and the experienced eye of the operator [191]. Radiomic analysis of adipose tissue is another novel method that requires investigation.

Further to lipolysis, reduced adipogenesis and water accumulation within PVAT, vascular inflammation also triggers more permanent changes in the perivascular space, such as fibrosis and neoangiogenesis [1, 109] which could also be captured by CCTA. In a radiotranscriptomic experiment using adipose tissue biopsies from 167 patients undergoing cardiac surgery, I searched for radiomic features that would best describe the gene expression of *TNFA* (marker of inflammation), *COL1A1* (marker of fibrosis) and *CD31* (marker of vascularity). Indeed, as expected [126], features describing adipose tissue attenuation (captured by the FAI) were the most descriptive of *TNFA* expression. However, features associated with the radiomic texture of adipose tissue enabled a more accurate detection of more permanent changes in its phenotype, such as fibrosis (*COLA1* expression) and vascularity (*CD31* expression) that affect the histological (and therefore radiomic) heterogeneity of adipose tissue. Of note, different radiomic patterns were differentially associated with tissue inflammation, fibrosis and vascularity, suggesting that a comprehensive radiomic phenotyping approach is needed to describe fully the biological variation of human adipose tissue (Figure 5.12).

5.4.2. Developing and validating the high-risk Fat Radiomic Profile (FRP)

In a nested study that included individuals who developed a MACE within five years from the CCTA and matched controls from the CRISP-CT [142] and SCOT-HEART [143] studies, I applied a machine learning-based approach with multiple rounds of validation, which enabled us to discover a high-risk PVAT radiomic profile (FRP) that is linked to increased cardiac risk. Importantly, FRP offered incremental prognostic information beyond current CCTA-based tools, suggesting a residual level of cardiac risk that is not

detected by traditional risk stratification algorithms. This signature captured not only the attenuation features included in FAI, but also features capturing fibrosis and vascularity of PVAT. To see whether this radiomic signature captures permanent changes induced by chronic inflammation in PVAT, it was validated in the entire CCTA arm of the SCOT-HEART study. This population had CCTA-guided management, with many risk-modifying interventions post-CCTA, thus affecting the clinical value of their baseline FAI measurement. Despite this, I observed that FRP retained its prognostic value for

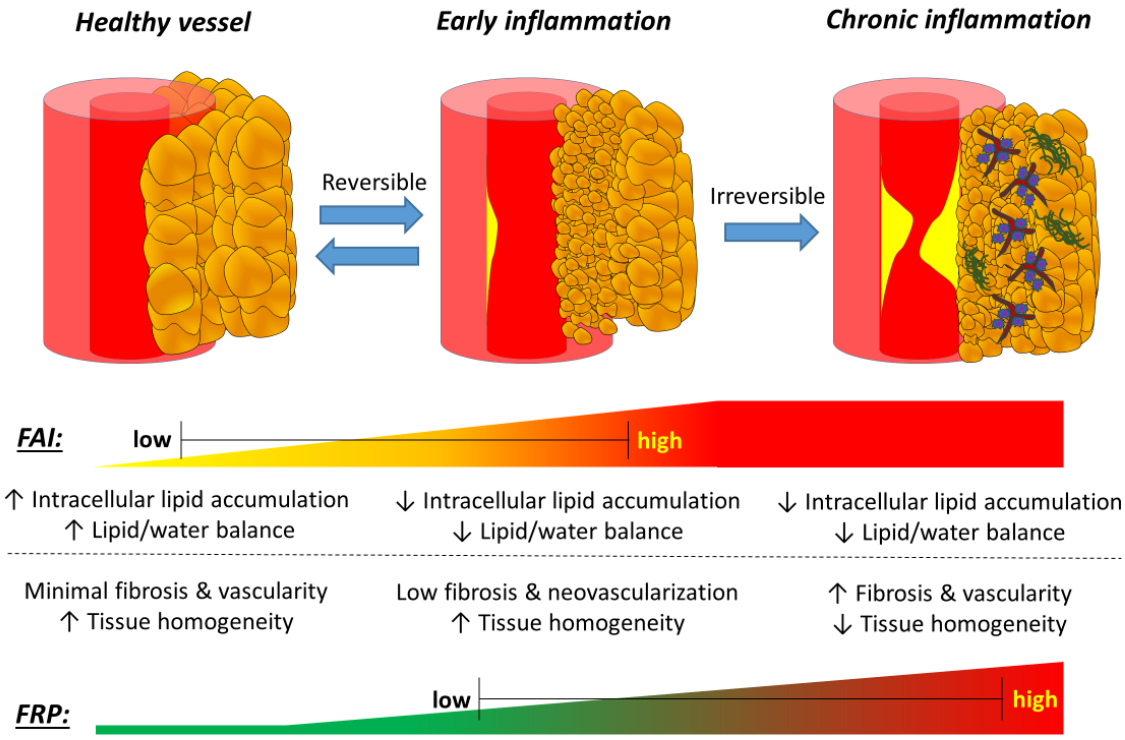

Figure 5.12. Proposed biological meaning of the PVAT radiomic profile. *Coronary inflammation is associated with phenotypic changes in PVAT, characterised by decreased adipocyte lipid accumulation. This phenotypic shift forms the basis of the CT-derived Fat Attenuation Index that characterizes attenuation changes in PVAT. However, chronic vascular inflammation and atherosclerotic disease are associated with further, irreversible changes in PVAT composition, such as increased extracellular fibrosis and vascular remodelling. Those can now be detected by analyzing the radiomic phenotype of PVAT on CCTA. A comprehensive analysis of attenuation- and texture-based metrics of coronary PVAT on CCTA imaging carries incremental prognostic value in cardiac risk prediction and highlights the critical role of PVAT in human atherosclerotic cardiovascular disease. CCTA: coronary computed tomography angiography; FAI: fat attenuation index; FRP: fat radiomic profile; PVAT: perivascular adipose tissue. Reproduced with permission from Oikonomou EK et al.* ***Eur Heart J****. 2019. doi: 10.1093/eurheartj/ehz592.*

future MACE, with incremental value beyond the current state-of-the-art in CCTA-based risk prediction.

5.4.3. Fat Radiomic Profile and Acute Myocardial Infarction

Chronic inflammation leads to accelerated atherogenesis and induces plaque instability leading to acute coronary syndromes [25]. In further analysis, FRP successfully discriminated AMI patients from stable controls. After performing serial CCTA scans in patients with AMI, FRP remained unchanged, whereas FAI was decreased following six months of optimal medical therapy. These findings suggest that FRP (a patient-specific index) may be a useful biomarker for first-time screening of individuals undergoing CCTA, while FAI (segment or plaque-specific index) captures the dynamic inflammatory burden of the coronary vasculature and can be used to track longitudinal changes in coronary inflammation, as also evidenced in chapter 3 of this thesis.

5.4.4. Radiomic phenotyping versus perivascular FAI mapping

A potential limitation of this high-throughput radiomic approach is the calculation of a large number of variables whose clinical significance and biological interpretation may be hard to interpret. For instance, Run Entropy and Zone Entropy quantify the uncertainty/randomness in the distribution of run lengths and gray level zones, and may indicate heterogeneity in the texture patterns. As we have previously shown, in the presence of vascular inflammation, vascular-derived signals induce local changes in the direct perivascular area. So how is this analysis different to perivascular FAI mapping?

First, as highlighted earlier, it is possible that further to a decrease in the adipocyte size/differentiation status, which is reflected by perivascular FAI, vascular disease is associated with fibrotic and vascular remodelling in PVAT which in turn affect the

histological homogeneity of adipose tissue, detected as an increase in radiomic heterogeneity. Similarly, first order statistics such as skewness may supplement the mean (FAI) attenuation by providing a more detailed description of the attenuation histogram. A high number of voxels close to the -30 side of the HU range may further shift the skewness towards more negative values and may be more sensitive than the mean in detecting such vessel-induced shifts in PVAT attenuation. Such spatial changes towards higher attenuation values may be also associated with higher Short Run High Gray Level Emphasis and lower Small Area Low Gray Level Emphasis values. Furthermore, additional wavelet filter transformations (especially high-frequency transformations such as HHH which capture discontinuities, ruptures and singularities in the original data, and low-frequency transformations such as LLL which characterise the coarse structure of the data to identify the long-term trends) can increase the signal-to-noise ratio and uncover or enhance the diagnostic and prognostic value of such radiomic features.

Second, radiomic phenotyping combines both *volumetric* and *qualitative* metrics of PVAT phenotype. Whereas spatial changes in PVAT attenuation have been found to be dependent on the biology and inflammatory burden of the adjacent coronary vessel (and independent of e.g. systemic insulin resistance [126]), epicardial adiposity is a well-established cardiometabolic risk factor, associated with CAD presence as well as insulin resistance [149, 193]. Treating the epicardial fat expansion and PVAT quality as two independent risk factors ignores the potential interactions between the two. A machine learning-based approach overcomes this by integrating the volume and attenuation features of PVAT, combining them in the best possible way to improve cardiovascular risk stratification.

5.4.5. Study limitations

This study has certain limitations. The limited number of adverse events in the SCOT-HEART arm (34 MACE events over a median follow-up of 4.8 years) which is typical of a low-risk patient cohort undergoing CCTA, means that further testing in independent study populations may be needed to extensively validate and calibrate the model.

In addition, future studies should explore the value of these findings in a wide range of clinical acquisition protocols in order to ensure their external validity. Nevertheless, the main value of the present study is the development of a methodological framework for comprehensive radiomic phenotyping of PVAT. While the optimal high-risk signature may further evolve as more data are added into the algorithm, this chapter represents the first application of a high-throughput radiomic phenotyping approach in PVAT.

Moreover, the proposed algorithm is rather time-consuming since I first developed it using a range of open-source software solutions. Having demonstrated the feasibility, biological meaning and clinical value of the method, efforts are currently underway to develop and automated platform that will speed up the analysis. This will also enable the application of this method in more coronary segments and in all CCTA scans of the CRISP-CT study (as opposed to the case-control study approach that was employed in this chapter), thus enabling its testing and validation in further prospective cohorts.

Finally, the pooling of scans from all available cohorts in both the training and validation sets was deemed necessary to account for technical variations between scanners and acquisition protocols in as many centers as possible. To this end, incorporating scans from more centers and scanners is expected to increase the external validity of these models.

5.5. Conclusions

In this chapter, I present a high-risk radiomic signature of coronary PVAT (FRP), derived from machine learning-based analysis of traditional CCTA scans, which detects adverse structural changes associated with PVAT fibrosis and vascular remodelling. FRP significantly improves risk prediction for adverse clinical events beyond the current state-of-the-art and discriminates patients with AMI from those with stable disease. Whereas FAI (attenuation) changes dynamically in response to acute coronary inflammation, FRP (radiomic texture) captures more permanent structural changes in PVAT and provides additional risk stratification. The combination of FAI (a component of FRP) and FRP facilitates the development of a more comprehensive, individualised cardiac risk profile for a patient. In conclusion, radiomic characterisation of PVAT by means of the FRP is a novel, promising approach to capture the biological interactions of the diseased vascular wall with its PVAT, and enables the detection of a residual cardiac risk not identified through traditional approaches.

6

Chapter 6. Limitations and future work

My project is not without limitations. Some of them are inherent to the technical aspects of cardiac CT imaging, as often acknowledged in many research studies. Others relate to concepts that were not adequately explored by the experimental designs employed in this thesis. This chapter discusses these limitations, as well as a future research framework to address gaps in our knowledge and further explore and validate the clinical value of CT-based perivascular fat phenotyping.

6.1. Technical considerations

Whilst CT imaging was originally developed to provide a more detailed anatomical description of the human anatomy based on the qualitative description of the morphological appearance of internal structures, radiomic approaches rely on the quantitative analysis of the absolute and relative attenuation (Hounsfield Unit) values. As such, they are much more sensitive to changes in CT acquisition parameters, which can influence the calculated raw values thus introducing an additional layer of complexity in the interpretation of radiomic indices [194]. This is a frequently debated concept in the field of CT imaging, with several studies showing that even the widely used Coronary Calcium Score (CCS) is very sensitive to changes in slice thickness and other technical parameters [195]. Since these metrics are often used to guide clinical recommendations, careful calibration of the acquisition and quantification methodology is of the utmost importance. For instance, the AHA/ACC guidelines recommend the use of CCS in

patients where a recommendation regarding the initiation of e.g. statin treatment remains uncertain. Rather than using CCS as a continuous variable, risk groups are often defined using absolute cut-offs, such as a CCS of 100 or 300 [7, 176]. Given this common dichotomisation in clinical practice, patients may be reclassified purely due to variation in the CT acquisition and analysis parameters.

The same considerations apply to the calculation of all radiomic features discussed in this thesis. In a recent study, investigators calculated a total of 177 radiomic features to assess their reproducibility across different technical parameters [194]. At different levels of tube voltage (kVp), milliamperage, field of view, section thickness, pitch value and reconstruction kernel, just 41.8%, 78.5%, 75.1% and 71.8%, 94.9% and 41.2% of all radiomic features were found to be stable (defined as an ICC of >0.9), respectively.

These findings confirm that technical acquisition parameters should be taken into account when interpreting the absolute values of radiomic features. In our studies, we have tried to standardise the acquisition protocols to minimise the effects of acquisition settings on the calculated metrics. While this has been feasible in prospective studies (i.e. AdipoRedox, ORFAN & Ox-IMPACT studies), this was not possible in retrospective analyses of real-life cohorts. However, appropriate conversion factors were used for scans performed at 100 vs 120 kVp, with further statistical adjustment for tube voltage in adjusted regression models, where appropriate [126, 142, 150]. In addition, in both arms of the CRISP-CT study, as well as in the SCOT-HEART study, more than two thirds of the patients in each cohort were scanned in the same scanner [126, 142, 150]. The same manufacturer-specific reconstruction kernels were used consistently in each scanner in order to minimise intra-scanner variations. In addition, intra- and inter-operator analyses were performed to assess the stability of the calculated radiomic features, with only radiomic features demonstrating inter-observer ICC values ≥0.9 selected for inclusion in

further analyses. Furthermore, in chapter 5, I pooled scans performed across six different scanners in three different countries in order to account for variations in clinical practice and imaging protocols. For instance, while some radiomic features or patterns could discriminate MACE cases from controls in one cohort, they failed to do so in other cohorts. By pooling these scanners and cohorts together, the radiomic patterns that were finally identified as prognostic of adverse events were less likely to be confounded by cohort-, scanner- or protocol-specific variations. This brings them closer to the "ground truth". Adding data from more scanners and centres will further improve the external validity of my observations and models, while converging towards the "ground truth" of the high-risk PVAT radiomic phenotype.

Similar to CCS, one needs to accept the inherent variability and some degree of noise attributed to the use of variable clinical protocols, software and hardware in each imaging centre. However, in the era of digital medicine and machine learning, attempts should be made to standardise protocols or at least identify appropriate conversion factors to allow the comparison of metrics derived from different scanners and using variable protocols. This is the aim of the VIP study (Validation study for introduction of novel computed tomography Imaging biomarkers in clinical Practice study), which will attempt to validate CT-derived radiomic biomarkers across hardware platforms and scanning settings. Eligible patients will undergo two CCTA scans within a few days to assess the intra-scan variability of such indices, whereas others will undergo a first CCTA in the same reference CT scanner, with the second scan in a CT scanner of a different manufacturer. In addition, ex vivo adipose tissue biopsies from patients undergoing cardiac surgery and recruited as part of the AdipoRedox study, will also be scanned using several permutations of CT acquisition parameters in a range of CT scanners in different hospitals in Oxford, London and Leicester. These datasets will then be used to standardise

acquisition protocols and identify appropriate correction methods for indices derived from different scanning protocols.

6.2. Residual cardiovascular risk & low event rates

As described throughout this thesis, the overall aim of CT-based PVAT phenotyping is to detect a "residual" risk not detected by traditional risk stratification methods, including traditional cardiovascular risk factors and the standard reporting of CCTA. Since the outcome of interest is the incidence of hard clinical endpoints (mortality and non-fatal cardiovascular events), both the statistical power of the study and the validity of the derived models will increase at higher event numbers. However, in both the CRISP-CT and SCOT-HEART studies the event rate was relatively low [42, 43, 142]. This can be attributed to the nature of the selected population. First, CCTA is traditionally reserved for individuals at low- to intermediate risk of CAD, while higher risk patients may be referred directly for invasive coronary angiography [40]. Second, the detection of significant CAD on CCTA may lead to treatment initiation and further interventions which may significantly alter an individual's cardiovascular risk. In other words, a "treatment paradox" may exist where individuals with significant CAD are more likely to qualify for medical intervention and risk reduction measures compared to individuals with evidence of "minor" atherosclerosis. Such interventions are likely to reduce the residual cardiovascular risk to even lower rates, thus reducing the statistical power of a study and the ability to fit a complex model with an adequate number of predictors. As discussed in section 5.4, the limited number of adverse events in the SCOT-HEART population (34 MACE events over a median follow-up of 4.8 years) which is typical of a low-risk patient cohort undergoing CCTA, means that further testing in independent cohorts may be needed to extensively validate and calibrate the model. This is even more

important in the era of machine learning that relies on "big data" and balanced datasets with several observations in each class of interest. Along these lines, the perivascular fat radiomic approach presented in chapter 5 will benefit from the inclusion of more datasets and events. Advances in medical informatics, such as comprehensive Electronic Health Records and national databases (e.g. NHS Digital data updated through the Office for National Statistics in the United Kingdom) that integrate patient demographics, status, laboratory and imaging tests, can contribute towards this goal. This will enable the training of machine learning algorithms such as deep neural networks that will continue to improve and learn as they incorporate more and more data.

6.3. Cardiac CT versus other imaging modalities and biomarkers

Another limitation of my thesis is the absence of a direct comparison of CT-based PVAT mapping against other novel biomarkers of atherosclerotic cardiovascular risk, such as high-sensitivity C-reactive protein, high-sensitivity troponin, or even alternative imaging biomarkers of coronary inflammation, such as the PET-CT derived ^{18}F-NaF. While the post-hoc nature of the CRISP-CT analysis did not enable the measurement of such circulating biomarkers [142], prospective studies such as the ORFAN study will enable this direct comparison. In addition, this thesis did not include prospective registries of patients with ^{18}F-NaF-based PET-CT imaging. However, given the strong association between PVAT CT attenuation and ^{18}F-NaF uptake from atherosclerotic plaques, as demonstrated in a recent study [161], it is likely that the two biomarkers may be describing two sides of the same coin, thus eliminating the need for more expensive and time-consuming PET-CT scans in cardiovascular disease diagnosis and risk stratification.

6.4. Future randomised controlled trials

The present thesis relies on data from several, independent observational studies. While observational studies can be used to validate the diagnostic and prognostic value of a novel biomarker, the real clinical value of CT-based PVAT characterisation needs to be assessed in the context of a randomised controlled trial. For instance, such a trial could assess the value of a FAI-guided risk stratification approach versus standard practice in patients undergoing CCTA. While it would be unethical to withhold treatment in patients with advanced atherosclerosis, our method could be tested in patients that do not have any evidence of obstructive CAD but appear to have abnormally high perivascular FAI values. Such patients are usually discharged without potentially life-saving medications due the absence of a plaque at the time of CT imaging. However, these findings do not necessarily exclude the presence of coronary inflammation or subclinical atherosclerosis which are not identified and therefore remain untreated. Considerations regarding the feasibility, power calculations and cost-effectiveness of this study should also take into account the expected low event rate in these low-risk populations. Furthermore, smaller randomised controlled trials of medications with known anti-inflammatory effects, such as high-dose statin therapy or treatment with novel biologics such as canakinumab, could be performed to further assess the ability of perivascular FAI to track dynamic changes in the coronary inflammatory burden.

6.5. Machine learning as a “black box”

The ability of machine learning to detect patterns in the data, which may be invisible to the human eye, yet carry important clinical value is a “double-edged sword”. On the one hand, this represents the main strength of machine learning compared to more traditional approaches for the identification of novel biomarkers, allowing clinicians to extract an

unprecedented amount of information and to make sense of complex sets of data. However, such complicated machine learning systems often function as a "black box", providing minimal insight into the logic behind a given algorithm [196]. As a result, there have been several concerns regarding the acceptance of such a tool by physicians and patients alike. It is my personal view that artificial and human intelligence are not competing. In fact, artificial intelligence systems can reduce the work burden for clinicians, who will remain responsible for patient management and care [197]. However, this may still be hard to accept in risk prognosis, where the future risk represents a stochastic rather than a deterministic concept. To overcome this, I have tried to provide potential links between the identified radiomic signatures and the underlying biological mechanisms. For instance, perivascular FAI has been associated with changes in adipocyte lipid accumulation induced by an exogenous inflammatory environment. On the other hand, the fat radiomic profile consists of a range of radiomic features, including mean attenuation (the basis of FAI), perivascular adipose tissue volume (reflecting adipose tissue expansion and potentially an obesity-associated cardiometabolic risk), as well as features describing the radiomic texture that has been linked with fibrotic and vascular remodelling in the "dysfunctional" adipose tissue. These links between imaging and biology may facilitate the clinical translation of these biomarkers by removing the "black box" label and providing a mechanistic and biological rationale for the clinical interpretation of the proposed risk biomarkers.

7

Chapter 7. Conclusions

The work presented in this thesis has introduced, developed and validated a novel CT-based method of PVAT characterisation as a method for improved cardiac risk stratification of individuals undergoing clinical CCTA. Building on the observation that coronary inflammation induces phenotypic changes in the adjacent PVAT, where it inhibits adipocyte differentiation and overall adipogenesis, I contributed to the development of a CCTA-based biomarker that captures the resulting spatial gradients in PVAT attenuation, which function as a surrogate marker of coronary inflammation and subclinical atherosclerosis. The biomarker in question, namely the perivascular Fat Attenuation Index, was extensively validated against in vivo and ex vivo CT scans of adipose tissue biopsies, as well as in experimental models of vascular inflammation. Building on this work, my doctoral project sought out to explore the potential diagnostic and prognostic value of this novel method of reading CCTA scans.

Following the natural history of coronary atherosclerosis, I investigated the association between perivascular fat imaging and the progression of coronary atherosclerosis, the presence of unstable lesions associated with acute coronary syndromes, as well as the incidence of hard clinical endpoints such as cardiac-related mortality or non-fatal acute myocardial infarction. In the first part of my thesis (chapter 3), I designed and conducted two single-centre clinical studies that demonstrated the role of perivascular fat phenotyping by means of perivascular FAI mapping to predict the future progression of coronary calcification, as well as the presence of unstable coronary lesions associated with acute myocardial infarction. Of note, a longitudinal study design

with follow-up CCTA scans revealed that perivascular FAI may be a dynamic marker, demonstrating significant changes around a ruptured coronary plaque a few months after the index event. Next (chapter 4), I conducted a post-hoc analysis of prospectively collected data from two large, real-life cohorts of patients undergoing clinical CCTA in two independent centres in Europe and the United States, demonstrating that perivascular FAI mapping detects a residual cardiac-specific risk not identified through common risk factors or the traditional interpretation of CCTA scans. Finally (chapter 5), I designed and applied an image analysis algorithm that captures the full extent of the radiomic heterogeneity in PVAT, thus enabling the detection of advanced fibrotic and vascular remodelling in PVAT, both hallmarks of the high-risk dysfunctional adipose tissue phenotype. Using scans from five different cohorts, I demonstrated that extensive radiomic phenotyping of PVAT may further boost the prognostic value of this approach, by incorporating information related to adipose tissue expansion (obesity), inflammation, fibrosis and microvascular remodelling.

When assessing the clinical value of this project, one needs to consider what was already known before it started and what was discovered during its course. It has long been known that atherosclerosis is an inflammatory disease, but the CANTOS trial, published one year into my DPhil project, provided compelling evidence for the causal role of inflammation in human atherothrombosis, highlighting its role not only as a prognostic marker but also as a therapeutic target [15, 24, 35]. Traditionally measured through the circulating levels of hs-CRP [35], inflammation is a rather generic term that does not necessarily describe a mechanism that is specific to the arterial wall. During the course of my work, several studies identified this unmet need to detect arterial inflammation, focusing on developing advanced molecular radiotracers that can provide a more specific signal from the inflamed vascular wall. This included ^{18}F-NaF, a PET

tracer that binds to areas of active micro-calcification [38, 160], as well as ^{68}Ga-dotatate that binds to receptors predominantly expressed on the surface of the pro-inflammatory M1 macrophages [39, 158]. Nevertheless, these approaches rely on expensive tracers and equipment, whereas PET-CT imaging is often expensive and not widely available. At the same time, the National Institute for Health and Care Excellence (NICE) of the United Kingdom published revised guidelines on the management of stable and unstable chest pain, highlighting the value of CCTA as a 1st line diagnostic test in certain scenarios, thanks to its high sensitivity for detection of CAD as well as low cost and wide availability [45, 46]. As a result, perivascular FAI mapping found itself at the cross-roads of these two major advancements, namely the publication of the CANTOS trial and the new NICE guidelines. Since FAI could offer a potential way of extracting functional information about the inflammatory burden of the coronary tree through a standard CCTA scan, examining its clinical and prognostic value became of the utmost importance. By analysing ~6000 CT scans from six different studies, I demonstrated that CT-based perivascular fat phenotyping detects a residual cardiac risk not detected by other commonly used methods. Even though it was impossible to provide a head-to-head comparison against all other biomarkers in the context of these studies, my findings support that perivascular fat is a rich source of diagnostic and prognostic biomarkers in human cardiovascular disease.

In an effort to explore and understand the phenotypic variation of pericoronary fat, I have attempted to link the CT "radiome" of PVAT with the underlying histological and biological patterns. This has introduced different, yet complementary biomarkers, such as the perivascular FAI that captures the average adipocyte size and lipid content of perivascular adipocytes (which is affected by the local pro- or anti-inflammatory environment) and the Fat Radiomic Profile that looks at the spatial heterogeneity of

PVAT attenuation as a surrogate marker of adipose tissue fibrotic and vascular remodelling. In a longitudinal study design, these biomarkers were found to behave in a different manner, with perivascular FAI decreasing around culprit coronary lesions in AMI patients when measured six months after the index event, while FRP remained unchanged (even showing a non-significant trend towards higher values, possibly reflecting its irreversible nature). These imaging biomarkers attempt to describe the biological and histological profile of the high-risk adipose tissue as it modifies its composition in response to difference stages of the natural history of coronary atherosclerosis. By dissociating risk prediction from the simple presence of a coronary lesions, these markers demonstrate significant incremental value beyond traditional risk factors. Nevertheless, despite their extensive validation in the context of this project, further studies in diverse cohorts may be needed to better understand the performance of these indices in different clinical settings.

One of the main strengths of this project is the fact that it introduces a novel framework and paradigm in non-invasive cardiovascular imaging. It highlights how significant advances can be made (in a cost-effective manner) by maximising the yield of existing imaging tests, rather than introducing new, expensive techniques. This "thinking outside the box" approach has led to the discovery of a new set of diagnostic and prognostic biomarkers that had been hiding in plain sight. However, this discovery was not random, but was informed by observations made in the laboratory and through extensive phenotyping of tissue samples from numerous research participants. This "bench-to-bedside" approach showcases how basic and clinical sciences can converge to facilitate advances in medicine and provides an example for future studies aiming to identify novel cardiometabolic risk biomarkers.

Along these lines, the introduction of the concept of the bidirectional interplay between adipose tissue and the cardiovascular system has identified a number of exciting projects for the future. For instance, could the peri-left atrial adipose tissue phenotype be a marker of adverse left atrial remodelling and biology that can initiate and sustain arrhythmias such as atrial fibrillation? Could peri-carotid adipose tissue phenotype flag an unstable carotid plaque phenotype? Is peri-aortic fat a potential marker of aortic aneurysm formation and rapid progression? Given the well-established role of CT imaging in a range of cardiovascular conditions, our group will aim to address these hypotheses by designing retrospective as well as prospective studies, in an attempt to link the adipose tissue radiomic phenotype in these depots to the underlying biology and clinical profile of study participants. These approaches will also benefit from the introduction of proteomic analysis methods that can facilitate the links between imaging and tissue composition, as well as the acquisition of large datasets obtained through national electronic health records and image archiving systems in future studies.

Perhaps the most promising message of this doctoral project is the demonstration of how quantitative, radiomic approaches, such as the ones discussed in this thesis, can advance non-invasive cardiovascular imaging, potentially improving the performance of healthcare pathways for both patients and medical professionals (Figure 7.1). The interpretation of CT scans, including CCTAs, has traditionally relied on the detection of macroscopic abnormalities by a trained human analyst/clinician. By combining clinical and other related information with the CT images, medical professionals are expected to reach a diagnostic conclusion and offer a management plan. However, this approach is limited to the information that can be visualised by the naked eye and is also subject to several kinds of bias.

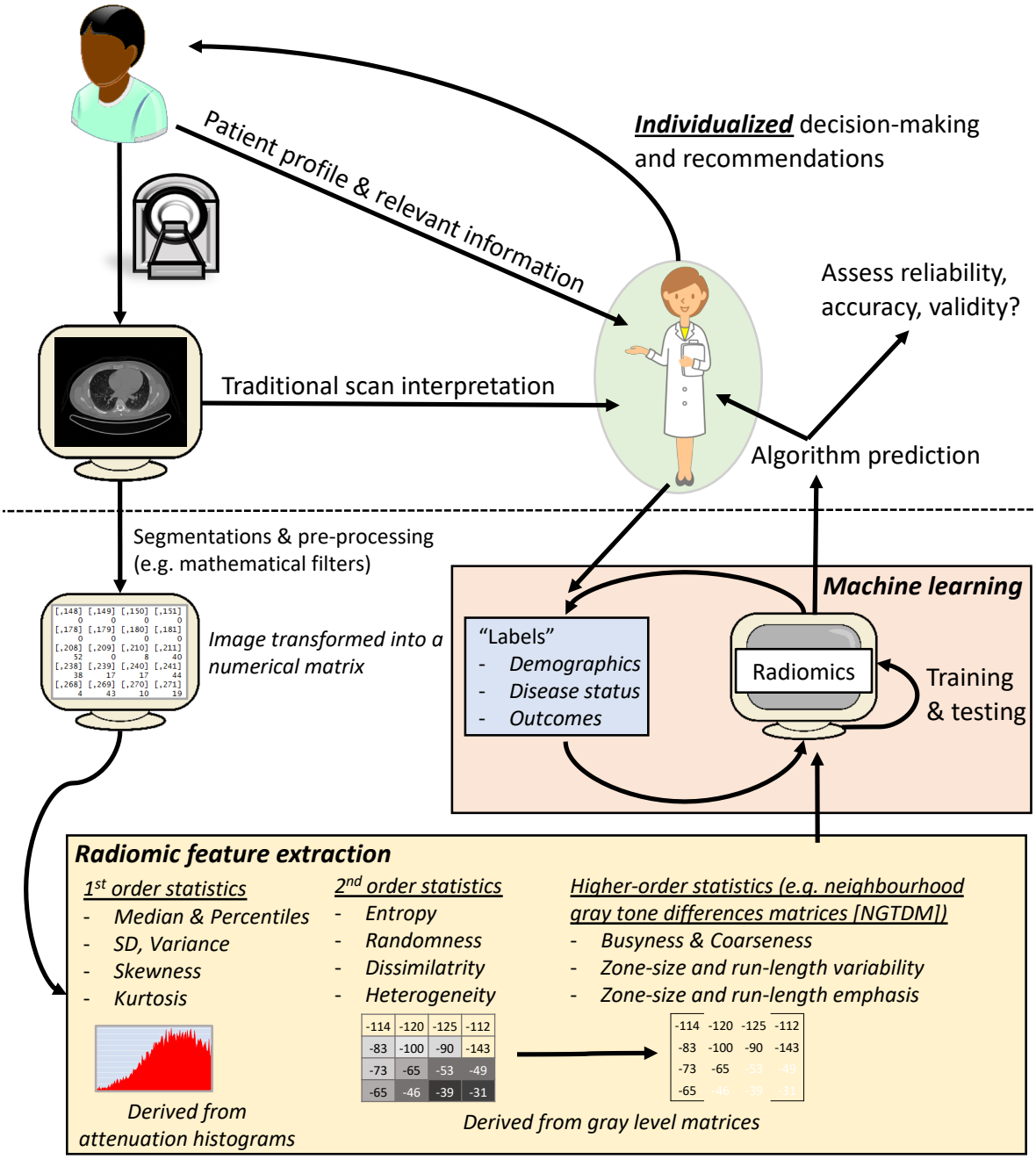

Figure 7.1. Integration of computed tomography radiomic approaches into a clinical workflow. *A proposed workflow for the incorporation of machine learning-powered radiomic analysis of cardiac computed tomography scans into clinical practice. Radiomic analysis can reduce the analysis time and when integrated with electronic health records can provide automated recommendations to the physician regarding diagnosis and patient prognosis. At this stage, artificial and human intelligence can converge to enable the physician to select the optimal management plan based on all available data.*

As hypothesised and discussed in this thesis, a radiomic approach that identifies invisible high- or low-risk patterns in the imaging data, whether that is the perivascular fat or a lung tumor, can now be used to supplement the traditional clinical assessment with a deeper phenotyping of a patient's anatomy. Thanks to advances in the available computational power, this process can now be performed within a few seconds and can also be integrated with electronic health records, thus providing automated recommendations to the physician regarding diagnosis and patient prognosis. At this stage, artificial and human intelligence can converge to enable the physician to select the optimal management plan based on all available data, which now includes both their traditional interpretation of the CT scan as well as a deeper "phenotyping" of the data. Such approaches may transform the structure of modern healthcare, by relieving the physician from time-consuming image processing tasks, maximising the diagnostic and prognostic yield of existing diagnostic tests and catalysing the transition towards a more personalised model of care.

8

References

1. Oikonomou, E.K. and C. Antoniades, *The role of adipose tissue in cardiovascular health and disease.* Nat Rev Cardiol, 2019. **16**(2): p. 83-99.

2. Oikonomou, E.K. and C. Antoniades, *Immunometabolic Regulation of Vascular Redox State: The Role of Adipose Tissue.* Antioxid Redox Signal, 2018. **29**(3): p. 313-337.

3. Oikonomou, E.K., H.W. West, and C. Antoniades, *Computed Tomography: Assessment of Coronary Inflammation and Other Plaque Features.* Arterioscler Thromb Vasc Biol, 2019: p. ATVBAHA119312899.

4. Oikonomou, E.K., M. Siddique, and C. Antoniades, *Artificial intelligence in medical imaging: A radiomic guide to precision phenotyping of cardiovascular disease.* Cardiovasc Res, 2020.

5. *British Heart Foundation Heart Statistics 2018*. [cited 2019 26/02/2019]; Available from: https://www.bhf.org.uk/what-we-do/our-research/heart-statistics.

6. Benjamin, E.J., S.S. Virani, C.W. Callaway, A.M. Chamberlain, A.R. Chang, S. Cheng, S.E. Chiuve, M. Cushman, F.N. Delling, R. Deo, S.D. de Ferranti, J.F. Ferguson, M. Fornage, C. Gillespie, C.R. Isasi, M.C. Jimenez, L.C. Jordan, S.E. Judd, D. Lackland, J.H. Lichtman, L. Lisabeth, S. Liu, C.T. Longenecker, P.L. Lutsey, J.S. Mackey, D.B. Matchar, K. Matsushita, M.E. Mussolino, K. Nasir, M. O'Flaherty, L.P. Palaniappan, A. Pandey, D.K. Pandey, M.J. Reeves, M.D. Ritchey, C.J. Rodriguez, G.A. Roth, W.D. Rosamond, U.K.A. Sampson, G.M. Satou, S.H. Shah, N.L. Spartano, D.L. Tirschwell, C.W. Tsao, J.H. Voeks, J.Z. Willey, J.T. Wilkins, J.H. Wu, H.M. Alger, S.S. Wong, P. Muntner, E. American Heart Association Council on, C. Prevention Statistics, and S. Stroke Statistics, *Heart Disease and Stroke Statistics-2018 Update: A Report From the American Heart Association.* Circulation, 2018. **137**(12): p. e67-e492.

7. Goff, D.C., Jr., D.M. Lloyd-Jones, G. Bennett, S. Coady, R.B. D'Agostino, Sr., R. Gibbons, P. Greenland, D.T. Lackland, D. Levy, C.J. O'Donnell, J.G. Robinson, J.S. Schwartz, S.T. Shero, S.C. Smith, Jr., P. Sorlie, N.J. Stone, P.W. Wilson, and G. American College of Cardiology/American Heart Association Task Force on Practice, *2013 ACC/AHA guideline on the assessment of cardiovascular risk: a report of the American College of Cardiology/American Heart Association Task Force on Practice Guidelines.* J Am Coll Cardiol, 2014. **63**(25 Pt B): p. 2935-59.

8. Muntner, P., L.D. Colantonio, M. Cushman, D.C. Goff, Jr., G. Howard, V.J. Howard, B. Kissela, E.B. Levitan, D.M. Lloyd-Jones, and M.M. Safford, *Validation of the atherosclerotic cardiovascular disease Pooled Cohort risk equations.* JAMA, 2014. **311**(14): p. 1406-15.

9. Rana, J.S., G.H. Tabada, M.D. Solomon, J.C. Lo, M.G. Jaffe, S.H. Sung, C.M. Ballantyne, and A.S. Go, *Accuracy of the Atherosclerotic Cardiovascular Risk Equation in a Large Contemporary, Multiethnic Population.* J Am Coll Cardiol, 2016. **67**(18): p. 2118-2130.

10. Stone, N.J., J.G. Robinson, A.H. Lichtenstein, C.N. Bairey Merz, C.B. Blum, R.H. Eckel, A.C. Goldberg, D. Gordon, D. Levy, D.M. Lloyd-Jones, P. McBride, J.S. Schwartz, S.T. Shero, S.C. Smith, Jr., K. Watson, P.W. Wilson, and G. American College of Cardiology/American Heart Association Task Force on Practice, *2013 ACC/AHA guideline on the treatment of blood cholesterol to reduce atherosclerotic cardiovascular risk in adults: a report of the American College of Cardiology/American Heart Association Task Force on Practice Guidelines.* J Am Coll Cardiol, 2014. **63**(25 Pt B): p. 2889-934.

11. Greenland, P., L. LaBree, S.P. Azen, T.M. Doherty, and R.C. Detrano, *Coronary artery calcium score combined with Framingham score for risk prediction in asymptomatic individuals.* JAMA., 2004. **291**(2): p. 210-5.

12. Greenland, P., J.S. Alpert, G.A. Beller, E.J. Benjamin, M.J. Budoff, Z.A. Fayad, E. Foster, M.A. Hlatky, J.M. Hodgson, F.G. Kushner, M.S. Lauer, L.J. Shaw, S.C. Smith, Jr., A.J. Taylor, W.S. Weintraub, N.K. Wenger, A.K. Jacobs, and G. American College of Cardiology Foundation/American Heart Asscoiation Tasl Force on Practice, *2010 ACCF/AHA guideline for assessment of cardiovascular risk in asymptomatic adults: executive summary: a report of the American College of Cardiology Foundation/American Heart Association Task Force on Practice Guidelines.* Circulation, 2010. **122**(25): p. 2748-64.

13. Task Force, M., G. Montalescot, U. Sechtem, S. Achenbach, F. Andreotti, C. Arden, A. Budaj, R. Bugiardini, F. Crea, T. Cuisset, C. Di Mario, J.R. Ferreira, B.J. Gersh, A.K. Gitt, J.S. Hulot, N. Marx, L.H. Opie, M. Pfisterer, E. Prescott, F. Ruschitzka, M. Sabate, R. Senior, D.P. Taggart, E.E. van der Wall, C.J. Vrints, E.S.C.C.f.P. Guidelines, J.L. Zamorano, S. Achenbach, H. Baumgartner, J.J. Bax, H. Bueno, V. Dean, C. Deaton, C. Erol, R. Fagard, R. Ferrari, D. Hasdai, A.W. Hoes, P. Kirchhof, J. Knuuti, P. Kolh, P. Lancellotti, A. Linhart, P. Nihoyannopoulos, M.F. Piepoli, P. Ponikowski, P.A. Sirnes, J.L. Tamargo, M. Tendera, A. Torbicki, W. Wijns, S. Windecker, R. Document, J. Knuuti, M. Valgimigli, H. Bueno, M.J. Claeys, N. Donner-Banzhoff, C. Erol, H. Frank, C. Funck-Brentano, O. Gaemperli, J.R. Gonzalez-Juanatey, M. Hamilos, D. Hasdai, S. Husted, S.K. James, K. Kervinen, P. Kolh, S.D. Kristensen, P. Lancellotti, A.P. Maggioni, M.F. Piepoli, A.R. Pries, F. Romeo, L. Ryden, M.L. Simoons, P.A. Sirnes, P.G. Steg, A. Timmis, W. Wijns, S. Windecker, A. Yildirir, and J.L. Zamorano, *2013 ESC guidelines on the management of stable coronary artery disease: the Task Force on the management of stable coronary artery disease of the European Society of Cardiology.* Eur Heart J, 2013. **34**(38): p. 2949-3003.

14. Patel, K.V., A. Pandey, and J.A. de Lemos, *Conceptual Framework for Addressing Residual Atherosclerotic Cardiovascular Disease Risk in the Era of Precision Medicine.* Circulation, 2018. **137**(24): p. 2551-2553.

15. Ridker, P.M., B.M. Everett, T. Thuren, J.G. MacFadyen, W.H. Chang, C. Ballantyne, F. Fonseca, J. Nicolau, W. Koenig, S.D. Anker, J.J.P. Kastelein, J.H. Cornel, P. Pais, D. Pella, J. Genest, R. Cifkova, A. Lorenzatti, T. Forster, Z. Kobalava, L. Vida-Simiti, M. Flather, H. Shimokawa, H. Ogawa, M. Dellborg, P.R.F. Rossi, R.P.T. Troquay, P. Libby,

R.J. Glynn, and C.T. Group, *Antiinflammatory Therapy with Canakinumab for Atherosclerotic Disease.* N Engl J Med, 2017. **377**: p. 1119-1131.

16. Sabatine, M.S., R.P. Giugliano, A.C. Keech, N. Honarpour, S.D. Wiviott, S.A. Murphy, J.F. Kuder, H. Wang, T. Liu, S.M. Wasserman, P.S. Sever, T.R. Pedersen, F.S. Committee, and Investigators, *Evolocumab and Clinical Outcomes in Patients with Cardiovascular Disease.* N Engl J Med, 2017. **376**(18): p. 1713-1722.

17. Schwartz, G.G., P.G. Steg, M. Szarek, D.L. Bhatt, V.A. Bittner, R. Diaz, J.M. Edelberg, S.G. Goodman, C. Hanotin, R.A. Harrington, J.W. Jukema, G. Lecorps, K.W. Mahaffey, A. Moryusef, R. Pordy, K. Quintero, M.T. Roe, W.J. Sasiela, J.F. Tamby, P. Tricoci, H.D. White, A.M. Zeiher, O.O. Committees, and Investigators, *Alirocumab and Cardiovascular Outcomes after Acute Coronary Syndrome.* N Engl J Med, 2018. **379**(22): p. 2097-2107.

18. Bhatt, D.L., P.G. Steg, M. Miller, E.A. Brinton, T.A. Jacobson, S.B. Ketchum, R.T. Doyle, Jr., R.A. Juliano, L. Jiao, C. Granowitz, J.C. Tardif, C.M. Ballantyne, and R.-I. Investigators, *Cardiovascular Risk Reduction with Icosapent Ethyl for Hypertriglyceridemia.* N Engl J Med, 2019. **380**(1): p. 11-22.

19. Marso, S.P., G.H. Daniels, K. Brown-Frandsen, P. Kristensen, J.F. Mann, M.A. Nauck, S.E. Nissen, S. Pocock, N.R. Poulter, L.S. Ravn, W.M. Steinberg, M. Stockner, B. Zinman, R.M. Bergenstal, J.B. Buse, L.S. Committee, and L.T. Investigators, *Liraglutide and Cardiovascular Outcomes in Type 2 Diabetes.* N Engl J Med, 2016. **375**(4): p. 311-22.

20. Neal, B., V. Perkovic, K.W. Mahaffey, D. de Zeeuw, G. Fulcher, N. Erondu, W. Shaw, G. Law, M. Desai, D.R. Matthews, and C.P.C. Group, *Canagliflozin and Cardiovascular and Renal Events in Type 2 Diabetes.* N Engl J Med, 2017. **377**(7): p. 644-657.

21. Mauri, L., D.J. Kereiakes, R.W. Yeh, P. Driscoll-Shempp, D.E. Cutlip, P.G. Steg, S.L. Normand, E. Braunwald, S.D. Wiviott, D.J. Cohen, D.R. Holmes, Jr., M.W. Krucoff, J. Hermiller, H.L. Dauerman, D.I. Simon, D.E. Kandzari, K.N. Garratt, D.P. Lee, T.K. Pow, P. Ver Lee, M.J. Rinaldi, J.M. Massaro, and D.S. Investigators, *Twelve or 30 months of dual antiplatelet therapy after drug-eluting stents.* N Engl J Med, 2014. **371**(23): p. 2155-66.

22. Eikelboom, J.W., S.J. Connolly, J. Bosch, G.R. Dagenais, R.G. Hart, O. Shestakovska, R. Diaz, M. Alings, E.M. Lonn, S.S. Anand, P. Widimsky, M. Hori, A. Avezum, L.S. Piegas, K.R.H. Branch, J. Probstfield, D.L. Bhatt, J. Zhu, Y. Liang, A.P. Maggioni, P. Lopez-Jaramillo, M. O'Donnell, A.K. Kakkar, K.A.A. Fox, A.N. Parkhomenko, G. Ertl, S. Stork, M. Keltai, L. Ryden, N. Pogosova, A.L. Dans, F. Lanas, P.J. Commerford, C. Torp-Pedersen, T.J. Guzik, P.B. Verhamme, D. Vinereanu, J.H. Kim, A.M. Tonkin, B.S. Lewis, C. Felix, K. Yusoff, P.G. Steg, K.P. Metsarinne, N. Cook Bruns, F. Misselwitz, E. Chen, D. Leong, S. Yusuf, and C. Investigators, *Rivaroxaban with or without Aspirin in Stable Cardiovascular Disease.* N Engl J Med, 2017. **377**(14): p. 1319-1330.

23. Cannon, C.P., M.A. Blazing, R.P. Giugliano, A. McCagg, J.A. White, P. Theroux, H. Darius, B.S. Lewis, T.O. Ophuis, J.W. Jukema, G.M. De Ferrari, W. Ruzyllo, P. De Lucca, K. Im, E.A. Bohula, C. Reist, S.D. Wiviott, A.M. Tershakovec, T.A. Musliner, E. Braunwald, R.M. Califf, and I.-I. Investigators, *Ezetimibe Added to Statin Therapy after Acute Coronary Syndromes.* N Engl J Med, 2015. **372**(25): p. 2387-97.

24. Sehested, T.S.G., J. Bjerre, S. Ku, A. Chang, A. Jahansouz, D.K. Owens, M.A. Hlatky, and J.D. Goldhaber-Fiebert, *Cost-effectiveness of Canakinumab for Prevention of Recurrent Cardiovascular Events.* JAMA Cardiol, 2019. **4**(2): p. 128-135.

25. Libby, P., J. Loscalzo, P.M. Ridker, M.E. Farkouh, P.Y. Hsue, V. Fuster, A.A. Hasan, and S. Amar, *Inflammation, Immunity, and Infection in Atherothrombosis: JACC Review Topic of the Week.* J Am Coll Cardiol, 2018. **72**(17): p. 2071-2081.

26. Jonasson, L., J. Holm, O. Skalli, G. Bondjers, and G.K. Hansson, *Regional accumulations of T cells, macrophages, and smooth muscle cells in the human atherosclerotic plaque.* Arteriosclerosis, 1986. **6**(2): p. 131-8.

27. Tsukada, T., M. Rosenfeld, R. Ross, and A.M. Gown, *Immunocytochemical analysis of cellular components in atherosclerotic lesions. Use of monoclonal antibodies with the Watanabe and fat-fed rabbit.* Arteriosclerosis, 1986. **6**(6): p. 601-13.

28. Libby, P. and G.K. Hansson, *Inflammation and immunity in diseases of the arterial tree: players and layers.* Circ Res, 2015. **116**(2): p. 307-11.

29. Grebe, A., F. Hoss, and E. Latz, *NLRP3 Inflammasome and the IL-1 Pathway in Atherosclerosis.* Circ Res, 2018. **122**(12): p. 1722-1740.

30. Bobryshev, Y.V., E.A. Ivanova, D.A. Chistiakov, N.G. Nikiforov, and A.N. Orekhov, *Macrophages and Their Role in Atherosclerosis: Pathophysiology and Transcriptome Analysis.* Biomed Res Int, 2016. **2016**: p. 9582430.

31. Hansson, G.K., P. Libby, and I. Tabas, *Inflammation and plaque vulnerability.* J Intern Med, 2015. **278**(5): p. 483-93.

32. Ridker, P.M., N. Rifai, L. Rose, J.E. Buring, and N.R. Cook, *Comparison of C-reactive protein and low-density lipoprotein cholesterol levels in the prediction of first cardiovascular events.* N Engl J Med, 2002. **347**(20): p. 1557-65.

33. Ridker, P.M., C.H. Hennekens, J.E. Buring, and N. Rifai, *C-reactive protein and other markers of inflammation in the prediction of cardiovascular disease in women.* N Engl J Med, 2000. **342**(12): p. 836-43.

34. Ridker, P.M., E. Danielson, F.A. Fonseca, J. Genest, A.M. Gotto, Jr., J.J. Kastelein, W. Koenig, P. Libby, A.J. Lorenzatti, J.G. MacFadyen, B.G. Nordestgaard, J. Shepherd, J.T. Willerson, R.J. Glynn, and J.S. Group, *Rosuvastatin to prevent vascular events in men and women with elevated C-reactive protein.* N Engl J Med, 2008. **359**(21): p. 2195-207.

35. Ridker, P.M., J.G. MacFadyen, B.M. Everett, P. Libby, T. Thuren, R.J. Glynn, and C.T. Group, *Relationship of C-reactive protein reduction to cardiovascular event reduction following treatment with canakinumab: a secondary analysis from the CANTOS randomised controlled trial.* Lancet, 2018. **391**(10118): p. 319-328.

36. Sproston, N.R. and J.J. Ashworth, *Role of C-Reactive Protein at Sites of Inflammation and Infection.* Front Immunol, 2018. **9**: p. 754.

37. Skagen, K., K. Johnsrud, K. Evensen, H. Scott, K. Krohg-Sorensen, F. Reier-Nilsen, M.E. Revheim, J.G. Fjeld, M. Skjelland, and D. Russell, *Carotid plaque inflammation assessed with (18)F-FDG PET/CT is higher in symptomatic compared with asymptomatic patients.* Int J Stroke, 2015. **10**(5): p. 730-6.

38. Joshi, N.V., A.T. Vesey, M.C. Williams, A.S. Shah, P.A. Calvert, F.H. Craighead, S.E. Yeoh, W. Wallace, D. Salter, A.M. Fletcher, E.J. van Beek, A.D. Flapan, N.G. Uren, M.W. Behan, N.L. Cruden, N.L. Mills, K.A. Fox, J.H. Rudd, M.R. Dweck, and D.E. Newby, *18F-fluoride positron emission tomography for identification of ruptured and high-risk coronary atherosclerotic plaques: a prospective clinical trial.* Lancet, 2014. **383**(9918): p. 705-13.

39. Tarkin, J.M., F.R. Joshi, N.R. Evans, M.M. Chowdhury, N.L. Figg, A.V. Shah, L.T. Starks, A. Martin-Garrido, R. Manavaki, E. Yu, R.E. Kuc, L. Grassi, R. Kreuzhuber, M.A. Kostadima, M. Frontini, P.J. Kirkpatrick, P.A. Coughlin, D. Gopalan, T.D. Fryer, J.R. Buscombe, A.M. Groves, W.H. Ouwehand, M.R. Bennett, E.A. Warburton, A.P. Davenport, and J.H. Rudd, *Detection of Atherosclerotic Inflammation by (68)Ga-DOTATATE PET Compared to [(18)F]FDG PET Imaging.* J Am Coll Cardiol, 2017. **69**(14): p. 1774-1791.

40. Montalescot, G., U. Sechtem, S. Achenbach, F. Andreotti, C. Arden, A. Budaj, R. Bugiardini, F. Crea, T. Cuisset, C. Di Mario, J.R. Ferreira, B.J. Gersh, A.K. Gitt, J.S. Hulot, N. Marx, L.H. Opie, M. Pfisterer, E. Prescott, F. Ruschitzka, M. Sabate, R. Senior, D.P. Taggart, E.E. van der Wall, C.J. Vrints, J.L. Zamorano, S. Achenbach, H. Baumgartner, J.J. Bax, H. Bueno, V. Dean, C. Deaton, C. Erol, R. Fagard, R. Ferrari, D. Hasdai, A.W. Hoes, P. Kirchhof, J. Knuuti, P. Kolh, P. Lancellotti, A. Linhart, P. Nihoyannopoulos, M.F. Piepoli, P. Ponikowski, P.A. Sirnes, J.L. Tamargo, M. Tendera, A. Torbicki, W. Wijns, S. Windecker, J. Knuuti, M. Valgimigli, H. Bueno, M.J. Claeys, N. Donner-Banzhoff, C. Erol, H. Frank, C. Funck-Brentano, O. Gaemperli, J.R. Gonzalez-Juanatey, M. Hamilos, D. Hasdai, S. Husted, S.K. James, K. Kervinen, P. Kolh, S.D. Kristensen, P. Lancellotti, A.P. Maggioni, M.F. Piepoli, A.R. Pries, F. Romeo, L. Ryden, M.L. Simoons, P.A. Sirnes, P.G. Steg, A. Timmis, W. Wijns, S. Windecker, A. Yildirir, and J.L. Zamorano, *2013 ESC guidelines on the management of stable coronary artery disease: the Task Force on the management of stable coronary artery disease of the European Society of Cardiology.* Eur Heart J, 2013. **34**(38): p. 2949-3003.

41. Douglas, P.S., U. Hoffmann, M.R. Patel, D.B. Mark, H.R. Al-Khalidi, B. Cavanaugh, J. Cole, R.J. Dolor, C.B. Fordyce, M. Huang, M.A. Khan, A.S. Kosinski, M.W. Krucoff, V. Malhotra, M.H. Picard, J.E. Udelson, E.J. Velazquez, E. Yow, L.S. Cooper, K.L. Lee, and P. Investigators, *Outcomes of anatomical versus functional testing for coronary artery disease.* N Engl J Med, 2015. **372**(14): p. 1291-300.

42. SCOT-HEART Investigators, *CT coronary angiography in patients with suspected angina due to coronary heart disease (SCOT-HEART): an open-label, parallel-group, multicentre trial.* Lancet, 2015. **385**(9985): p. 2383-91.

43. SCOT-HEART Investigators, *Coronary CT Angiography and 5-Year Risk of Myocardial Infarction.* N Engl J Med, 2018. **379**(10): p. 924-933.

44. Hoffmann, U., Q.A. Truong, D.A. Schoenfeld, E.T. Chou, P.K. Woodard, J.T. Nagurney, J.H. Pope, T.H. Hauser, C.S. White, S.G. Weiner, S. Kalanjian, M.E. Mullins, I. Mikati, W.F. Peacock, P. Zakroysky, D. Hayden, A. Goehler, H. Lee, G.S. Gazelle, S.D. Wiviott, J.L. Fleg, J.E. Udelson, and R.-I. Investigators, *Coronary CT angiography versus standard evaluation in acute chest pain.* N Engl J Med, 2012. **367**(4): p. 299-308.

45. National Institute for Health and Care Excellence (NICE), *Chest pain of recent onset: assessment and diagnosis.* Clinical guideline [CG95], 2016.

46. Moss, A.J., M.C. Williams, D.E. Newby, and E.D. Nicol, *The Updated NICE Guidelines: Cardiac CT as the First-Line Test for Coronary Artery Disease.* Curr Cardiovasc Imaging Rep, 2017. **10**(5): p. 15.

47. Knuuti, J., W. Wijns, A. Saraste, D. Capodanno, E. Barbato, C. Funck-Brentano, E. Prescott, R.F. Storey, C. Deaton, T. Cuisset, S. Agewall, K. Dickstein, T. Edvardsen, J. Escaned, B.J. Gersh, P. Svitil, M. Gilard, D. Hasdai, R. Hatala, F. Mahfoud, J. Masip, C. Muneretto, M. Valgimigli, S. Achenbach, J.J. Bax, and E.S.C.S.D. Group, *2019 ESC Guidelines for the diagnosis and management of chronic coronary syndromes.* Eur Heart J, 2019.

48. Leipsic, J., S. Abbara, S. Achenbach, R. Cury, J.P. Earls, G.J. Mancini, K. Nieman, G. Pontone, and G.L. Raff, *SCCT guidelines for the interpretation and reporting of coronary CT angiography: a report of the Society of Cardiovascular Computed Tomography Guidelines Committee.* J Cardiovasc Comput Tomogr, 2014. **8**(5): p. 342-58.

49. Maddox, T.M., M.A. Stanislawski, G.K. Grunwald, S.M. Bradley, P.M. Ho, T.T. Tsai, M.R. Patel, A. Sandhu, J. Valle, D.J. Magid, B. Leon, D.L. Bhatt, S.D. Fihn, and J.S. Rumsfeld, *Nonobstructive coronary artery disease and risk of myocardial infarction.* JAMA, 2014. **312**(17): p. 1754-63.

50. Min, J.K., L.J. Shaw, R.B. Devereux, P.M. Okin, J.W. Weinsaft, D.J. Russo, N.J. Lippolis, D.S. Berman, and T.Q. Callister, *Prognostic value of multidetector coronary computed tomographic angiography for prediction of all-cause mortality.* J Am Coll Cardiol, 2007. **50**(12): p. 1161-70.

51. Hadamitzky, M., S. Achenbach, M. Al-Mallah, D. Berman, M. Budoff, F. Cademartiri, T. Callister, H.J. Chang, V. Cheng, K. Chinnaiyan, B.J. Chow, R. Cury, A. Delago, A. Dunning, G. Feuchtner, M. Gomez, P. Kaufmann, Y.J. Kim, J. Leipsic, F.Y. Lin, E. Maffei, J.K. Min, G. Raff, L.J. Shaw, T.C. Villines, J. Hausleiter, and C. Investigators, *Optimized prognostic score for coronary computed tomographic angiography: results from the CONFIRM registry (COronary CT Angiography EvaluatioN For Clinical Outcomes: An InteRnational Multicenter Registry).* J Am Coll Cardiol, 2013. **62**(5): p. 468-76.

52. Fishbein, M.C. and R.J. Siegel, *How Big Are Coronary Atherosclerotic Plaques That Rupture?* Circulation, 1996. **94**(10): p. 2662-2666.

53. Detrano, R., A.D. Guerci, J.J. Carr, D.E. Bild, G. Burke, A.R. Folsom, K. Liu, S. Shea, M. Szklo, D.A. Bluemke, D.H. O'Leary, R. Tracy, K. Watson, N.D. Wong, and R.A. Kronmal, *Coronary calcium as a predictor of coronary events in four racial or ethnic groups.* N Engl J Med, 2008. **358**(13): p. 1336-45.

54. Budoff, M.J., R. Young, V.A. Lopez, R.A. Kronmal, K. Nasir, R.S. Blumenthal, R.C. Detrano, D.E. Bild, A.D. Guerci, K. Liu, S. Shea, M. Szklo, W. Post, J. Lima, A. Bertoni, and N.D. Wong, *Progression of coronary calcium and incident coronary heart disease events: MESA (Multi-Ethnic Study of Atherosclerosis).* J Am Coll Cardiol, 2013. **61**(12): p. 1231-9.

55. Puri, R., S.J. Nicholls, M. Shao, Y. Kataoka, K. Uno, S.R. Kapadia, E.M. Tuzcu, and S.E. Nissen, *Impact of statins on serial coronary calcification during atheroma progression and regression.* J Am Coll Cardiol, 2015. **65**(13): p. 1273-1282.

56. Zeb, I., D. Li, K. Nasir, J. Malpeso, A. Batool, F. Flores, C. Dailing, R.P. Karlsberg, and M. Budoff, *Effect of statin treatment on coronary plaque progression - a serial coronary CT angiography study.* Atherosclerosis, 2013. **231**(2): p. 198-204.

57. Obaid, D.R., P.A. Calvert, D. Gopalan, R.A. Parker, S.P. Hoole, N.E. West, M. Goddard, J.H. Rudd, and M.R. Bennett, *Atherosclerotic plaque composition and classification identified by coronary computed tomography: assessment of computed tomography-generated plaque maps compared with virtual histology intravascular ultrasound and histology.* Circ Cardiovasc Imaging, 2013. **6**(5): p. 655-64.

58. Liu, T., P. Maurovich-Horvat, T. Mayrhofer, S.B. Puchner, M.T. Lu, K. Ghemigian, P.H. Kitslaar, A. Broersen, A. Pursnani, U. Hoffmann, and M. Ferencik, *Quantitative coronary plaque analysis predicts high-risk plaque morphology on coronary computed tomography angiography: results from the ROMICAT II trial.* Int J Cardiovasc Imaging, 2018. **34**(2): p. 311-319.

59. Cury, R.C., S. Abbara, S. Achenbach, A. Agatston, D.S. Berman, M.J. Budoff, K.E. Dill, J.E. Jacobs, C.D. Maroules, G.D. Rubin, F.J. Rybicki, U.J. Schoepf, L.J. Shaw, A.E. Stillman, C.S. White, P.K. Woodard, and J.A. Leipsic, *CAD-RADS(TM) Coronary Artery Disease - Reporting and Data System. An expert consensus document of the Society of Cardiovascular Computed Tomography (SCCT), the American College of Radiology (ACR) and the North American Society for Cardiovascular Imaging (NASCI). Endorsed by the American College of Cardiology.* J Cardiovasc Comput Tomogr, 2016. **10**(4): p. 269-81.

60. Puchner, S.B., T. Liu, T. Mayrhofer, Q.A. Truong, H. Lee, J.L. Fleg, J.T. Nagurney, J.E. Udelson, U. Hoffmann, and M. Ferencik, *High-risk plaque detected on coronary CT angiography predicts acute coronary syndromes independent of significant stenosis in acute chest pain: results from the ROMICAT-II trial.* J Am Coll Cardiol, 2014. **64**(7): p. 684-92.

61. Kashiwagi, M., A. Tanaka, H. Kitabata, H. Tsujioka, H. Kataiwa, K. Komukai, T. Tanimoto, K. Takemoto, S. Takarada, T. Kubo, K. Hirata, N. Nakamura, M. Mizukoshi, T. Imanishi, and T. Akasaka, *Feasibility of noninvasive assessment of thin-cap fibroatheroma by multidetector computed tomography.* JACC Cardiovasc Imaging, 2009. **2**(12): p. 1412-9.

62. Motoyama, S., M. Sarai, H. Harigaya, H. Anno, K. Inoue, T. Hara, H. Naruse, J. Ishii, H. Hishida, N.D. Wong, R. Virmani, T. Kondo, Y. Ozaki, and J. Narula, *Computed tomographic angiography characteristics of atherosclerotic plaques subsequently resulting in acute coronary syndrome.* J Am Coll Cardiol, 2009. **54**(1): p. 49-57.

63. Yang, D.H., S.J. Kang, H.J. Koo, M. Chang, J.W. Kang, T.H. Lim, S. Baek, S. Han, P.H. Lee, J.H. Roh, J.M. Ahn, D.W. Park, S.W. Lee, C.W. Lee, S.W. Park, S.J. Park, G.S. Mintz, and Y.H. Kim, *Coronary CT angiography characteristics of OCT-defined thin-cap fibroatheroma: a section-to-section comparison study.* Eur Radiol, 2018. **28**(2): p. 833-843.

64. Kim, U., J.A. Leipsic, S.L. Sellers, M. Shao, P. Blanke, M. Hadamitzky, Y.J. Kim, E. Conte, D. Andreini, G. Pontone, M.J. Budoff, I. Gottlieb, B.K. Lee, E.J. Chun, F. Cademartiri, E. Maffei, H. Marques, S. Shin, J.H. Choi, R. Virmani, H. Samady, P.H. Stone, D.S. Berman, J. Narula, L.J. Shaw, J.J. Bax, J.K. Min, and H.J. Chang, *Natural History of Diabetic Coronary Atherosclerosis by Quantitative Measurement of Serial Coronary Computed Tomographic Angiography: Results of the PARADIGM Study (Progression of Atherosclerotic Plaque Determined by Computed Tomographic Angiography Imaging).* JACC Cardiovasc Imaging, 2018.

65. Lee, S.E., H.J. Chang, J.M. Sung, H.B. Park, R. Heo, A. Rizvi, F.Y. Lin, A. Kumar, M. Hadamitzky, Y.J. Kim, E. Conte, D. Andreini, G. Pontone, M.J. Budoff, I. Gottlieb, B.K. Lee, E.J. Chun, F. Cademartiri, E. Maffei, H. Marques, J.A. Leipsic, S. Shin, J.H. Choi, K. Chinnaiyan, G. Raff, R. Virmani, H. Samady, P.H. Stone, D.S. Berman, J. Narula, L.J. Shaw, J.J. Bax, and J.K. Min, *Effects of Statins on Coronary Atherosclerotic Plaques: The PARADIGM (Progression of AtheRosclerotic PlAque DetermIned by Computed TomoGraphic Angiography Imaging) Study.* JACC Cardiovasc Imaging, 2018.

66. Galis, Z.S. and J.J. Khatri, *Matrix metalloproteinases in vascular remodeling and atherogenesis: the good, the bad, and the ugly.* Circ Res, 2002. **90**(3): p. 251-62.

67. Fleg, J.L., G.W. Stone, Z.A. Fayad, J.F. Granada, T.S. Hatsukami, F.D. Kolodgie, J. Ohayon, R. Pettigrew, M.S. Sabatine, G.J. Tearney, S. Waxman, M.J. Domanski, P.R. Srinivas, and J. Narula, *Detection of high-risk atherosclerotic plaque: report of the NHLBI Working Group on current status and future directions.* JACC Cardiovasc Imaging, 2012. **5**(9): p. 941-55.

68. Maurovich-Horvat, P., M. Ferencik, S. Voros, B. Merkely, and U. Hoffmann, *Comprehensive plaque assessment by coronary CT angiography.* Nat Rev Cardiol, 2014. **11**(7): p. 390-402.

69. Aikawa, E., M. Nahrendorf, J.L. Figueiredo, F.K. Swirski, T. Shtatland, R.H. Kohler, F.A. Jaffer, M. Aikawa, and R. Weissleder, *Osteogenesis associates with inflammation in early-stage atherosclerosis evaluated by molecular imaging in vivo.* Circulation, 2007. **116**(24): p. 2841-50.

70. Min, J.K., J. Leipsic, M.J. Pencina, D.S. Berman, B.K. Koo, C. van Mieghem, A. Erglis, F.Y. Lin, A.M. Dunning, P. Apruzzese, M.J. Budoff, J.H. Cole, F.A. Jaffer, M.B. Leon, J. Malpeso, G.B. Mancini, S.J. Park, R.S. Schwartz, L.J. Shaw, and L. Mauri, *Diagnostic accuracy of fractional flow reserve from anatomic CT angiography.* JAMA, 2012. **308**(12): p. 1237-45.

71. Marwan, M., *Computational fluid dynamics: can computed tomography imaging compete with cath-lab physiology?* Cardiovasc Res, 2019. **115**(4): p. e41-e43.

72. Douglas, P.S., B. De Bruyne, G. Pontone, M.R. Patel, B.L. Norgaard, R.A. Byrne, N. Curzen, I. Purcell, M. Gutberlet, G. Rioufol, U. Hink, H.W. Schuchlenz, G. Feuchtner, M. Gilard, D. Andreini, J.M. Jensen, M. Hadamitzky, K. Chiswell, D. Cyr, A. Wilk, F. Wang, C. Rogers, M.A. Hlatky, and P. Investigators, *1-Year Outcomes of FFRCT-Guided Care in Patients With Suspected Coronary Disease: The PLATFORM Study.* J Am Coll Cardiol, 2016. **68**(5): p. 435-445.

73. Norgaard, B.L., C.J. Terkelsen, O.N. Mathiassen, E.L. Grove, H.E. Botker, E. Parner, J. Leipsic, F.H. Steffensen, A.H. Riis, K. Pedersen, E.H. Christiansen, M. Maeng, L.R. Krusell, S.D. Kristensen, A. Eftekhari, L. Jakobsen, and J.M. Jensen, *Clinical Outcomes Using Coronary CT Angiography and FFRCT-Guided Management of Stable Chest Pain Patients.* J Am Coll Cardiol, 2018.

74. Oikonomou, E.K., H.W. West, and C. Antoniades, *Cardiac Computed Tomography: Assessment of Coronary Inflammation and Other Plaque Features.* Arterioscler Thromb Vasc Biol, 2019. **39**(11): p. 2207-2219.

75. Gronthos, S., D.M. Franklin, H.A. Leddy, P.G. Robey, R.W. Storms, and J.M. Gimble, *Surface protein characterization of human adipose tissue-derived stromal cells.* J Cell Physiol, 2001. **189**(1): p. 54-63.

76. Silva, K.R., I. Cortes, S. Liechocki, J.R. Carneiro, A.A. Souza, R. Borojevic, C.M. Maya-Monteiro, and L.S. Baptista, *Characterization of stromal vascular fraction and adipose stem cells from subcutaneous, preperitoneal and visceral morbidly obese human adipose tissue depots.* PLoS One, 2017. **12**(3): p. e0174115.

77. Antonopoulos, A.S., M. Margaritis, P. Coutinho, J. Digby, R. Patel, C. Psarros, N. Ntusi, T.D. Karamitsos, R. Lee, R. De Silva, M. Petrou, R. Sayeed, M. Demosthenous, C. Bakogiannis, P.B. Wordsworth, D. Tousoulis, S. Neubauer, K.M. Channon, and C. Antoniades, *Reciprocal effects of systemic inflammation and brain natriuretic peptide on adiponectin biosynthesis in adipose tissue of patients with ischemic heart disease.* Arterioscler Thromb Vasc Biol, 2014. **34**(9): p. 2151-9.

78. Rimm, E.B., M.J. Stampfer, E. Giovannucci, A. Ascherio, D. Spiegelman, G.A. Colditz, and W.C. Willett, *Body size and fat distribution as predictors of coronary heart disease among middle-aged and older US men.* Am J Epidemiol, 1995. **141**(12): p. 1117-27.

79. Dale, C.E., G. Fatemifar, T.M. Palmer, J. White, D. Prieto-Merino, D. Zabaneh, J.E.L. Engmann, T. Shah, A. Wong, H.R. Warren, S. McLachlan, S. Trompet, M. Moldovan, R.W. Morris, R. Sofat, M. Kumari, E. Hypponen, B.J. Jefferis, T.R. Gaunt, Y. Ben-Shlomo, A. Zhou, A. Gentry-Maharaj, A. Ryan, R. Mutsert, R. Noordam, M.J. Caulfield, J.W. Jukema, B.B. Worrall, P.B. Munroe, U. Menon, C. Power, D. Kuh, D.A. Lawlor, S.E. Humphries, D.O. Mook-Kanamori, N. Sattar, M. Kivimaki, J.F. Price, G. Davey Smith, F. Dudbridge, A.D. Hingorani, M.V. Holmes, and J.P. Casas, *Causal Associations of Adiposity and Body Fat Distribution With Coronary Heart Disease, Stroke Subtypes, and Type 2*

Diabetes Mellitus: A Mendelian Randomization Analysis. Circulation, 2017. **135**(24): p. 2373-2388.

80. Chandra, A., I.J. Neeland, J.D. Berry, C.R. Ayers, A. Rohatgi, S.R. Das, A. Khera, D.K. McGuire, J.A. de Lemos, and A.T. Turer, *The relationship of body mass and fat distribution with incident hypertension: observations from the Dallas Heart Study.* J Am Coll Cardiol, 2014. **64**(10): p. 997-1002.

81. Neeland, I.J., A.T. Turer, C.R. Ayers, J.D. Berry, A. Rohatgi, S.R. Das, A. Khera, G.L. Vega, D.K. McGuire, S.M. Grundy, and J.A. de Lemos, *Body fat distribution and incident cardiovascular disease in obese adults.* J Am Coll Cardiol, 2015. **65**(19): p. 2150-1.

82. Britton, K.A., J.M. Massaro, J.M. Murabito, B.E. Kreger, U. Hoffmann, and C.S. Fox, *Body fat distribution, incident cardiovascular disease, cancer, and all-cause mortality.* J Am Coll Cardiol, 2013. **62**(10): p. 921-5.

83. Aune, D., A. Sen, M. Prasad, T. Norat, I. Janszky, S. Tonstad, P. Romundstad, and L.J. Vatten, *BMI and all cause mortality: systematic review and non-linear dose-response meta-analysis of 230 cohort studies with 3.74 million deaths among 30.3 million participants.* BMJ, 2016. **353**: p. i2156.

84. Uretsky, S., F.H. Messerli, S. Bangalore, A. Champion, R.M. Cooper-Dehoff, Q. Zhou, and C.J. Pepine, *Obesity paradox in patients with hypertension and coronary artery disease.* Am J Med, 2007. **120**(10): p. 863-70.

85. Powell-Wiley, T.M., J. Ngwa, S. Kebede, D. Lu, P.J. Schulte, D.L. Bhatt, C. Yancy, G.C. Fonarow, and M.A. Albert, *Impact of Body Mass Index on Heart Failure by Race/Ethnicity From Get With The Guidelines-Heart Failure (GWTG-HF) Registry.* JACC Heart Fail, 2018.

86. Antonopoulos, A.S., E.K. Oikonomou, C. Antoniades, and D. Tousoulis, *From the BMI paradox to the obesity paradox: the obesity-mortality association in coronary heart disease.* Obes Rev, 2016. **17**(10): p. 989-1000.

87. Lavie, C.J., L.P. Cahalin, P. Chase, J. Myers, D. Bensimhon, M.A. Peberdy, E. Ashley, E. West, D.E. Forman, M. Guazzi, and R. Arena, *Impact of cardiorespiratory fitness on the obesity paradox in patients with heart failure.* Mayo Clin Proc, 2013. **88**(3): p. 251-8.

88. Lavie, C.J., A.F. Osman, R.V. Milani, and M.R. Mehra, *Body composition and prognosis in chronic systolic heart failure: the obesity paradox.* Am J Cardiol, 2003. **91**(7): p. 891-4.

89. Khawaja, T., C. Greer, A. Chokshi, N. Chavarria, S. Thadani, M. Jones, K. Schaefle, K. Bhatia, J.E. Collado, D. Shimbo, A.J. Einstein, and P.C. Schulze, *Epicardial fat volume in patients with left ventricular systolic dysfunction.* Am J Cardiol, 2011. **108**(3): p. 397-401.

90. Wajchenberg, B.L., *Subcutaneous and visceral adipose tissue: their relation to the metabolic syndrome.* Endocr Rev, 2000. **21**(6): p. 697-738.

91. Iacobellis, G., *Local and systemic effects of the multifaceted epicardial adipose tissue depot.* Nat Rev Endocrinol, 2015. **11**(6): p. 363-71.

92. Vohl, M.C., R. Sladek, J. Robitaille, S. Gurd, P. Marceau, D. Richard, T.J. Hudson, and A. Tchernof, *A survey of genes differentially expressed in subcutaneous and visceral adipose tissue in men.* Obes Res, 2004. **12**(8): p. 1217-22.

93. Salgado-Somoza, A., E. Teijeira-Fernandez, A.L. Fernandez, J.R. Gonzalez-Juanatey, and S. Eiras, *Proteomic analysis of epicardial and subcutaneous adipose tissue reveals differences in proteins involved in oxidative stress.* Am J Physiol Heart Circ Physiol, 2010. **299**(1): p. H202-9.

94. Passaro, A., M.A. Miselli, J.M. Sanz, E. Dalla Nora, M.L. Morieri, R. Colonna, R. Pisot, and G. Zuliani, *Gene expression regional differences in human subcutaneous adipose tissue.* BMC Genomics, 2017. **18**(1): p. 202.

95. Gaborit, B., N. Venteclef, P. Ancel, V. Pelloux, V. Gariboldi, P. Leprince, J. Amour, S.N. Hatem, E. Jouve, A. Dutour, and K. Clément, *Human epicardial adipose tissue has a specific transcriptomic signature depending on its anatomical peri-atrial, peri-ventricular, or peri-coronary location.* Cardiovasc Res, 2015. **108**(1): p. 62-73.

96. Ibrahim, M.M., *Subcutaneous and visceral adipose tissue: structural and functional differences.* Obes Rev, 2010. **11**(1): p. 11-8.

97. Kiefer, F.W., P. Cohen, and J. Plutzky, *Fifty shades of brown: perivascular fat, thermogenesis, and atherosclerosis.* Circulation, 2012. **126**(9): p. 1012-5.

98. Harms, M. and P. Seale, *Brown and beige fat: development, function and therapeutic potential.* Nat Med, 2013. **19**(10): p. 1252-63.

99. Villarroya, F., R. Cereijo, J. Villarroya, and M. Giralt, *Brown adipose tissue as a secretory organ.* Nature Reviews Endocrinology, 2017. **13**(1): p. 26-35.

100. Srikakulapu, P., A. Upadhye, S.M. Rosenfeld, M.A. Marshall, C. McSkimming, A.W. Hickman, I.S. Mauldin, G. Ailawadi, M.B.S. Lopes, A.M. Taylor, and C.A. McNamara, *Perivascular Adipose Tissue Harbors Atheroprotective IgM-Producing B Cells.* Front Physiol, 2017. **8**: p. 719.

101. Zuk, P.A., M. Zhu, P. Ashjian, D.A. De Ugarte, J.I. Huang, H. Mizuno, Z.C. Alfonso, J.K. Fraser, P. Benhaim, and M.H. Hedrick, *Human adipose tissue is a source of multipotent stem cells.* Mol Biol Cell, 2002. **13**(12): p. 4279-95.

102. Tilg, H. and A.R. Moschen, *Adipocytokines: mediators linking adipose tissue, inflammation and immunity.* Nat Rev Immunol, 2006. **6**(10): p. 772-83.

103. Margaritis, M., A.S. Antonopoulos, J. Digby, R. Lee, S. Reilly, P. Coutinho, C. Shirodaria, R. Sayeed, M. Petrou, R. De Silva, S. Jalilzadeh, M. Demosthenous, C. Bakogiannis, D.

Tousoulis, C. Stefanadis, R.P. Choudhury, B. Casadei, K.M. Channon, and C. Antoniades, *Interactions between vascular wall and perivascular adipose tissue reveal novel roles for adiponectin in the regulation of endothelial nitric oxide synthase function in human vessels.* Circulation, 2013. **127**(22): p. 2209-21.

104. Thomou, T., M.A. Mori, J.M. Dreyfuss, M. Konishi, M. Sakaguchi, C. Wolfrum, T.N. Rao, J.N. Winnay, R. Garcia-Martin, S.K. Grinspoon, P. Gorden, and C.R. Kahn, *Adipose-derived circulating miRNAs regulate gene expression in other tissues.* Nature, 2017. **542**(7642): p. 450-455.

105. King, A.L., D.J. Polhemus, S. Bhushan, H. Otsuka, K. Kondo, C.K. Nicholson, J.M. Bradley, K.N. Islam, J.W. Calvert, Y.X. Tao, T.R. Dugas, E.E. Kelley, J.W. Elrod, P.L. Huang, R. Wang, and D.J. Lefer, *Hydrogen sulfide cytoprotective signaling is endothelial nitric oxide synthase-nitric oxide dependent.* Proc Natl Acad Sci U S A, 2014. **111**(8): p. 3182-7.

106. Xie, Z., X. Wang, X. Liu, H. Du, C. Sun, X. Shao, J. Tian, X. Gu, H. Wang, J. Tian, and B. Yu, *Adipose-Derived Exosomes Exert Proatherogenic Effects by Regulating Macrophage Foam Cell Formation and Polarization.* J Am Heart Assoc, 2018. **7**(5).

107. Lee, Y.C., H.H. Chang, C.L. Chiang, C.H. Liu, J.I. Yeh, M.F. Chen, P.Y. Chen, J.S. Kuo, and T.J. Lee, *Role of perivascular adipose tissue-derived methyl palmitate in vascular tone regulation and pathogenesis of hypertension.* Circulation, 2011. **124**(10): p. 1160-71.

108. Kleemann, R., M. van Erk, L. Verschuren, A.M. van den Hoek, M. Koek, P.Y. Wielinga, A. Jie, L. Pellis, I. Bobeldijk-Pastorova, T. Kelder, K. Toet, S. Wopereis, N. Cnubben, C. Evelo, B. van Ommen, and T. Kooistra, *Time-resolved and tissue-specific systems analysis of the pathogenesis of insulin resistance.* PLoS One, 2010. **5**(1): p. e8817.

109. Crewe, C., Y.A. An, and P.E. Scherer, *The ominous triad of adipose tissue dysfunction: inflammation, fibrosis, and impaired angiogenesis.* J Clin Invest, 2017. **127**(1): p. 74-82.

110. Halberg, N., T. Khan, M.E. Trujillo, I. Wernstedt-Asterholm, A.D. Attie, S. Sherwani, Z.V. Wang, S. Landskroner-Eiger, S. Dineen, U.J. Magalang, R.A. Brekken, and P.E. Scherer, *Hypoxia-inducible factor 1alpha induces fibrosis and insulin resistance in white adipose tissue.* Mol Cell Biol, 2009. **29**(16): p. 4467-83.

111. Pasarica, M., O.R. Sereda, L.M. Redman, D.C. Albarado, D.T. Hymel, L.E. Roan, J.C. Rood, D.H. Burk, and S.R. Smith, *Reduced adipose tissue oxygenation in human obesity: evidence for rarefaction, macrophage chemotaxis, and inflammation without an angiogenic response.* Diabetes, 2009. **58**(3): p. 718-25.

112. Pang, C., Z. Gao, J. Yin, J. Zhang, W. Jia, and J. Ye, *Macrophage infiltration into adipose tissue may promote angiogenesis for adipose tissue remodeling in obesity.* Am J Physiol Endocrinol Metab, 2008. **295**(2): p. E313-22.

113. Britton, K.A. and C.S. Fox, *Perivascular adipose tissue and vascular disease.* Clin Lipidol, 2011. **6**(1): p. 79-91.

114. Akoumianakis, I. and C. Antoniades, *The interplay between adipose tissue and the cardiovascular system: is fat always bad?* Cardiovasc Res, 2017. **113**(9): p. 999-1008.

115. Mancio, J., E.K. Oikonomou, and C. Antoniades, *Perivascular adipose tissue and coronary atherosclerosis.* Heart, 2018. **104**(20): p. 1654-1662.

116. Chen, H., M. Montagnani, T. Funahashi, I. Shimomura, and M.J. Quon, *Adiponectin stimulates production of nitric oxide in vascular endothelial cells.* J Biol Chem, 2003. **278**(45): p. 45021-6.

117. Chang, L., W. Xiong, X. Zhao, Y. Fan, Y. Guo, M. Garcia-Barrio, J. Zhang, Z. Jiang, J.D. Lin, and Y.E. Chen, *Bmal1 in Perivascular Adipose Tissue Regulates Resting Phase Blood Pressure Through Transcriptional Regulation of Angiotensinogen.* Circulation, 2018.

118. Ayala-Lopez, N., J.M. Thompson, and S.W. Watts, *Perivascular Adipose Tissue's Impact on Norepinephrine-Induced Contraction of Mesenteric Resistance Arteries.* Front Physiol, 2017. **8**: p. 37.

119. Antonopoulos, A.S., M. Margaritis, P. Coutinho, C. Shirodaria, C. Psarros, L. Herdman, F. Sanna, R. De Silva, M. Petrou, R. Sayeed, G. Krasopoulos, R. Lee, J. Digby, S. Reilly, C. Bakogiannis, D. Tousoulis, B. Kessler, B. Casadei, K.M. Channon, and C. Antoniades, *Adiponectin as a link between type 2 diabetes and vascular NADPH oxidase activity in the human arterial wall: the regulatory role of perivascular adipose tissue.* Diabetes, 2015. **64**(6): p. 2207-19.

120. Neves, K.B., N.S. Lobato, R.A. Lopes, F.P. Filgueira, C.Z. Zanotto, A.M. Oliveira, and R.C. Tostes, *Chemerin reduces vascular nitric oxide/cGMP signalling in rat aorta: a link to vascular dysfunction in obesity?* Clin Sci (Lond), 2014. **127**(2): p. 111-22.

121. Lee, W.J., C.S. Wu, H. Lin, I.T. Lee, C.M. Wu, J.J. Tseng, M.M. Chou, and W.H. Sheu, *Visfatin-induced expression of inflammatory mediators in human endothelial cells through the NF-kappaB pathway.* Int J Obes (Lond), 2009. **33**(4): p. 465-72.

122. Takaoka, M., H. Suzuki, S. Shioda, K. Sekikawa, Y. Saito, R. Nagai, and M. Sata, *Endovascular injury induces rapid phenotypic changes in perivascular adipose tissue.* Arterioscler Thromb Vasc Biol, 2010. **30**(8): p. 1576-82.

123. Cybularz, M., H. Langbein, B. Zatschler, C. Brunssen, A. Deussen, K. Matschke, and H. Morawietz, *Endothelial function and gene expression in perivascular adipose tissue from internal mammary arteries of obese patients with coronary artery disease.* Atheroscler Suppl, 2017. **30**: p. 149-158.

124. Ohyama, K., Y. Matsumoto, H. Amamizu, H. Uzuka, K. Nishimiya, S. Morosawa, M. Hirano, H. Watabe, Y. Funaki, S. Miyata, J. Takahashi, K. Ito, and H. Shimokawa, *Association of Coronary Perivascular Adipose Tissue Inflammation and Drug-Eluting Stent-Induced Coronary Hyperconstricting Responses in Pigs: (18)F-Fluorodeoxyglucose Positron Emission Tomography Imaging Study.* Arterioscler Thromb Vasc Biol, 2017. **37**(9): p. 1757-1764.

125. Antonopoulos, A.S., M. Margaritis, S. Verheule, A. Recalde, F. Sanna, L. Herdman, C. Psarros, H. Nasrallah, P. Coutinho, I. Akoumianakis, A.C. Brewer, R. Sayeed, G. Krasopoulos, M. Petrou, A. Tarun, D. Tousoulis, A.M. Shah, B. Casadei, K.M. Channon, and C. Antoniades, *Mutual Regulation of Epicardial Adipose Tissue and Myocardial Redox State by PPAR-gamma/Adiponectin Signalling.* Circ Res, 2016. **118**(5): p. 842-55.

126. Antonopoulos, A.S., F. Sanna, N. Sabharwal, S. Thomas, E.K. Oikonomou, L. Herdman, M. Margaritis, C. Shirodaria, A.M. Kampoli, I. Akoumianakis, M. Petrou, R. Sayeed, G. Krasopoulos, C. Psarros, P. Ciccone, C.M. Brophy, J. Digby, A. Kelion, R. Uberoi, S. Anthony, N. Alexopoulos, D. Tousoulis, S. Achenbach, S. Neubauer, K.M. Channon, and C. Antoniades, *Detecting human coronary inflammation by imaging perivascular fat.* Sci Transl Med., 2017. **9**(398).

127. Kaul, S., M.P. Rothney, D.M. Peters, W.K. Wacker, C.E. Davis, M.D. Shapiro, and D.L. Ergun, *Dual-energy X-ray absorptiometry for quantification of visceral fat.* Obesity (Silver Spring), 2012. **20**(6): p. 1313-8.

128. Marinou, K., L. Hodson, S.K. Vasan, B.A. Fielding, R. Banerjee, K. Brismar, M. Koutsilieris, A. Clark, M.J. Neville, and F. Karpe, *Structural and functional properties of deep abdominal subcutaneous adipose tissue explain its association with insulin resistance and cardiovascular risk in men.* Diabetes Care, 2014. **37**(3): p. 821-9.

129. Iacobellis, G., M.C. Ribaudo, F. Assael, E. Vecci, C. Tiberti, A. Zappaterreno, U. Di Mario, and F. Leonetti, *Echocardiographic epicardial adipose tissue is related to anthropometric and clinical parameters of metabolic syndrome: a new indicator of cardiovascular risk.* J Clin Endocrinol Metab, 2003. **88**(11): p. 5163-8.

130. Davidovich, D., A. Gastaldelli, and R. Sicari, *Imaging cardiac fat.* Eur Heart J Cardiovasc Imaging, 2013. **14**(7): p. 625-30.

131. Mahabadi, A.A., B. Balcer, I. Dykun, M. Forsting, T. Schlosser, G. Heusch, and T. Rassaf, *Cardiac computed tomography-derived epicardial fat volume and attenuation independently distinguish patients with and without myocardial infarction.* PLoS One, 2017. **12**(8): p. e0183514.

132. Franssens, B.T., H.M. Nathoe, T. Leiner, Y. van der Graaf, and F.L. Visseren, *Relation between cardiovascular disease risk factors and epicardial adipose tissue density on cardiac computed tomography in patients at high risk of cardiovascular events.* Eur J Prev Cardiol, 2017. **24**(6): p. 660-670.

133. Mazurek, T., M. Kobylecka, M. Zielenkiewicz, A. Kurek, J. Kochman, K.J. Filipiak, K. Mazurek, Z. Huczek, L. Krolicki, and G. Opolski, *PET/CT evaluation of (18)F-FDG uptake in pericoronary adipose tissue in patients with stable coronary artery disease: Independent predictor of atherosclerotic lesions' formation?* J Nucl Cardiol, 2017. **24**(3): p. 1075-1084.

134. Ohyama, K., Y. Matsumoto, K. Takanami, H. Ota, K. Nishimiya, J. Sugisawa, S. Tsuchiya, H. Amamizu, H. Uzuka, A. Suda, T. Shindo, Y. Kikuchi, K. Hao, R. Tsuburaya, J. Takahashi, S. Miyata, Y. Sakata, K. Takase, and H. Shimokawa, *Coronary*

Adventitial and Perivascular Adipose Tissue Inflammation in Patients With Vasospastic Angina. J Am Coll Cardiol, 2018. **71**(4): p. 414-425.

135. Mazonakis, M. and J. Damilakis, *Computed tomography: What and how does it measure?* Eur J Radiol, 2016. **85**(8): p. 1499-504.

136. Liu, J., C.S. Fox, D.A. Hickson, W.D. May, K.G. Hairston, J.J. Carr, and H.A. Taylor, *Impact of abdominal visceral and subcutaneous adipose tissue on cardiometabolic risk factors: the Jackson Heart Study.* J Clin Endocrinol Metab, 2010. **95**(12): p. 5419-26.

137. Gillies, R.J., P.E. Kinahan, and H. Hricak, *Radiomics: Images Are More than Pictures, They Are Data.* Radiology, 2016. **278**(2): p. 563-77.

138. Parekh, V. and M.A. Jacobs, *Radiomics: a new application from established techniques.* Expert Rev Precis Med Drug Dev, 2016. **1**(2): p. 207-226.

139. Kolossvary, M., M. Kellermayer, B. Merkely, and P. Maurovich-Horvat, *Cardiac Computed Tomography Radiomics: A Comprehensive Review on Radiomic Techniques.* J Thorac Imaging, 2018. **33**(1): p. 26-34.

140. Reuze, S., A. Schernberg, F. Orlhac, R. Sun, C. Chargari, L. Dercle, E. Deutsch, I. Buvat, and C. Robert, *Radiomics in Nuclear Medicine Applied to Radiation Therapy: Methods, Pitfalls, and Challenges.* Int J Radiat Oncol Biol Phys, 2018. **102**(4): p. 1117-1142.

141. Aerts, H.J., E.R. Velazquez, R.T. Leijenaar, C. Parmar, P. Grossmann, S. Carvalho, J. Bussink, R. Monshouwer, B. Haibe-Kains, D. Rietveld, F. Hoebers, M.M. Rietbergen, C.R. Leemans, A. Dekker, J. Quackenbush, R.J. Gillies, and P. Lambin, *Decoding tumour phenotype by noninvasive imaging using a quantitative radiomics approach.* Nat Commun, 2014. **5**: p. 4006.

142. Oikonomou, E.K., M. Marwan, M.Y. Desai, J. Mancio, A. Alashi, E. Hutt Centeno, S. Thomas, L. Herdman, C.P. Kotanidis, K.E. Thomas, B.P. Griffin, S.D. Flamm, A.S. Antonopoulos, C. Shirodaria, N. Sabharwal, J. Deanfield, S. Neubauer, J.C. Hopewell, K.M. Channon, S. Achenbach, and C. Antoniades, *Non-invasive detection of coronary inflammation using computed tomography and prediction of residual cardiovascular risk (the CRISP CT study): a post-hoc analysis of prospective outcome data.* Lancet, 2018. **392**(10151): p. 929-939.

143. Investigators, S.-H., D.E. Newby, P.D. Adamson, C. Berry, N.A. Boon, M.R. Dweck, M. Flather, J. Forbes, A. Hunter, S. Lewis, S. MacLean, N.L. Mills, J. Norrie, G. Roditi, A.S.V. Shah, A.D. Timmis, E.J.R. van Beek, and M.C. Williams, *Coronary CT Angiography and 5-Year Risk of Myocardial Infarction.* N Engl J Med, 2018. **379**(10): p. 924-933.

144. Min, J.K. and F.Y. Lin, *What makes a coronary CT angiogram nondiagnostic?* J Cardiovasc Comput Tomogr, 2008. **2**(6): p. 351-9.

145. Agatston, A.S., W.R. Janowitz, F.J. Hildner, N.R. Zusmer, M. Viamonte, Jr., and R. Detrano, *Quantification of coronary artery calcium using ultrafast computed tomography.* J Am Coll Cardiol, 1990. **15**(4): p. 827-32.

146. Cury, R.C., S. Abbara, S. Achenbach, A. Agatston, D.S. Berman, M.J. Budoff, K.E. Dill, J.E. Jacobs, C.D. Maroules, G.D. Rubin, F.J. Rybicki, U.J. Schoepf, L.J. Shaw, A.E. Stillman, C.S. White, P.K. Woodard, and J.A. Leipsic, *Coronary Artery Disease - Reporting and Data System (CAD-RADS): An Expert Consensus Document of SCCT, ACR and NASCI: Endorsed by the ACC*. JACC Cardiovasc Imaging, 2016. **9**(9): p. 1099-1113.

147. Williams, M.C., A.J. Moss, M. Dweck, P.D. Adamson, S. Alam, A. Hunter, A.S.V. Shah, T. Pawade, J.R. Weir-McCall, G. Roditi, E.J.R. van Beek, D.E. Newby, and E.D. Nicol, *Coronary Artery Plaque Characteristics Associated With Adverse Outcomes in the SCOT-HEART Study*. J Am Coll Cardiol, 2019. **73**(3): p. 291-301.

148. Dey, D., T. Schepis, M. Marwan, P.J. Slomka, D.S. Berman, and S. Achenbach, *Automated three-dimensional quantification of noncalcified coronary plaque from coronary CT angiography: comparison with intravascular US*. Radiology, 2010. **257**(2): p. 516-22.

149. Mancio, J., D. Azevedo, F. Saraiva, A.I. Azevedo, G. Pires-Morais, A. Leite-Moreira, I. Falcao-Pires, N. Lunet, and N. Bettencourt, *Epicardial adipose tissue volume assessed by computed tomography and coronary artery disease: a systematic review and meta-analysis*. Eur Heart J Cardiovasc Imaging, 2018. **19**(5): p. 490-497.

150. Okayama, S., T. Soeda, Y. Takami, R. Kawakami, S. Somekawa, S. Uemura, and Y. Saito, *The influence of effective energy on computed tomography number depends on tissue characteristics in monoenergetic cardiac imaging*. Radiol Res Pract, 2012. **2012**: p. 150980.

151. van Griethuysen, J.J.M., A. Fedorov, C. Parmar, A. Hosny, N. Aucoin, V. Narayan, R.G.H. Beets-Tan, J.C. Fillion-Robin, S. Pieper, and H. Aerts, *Computational Radiomics System to Decode the Radiographic Phenotype*. Cancer Res, 2017. **77**(21): p. e104-e107.

152. Haralick, R.M., K. Shanmugam, and I. Dinstein, *Textural Features for Image Classification*. Ieee Transactions on Systems Man and Cybernetics, 1973. **Smc3**(6): p. 610-621.

153. Guo, X., X. Liu, H. Wang, Z. Liang, W. Wu, Q. He, K. Li, and W. Wang, *Enhanced CT images by the wavelet transform improving diagnostic accuracy of chest nodules*. J Digit Imaging, 2011. **24**(1): p. 44-9.

154. Aerts, H.J.W.L., E.R. Velazquez, R.T.H. Leijenaar, C. Parmar, P. Grossmann, S. Cavalho, J. Bussink, R. Monshouwer, B. Haibe-Kains, D. Rietveld, F. Hoebers, M.M. Rietbergen, C.R. Leemans, A. Dekker, J. Quackenbush, R.J. Gillies, and P. Lambin, *Decoding tumour phenotype by noninvasive imaging using a quantitative radiomics approach*. Nature Communications, 2014. **5**.

155. Fedorov, A., R. Beichel, J. Kalpathy-Cramer, J. Finet, J.C. Fillion-Robin, S. Pujol, C. Bauer, D. Jennings, F. Fennessy, M. Sonka, J. Buatti, S. Aylward, J.V. Miller, S. Pieper, and R. Kikinis, *3D Slicer as an image computing platform for the Quantitative Imaging Network*. Magn Reson Imaging, 2012. **30**(9): p. 1323-41.

156. Leijenaar, R.T., G. Nalbantov, S. Carvalho, W.J. van Elmpt, E.G. Troost, R. Boellaard, H.J. Aerts, R.J. Gillies, and P. Lambin, *The effect of SUV discretization in quantitative FDG-*

PET Radiomics: the need for standardized methodology in tumor texture analysis. Sci Rep, 2015. **5**: p. 11075.

157. Camici, P.G., O.E. Rimoldi, O. Gaemperli, and P. Libby, *Non-invasive anatomic and functional imaging of vascular inflammation and unstable plaque.* Eur Heart J, 2012. **33**(11): p. 1309-17.

158. Tarkin, J.M., M.R. Dweck, N.R. Evans, R.A. Takx, A.J. Brown, A. Tawakol, Z.A. Fayad, and J.H. Rudd, *Imaging Atherosclerosis.* Circ Res, 2016. **118**(4): p. 750-69.

159. Komatsu, S., T. Kamata, A. Imai, T. Ohara, K. Miyaji, Y. Kobayashi, and K. Kodama, *Quantitative analysis of coronary vessels with optimized intracoronary CT number.* PLoS One, 2014. **9**(1): p. e85312.

160. Forsythe, R.O., M.R. Dweck, O.M.B. McBride, A.T. Vesey, S.I. Semple, A.S.V. Shah, P.D. Adamson, W.A. Wallace, J. Kaczynski, W. Ho, E.J.R. van Beek, C.D. Gray, A. Fletcher, C. Lucatelli, A. Marin, P. Burns, A. Tambyraja, R.T.A. Chalmers, G. Weir, N. Mitchard, A. Tavares, J.M.J. Robson, and D.E. Newby, *(18)F-Sodium Fluoride Uptake in Abdominal Aortic Aneurysms: The SoFIA(3) Study.* J Am Coll Cardiol, 2018. **71**(5): p. 513-523.

161. Kwiecinski, J., D. Dey, S. Cadet, S.E. Lee, Y. Otaki, P.T. Huynh, M.K. Doris, E. Eisenberg, M. Yun, M.A. Jansen, M.C. Williams, B.K. Tamarappoo, J.D. Friedman, M.R. Dweck, D.E. Newby, H.J. Chang, P.J. Slomka, and D.S. Berman, *Peri-Coronary Adipose Tissue Density Is Associated With (18)F-Sodium Fluoride Coronary Uptake in Stable Patients With High-Risk Plaques.* JACC Cardiovasc Imaging, 2019.

162. Ghekiere, O., R. Salgado, N. Buls, T. Leiner, I. Mancini, P. Vanhoenacker, P. Dendale, and A. Nchimi, *Image quality in coronary CT angiography: challenges and technical solutions.* Br J Radiol, 2017. **90**(1072): p. 20160567.

163. Wong, K.K., P. Thavornpattanapong, S.C. Cheung, Z. Sun, and J. Tu, *Effect of calcification on the mechanical stability of plaque based on a three-dimensional carotid bifurcation model.* BMC Cardiovasc Disord, 2012. **12**: p. 7.

164. Goeller, M., S. Achenbach, S. Cadet, A.C. Kwan, F. Commandeur, P.J. Slomka, H. Gransar, M.H. Albrecht, B.K. Tamarappoo, D.S. Berman, M. Marwan, and D. Dey, *Pericoronary Adipose Tissue Computed Tomography Attenuation and High-Risk Plaque Characteristics in Acute Coronary Syndrome Compared With Stable Coronary Artery Disease.* JAMA Cardiol, 2018. **3**(9): p. 858-863.

165. Hedgire, S., V. Baliyan, E.J. Zucker, D.O. Bittner, P.V. Staziaki, R.A.P. Takx, J.E. Scholtz, N. Meyersohn, U. Hoffmann, and B. Ghoshhajra, *Perivascular Epicardial Fat Stranding at Coronary CT Angiography: A Marker of Acute Plaque Rupture and Spontaneous Coronary Artery Dissection.* Radiology, 2018: p. 171568.

166. Libby, P., *Inflammation in atherosclerosis.* Arterioscler Thromb Vasc Biol, 2012. **32**(9): p. 2045-51.

167. Lerman, J.B., A.A. Joshi, A. Chaturvedi, T.M. Aberra, A.K. Dey, J.A. Rodante, T. Salahuddin, J.H. Chung, A. Rana, H.L. Teague, J.J. Wu, M.P. Playford, B.A. Lockshin, M.Y. Chen, V. Sandfort, D.A. Bluemke, and N.N. Mehta, *Coronary Plaque Characterization in Psoriasis Reveals High-Risk Features That Improve After Treatment in a Prospective Observational Study.* Circulation, 2017. **136**(3): p. 263-276.

168. Elnabawi, Y.A., E.K. Oikonomou, A.K. Dey, J. Mancio, J.A. Rodante, M. Aksentijevich, H. Choi, A. Keel, J. Erb-Alvarez, H.L. Teague, A.A. Joshi, M.P. Playford, B. Lockshin, A.D. Choi, J.M. Gelfand, M.Y. Chen, D.A. Bluemke, C. Shirodaria, C. Antoniades, and N.N. Mehta, *Association of Biologic Therapy With Coronary Inflammation in Patients With Psoriasis as Assessed by Perivascular Fat Attenuation Index.* JAMA Cardiol, 2019.

169. Matter, C.M., M. Stuber, and M. Nahrendorf, *Imaging of the unstable plaque: how far have we got?* Eur Heart J, 2009. **30**(21): p. 2566-2574.

170. Ross, R., *Atherosclerosis--an inflammatory disease.* N Engl J Med, 1999. **340**(2): p. 115-26.

171. Ridker, P.M., B.M. Everett, T. Thuren, J.G. MacFadyen, W.H. Chang, C. Ballantyne, F. Fonseca, J. Nicolau, W. Koenig, S.D. Anker, J.J.P. Kastelein, J.H. Cornel, P. Pais, D. Pella, J. Genest, R. Cifkova, A. Lorenzatti, T. Forster, Z. Kobalava, L. Vida-Simiti, M. Flather, H. Shimokawa, H. Ogawa, M. Dellborg, P.R.F. Rossi, R.P.T. Troquay, P. Libby, R.J. Glynn, and C.T. Group, *Antiinflammatory Therapy with Canakinumab for Atherosclerotic Disease.* N Engl J Med, 2017.

172. Weintraub, W.S. and D.G. Harrison, *C-reactive protein, inflammation and atherosclerosis: do we really understand it yet?* Eur Heart J, 2000. **21**(12): p. 958-60.

173. Alexopoulos, N., B.H. Melek, C.D. Arepalli, G.R. Hartlage, Z. Chen, S. Kim, A.E. Stillman, and P. Raggi, *Effect of intensive versus moderate lipid-lowering therapy on epicardial adipose tissue in hyperlipidemic post-menopausal women: a substudy of the BELLES trial (Beyond Endorsed Lipid Lowering with EBT Scanning).* J Am Coll Cardiol 2013. **61**(19): p. 1956-61.

174. Knaapen, P., S. de Haan, O.S. Hoekstra, R. Halbmeijer, Y.E. Appelman, J.G. Groothuis, E.F. Comans, M.R. Meijerink, A.A. Lammertsma, M. Lubberink, M.J. Gotte, and A.C. van Rossum, *Cardiac PET-CT: advanced hybrid imaging for the detection of coronary artery disease.* Neth Heart J, 2010. **18**(2): p. 90-8.

175. Robinson, J.G., R. Huijgen, K. Ray, J. Persons, J.J.P. Kastelein, and M.J. Pencina, *Determining When to Add Nonstatin Therapy A Quantitative Approach.* J Am Coll Cardiol, 2016. **68**(22): p. 2412-2421.

176. Taylor, A.J., M. Cerqueira, J.M. Hodgson, D. Mark, J. Min, P. O'Gara, G.D. Rubin, C.M. Kramer, A.J. Taylor, D. Berman, A. Brown, F.A. Chaudhry, R.C. Cury, M.Y. Desai, A.J. Einstein, A.S. Gomes, R. Harrington, U. Hoffmann, R. Khare, J. Lesser, C. McGann, A. Rosenberg, R. Schwartz, M. Shelton, G.W. Smetana, S.C. Smith, M.J. Wolk, J.M. Allen, S. Bailey, P.S. Douglas, R.C. Hendel, C.M. Kramer, J. Min, M.R. Patel, L. Shaw, and R.F. Stainback, *ACCF/SCCT/ACR/AHA/ASE/ASNC/SCAI/SCMR 2010 Appropriate*

Use Criteria for Cardiac Computed Tomography. J Cardiovasc Comput Tomogr, 2010. **4**(6): p. 407-413.

177. Budoff, M.J., S. Achenbach, R.S. Blumenthal, J.J. Carr, J.G. Goldin, P. Greenland, A.D. Guerci, J.A. Lima, D.J. Rader, G.D. Rubin, L.J. Shaw, S.E. Wiegers, I. American Heart Association Committee on Cardiovascular, Intervention, R. American Heart Association Council on Cardiovascular, Intervention, and C.o.C.C. American Heart Association Committee on Cardiac Imaging, *Assessment of coronary artery disease by cardiac computed tomography: a scientific statement from the American Heart Association Committee on Cardiovascular Imaging and Intervention, Council on Cardiovascular Radiology and Intervention, and Committee on Cardiac Imaging, Council on Clinical Cardiology*. Circulation, 2006. **114**(16): p. 1761-91.

178. Hicks, K.A., J.E. Tcheng, B. Bozkurt, B.R. Chaitman, D.E. Cutlip, A. Farb, G.C. Fonarow, J.P. Jacobs, M.R. Jaff, J.H. Lichtman, M.C. Limacher, K.W. Mahaffey, R. Mehran, S.E. Nissen, E.E. Smith, and S.L. Targum, *2014 ACC/AHA Key Data Elements and Definitions for Cardiovascular Endpoint Events in Clinical Trials: A Report of the American College of Cardiology/American Heart Association Task Force on Clinical Data Standards (Writing Committee to Develop Cardiovascular Endpoints Data Standards)*. J Am Coll Cardiol, 2015. **66**(4): p. 403-69.

179. Cutlip, D.E., S. Windecker, R. Mehran, A. Boam, D.J. Cohen, G.A. van Es, P.G. Steg, M.A. Morel, L. Mauri, P. Vranckx, E. McFadden, A. Lansky, M. Hamon, M.W. Krucoff, P.W. Serruys, and C. Academic Research, *Clinical end points in coronary stent trials: a case for standardized definitions*. Circulation, 2007. **115**(17): p. 2344-51.

180. James, P.A., S. Oparil, B.L. Carter, W.C. Cushman, C. Dennison-Himmelfarb, J. Handler, D.T. Lackland, M.L. LeFevre, T.D. MacKenzie, O. Ogedegbe, S.C. Smith, Jr., L.P. Svetkey, S.J. Taler, R.R. Townsend, J.T. Wright, Jr., A.S. Narva, and E. Ortiz, *2014 evidence-based guideline for the management of high blood pressure in adults: report from the panel members appointed to the Eighth Joint National Committee (JNC 8)*. JAMA, 2014. **311**(5): p. 507-20.

181. American Diabetes, A., *Diagnosis and classification of diabetes mellitus*. Diabetes Care, 2014. **37 Suppl 1**: p. S81-90.

182. Genders, T.S., E.W. Steyerberg, M.G. Hunink, K. Nieman, T.W. Galema, N.R. Mollet, P.J. de Feyter, G.P. Krestin, H. Alkadhi, S. Leschka, L. Desbiolles, M.F. Meijs, M.J. Cramer, J. Knuuti, S. Kajander, J. Bogaert, K. Goetschalckx, F. Cademartiri, E. Maffei, C. Martini, S. Seitun, A. Aldrovandi, S. Wildermuth, B. Stinn, J. Fornaro, G. Feuchtner, T. De Zordo, T. Auer, F. Plank, G. Friedrich, F. Pugliese, S.E. Petersen, L.C. Davies, U.J. Schoepf, G.W. Rowe, C.A. van Mieghem, L. van Driessche, V. Sinitsyn, D. Gopalan, K. Nikolaou, F. Bamberg, R.C. Cury, J. Battle, P. Maurovich-Horvat, A. Bartykowszki, B. Merkely, D. Becker, M. Hadamitzky, J. Hausleiter, M. Dewey, E. Zimmermann, and M. Laule, *Prediction model to estimate presence of coronary artery disease: retrospective pooled analysis of existing cohorts*. BMJ, 2012. **344**: p. e3485.

183. Pencina, M.J., R.B. D'Agostino, K.M. Pencina, A.C. Janssens, and P. Greenland, *Interpreting incremental value of markers added to risk prediction models*. Am J Epidemiol, 2012. **176**(6): p. 473-81.

184. Hong, M.K., G.S. Mintz, C.W. Lee, B.K. Lee, T.H. Yang, Y.H. Kim, J.M. Song, K.H. Han, D.H. Kang, S.S. Cheong, J.K. Song, J.J. Kim, S.W. Park, and S.J. Park, *The site of plaque rupture in native coronary arteries: a three-vessel intravascular ultrasound analysis.* J Am Coll Cardiol, 2005. **46**(2): p. 261-5.

185. Otero, H.J., M.L. Steigner, and F.J. Rybicki, *The "post-64" era of coronary CT angiography: understanding new technology from physical principles.* Radiol Clin North Am, 2009. **47**(1): p. 79-90.

186. Oikonomou, E.K., M.C. Williams, C.P. Kotanidis, M.Y. Desai, M. Marwan, A.S. Antonopoulos, K.E. Thomas, S. Thomas, I. Akoumianakis, L.M. Fan, S. Kesavan, L. Herdman, A. Alashi, E.H. Centeno, M. Lyasheva, B.P. Griffin, S.D. Flamm, C. Shirodaria, N. Sabharwal, A. Kelion, M.R. Dweck, E.J.R. Van Beek, J. Deanfield, J.C. Hopewell, S. Neubauer, K.M. Channon, S. Achenbach, D.E. Newby, and C. Antoniades, *A novel machine learning-derived radiotranscriptomic signature of perivascular fat improves cardiac risk prediction using coronary CT angiography.* Eur Heart J, 2019.

187. Austen, W.G., J.E. Edwards, R.L. Frye, G.G. Gensini, V.L. Gott, L.S. Griffith, D.C. McGoon, M.L. Murphy, and B.B. Roe, *A reporting system on patients evaluated for coronary artery disease. Report of the Ad Hoc Committee for Grading of Coronary Artery Disease, Council on Cardiovascular Surgery, American Heart Association.* Circulation, 1975. **51**(4 Suppl): p. 5-40.

188. Marcelin, G., A. Ferreira, Y. Liu, M. Atlan, J. Aron-Wisnewsky, V. Pelloux, Y. Botbol, M. Ambrosini, M. Fradet, C. Rouault, C. Henegar, J.S. Hulot, C. Poitou, A. Torcivia, R. Nail-Barthelemy, J.C. Bichet, E.L. Gautier, and K. Clement, *A PDGFRalpha-Mediated Switch toward CD9(high) Adipocyte Progenitors Controls Obesity-Induced Adipose Tissue Fibrosis.* Cell Metab, 2017. **25**(3): p. 673-685.

189. Villaret, A., J. Galitzky, P. Decaunes, D. Esteve, M.A. Marques, C. Sengenes, P. Chiotasso, T. Tchkonia, M. Lafontan, J.L. Kirkland, and A. Bouloumie, *Adipose tissue endothelial cells from obese human subjects: differences among depots in angiogenic, metabolic, and inflammatory gene expression and cellular senescence.* Diabetes, 2010. **59**(11): p. 2755-63.

190. Berg, A.H. and P.E. Scherer, *Adipose tissue, inflammation, and cardiovascular disease.* Circ Res, 2005. **96**(9): p. 939-49.

191. Kolossvary, M., J. Karady, B. Szilveszter, P. Kitslaar, U. Hoffmann, B. Merkely, and P. Maurovich-Horvat, *Radiomic Features Are Superior to Conventional Quantitative Computed Tomographic Metrics to Identify Coronary Plaques With Napkin-Ring Sign.* Circ Cardiovasc Imaging, 2017. **10**(12).

192. Lee, J., *Patient-Specific Predictive Modeling Using Random Forests: An Observational Study for the Critically Ill.* JMIR Med Inform, 2017. **5**(1): p. e3.

193. Levelt, E., M. Pavlides, R. Banerjee, M. Mahmod, C. Kelly, J. Sellwood, R. Ariga, S. Thomas, J. Francis, C. Rodgers, W. Clarke, N. Sabharwal, C. Antoniades, J. Schneider, M. Robson, K. Clarke, T. Karamitsos, O. Rider, and S. Neubauer, *Ectopic and Visceral Fat*

Deposition in Lean and Obese Patients With Type 2 Diabetes. J Am Coll Cardiol, 2016. **68**(1): p. 53-63.

194. Berenguer, R., M.D.R. Pastor-Juan, J. Canales-Vazquez, M. Castro-Garcia, M.V. Villas, F. Mansilla Legorburo, and S. Sabater, *Radiomics of CT Features May Be Nonreproducible and Redundant: Influence of CT Acquisition Parameters*. Radiology, 2018. **288**(2): p. 407-415.

195. van der Bijl, N., P.W. de Bruin, J. Geleijns, J.J. Bax, J.D. Schuijf, A. de Roos, and L.J. Kroft, *Assessment of coronary artery calcium by using volumetric 320-row multi-detector computed tomography: comparison of 0.5 mm with 3.0 mm slice reconstructions*. Int J Cardiovasc Imaging, 2010. **26**(4): p. 473-82.

196. Deo, R.C., *Machine Learning in Medicine*. Circulation, 2015. **132**(20): p. 1920-30.

197. Topol, E.J., *High-performance medicine: the convergence of human and artificial intelligence*. Nat Med, 2019. **25**(1): p. 44-56.

9

Appendix

Appendix 1. Sample ORFAN study consent form

Study Full Title	The **O**xford **R**isk **F**actors **A**nd **N**on-invasive Imaging Study (The ORFAN study)
Patient ID	
Principal Investigator	Prof. Charalambos Antoniades (tel: 01865 228340)

Please initial box

1. I confirm that I have read and understand the information sheet (Version 1, June 2015) for the above study. I have had the opportunity to consider the information, ask questions and have had these answered satisfactorily. ☐
2. I understand that my participation is voluntary and that I am free to withdraw at any time without giving any reason, without my medical care or legal rights being affected. ☐
3. I understand that my medical notes as well as data collected during the study may be looked at by the study investigators and from authorized individuals from the University of Oxford, the regulatory authorities, the NHS Trust and the NIHR Bioresource. I permit these individuals access to my records. ☐
4. I understand that long term health outcome data will be collected by study investigators by securely accessing records held with the NHS, Health and Social Care Information centre (HSCIC) and Office of National Statistics (ONS). I give permission for this. ☐
5. I understand that images and blood samples may be obtained as part of this study. I also understand these data and samples will be stored in anonymized format as outlined in the information sheet and also for use in future ethically approved research and research publications. I give permission for this. I understand that my anonymized data, images and samples may be sent to other centers for processing (including collaborators in UK or abroad and centres within the NIHR Bioresource). ☐
6. I understand that my blood samples will be used in genetic research but the results will not be disclosed to me. ☐
7. I agree to gift blood samples and images taken for the purpose of the research study to the University of Oxford. If a commercial product were developed as a result of this study, I will not profit financially from such a product. ☐
8. I understand that anonymized images of my body (such as computed tomography and ultrasound images) obtained as part of this study or retrieved from my medical records, may be used in research publications. I give my consent for future use of these images for any publications that may arise from the research. ☐
9. I agree to take part in the above study. ☐
10. I agree to being contacted in the future to ask if I am interested in future studies. ☐

Study Full Title	The **O**xford **R**isk **F**actors **A**nd **N**on-invasive Imaging Study (The ORFAN study)
Patient ID	
Principal Investigator	Prof. Charalambos Antoniades (tel: 01865 228340)

Please initial box

CT Participants only-optional

11. I agree to undergo a computed tomography angiography scan at a follow up study visit for research purposes. ☐

12. In the case of any incidental findings during the follow up CT scan, I permit the study investigators to discuss the results with a relevant clinical specialist and to inform my General Practitioner or referring physician. ☐

Name of participant	Signature	Date
Name of person taking consent	Signature	Date

Appendix 2. Sample Ox-IMPACT consent form

CONSENT FORM Arm 1 version 2.0

Study Full Title	The **Oxford Im**aging of **P**erivascular adipose tissue in **A**cute coronary syndromes using **C**omputed **T**omography (The **Ox-IMPACT** study)
Patient ID	
Principal Investigator	Prof. Charalambos Antoniades (tel: 01865 228340)

Please initial box

1. I confirm that I have read and I understand the information sheet (Version 2.0, April 2017) for the above study. I have had the opportunity to consider the information, ask questions and have had these answered satisfactorily. ☐

2. I understand that my participation is voluntary and that I am free to withdraw at any time without giving any reason, without my medical care or legal rights being affected. ☐

3. I understand that relevant sections of my medical notes and data collected during the study may be looked at by individuals from the University of Oxford and the NHS Trust, where it is relevant to my taking part in this research. I permit these individuals access to my records. ☐

4. I understand that images and blood samples will be obtained as part of this study. I consider these samples a gift to the University of Oxford and I understand I will not gain any direct personal or financial benefit from them. If a commercial product were developed as a result of this study, I will not profit financially from such a product. ☐

5. I understand that the information held and maintained by NHS Digital and other central UK NHS bodies may be used to help contact me or provide information about my health status. ☐

6. I understand that the samples, images and information collected about me may be used in an anonymous form to support other research (or research publications) in the future, here or abroad (in EEA or non-EEA countries), which has ethical approval. It will not be possible for me to be identified by these. ☐

7. I agree to undergo computed tomography angiography scans for research purposes. ☐

DIVISION OF CARDIOVASCULAR MEDICINE Oxford University Hospitals NHS NHS Foundation Trust

Study Full Title	The **Oxford Im**aging of **P**erivascular adipose tissue in **A**cute coronary syndromes using **C**omputed **T**omography (The **Ox-IMPACT** study)
Patient ID	
Principal Investigator	Prof. Charalambos Antoniades (tel: 01865 228340)

Please initial box

8. I understand that these are research scans and they will not be used for medical diagnosis, as they are not routinely looked at by a doctor. However, if a concern is raised about a possible abnormality on my scan, I will only be informed if a doctor thinks it is medically important such that the finding has clear implications for my current or future health. ☐

9. **OPTIONAL:** I understand and agree that my blood samples will be used in research aimed at understanding the genetic influences on disease and that the results of these investigations are unlikely to have any implications for me personally. ☐

10. **OPTIONAL:** I agree to be contacted about ethically approved research studies for which I may be suitable. I understand that agreeing to be contacted does not oblige me to participate in any further studies. ☐

11. I agree to take part in the above study. ☐

Name of participant	Signature	Date

Name of person taking consent	Signature	Date

For researchers (✓) to document: original kept & copy given to participant (__); copy inserted into medical notes (_)

Appendix 3. Radiomic definitions

(Adapted from http://pyradiomics.readthedocs.io/en/latest/features.html – last accessed March 22, 2018)

The definitions of the radiomic features have been derived from the pyradiomics library and the pyradiomics community maintains the copyright for the definitions mentioned below (© Copyright 2016, pyradiomics community, http://github.com/radiomics/pyradiomics Revision eae15eff, last accessed July 27, 2019).

The pyradiomics package is covered by the open source 3-clause BSD License (© 2017 Harvard Medical School: https://github.com/Radiomics/pyradiomics/blob/master/LICENSE.txt, last accessed on July 27, 2019)

In my analysis, I measured a total of 843 radiomic features in PVAT, as summarised in Appendix Table A1.

Appendix Table A1. Breakdown of PVAT radiomic features.

	Original	Wavelets transformations (n=8)	All
First order	18	144	162
Shape-related	15	-	15
GLCM	23	184	207
GLDM	14	112	126
GLRLM	16	128	144
GLSZM	16	128	144
NGTDM	5	40	45
Total	107	736	843

GLCM: gray level co-occurrence matrix; GLDM: gray level dependence matrix; GLRLM: gray level run length matrix; GLSZM: gray level size zone matrix; NGTDM: neighbouring gray tone dependence matrix; PVAT: perivascular adipose tissue.

a. First Order Statistics

These statistics describe the central tendency, variability, uniformity, asymmetry, skewness and magnitude of the attenuation values in a given region of interest (ROI), disregarding the spatial relationship of the individual voxels. As such, they describe quantitative and qualitative features of the whole ROI (PVAT). A total of 19 features were calculated for each one of the eight wavelet transformations and the original CT image, as follows:

Let:

- $\boldsymbol{X}$ be a set of $\boldsymbol{N_p}$ voxels included in the region of interest (ROI)
- $\boldsymbol{P(i)}$ be the first order histogram with $\boldsymbol{N_g}$ discrete intensity levels, where $\boldsymbol{N_g}$ is the number of non-zero bins, equally spaced from 0 with a width.
- $\boldsymbol{p(i)}$ be the normalised first order histogram and equal to $\frac{\mathbf{P}(i)}{N_p}$
- $\mathbf{c}$ is a value that shifts the intensities to prevent negative values in X. This ensures that voxels with the lowest gray values contribute the least to Energy, instead of voxels with gray level intensity closest to 0. Since the HU range of AT (-190 to -30 HU) does not include zero, c was set at c=0. Therefore, higher energy corresponds to less radiodense AT, and therefore a higher lipophilic content.
- $\boldsymbol{\epsilon}$ is an arbitrarily small positive number ($\approx 2.2\times10^{-16}$)

Appendix Table A2. First-order radiomic features for PVAT characterisation

Radiomic feature	Interpretation
Energy $= \sum_{i=1}^{N_p} (\mathrm{X}(i) + c)^2$	**Energy** is a measure of the magnitude of voxel values in an image. A larger value implies a greater sum of the squares of these values.
Total Energy $= V_{voxel} \sum_{i=1}^{N_p} (\mathrm{X}(i) + c)^2$	**Total Energy** is the value of Energy feature scaled by the volume of the voxel in cubic mm.
Entropy $= -\sum_{i=1}^{N_g} p(i) \log_2 (p(i) + \epsilon)$	**Entropy** specifies the uncertainty/randomness in the image values. It measures the average amount of information required to encode the image values
Minimum $= min(\mathrm{X})$	The **minimum** gray level intensity within the ROI.
The **10th percentile** of X	The **10th percentile** of X
The **90th percentile** of X	The **90th percentile** of X
Maximum $= max(\mathrm{X})$	The **maximum** gray level intensity within the ROI.
Mean $= \frac{1}{N_p} \sum_{i=1}^{N_p} \mathrm{X}(i)$	The average (**mean**) gray level intensity within the ROI.
Median	The **median** gray level intensity within the ROI.
Interquartile range $= \mathrm{P}_{75} - \mathrm{P}_{25}$	Here P_{25} and P_{75} are the 25th and 75th percentile of the image array, respectively.
Range $= max(\mathrm{X}) - min(\mathrm{X})$	The range of gray values in the ROI.
MAD $= \frac{1}{N_p} \sum_{i=1}^{N_p} \lvert \mathrm{X}(i) - \overline{X} \rvert$	**Mean Absolute Deviation (MAD)** is the mean distance of all intensity values from the Mean Value of the image array.
rMAD $= \frac{1}{N_{10-90}} \sum_{i=1}^{N_{10-90}} \lvert \mathrm{X}_{10-90}(i) - \overline{X}_{10-90} \rvert$	**Robust Mean Absolute Deviation (rMAD)** is the mean distance of all intensity values from the Mean Value calculated on the subset of image array with gray levels in between, or equal to the 10th and 90th percentile.
RMS $= \sqrt{\frac{1}{N_p} \sum_{i=1}^{N_p} (\mathrm{X}(i) + c)^2}$	**Root Mean Squared (RMS)** is the square-root of the mean of all the squared intensity values. It is another measure of the magnitude of the image values. This feature is volume-confounded, a larger value of c increases the effect of volume-confounding.
Skewness $= \frac{\mu_3}{\sigma^3} = \frac{\frac{1}{N_p} \sum_{i=1}^{N_p} (\mathrm{X}(i) - \overline{X})^3}{(\sqrt{\frac{1}{N_p} \sum_{i=1}^{N_p} (\mathrm{X}(i) - \overline{X})^2})^3}$	**Skewness** measures the *asymmetry* of the distribution of values about the Mean value. Depending on where the tail is elongated and the mass of the distribution is concentrated, this value can be positive or negative. (Where μ^3 is the 3rd central moment).
Kurtosis $= \frac{\mu_4}{\sigma^4} = \frac{\frac{1}{N_p} \sum_{i=1}^{N_p} (\mathrm{X}(i) - \overline{X})^4}{(\frac{1}{N_p} \sum_{i=1}^{N_p} (\mathrm{X}(i) - \overline{X})^2)^2}$	**Kurtosis** is a measure of the '*peakedness*' of the distribution of values in the image ROI. A higher kurtosis implies that the mass of the distribution is concentrated towards the tail(s) rather than towards the mean. A lower kurtosis implies the reverse: that the mass of the distribution is concentrated towards a spike near the Mean value. (Where μ4 is the 4th central moment).
Variance $= \frac{1}{N_p} \sum_{i=1}^{N_p} (\mathrm{X}(i) - \overline{X})^2$	**Variance** is the the mean of the squared distances of each intensity value from the Mean value. This is a measure of the spread of the distribution about the mean.

Uniformity $= \sum_{i=1}^{N_g} p(i)^2$	**Uniformity** is a measure of the sum of the squares of each intensity value. This is a measure of the heterogeneity of the image array, ***where a greater uniformity implies a greater heterogeneity or a greater range of discrete intensity values***.

b. Shape-related Statistics

Shape-related statistics describe the size and shape of a given ROI, without taking into account the attenuation values of its voxels. Since they are independent of the gray level intensities, shape-related statistics were consistent across all wavelet transformation and the original CT image, and therefore were only calculated once. These were defined as follows:

Let:

V the volume of the ROI in mm^3

A the surface area of the ROI in mm^2

Appendix Table A3. Shape-related radiomic features for PVAT characterisation

Radiomic feature	Interpretation
$\mathbf{Volume} = \sum_{i=1}^{N} V_i$	The **volume** of the ROI V is approximated by multiplying the number of voxels in the ROI by the volume of a single voxel $\mathbf{V_i}$.
$\mathbf{Surface\ Area} = \sum_{i=1}^{N} \frac{1}{2}\lvert a_i b_i \times a_i c_i \rvert$	**Surface Area** is an approximation of the surface of the ROI in mm^2, calculated using a marching cubes algorithm, where ***N*** is the number of triangles forming the surface mesh of the volume (ROI), $\boldsymbol{a_i b_i}$ and $\boldsymbol{a_i c_i}$ are the edges of the $\boldsymbol{i^{th}}$ triangle formed by points $\boldsymbol{a_i}$, $\boldsymbol{b_i}$ and $\boldsymbol{c_i}$.
Surface to volume ratio $= \frac{A}{V}$	Here, a lower value indicates a more compact (sphere-like) shape. This feature is not dimensionless, and is therefore (partly) dependent on the volume of the ROI.
Sphericity $= \frac{\sqrt[3]{36\pi V^2}}{A}$	**Sphericity** is a measure of the roundness of the shape of the tumor region relative to a sphere. It is a dimensionless measure, independent of scale and orientation. The value range is 0<sphericity≤1, where a value of 1 indicates a perfect sphere (a sphere has the smallest possible surface area for a given volume, compared to other solids).
Volume Number	Total number of discrete volumes in the ROI.
Voxel Number	Total number of discrete voxels in the ROI.
Maximum 3D diameter	Maximum 3D diameter is defined as the largest pairwise Euclidean distance between surface voxels in the ROI (Feret Diameter).
Maximum 2D diameter (Slice)	Maximum 2D diameter (Slice) is defined as the largest pairwise Euclidean distance between ROI surface voxels in the row-column (generally the axial) plane.
Maximum 2D diameter (Column)	Maximum 2D diameter (Column) is defined as the largest pairwise Euclidean distance between ROI surface voxels in the row-slice (usually the coronal) plane.
Maximum 2D diameter (Row)	Maximum 2D diameter (Row) is defined as the largest pairwise Euclidean distance between tumor surface voxels in the column-slice (usually the sagittal) plane.
Major axis $= 4\sqrt{\lambda_{major}}$	
Minor axis $= 4\sqrt{\lambda_{minor}}$	
Least axis $= 4\sqrt{\lambda_{least}}$	

Elongation $= \sqrt{\frac{\lambda_{minor}}{\lambda_{major}}}$	Here, $\boldsymbol{\lambda_{major}}$ and $\boldsymbol{\lambda_{minor}}$ are the lengths of the largest and second largest principal component axes. The values range between 1 (circle-like (non-elongated)) and 0 (single point or 1 dimensional line).
Flatness $= \sqrt{\frac{\lambda_{least}}{\lambda_{major}}}$	Here, $\boldsymbol{\lambda_{major}}$ and $\boldsymbol{\lambda_{minor}}$ are the lengths of the largest and smallest principal component axes. The values range between 1 (non-flat, sphere-like) and 0 (a flat object).

Adapted from http://pyradiomics.readthedocs.io/en/latest/features.html – last accessed March 22, 2018. © Copyright 2016, pyradiomics community, http://github.com/radiomics/pyradiomics Revision eae15eff.

c. Gray Level Co-occurrence Matrix (GLCM)

In simple words, a GLCM describes the number of times a voxel of a given attenuation value $\boldsymbol{i}$ is located next to a voxel of $\boldsymbol{j}$. A GLCM of size $\boldsymbol{N_g \times N_g}$ describes the second-order joint probability function of an image region constrained by the mask and is defined as $P(\boldsymbol{i,j}|\boldsymbol{\delta,\theta})$. The $(\boldsymbol{i,j})^{th}$ element of this matrix represents the number of times the combination of levels $\boldsymbol{i}$ and $\boldsymbol{j}$ occur in two pixels in the image, that are separated by a distance of $\boldsymbol{\delta}$ pixels along angle $\boldsymbol{\theta}$. The distance $\boldsymbol{\delta}$ from the center voxel is defined as the distance according to the infinity norm. For $\boldsymbol{\delta=1}$, this results in 2 neighbors for each of 13 angles in 3D (26-connectivity) and for $\boldsymbol{\delta=2}$ a 98-connectivity (49 unique angles). In order to get rotationally invariant results, statistics are calculated in all directions and then averaged, to ensure a symmetrical GLCM.

Let:

$\boldsymbol{\epsilon}$ be an arbitrarily small positive number ($\approx \boldsymbol{2.2\times10-16}$)

$\mathbf{P}(\boldsymbol{i,j})$ be the co-occurence matrix for an arbitrary $\boldsymbol{\delta}$ and $\boldsymbol{\theta}$

$\mathbf{p}(\boldsymbol{i,j})$ be the normalised co-occurence matrix and equal to $\frac{P(i,j)}{\sum P(i,j)}$

Ng be the number of discrete intensity levels in the image

$\boldsymbol{p_x(i)} = \sum_{\boldsymbol{j=1}}^{\boldsymbol{N_g}} \boldsymbol{P(i,j)}$ be the marginal row probabilities

$\boldsymbol{p_y(j)} = \sum_{\boldsymbol{i=1}}^{\boldsymbol{N_g}} \boldsymbol{P(i,j)}$ be the marginal column probabilities

$\boldsymbol{\mu_x}$ be the mean gray level intensity of $\boldsymbol{p_x}$ and defined as $\boldsymbol{\mu_x} = \sum_{\boldsymbol{i=1}}^{\boldsymbol{N_g}} \boldsymbol{p_x(i)i}$

$\boldsymbol{\mu_y}$ be the mean gray level intensity of $\boldsymbol{p_y}$ and defined as $\boldsymbol{\mu_y} = \sum_{\boldsymbol{j=1}}^{\boldsymbol{N_g}} \boldsymbol{p_y(j)j}$

$\boldsymbol{\sigma_x}$ be the standard deviation of $\boldsymbol{p_x}$

$\boldsymbol{\sigma_y}$ be the standard deviation of $\boldsymbol{p_y}$

$$p_{x+y}(k) = \sum_{i=1}^{N_g} \sum_{j=1}^{N_g} p(i,j) \text{, where } i+j=k, \text{ and } k = 2,3,\dots,2N_g$$

$$p_{x-y}(k) = \sum_{i=1}^{N_g} \sum_{j=1}^{N_g} p(i,j) \text{, where } |i-j|=k, \text{ and } k = 0,1,\dots,N_g-1$$

$HX = -\sum_{i=1}^{N_g} p_x(i)\log_2(p_x(i)+\epsilon)$ be the entropy of $\boldsymbol{p_x}$

$HY = -\sum_{j=1}^{N_g} p_y(j)\log_2(p_y(j)+\epsilon)$ be the entropy of $\boldsymbol{p_y}$

$$HXY1 = -\sum_{i=1}^{N_g} \sum_{j=1}^{N_g} p(i,j)\log_2(p_x(i)p_y(j)+\epsilon)$$

$$HXY2 = -\sum_{i=1}^{N_g} \sum_{j=1}^{N_g} p_x(i)p_y(j)\log_2(p_x(i)p_y(j)+\epsilon)$$

For distance weighting, GLCM matrices are weighted by weighting factor W and then summed and normalised.. Weighting factor W is calculated for the distance between neighbouring voxels by $\boldsymbol{W = e^{-\|d\|^2}}$, where d is the distance for the associated angle.

Appendix Table A4. Gray Level Co-occurrence Matrix (GLCM) statistics for PVAT characterisation

Radiomic feature	Interpretation
Autocorrelation $= \sum_{i=1}^{N_g} \sum_{j=1}^{N_g} p(i,j)ij$	**Autocorrelation** is a measure of the magnitude of the fineness and coarseness of texture.
Joint average $= \mu_x = \sum_{i=1}^{N_g} \sum_{j=1}^{N_g} p(i,j)i$	Returns the mean gray level intensity of the i distribution.
Cluster prominence $= \sum_{i=1}^{N_g} \sum_{j=1}^{N_g} (i + j - \mu_x - \mu_y)^4 p(i,j)$	**Cluster Prominence** is a measure of the skewness and asymmetry of the GLCM. A higher value implies more asymmetry around the mean while a lower value indicates a peak near the mean value and less variation around the mean.
Cluster tendency $= \sum_{i=1}^{N_g} \sum_{j=1}^{N_g} (i + j - \mu_x - \mu_y)^2 p(i,j)$	**Cluster Tendency** is a measure of groupings of voxels with similar gray-level values.
Cluster shade $= \sum_{i=1}^{N_g} \sum_{j=1}^{N_g} (i + j - \mu_x - \mu_y)^3 p(i,j)$	**Cluster Shade** is a measure of the skewness and uniformity of the GLCM. A higher cluster shade implies greater asymmetry about the mean.
Contrast $= \sum_{i=1}^{N_g} \sum_{j=1}^{N_g} (i - j)^2 p(i,j)$	**Contrast** is a measure of the local intensity variation, favoring values away from the diagonal (i=j). A larger value correlates with a greater disparity in intensity values among neighbouring voxels.
Correlation $= \frac{\sum_{i=1}^{N_g} \sum_{j=1}^{N_g} p(i,j)ij - \mu_x \mu_y}{\sigma_x(i)\sigma_y(j)}$	**Correlation** is a value between 0 (uncorrelated) and 1 (perfectly correlated) showing the linear dependency of gray level values to their respective voxels in the GLCM.
Difference average $= \sum_{k=0}^{N_g-1} k p_{x-y}(k)$	**Difference Average** measures the relationship between occurrences of pairs with similar intensity values and occurrences of pairs with differing intensity values.
Difference entropy $= \sum_{k=0}^{N_g-1} p_{x-y}(k) \log_2 (p_{x-y}(k) + \epsilon)$	**Difference Entropy** is a measure of the randomness/variability in neighborhood intensity value differences.
Difference variance $= \sum_{k=0}^{N_g-1} (k - DA)^2 p_{x-y}(k)$	**Difference Variance** is a measure of heterogeneity that places higher weights on differing intensity level pairs that deviate more from the mean.

Joint energy $= \sum_{i=1}^{N_g} \sum_{j=1}^{N_g} (p(i,j))^2$	**Joint energy** is a measure of homogeneous patterns in the image. A greater **joint energy** implies that there are more instances of intensity value pairs in the image that neighbor each other at higher frequencies. (also known as Angular Second Moment).
Joint entropy $= -\sum_{i=1}^{N_g} \sum_{j=1}^{N_g} p(i,j) \log_2 (p(i,j) + \epsilon)$	**Joint entropy** is a measure of the randomness/variability in neighborhood intensity values.
IMC 1 $= \frac{HXY - HXY1}{\max\{HX, HY\}}$	**Informational measure of correlation 1**
IMC 2 $= \sqrt{1 - e^{-2(HXY2 - HXY)}}$	**Informational measure of correlation 2**
IDM $= \sum_{i=1}^{N_g} \sum_{j=1}^{N_g} \frac{p(i,j)}{1 + \lvert i-j \rvert^2}$	IDM (**inverse difference moment** a.k.a Homogeneity 2) is a measure of the local homogeneity of an image. IDM weights are the inverse of the Contrast weights (decreasing exponentially from the diagonal i=j in the GLCM).
IDMN $= \sum_{i=1}^{N_g} \sum_{j=1}^{N_g} \frac{p(i,j)}{1 + (\frac{\lvert i-j \rvert^2}{N_g^2})}$	IDMN (**inverse difference moment normalised**) is a measure of the local homogeneity of an image. IDMN weights are the inverse of the Contrast weights (decreasing exponentially from the diagonal i=j in the GLCM). Unlike Homogeneity2, IDMN normalises the square of the difference between neighbouring intensity values by dividing over the square of the total number of discrete intensity values.
ID $= \sum_{i=1}^{N_g} \sum_{j=1}^{N_g} \frac{p(i,j)}{1 + \lvert i-j \rvert}$	ID (**inverse difference** a.k.a. Homogeneity 1) is another measure of the local homogeneity of an image. With more uniform gray levels, the denominator will remain low, resulting in a higher overall value.
IDN $= \sum_{i=1}^{N_g} \sum_{j=1}^{N_g} \frac{p(i,j)}{1 + (\frac{\lvert i-j \rvert}{N_g})}$	IDN (**inverse difference normalised**) is another measure of the local homogeneity of an image. Unlike Homogeneity1, IDN normalises the difference between the neighbouring intensity values by dividing over the total number of discrete intensity values.
Inverse variance $= \sum_{i=1}^{N_g} \sum_{j=1}^{N_g} \frac{p(i,j)}{\lvert i-j \rvert^2}, i \neq j$	
Maximum probability $= max(p(i,j))$	**Maximum Probability** is occurrences of the most predominant pair of neighbouring intensity values (also known as Joint maximum).
Sum average $= \sum_{k=2}^{2N_g} p_{x+y}(k) k$	**Sum Average** measures the relationship between occurrences of pairs with lower

	intensity values and occurrences of pairs with higher intensity values.
Sum entropy $= \sum_{k=2}^{2N_g} p_{x+y}(k)\log_2\left(p_{x+y}(k)+\epsilon\right)$	**Sum Entropy** is a sum of neighborhood intensity value differences.
Sum squares $= \sum_{i=1}^{N_g}\sum_{j=1}^{N_g}(i-\mu_x)^2 p(i,j)$	**Sum of Squares** or Variance is a measure in the distribution of neigboring intensity level pairs about the mean intensity level in the GLCM. (Defined by IBSI as Joint Variance).

Adapted from http://pyradiomics.readthedocs.io/en/latest/features.html – last accessed March 22, 2018. © Copyright 2016, pyradiomics community, http://github.com/radiomics/pyradiomics Revision eae15eff.

d. Gray Level Size Zone Matrix (GLSZM)

A Gray Level Size Zone (GLSZM) describes gray level zones in a ROI, which are defined as the number of connected voxels that share the same gray level intensity. A voxel is considered connected if the distance is 1 according to the infinity norm (26-connected region in a 3D, 8-connected region in 2D). In a gray level size zone matrix $\boldsymbol{P(i,j)}$ the $\mathbf{(i,j)^{th}}$ element equals the number of zones with gray level $\boldsymbol{i}$ and size $\boldsymbol{j}$ appear in image. Contrary to GLCM and GLRLM, the GLSZM is rotation independent, with only one matrix calculated for all directions in the ROI.

Let:
$\mathbf{N_g}$ be the number of discreet intensity values in the image
$\mathbf{N_s}$ be the number of discreet zone sizes in the image
$\mathbf{N_p}$ be the number of voxels in the image
$\mathbf{N_z}$ be the number of zones in the ROI, which is equal to $\sum_{i=1}^{N_g}\sum_{j=1}^{N_s} \mathrm{P}(i,j)$ and $\boldsymbol{1 \le N_z \le N_p}$
$\boldsymbol{P(i,j)}$ be the size zone matrix
$\boldsymbol{p(i,j)}$ be the normalised size zone matrix, defined as $p(i,j) = \frac{\mathrm{P}(i,j)}{N_z}$
$\boldsymbol{\epsilon}$ is an arbitrarily small positive number ($\approx 2.2\times10-16$).

Appendix Table A5. Gray Level Size Zone Matrix (GLSZM) statistics for PVAT characterisation

Radiomic feature	Interpretation
SAE $= \frac{\sum_{i=1}^{N_g}\sum_{j=1}^{N_s}\frac{\mathrm{P}(i,j)}{j^2}}{N_z}$	**SAE (small area emphasis)** is a measure of the distribution of small size zones, with a greater value indicative of smaller size zones and more fine textures.
LAE $= \frac{\sum_{i=1}^{N_g}\sum_{j=1}^{N_s}\mathrm{P}(i,j)j^2}{N_z}$	**LAE (large area emphasis)** is a measure of the distribution of large area size zones, with a greater value indicative of larger size zones and more coarse textures.
GLN $= \frac{\sum_{i=1}^{N_g}(\sum_{j=1}^{N_s}\mathrm{P}(i,j))^2}{N_z}$	**GLN (gray level non-uniformity)** measures the variability of gray-level intensity values in the image, with a lower value indicating more homogeneity in intensity values.
GLNN $= \frac{\sum_{i=1}^{N_g}(\sum_{j=1}^{N_s}\mathrm{P}(i,j))^2}{N_z^2}$	**GLNN (gray level non-uniformity normalised)** measures the variability of gray-level intensity values in the image, with a lower value indicating a greater similarity in intensity values. This is the normalised version of the GLN formula.
SZN $= \frac{\sum_{j=1}^{N_s}(\sum_{i=1}^{N_g}\mathrm{P}(i,j))^2}{N_z}$	**SZN (size zone non-uniformity)** measures the variability of size zone volumes in the image, with

	a lower value indicating more homogeneity in size zone volumes.
SZNN $= \frac{\sum_{j=1}^{N_s} (\sum_{i=1}^{N_g} \mathrm{P}(i,j))^2}{N_z^2}$	**SZNN (size zone non-uniformity normalised)** measures the variability of size zone volumes throughout the image, with a lower value indicating more homogeneity among zone size volumes in the image. This is the normalised version of the SZN formula.
Zone Percentage $= \frac{N_z}{N_p}$	**ZP (Zone Percentage)** measures the coarseness of the texture by taking the ratio of number of zones and number of voxels in the ROI. Values are in range $\frac{1}{N_p} \leq ZP \leq 1$, with higher values indicating a larger portion of the ROI consists of small zones (indicates a more fine texture).
GLV $= \sum_{i=1}^{N_g} \sum_{j=1}^{N_s} p(i,j)(i-\mu)^2,$ where $\mu = \sum_{i=1}^{N_g} \sum_{j=1}^{N_s} p(i,j)i$	**Gray level variance (GLV)** measures the variance in gray level intensities for the zones.
ZV $= \sum_{i=1}^{N_g} \sum_{j=1}^{N_s} p(i,j)(j-\mu)^2,$ where $\mu = \sum_{i=1}^{N_g} \sum_{j=1}^{N_s} p(i,j)j$	**Zone Variance (ZV)** measures the variance in zone size volumes for the zones.
ZE $= -\sum_{i=1}^{N_g} \sum_{j=1}^{N_s} p(i,j)\log_2(p(i,j)+\epsilon)$	**Zone Entropy (ZE)** measures the uncertainty/randomness in the distribution of zone sizes and gray levels. A higher value indicates more heterogeneneity in the texture patterns.
LGLZE $= \frac{\sum_{i=1}^{N_g} \sum_{j=1}^{N_s} \frac{\mathrm{P}(i,j)}{i^2}}{N_z}$	**LGLZE (low gray level zone emphasis)** measures the distribution of lower gray-level size zones, with a higher value indicating a greater proportion of lower gray-level values and size zones in the image.
HGLZE $= \frac{\sum_{i=1}^{N_g} \sum_{j=1}^{N_s} \mathrm{P}(i,j)i^2}{N_z}$	**HGLZE (high gray level zone emphasis)** measures the distribution of the higher gray-level values, with a higher value indicating a greater proportion of higher gray-level values and size zones in the image.
SALGLE $= \frac{\sum_{i=1}^{N_g} \sum_{j=1}^{N_s} \frac{\mathrm{P}(i,j)}{i^2 j^2}}{N_z}$	**SALGLE (small area low gray level emphasis)** measures the proportion in the image of the joint distribution of smaller size zones with lower gray-level values.
SAHGLE $= \frac{\sum_{i=1}^{N_g} \sum_{j=1}^{N_s} \frac{\mathrm{P}(i,j)i^2}{j^2}}{N_z}$	**SAHGLE (small area high gray level emphasis)** measures the proportion in the image of the joint distribution of smaller size zones with higher gray-level values.
LALGLE $= \frac{\sum_{i=1}^{N_g} \sum_{j=1}^{N_s} \frac{\mathrm{P}(i,j)j^2}{i^2}}{N_z}$	**LALGLE (low area low gray level emphasis)** measures the proportion in the image of the joint distribution of larger size zones with lower gray-level values.
LAHGLE $= \frac{\sum_{i=1}^{N_g} \sum_{j=1}^{N_s} \mathrm{P}(i,j)i^2 j^2}{N_z}$	**LAHGLE (low area high gray level emphasis)** measures the proportion in the image of the joint distribution of larger size zones with higher gray-level values.

Adapted from http://pyradiomics.readthedocs.io/en/latest/features.html – last accessed March 22, 2018.

e. Gray Level Run Length Matrix (GLRLM)

A Gray Level Run Length Matrix (GLRLM) describes gray level runs, which are defined as the length in number of pixels, of consecutive pixels that have the same gray level value. In a gray level run length matrix $\boldsymbol{P(i,j|\theta)}$, the $\boldsymbol{(i,j)^{th}}$ element describes the number of runs with gray level $\boldsymbol{i}$ and length $\boldsymbol{j}$ occur in the image (ROI) along angle $\boldsymbol{\theta}$.

Let:
$\boldsymbol{N_g}$ be the number of discreet intensity values in the image
$\boldsymbol{N_r}$ be the number of discreet run lengths in the image
$\boldsymbol{N_p}$ be the number of voxels in the image
$\boldsymbol{N_z(\theta)}$ be the number of runs in the image along angle θ, which is equal to $\sum_{i=1}^{N_g} \sum_{j=1}^{N_r} \mathrm{P}(i,j|\theta)$ and $1 \leq \mathrm{N_z}(\theta) \leq \mathrm{N_p}$
$\boldsymbol{P(i,j|\theta)}$ be the run length matrix for an arbitrary direction θ
$\boldsymbol{p(i,j|\theta)}$ be the normalised run length matrix, defined as $p(i,j|\theta) = \frac{\mathrm{P}(i,j|\theta)}{N_z(\theta)}$
$\boldsymbol{\epsilon}$ is an arbitrarily small positive number (≈2.2×10−16).
By default, the value of a feature is calculated on the GLRLM for each angle separately, after which the mean of these values is returned. If distance weighting is enabled, GLRLMs are weighted by the distance between neighbouring voxels and then summed and normalised. Features are then calculated on the resultant matrix. The distance between neighbouring voxels is calculated for each angle using the norm specified in 'weightingNorm'.

Appendix Table A6. Gray Level Run Length Matrix (GLRLM) statistics for PVAT characterization

Radiomic feature	Interpretation
$\mathbf{SRE} = \frac{\sum_{i=1}^{N_g} \sum_{j=1}^{N_r} \frac{\mathrm{P}(i,j\|\theta)}{j^2}}{N_z(\theta)}$	**SRE (Short Run Emphasis)** is a measure of the distribution of short run lengths, with a greater value indicative of shorter run lengths and more fine textural textures.
$\mathbf{LRE} = \frac{\sum_{i=1}^{N_g} \sum_{j=1}^{N_r} \mathrm{P}(i,j\|\theta) j^2}{N_z(\theta)}$	**LRE (Long Run Emphasis)** is a measure of the distribution of long run lengths, with a greater value indicative of longer run lengths and more coarse structural textures.
$\mathbf{GLN} = \frac{\sum_{i=1}^{N_g} (\sum_{j=1}^{N_r} \mathrm{P}(i,j\|\theta))^2}{N_z(\theta)}$	**GLN (Gray Level Non-uniformity)** measures the similarity of gray-level intensity values in the image, where a lower GLN value correlates with a greater similarity in intensity values.
$\mathbf{GLNN} = \frac{\sum_{i=1}^{N_g} (\sum_{j=1}^{N_r} \mathrm{P}(i,j\|\theta))^2}{N_z(\theta)^2}$	**GLNN (Gray Level Non-uniformity Normalised)** measures the similarity of gray-level intensity values in the image, where a lower GLNN value correlates with a greater similarity in intensity values. This is the normalised version of the GLN formula.
$\mathbf{RLN} = \frac{\sum_{j=1}^{N_r} (\sum_{i=1}^{N_g} \mathrm{P}(i,j\|\theta))^2}{N_z(\theta)}$	**RLN (Run Length Non-uniformity)** measures the similarity of run lengths throughout the image, with a lower value indicating more homogeneity among run lengths in the image.

$\textbf{RLNN} = \frac{\sum_{j=1}^{N_r} (\sum_{i=1}^{N_g} \mathrm{P}(,j\|\theta))^2}{N_z(\theta)^2}$	**RLNN (Run Length Non-uniformity)** measures the similarity of run lengths throughout the image, with a lower value indicating more homogeneity among run lengths in the image. This is the normalised version of the RLN formula.
$\textbf{RP} = \frac{N_z(\theta)}{N_p}$	**RP (Run Percentage)** measures the coarseness of the texture by taking the ratio of number of runs and number of voxels in the ROI. Values are in range $\frac{1}{N_p} \leq RP \leq 1$, with higher values indicating a larger portion of the ROI consists of short runs (indicates a more fine texture).
$\textbf{GLV} = \sum_{i=1}^{N_g} \sum_{j=1}^{N_r} p(i,j\|\theta)(i-\mu)^2,$ where $\mu = \sum_{i=1}^{N_g} \sum_{j=1}^{N_r} p(i,j\|\theta) i$	**GLV (Gray Level Variance)** measures the variance in gray level intensity for the runs.
$\textbf{RV} = \sum_{i=1}^{N_g} \sum_{j=1}^{N_r} p(i,j\|\theta)(j-\mu)^2,$ where $\mu = \sum_{i=1}^{N_g} \sum_{j=1}^{N_r} p(i,j\|\theta) j$	**RV (Run Variance)** is a measure of the variance in runs for the run lengths.
$\textbf{RE} = -\sum_{i=1}^{N_g} \sum_{j=1}^{N_r} p(i,j\|\theta) \log_2 (p(i,j\|\theta) + \epsilon)$	**RE (Run Entropy)** measures the uncertainty/randomness in the distribution of run lengths and gray levels. A higher value indicates more heterogeneity in the texture patterns.
$\textbf{LGLRE} = \frac{\sum_{i=1}^{N_g} \sum_{j=1}^{N_r} \frac{\mathrm{P}(i,j\|\theta)}{i^2}}{N_z(\theta)}$	**LGLRE (low gray level run emphasis)** measures the distribution of low gray-level values, with a higher value indicating a greater concentration of low gray-level values in the image.
$\textbf{HGLRE} = \frac{\sum_{i=1}^{N_g} \sum_{j=1}^{N_r} \mathrm{P}(i,j\|\theta) i^2}{N_z(\theta)}$	**HGLRE (high gray level run emphasis)** measures the distribution of the higher gray-level values, with a higher value indicating a greater concentration of high gray-level values in the image.
$\textbf{SRLGLE} = \frac{\sum_{i=1}^{N_g} \sum_{j=1}^{N_r} \frac{\mathrm{P}(i,j\|\theta)}{i^2 j^2}}{N_z(\theta)}$	**SRLGLE (short run low gray level emphasis)** measures the joint distribution of shorter run lengths with lower gray-level values.
$\textbf{SRHGLE} = \frac{\sum_{i=1}^{N_g} \sum_{j=1}^{N_r} \frac{\mathrm{P}(i,j\|\theta) i^2}{j^2}}{N_z(\theta)}$	**SRHGLE (short run high gray level emphasis)** measures the joint distribution of shorter run lengths with higher gray-level values.
$\textbf{LRLGLRE} = \frac{\sum_{i=1}^{N_g} \sum_{j=1}^{N_r} \frac{\mathrm{P}(i,j\|\theta) j^2}{i^2}}{N_z(\theta)}$	**LRLGLRE (long run low gray level emphasis)** measures the joint distribution of long run lengths with lower gray-level values.
$\textbf{LRHGLRE} = \frac{\sum_{i=1}^{N_g} \sum_{j=1}^{N_r} \mathrm{P}(i,j\|\theta) i^2 j^2}{N_z(\theta)}$	**LRHGLRE (long run high gray level run emphasis)** measures the joint distribution of long run lengths with higher gray-level values.

Adapted from http://pyradiomics.readthedocs.io/en/latest/features.html – last accessed March 22, 2018. © Copyright 2016, pyradiomics community, http://github.com/radiomics/pyradiomics Revision eae15eff.

f. Neigbouring Gray Tone Difference Matrix (NGTDM) Features

A Neighbouring Gray Tone Difference Matrix quantifies the difference between a gray value and the average gray value of its neighbours within distance $\boldsymbol{\delta}$. The sum of absolute differences for gray level $\boldsymbol{i}$ is stored in the matrix. Let $\mathbf{X_{gl}}$ be a set of segmented voxels and $x_{gl}(j_x, j_y, j_z) \in \mathrm{X}_{gl}$ be the gray level of a voxel at postion (j_x, j_y, j_z), then the average gray level of the neigbourhood is:

$$\overline{A}_i = \overline{A}(j_x, j_y, j_z)$$
$$= \frac{1}{W} \sum_{k_x=-\delta}^{\delta} \sum_{k_y=-\delta}^{\delta} \sum_{k_z=-\delta}^{\delta} x_{gl}(j_x + k_x, j_y + k_y, j_z + k_z),$$

where $(k_x, k_y, k_z) \neq (0,0,0)$ and $x_{gl}(j_x + k_x, j_y + k_y, j_z + k_z) \in \mathrm{X}_{gl}$

Here, $\boldsymbol{W}$ is the number of voxels in the neighbourhood that are also in $\boldsymbol{X_{gl}}$.

Let:
$\boldsymbol{n_i}$ be the number of voxels in $\boldsymbol{X_{gl}}$ with gray level $\boldsymbol{i}$
$\boldsymbol{N_{v,p}}$ be the total number of voxels in $\boldsymbol{X_{gl}}$ and equal to $\sum n_i$ (i.e. the number of voxels with a valid region; at least 1 neighbor). $N_{v,p} \leq N_p$, where N_p is the total number of voxels in the ROI.
$\boldsymbol{p_i}$ be the gray level probability and equal to n_i/N_v

$s_i = \begin{cases} \sum^{n_i} |i - \overline{A}_i| & \text{for } n_i \neq 0 \\ 0 & \text{for } n_i = 0 \end{cases}$ be the sum of absolute differences for gray level i

$\boldsymbol{N_g}$ be the number of discreet gray levels
$\boldsymbol{N_{g,p}}$ be the number of gray levels where $\boldsymbol{p_i} \neq 0$

Appendix Table A7. Neigbouring Gray Tone Difference Matrix (NGTDM) for PVAT characterization

Radiomic feature	Interpretation
$\boldsymbol{Coarseness} = \frac{1}{\sum_{i=1}^{N_g} p_i s_i}$	**Coarseness** is a measure of average difference between the center voxel and its neighbourhood and is an indication of the spatial rate of change. A higher value indicates a lower spatial change rate and a locally more uniform texture.
$\boldsymbol{Contrast} = \left(\frac{1}{N_{g,p}(N_{g,p}-1)} \sum_{i=1}^{N_g} \sum_{j=1}^{N_g} p_i p_j (i - j)^2 \right) \left(\frac{1}{N_{v,p}} \sum_{i=1}^{N_g} s_i \right),$ where $p_i \neq 0, p_j \neq 0$	**Contrast** is a measure of the spatial intensity change, but is also dependent on the overall gray level dynamic range. Contrast is high when both the dynamic range and the spatial change rate are high, i.e. an image with a large range of gray levels, with large changes between voxels and their neighbourhood.

$\boldsymbol{Busyness} = \frac{\sum_{i=1}^{N_g} p_i s_i}{\sum_{i=1}^{N_g} \quad \sum_{j=1}^{N_g} \lvert i p_i - j p_j \rvert}$, where $p_i \neq 0, p_j \neq 0$	A measure of the change from a pixel to its neighbour. A high value for busyness indicates a 'busy' image, with rapid changes of intensity between pixels and its neighbourhood.
$\boldsymbol{Complexity} = \frac{1}{N_{v,p}} \sum_{i=1}^{N_g} \sum_{j=1}^{N_g} \lvert i - j \rvert \frac{p_i s_i + p_j s_j}{p_i + p_j}$, where $p_i \neq 0, p_j \neq 0$	An image is considered complex when there are many primitive components in the image, i.e. the image is non-uniform and there are many rapid changes in gray level intensity.
$\boldsymbol{Strength} = \frac{\sum_{i=1}^{N_g} \quad \sum_{j=1}^{N_g} (p_i + p_j)(i - j)^2}{\sum_{i=1}^{N_g} s_i}$, where $p_i \neq 0, p_j \neq 0$	**Strength** is a measure of the primitives in an image. Its value is high when the primitives are easily defined and visible, i.e. an image with slow change in intensity but more large coarse differences in gray level intensities.

Adapted from http://pyradiomics.readthedocs.io/en/latest/features.html – last accessed March 22, 2018. © Copyright 2016, pyradiomics community, http://github.com/radiomics/pyradiomics Revision eae15eff.

g. Gray Level Dependence Matrix (GLDM)

A Gray Level Dependence Matrix (GLDM) quantifies gray level dependencies in an image. A gray level dependency is defined as the number of connected voxels within distance $\boldsymbol{\delta}$ that are dependent on the center voxel. A neighbouring voxel with gray level $\boldsymbol{j}$ is considered dependent on center voxel with gray level $\boldsymbol{i}$ if $\boldsymbol{|i-j| \leq \alpha}$. In a gray level dependence matrix $\boldsymbol{P(i,j)}$ the $\boldsymbol{(i,j)^{th}}$ element describes the number of times a voxel with gray level $\boldsymbol{i}$ with $\boldsymbol{j}$ dependent voxels in its neighbourhood appears in image.

$\boldsymbol{N_g}$ be the number of discreet intensity values in the image
$\boldsymbol{N_d}$ be the number of discreet dependency sizes in the image
$\boldsymbol{N_z}$ be the number of dependency zones in the image, which is equal to $\sum_{i=1}^{N_g} \quad \sum_{j=1}^{N_d} \mathrm{P}(i,j)$
$\boldsymbol{P(i,j)}$ be the dependence matrix
$\boldsymbol{p(i,j)}$ be the normalised dependence matrix, defined as $p(i,j) = \frac{\mathrm{P}(i,j)}{N_z}$

Appendix Table A7. Gray Level Dependence Matrix (GLDM) statistics for PVAT characterization

Radiomic feature	Interpretation
$\boldsymbol{SDE} = \frac{\sum_{i=1}^{N_g} \quad \sum_{j=1}^{N_d} \frac{\mathrm{P}(i,j)}{i^2}}{N_z}$	**SDE (Small Dependence Emphasis)**: A measure of the distribution of small dependencies, with a greater value indicative of smaller dependence and less homogeneous textures.
$\boldsymbol{LDE} = \frac{\sum_{i=1}^{N_g} \quad \sum_{j=1}^{N_d} \mathrm{P}(i,j) j^2}{N_z}$	**LDE (Large Dependence Emphasis)**: A measure of the distribution of large dependencies, with a greater value indicative of larger dependence and more homogeneous textures.
$\boldsymbol{GLN} = \frac{\sum_{i=1}^{N_g} \quad (\sum_{j=1}^{N_d} \mathrm{P}(i,j))^2}{\sum_{i=1}^{N_g} \quad \sum_{j=1}^{N_d} \quad \mathrm{P}(i,j)}$	**GLN (Gray Level Non-Uniformity)**: Measures the similarity of gray-level intensity values in the image, where a lower GLN value correlates with a greater similarity in intensity values.
$\boldsymbol{DN} = \frac{\sum_{j=1}^{N_d} \quad (\sum_{i=1}^{N_g} \mathrm{P}(i,j))^2}{N_z}$	**DN (Dependence Non-Uniformity)**: Measures the similarity of dependence throughout the image, with a lower value indicating more homogeneity among dependencies in the image.

$$\boldsymbol{DNN} = \frac{\sum_{j=1}^{N_d} (\sum_{i=1}^{N_g} \mathrm{P}(i,j))^2}{N_z^2}$$	**DNN (Dependence Non-Uniformity Normalised)**: Measures the similarity of dependence throughout the image, with a lower value indicating more homogeneity among dependencies in the image. This is the normalised version of the DLN formula.
$$\boldsymbol{GLV} = \sum_{i=1}^{N_g} \sum_{j=1}^{N_d} p(i,j)(i-\mu)^2 ,$$ where $\mu = \sum_{i=1}^{N_g} \sum_{j=1}^{N_d} ip(i,j)$	**GLV (Gray Level Variance)**: Measures the variance in grey level in the image.
$$\boldsymbol{DV} = \sum_{i=1}^{N_g} \sum_{j=1}^{N_d} p(i,j)(j-\mu)^2 ,$$ where $\mu = \sum_{i=1}^{N_g} \sum_{j=1}^{N_d} jp(i,j)$	**DV (Dependence Variance)**: Measures the variance in dependence size in the image.
$$\boldsymbol{DE} = -\sum_{i=1}^{N_g} \sum_{j=1}^{N_d} p(i,j)\log_2 (p(i,j) + \epsilon)$$	**DE (Dependence Entropy)**: Measures the entropy in dependence size in the image.
$$\boldsymbol{LGLE} = \frac{\sum_{i=1}^{N_g} \sum_{j=1}^{N_d} \frac{\mathrm{P}(i,j)}{i^2}}{N_z}$$	**LGLE (Low Gray Level Emphasis)**: Measures the distribution of low gray-level values, with a higher value indicating a greater concentration of low gray-level values in the image.
$$\boldsymbol{HGLE} = \frac{\sum_{i=1}^{N_g} \sum_{j=1}^{N_d} \mathrm{P}(i,j)i^2}{N_z}$$	**HGLE (High Gray Level Emphasis)**: Measures the distribution of the higher gray-level values, with a higher value indicating a greater concentration of high gray-level values in the image.
$$\boldsymbol{SDLGLE} = \frac{\sum_{i=1}^{N_g} \sum_{j=1}^{N_d} \frac{\mathrm{P}(i,j)}{i^2 j^2}}{N_z}$$	**SDLGLE (Small Dependence Low Gray Level Emphasis)**: Measures the joint distribution of small dependence with lower gray-level values.C
$$\boldsymbol{SDHGLE} = \frac{\sum_{i=1}^{N_g} \sum_{j=1}^{N_d} \frac{\mathrm{P}(i,j)i^2}{j^2}}{N_z}$$	**SDHGLE (Small Dependence High Gray Level Emphasis)**: Measures the joint distribution of small dependence with higher gray-level values.
$$\boldsymbol{LDLGLE} = \frac{\sum_{i=1}^{N_g} \sum_{j=1}^{N_d} \frac{\mathrm{P}(i,j)j^2}{i^2}}{N_z}$$	**LDLGLE (Large Dependence Low Gray Level Emphasis)**: Measures the joint distribution of large dependence with lower gray-level values.
$$\boldsymbol{LDHGLE} = \frac{\sum_{i=1}^{N_g} \sum_{j=1}^{N_d} \mathrm{P}(i,j)i^2 j^2}{N_z}$$	**LDHGLE (Large Dependence High Gray Level Emphasis)**: Measures the joint distribution of large dependence with higher gray-level values.

Adapted from http://pyradiomics.readthedocs.io/en/latest/features.html – last accessed March 22, 2018. © Copyright 2016, pyradiomics community, http://github.com/radiomics/pyradiomics Revision eae15eff.

Appendix 4. Individual perivascular fat radiomic features & cardiac risk

This table represents the P values for discrimination of 5-year major adverse cardiac events from matched "healthy" controls using pericoronary adipose tissue radiomic features, as calculated in Chapter 5, Arm 2 (n=202 patients, n=101 in each group).

P values are derived from a discrimination analysis using receiver operating characteristic curves and C-statistics. Individual radiomic features are ranked in a descending order using the negative logarithm (log_{10}) of the corresponding P value.

Radiomic features are presented in the following format: [Name Wavelet Vessel], where LCA=left coronary artery, RCA=right coronary artery.

Rank	Radiomic feature	P value	-log(P value)
1	Energy HLL RCA	.000	3.915592
2	Median RCA	.000	3.845601
3	Skewness LLL RCA	.000	3.755377
4	Median LLL RCA	.000	3.635426
5	RunEntropy LLL RCA	.000	3.537673
6	X90Percentile RCA	.000	3.503381
7	Mean RCA	.000	3.385701
8	Kurtosis RCA	.000	3.385701
9	Mean LLL RCA	.000	3.35021
10	RootMeanSquared RCA	.000	3.346279
11	RootMeanSquared LLL RCA	.000	3.34235
12	Uniformity LLL RCA	.000	3.330576
13	RunEntropy HHL RCA	.000	3.318824
14	GrayLevelNonUniformityNormalised LLL RCA	.001	3.299285
15	Uniformity RCA	.001	3.256508
16	GrayLevelNonUniformityNormalised RCA	.001	3.129897
17	Skewness RCA	.001	3.118514
18	GrayLevelNonUniformityNormalised LLL RCA.1	.001	3.099591
19	Entropy LLL RCA	.001	3.061922
20	Kurtosis LLL RCA	.001	3.054417
21	SmallAreaLowGrayLevelEmphasis RCA	.001	3.050667
22	GrayLevelNonUniformityNormalised RCA.1	.001	3.035694
23	X10Percentile LLL RCA	.001	2.965088
24	GrayLevelVariance RCA.2	.001	2.942968
25	X10Percentile RCA	.001	2.915437
26	Entropy RCA	.001	2.909947
27	GrayLevelVariance HLL RCA.2	.001	2.884397
28	InterquartileRange LLL RCA	.001	2.873482
29	SumEntropy LLL RCA	.001	2.830034
30	SizeZoneNonUniformity HLL RCA	.002	2.815626
31	RobustMeanAbsoluteDeviation LLL RCA	.002	2.79767
32	InterquartileRange RCA	.002	2.749481
33	MaximumProbability RCA	.002	2.715827
34	SumEntropy RCA	.002	2.715827
35	LowGrayLevelZoneEmphasis RCA	.002	2.680631
36	MeanAbsoluteDeviation LLL RCA	.002	2.677124
37	RobustMeanAbsoluteDeviation RCA	.002	2.614404
38	GrayLevelVariance LLL RCA.2	.002	2.610942
39	RunEntropy RCA	.002	2.604024
40	Variance LLL RCA	.003	2.566146
41	RunEntropy HLL RCA	.003	2.562717
42	GrayLevelVariance LLL RCA	.003	2.562717
43	SizeZoneNonUniformity HHL RCA	.003	2.55929
44	SmallAreaEmphasis HHH RCA	.003	2.555865
45	GrayLevelVariance LLL RCA.1	.003	2.542189
46	Energy HHH RCA	.003	2.521746
47	MeanAbsoluteDeviation RCA	.003	2.494619

Rank	Radiomic feature	P value	-log(P value)
48	SizeZoneNonUniformityNormalised HHH RCA	.003	2.474371
49	MaximumProbability LLL RCA	.004	2.450856
50	DependenceEntropy HLL RCA	.004	2.450856
51	JointEnergy RCA	.004	2.447506
52	GrayLevelVariance HHL RCA.2	.004	2.440813
53	GrayLevelNonUniformityNormalised HLL RCA.1	.004	2.414134
54	GrayLevelVariance RCA.1	.004	2.371098
55	Variance RCA	.004	2.348088
56	LowGrayLevelEmphasis RCA	.005	2.338262
57	GrayLevelVariance RCA	.005	2.334991
58	JointEntropy RCA	.005	2.331722
59	LowGrayLevelRunEmphasis RCA	.005	2.328456
60	ShortRunLowGrayLevelEmphasis RCA	.006	2.234747
61	Idn LHL LCA	.006	2.23155
62	JointEnergy LLL RCA	.006	2.23155
63	LongRunHighGrayLevelEmphasis HLL RCA	.006	2.206061
64	SmallDependenceLowGrayLevelEmphasis RCA	.006	2.206061
65	LowGrayLevelEmphasis HLL RCA	.006	2.196541
66	ShortRunLowGrayLevelEmphasis HLL RCA	.006	2.193372
67	ZoneEntropy HHH RCA	.007	2.174408
68	Minimum HLL RCA	.007	2.174408
69	LongRunLowGrayLevelEmphasis RCA	.007	2.164957
70	LowGrayLevelRunEmphasis HLL RCA	.007	2.164957
71	Energy HLH RCA	.007	2.161812
72	ClusterTendency RCA	.007	2.155527
73	SmallAreaHighGrayLevelEmphasis HLL RCA	.007	2.155527
74	HighGrayLevelZoneEmphasis HLL RCA	.007	2.146118
75	X90Percentile LLL RCA	.008	2.114905
76	Idmn HLH LCA	.008	2.09474
77	ClusterTendency LLL RCA	.008	2.090101
78	JointEntropy LLL RCA	.008	2.090101
79	ShortRunHighGrayLevelEmphasis HLL RCA	.008	2.080837
80	X10Percentile HLL RCA	.009	2.068518
81	HighGrayLevelEmphasis HLL RCA	.009	2.066981
82	SumSquares LLL RCA	.009	2.050108
83	Idmn LHL LCA	.009	2.048578
84	LowGrayLevelZoneEmphasis HLL RCA	.009	2.04399
85	HighGrayLevelRunEmphasis HLL RCA	.009	2.037882
86	SumSquares RCA	.009	2.037882
87	Kurtosis LHL LCA	.010	2.013538
88	JointAverage HLL RCA	.010	2.004448
89	SumAverage HLL RCA	.010	2.004448
90	RunEntropy HLL LCA	.010	2.001422
91	SmallAreaLowGrayLevelEmphasis HLL RCA	.010	2.001422
92	LongRunLowGrayLevelEmphasis HLL RCA	.010	1.995378
93	Autocorrelation HLL RCA	.010	1.986328
94	GrayLevelVariance HLL RCA	.011	1.975797
95	GrayLevelNonUniformityNormalised HLL LCA.1	.012	1.938415
96	DependenceEntropy LLL RCA	.012	1.920599
97	SumEntropy HLL RCA	.012	1.917637
98	DifferenceVariance HLL RCA	.012	1.917637
99	GrayLevelVariance HLL RCA.1	.012	1.914678
100	ZoneEntropy RCA	.012	1.908767
101	SmallAreaLowGrayLevelEmphasis HLL LCA	.013	1.901391
102	ClusterTendency HLL RCA	.013	1.89403
103	GrayLevelNonUniformityNormalised HLL RCA	.013	1.882281
104	Entropy HLL RCA	.013	1.873493
105	SumSquares HLL RCA	.014	1.864726
106	Variance HLL RCA	.014	1.855979
107	MeanAbsoluteDeviation HLL RCA	.014	1.85016
108	DifferenceVariance HLL LCA	.014	1.84435
109	GrayLevelNonUniformityNormalised HLL LCA	.014	1.84435
110	Uniformity HLL LCA	.015	1.828418

Rank	Radiomic feature	P value	-log(P value)
111	LowGrayLevelZoneEmphasis HLL LCA	.015	1.824085
112	SumEntropy HLL LCA	.015	1.818316
113	Contrast HLL LCA	.015	1.818316
114	JointEntropy HLL RCA	.015	1.815435
115	X10Percentile HLL LCA	.016	1.795331
116	RootMeanSquared HLL RCA	.016	1.789607
117	SmallDependenceHighGrayLevelEmphasis HLL RCA	.017	1.782465
118	Uniformity HLL RCA	.017	1.781039
119	LargeDependenceLowGrayLevelEmphasis HLL LCA	.017	1.778187
120	RobustMeanAbsoluteDeviation HLL LCA	.017	1.775338
121	SizeZoneNonUniformity HLH RCA	.017	1.772491
122	Entropy HLL LCA	.017	1.772491
123	InterquartileRange HLL LCA	.017	1.772491
124	Contrast HLL RCA	.017	1.772491
125	ClusterProminence HLL RCA	.017	1.769647
126	LargeDependenceLowGrayLevelEmphasis HLL RCA	.017	1.763964
127	RobustMeanAbsoluteDeviation HLL RCA	.017	1.758291
128	LongRunLowGrayLevelEmphasis HLL LCA	.018	1.749798
129	Median HHH LCA	.018	1.748384
130	MeanAbsoluteDeviation HLL LCA	.018	1.746971
131	InterquartileRange HLL RCA	.018	1.744147
132	LowGrayLevelRunEmphasis HLL LCA	.018	1.739915
133	DifferenceEntropy HLL RCA	.018	1.738506
134	HighGrayLevelZoneEmphasis HLL LCA	.019	1.730061
135	ShortRunLowGrayLevelEmphasis HLL LCA	.019	1.723039
136	JointEnergy HLL LCA	.019	1.721636
137	GrayLevelNonUniformity HLH RCA	.019	1.718832
138	JointEntropy HLL LCA	.019	1.718832
139	ShortRunHighGrayLevelEmphasis HLL LCA	.019	1.716031
140	LowGrayLevelEmphasis HLL LCA	.019	1.714631
141	SmallDependenceHighGrayLevelEmphasis HLL LCA	.019	1.713232
142	HighGrayLevelRunEmphasis HLL LCA	.019	1.713232
143	DifferenceAverage HLL LCA	.020	1.706244
144	HighGrayLevelEmphasis HLL LCA	.020	1.69927
145	RunEntropy HLH RCA	.020	1.69927
146	JointEnergy HLL RCA	.021	1.688142
147	Autocorrelation HLL LCA	.021	1.67705
148	SmallAreaHighGrayLevelEmphasis HLL LCA	.022	1.665995
149	X90Percentile HLL LCA	.022	1.663236
150	DifferenceAverage HLL RCA	.022	1.66048
151	JointAverage HLL LCA	.022	1.66048
152	SumAverage HLL LCA	.022	1.66048
153	LargeDependenceHighGrayLevelEmphasis LLH RCA	.023	1.638514
154	DifferenceEntropy HLL LCA	.023	1.637146
155	Minimum HLL LCA	.024	1.613976
156	Maximum2DDiameterSlice LCA	.024	1.611261
157	Energy HLL LCA	.024	1.611261
158	LongRunHighGrayLevelEmphasis HLL LCA	.025	1.603129
159	Minimum LLL RCA	.025	1.597719
160	Range LLL RCA	.025	1.595018
161	SizeZoneNonUniformity HHH RCA	.026	1.589621
162	GrayLevelVariance HLL LCA	.026	1.584234
163	SumSquares HLL LCA	.026	1.581544
164	Variance HLL LCA	.026	1.578856
165	MaximumProbability HLL LCA	.026	1.577512
166	RootMeanSquared HLL LCA	.027	1.57617
167	Id HLL RCA	.027	1.568126
168	InverseVariance HLL LCA	.027	1.566788
169	GrayLevelVariance HLL LCA.1	.028	1.560103
170	MaximumProbability HLL RCA	.028	1.560103
171	Id HLL LCA	.028	1.560103
172	Idm HLL RCA	.028	1.546776
173	SizeZoneNonUniformity LHH RCA	.029	1.544117

Rank	Radiomic feature	P value	-log(P value)
174	GrayLevelVariance HHL RCA.1	.029	1.541461
175	JointEnergy LCA	.029	1.538806
176	Autocorrelation HHL RCA	.029	1.533505
177	X90Percentile HLL RCA	.029	1.530857
178	Idm HLL LCA	.030	1.529535
179	SmallDependenceLowGrayLevelEmphasis HLL RCA	.030	1.518972
180	Mean HHL RCA	.031	1.507132
181	DifferenceVariance LLL RCA	.031	1.507132
182	DifferenceVariance HHL RCA	.031	1.504508
183	InverseVariance HLL RCA	.031	1.501885
184	DependenceEntropy HLL LCA	.032	1.500574
185	RunEntropy HHH RCA	.032	1.496646
186	GrayLevelNonUniformityNormalised HHL RCA	.032	1.491417
187	GrayLevelVariance HHH RCA.2	.033	1.486196
188	MaximumProbability LCA	.033	1.484893
189	DifferenceEntropy HHL RCA	.034	1.473185
190	ClusterTendency HLL LCA	.034	1.467996
191	Maximum HHL RCA	.034	1.462816
192	JointEntropy HHL RCA	.035	1.457645
193	Skewness HHH RCA	.035	1.455062
194	LargeDependenceHighGrayLevelEmphasis HLL RCA	.035	1.453772
195	SumSquares HHL RCA	.036	1.447329
196	GrayLevelVariance HHL RCA	.036	1.444756
197	Entropy HHL RCA	.036	1.442185
198	JointAverage HHL RCA	.036	1.439617
199	SumAverage HHL RCA	.036	1.439617
200	Contrast LLL RCA	.037	1.43705
201	Uniformity HHL RCA	.037	1.434486
202	RunEntropy HHL LCA	.037	1.433205
203	GrayLevelVariance HLL LCA.2	.037	1.426807
204	ClusterProminence HHL RCA	.037	1.426807
205	ClusterShade HLL LCA	.038	1.424252
206	Range HLL RCA	.038	1.421699
207	JointEntropy LCA	.039	1.412781
208	Contrast RCA	.039	1.411509
209	SumEntropy HHL RCA	.039	1.408967
210	DifferenceVariance RCA	.039	1.408967
211	Contrast HHL RCA	.039	1.40389
212	SmallAreaEmphasis HHL RCA	.039	1.40389
213	Variance HHL RCA	.040	1.396292
214	JointEnergy LLL LCA	.040	1.396292
215	RootMeanSquared HHL RCA	.040	1.393763
216	Maximum LHH LCA	.041	1.388713
217	X90Percentile HHL RCA	.042	1.381155
218	JointEnergy HHL RCA	.042	1.376127
219	Range HHL RCA	.043	1.366099
220	HighGrayLevelZoneEmphasis HHL RCA	.043	1.363597
221	HighGrayLevelEmphasis HHL RCA	.044	1.358601
222	DifferenceEntropy LLL RCA	.044	1.358601
223	DifferenceAverage RCA	.044	1.356106
224	Id RCA	.045	1.348635
225	Idm RCA	.045	1.348635
226	Idmn RCA	.045	1.348635
227	Mean HHH LCA	.045	1.344907
228	ZoneEntropy LLL RCA	.045	1.343665
229	MaximumProbability HHL RCA	.047	1.33128
230	InverseVariance LLL RCA	.047	1.32881
231	LongRunHighGrayLevelEmphasis HHL RCA	.047	1.326341
232	DifferenceAverage LLL RCA	.047	1.326341
233	ClusterTendency HHL RCA	.047	1.323876
234	MeanAbsoluteDeviation HHL RCA	.047	1.323876
235	LongRunHighGrayLevelEmphasis LCA	.047	1.323876
236	Skewness LLL LCA	.048	1.320181

Rank	Radiomic feature	P value	-log(P value)
237	Idn RCA	.048	1.316491
238	InterquartileRange LCA	.048	1.316491
239	X10Percentile HHL RCA	.049	1.314034
240	Idm LLL RCA	.049	1.31158
241	Id LLL RCA	.049	1.309127
242	InverseVariance RCA	.050	1.304229
243	Kurtosis HHL LCA	.050	1.301783
244	DifferenceEntropy RCA	.050	1.301783
245	Median HHL RCA	.050	1.301783
246	HighGrayLevelRunEmphasis HHL RCA	.050	1.299339
247	Kurtosis LCA	.051	1.295678
248	Idmn HLL LCA	.051	1.28837
249	LargeDependenceHighGrayLevelEmphasis HHL RCA	.052	1.287154
250	Uniformity LLL LCA	.052	1.285939
251	DifferenceAverage HHL RCA	.052	1.284724
252	InterquartileRange LLL LCA	.053	1.277446
253	GrayLevelVariance HHL LCA.2	.053	1.275025
254	MaximumProbability LLL LCA	.053	1.273815
255	RobustMeanAbsoluteDeviation HHL RCA	.054	1.270189
256	GrayLevelNonUniformityNormalised LLL LCA	.054	1.270189
257	JointEntropy LLL LCA	.055	1.25934
258	ClusterProminence LLL RCA	.056	1.253332
259	InterquartileRange HHL RCA	.056	1.250933
260	Range LHH LCA	.057	1.246141
261	RobustMeanAbsoluteDeviation LCA	.058	1.240163
262	Uniformity LCA	.058	1.236584
263	Idn LLH LCA	.058	1.2342
264	Idm HHL RCA	.060	1.222314
265	RobustMeanAbsoluteDeviation LLL LCA	.061	1.212845
266	Maximum LLL RCA	.062	1.208124
267	Entropy LLL LCA	.062	1.206945
268	GrayLevelNonUniformityNormalised LCA	.062	1.204589
269	SmallAreaLowGrayLevelEmphasis HHH RCA	.063	1.201059
270	RunLengthNonUniformityNormalised HLL LCA	.064	1.19636
271	Idmn LLH LCA	.064	1.19167
272	ShortRunEmphasis HLL LCA	.065	1.188158
273	ClusterProminence RCA	.065	1.184651
274	Id HHL RCA	.066	1.177652
275	Kurtosis LHH RCA	.066	1.177652
276	SizeZoneNonUniformity HLL LCA	.066	1.177652
277	Idn HLL LCA	.067	1.176488
278	DependenceNonUniformityNormalised HLL LCA	.067	1.175324
279	SizeZoneNonUniformityNormalised HHL RCA	.067	1.175324
280	LargeDependenceEmphasis HLL LCA	.068	1.170673
281	SmallAreaLowGrayLevelEmphasis LHH LCA	.068	1.168351
282	Autocorrelation LCA	.068	1.166032
283	SmallDependenceEmphasis HLL LCA	.068	1.164873
284	RunPercentage HLL LCA	.069	1.163714
285	X10Percentile LCA	.069	1.163714
286	LongRunEmphasis HLL LCA	.070	1.156775
287	Minimum HHL RCA	.070	1.152159
288	JointAverage LCA	.071	1.151007
289	SumAverage LCA	.071	1.151007
290	LargeAreaLowGrayLevelEmphasis HLL LCA	.071	1.147553
291	Entropy LCA	.072	1.145253
292	Maximum LHL LCA	.072	1.140659
293	MeanAbsoluteDeviation LLL LCA	.072	1.140659
294	GrayLevelVariance HLH RCA.2	.072	1.140659
295	Imc1 HHL RCA	.072	1.140659
296	ZonePercentage HLL LCA	.073	1.13493
297	LowGrayLevelEmphasis LHH LCA	.075	1.123513
298	DependenceVariance HLL LCA	.075	1.122374
299	MeanAbsoluteDeviation LCA	.076	1.120098

Rank	Radiomic feature	P value	-log(P value)
300	ClusterShade LHH RCA	.076	1.117825
301	TotalEnergy HHH RCA	.077	1.115553
302	LowGrayLevelRunEmphasis LHH LCA	.077	1.113284
303	SmallAreaHighGrayLevelEmphasis HHL RCA	.078	1.108752
304	GrayLevelNonUniformityNormalised LLL LCA.1	.078	1.108752
305	X10Percentile LLL LCA	.078	1.106489
306	SmallDependenceLowGrayLevelEmphasis LLH RCA	.078	1.106489
307	RunVariance HLL LCA	.079	1.101971
308	ShortRunLowGrayLevelEmphasis HHL RCA	.079	1.099715
309	Correlation HLL RCA	.079	1.099715
310	SizeZoneNonUniformityNormalised HLL LCA	.080	1.098587
311	InterquartileRange HHL LCA	.081	1.092959
312	DifferenceVariance HHL LCA	.082	1.083983
313	GrayLevelNonUniformityNormalised HHL LCA	.082	1.083983
314	Mean LCA	.083	1.081745
315	X90Percentile HHL LCA	.083	1.079508
316	LowGrayLevelZoneEmphasis LHH LCA	.083	1.078391
317	RobustMeanAbsoluteDeviation HHL LCA	.084	1.077274
318	SmallAreaEmphasis HLL LCA	.084	1.073927
319	RootMeanSquared LCA	.085	1.070584
320	Kurtosis LLH LCA	.086	1.066136
321	Skewness LHH RCA	.087	1.061696
322	LowGrayLevelEmphasis HHL RCA	.087	1.059479
323	X10Percentile HHL LCA	.087	1.059479
324	DifferenceEntropy HHL LCA	.088	1.055052
325	SumSquares LCA	.089	1.050634
326	Kurtosis HLL LCA	.089	1.050634
327	SumEntropy LLL LCA	.090	1.045123
328	SumEntropy HHL LCA	.090	1.045123
329	LargeDependenceHighGrayLevelEmphasis LCA	.090	1.044023
330	SizeZoneNonUniformityNormalised HLL RCA	.091	1.041823
331	Idm HHL LCA	.091	1.041823
332	DifferenceAverage HHL LCA	.091	1.040724
333	DependenceEntropy RCA	.091	1.039626
334	GrayLevelVariance LLL LCA	.092	1.037431
335	Entropy HHL LCA	.093	1.033048
336	Mean LHL RCA	.093	1.033048
337	JointEntropy HHL LCA	.093	1.033048
338	Contrast HHL LCA	.093	1.033048
339	Variance LLL LCA	.093	1.033048
340	MeanAbsoluteDeviation HHL LCA	.093	1.030859
341	Uniformity HHL LCA	.093	1.030859
342	DependenceEntropy HHL RCA	.093	1.030859
343	Median LCA	.093	1.029766
344	GrayLevelVariance HHL LCA.1	.094	1.028673
345	Id HHL LCA	.094	1.027581
346	Variance HHL LCA	.095	1.024307
347	GrayLevelVariance LLL LCA.1	.095	1.024307
348	LowGrayLevelRunEmphasis HHL RCA	.095	1.024307
349	RootMeanSquared HHL LCA	.095	1.023217
350	SumSquares HHL LCA	.095	1.023217
351	SumEntropy LCA	.095	1.023217
352	Mean LLH RCA	.096	1.01995
353	DifferenceAverage LLL LCA	.096	1.01995
354	SmallAreaEmphasis HLL RCA	.096	1.015601
355	JointEnergy HHL LCA	.097	1.012346
356	ClusterTendency LLL LCA	.097	1.011261
357	SumSquares LLL LCA	.097	1.011261
358	ShortRunHighGrayLevelEmphasis HHL RCA	.098	1.009095
359	InverseVariance LLL LCA	.098	1.009095
360	Maximum LLH LCA	.098	1.009095
361	Idm LLL LCA	.100	0.999371
362	MaximumProbability HHL LCA	.100	0.999371

Rank	Radiomic feature	P value	-log(P value)
363	Idn LCA	.100	0.998294
364	ClusterTendency HHL LCA	.101	0.99614
365	RootMeanSquared LLL LCA	.101	0.993989
366	DependenceEntropy HHL LCA	.101	0.993989
367	DifferenceAverage LCA	.102	0.992914
368	ClusterProminence HLL LCA	.102	0.991839
369	SmallAreaLowGrayLevelEmphasis HHL RCA	.102	0.991839
370	GrayLevelNonUniformityNormalised HHH RCA	.103	0.985404
371	ShortRunEmphasis HLL RCA	.103	0.985404
372	Id LLL LCA	.103	0.985404
373	LargeDependenceLowGrayLevelEmphasis HHL RCA	.103	0.985404
374	InverseVariance LCA	.104	0.984334
375	RunLengthNonUniformityNormalised HLL RCA	.104	0.983264
376	RunEntropy LLL LCA	.105	0.980057
377	GrayLevelNonUniformity HHH RCA	.105	0.976855
378	Kurtosis HLH LCA	.108	0.966216
379	Maximum HHL LCA	.109	0.964095
380	GrayLevelVariance LCA	.110	0.959859
381	Id LCA	.111	0.955632
382	Variance LCA	.111	0.955632
383	Skewness LCA	.111	0.954576
384	Idm LCA	.111	0.953521
385	Skewness LLH LCA	.111	0.953521
386	GrayLevelVariance LCA.1	.111	0.953521
387	Range LLH LCA	.112	0.949307
388	DependenceVariance HLL RCA	.114	0.943002
389	RunPercentage HLL RCA	.115	0.940904
390	LargeDependenceLowGrayLevelEmphasis RCA	.116	0.936716
391	Uniformity HHH RCA	.116	0.934625
392	GrayLevelVariance HHL LCA	.117	0.930449
393	LongRunLowGrayLevelEmphasis HHL RCA	.117	0.930449
394	Idmn LCA	.118	0.927323
395	Contrast LCA	.118	0.926283
396	LargeAreaHighGrayLevelEmphasis HHL LCA	.118	0.926283
397	LargeDependenceEmphasis HLL RCA	.119	0.924202
398	DifferenceEntropy LCA	.119	0.923163
399	Mean HHH RCA	.120	0.922124
400	DifferenceEntropy LLL LCA	.122	0.913834
401	SmallDependenceHighGrayLevelEmphasis HHL RCA	.122	0.913834
402	SmallDependenceEmphasis HLL RCA	.122	0.913834
403	DependenceNonUniformityNormalised HLL RCA	.123	0.911766
404	Skewness HHL LCA	.123	0.911766
405	Maximum HLL RCA	.123	0.909701
406	GrayLevelVariance HHH RCA.1	.124	0.907638
407	SumSquares HHH RCA	.124	0.905577
408	Entropy HHH RCA	.125	0.901462
409	Idmn HHL RCA	.125	0.901462
410	Skewness HLL LCA	.126	0.899408
411	Contrast LLL LCA	.127	0.897355
412	HighGrayLevelRunEmphasis LCA	.127	0.897355
413	Median HLH LCA	.128	0.894281
414	LowGrayLevelZoneEmphasis HHL RCA	.128	0.893257
415	HighGrayLevelEmphasis LCA	.128	0.891211
416	ClusterTendency LCA	.129	0.889168
417	ClusterProminence HHL LCA	.131	0.88305
418	ZoneEntropy HLL RCA	.132	0.881014
419	GrayLevelVariance HHH RCA	.136	0.866829
420	SmallDependenceLowGrayLevelEmphasis HLL LCA	.136	0.866829
421	LongRunEmphasis HLL RCA	.137	0.864811
422	ZonePercentage HHL LCA	.138	0.860781
423	X90Percentile LCA	.138	0.859775
424	Range LHL LCA	.142	0.848744
425	Energy HHL LCA	.142	0.848744

Rank	Radiomic feature	P value	-log(P value)
426	Median LLL LCA	.142	0.848744
427	Imc2 HLH RCA	.142	0.848744
428	ZonePercentage HLL RCA	.145	0.838771
429	Mean LLL LCA	.146	0.834797
430	Maximum HLH RCA	.147	0.832813
431	RunVariance HLL RCA	.147	0.832813
432	LargeAreaEmphasis HLL LCA	.148	0.828852
433	Imc2 LHL RCA	.149	0.826874
434	SmallAreaEmphasis HHH LCA	.151	0.82194
435	ZoneVariance HLL LCA	.151	0.820955
436	LargeAreaHighGrayLevelEmphasis LLH RCA	.152	0.817019
437	ClusterProminence HHH RCA	.152	0.817019
438	ClusterShade HLL RCA	.153	0.815054
439	SmallAreaHighGrayLevelEmphasis HHH RCA	.154	0.813092
440	TotalEnergy HLH RCA	.154	0.811131
441	JointEntropy HHH RCA	.157	0.805263
442	LargeAreaHighGrayLevelEmphasis LLL LCA	.157	0.805263
443	Skewness LLH RCA	.160	0.795524
444	SizeZoneNonUniformityNormalised HHH LCA	.160	0.794553
445	Imc2 HLH LCA	.161	0.793583
446	SmallDependenceEmphasis HHL LCA	.162	0.791643
447	RunLengthNonUniformityNormalised LCA	.164	0.785839
448	X10Percentile HHH RCA	.165	0.781979
449	SmallAreaEmphasis HHL LCA	.166	0.780053
450	ZoneEntropy HHL RCA	.167	0.776206
451	Median LLH RCA	.167	0.776206
452	ShortRunEmphasis LCA	.169	0.771409
453	DifferenceVariance LCA	.172	0.764716
454	Imc1 HLH RCA	.173	0.762809
455	Correlation HLL LCA	.174	0.759952
456	RunLengthNonUniformityNormalised LLL LCA	.174	0.759
457	ZoneEntropy LHL LCA	.175	0.758049
458	X90Percentile HHH LCA	.175	0.757099
459	X10Percentile HHH LCA	.176	0.7552
460	RunVariance HHH RCA	.176	0.753303
461	ShortRunEmphasis LLL LCA	.177	0.752355
462	RunPercentage LCA	.179	0.747625
463	Skewness HLH LCA	.179	0.74668
464	Kurtosis LLL LCA	.180	0.745736
465	Imc1 LHL RCA	.180	0.745736
466	RobustMeanAbsoluteDeviation HHH LCA	.180	0.744793
467	LargeDependenceEmphasis LCA	.180	0.74385
468	TotalEnergy HLL LCA	.181	0.741966
469	InterquartileRange HHH LCA	.181	0.741966
470	RootMeanSquared HHH LCA	.182	0.740083
471	Variance HHH LCA	.183	0.738203
472	DependenceNonUniformityNormalised LLL LCA	.183	0.737264
473	X90Percentile HHH RCA	.184	0.734449
474	Variance HHH RCA	.187	0.728834
475	RobustMeanAbsoluteDeviation HHH RCA	.187	0.728834
476	MeanAbsoluteDeviation HHH RCA	.188	0.726967
477	RootMeanSquared HHH RCA	.188	0.726967
478	GrayLevelVariance HLH RCA.1	.188	0.725101
479	InterquartileRange HHH RCA	.190	0.721377
480	SizeZoneNonUniformityNormalised HHL LCA	.190	0.720447
481	RunPercentage LLL LCA	.190	0.720447
482	LongRunHighGrayLevelEmphasis LLH RCA	.191	0.719518
483	LargeDependenceEmphasis LLL LCA	.191	0.719518
484	LargeDependenceHighGrayLevelEmphasis LLL LCA	.192	0.717661
485	DependenceNonUniformityNormalised LCA	.193	0.714879
486	ClusterTendency HHH RCA	.193	0.713953
487	MeanAbsoluteDeviation HHH LCA	.193	0.713953
488	Idn HHL RCA	.193	0.713953

Rank	Radiomic feature	P value	-log(P value)
489	MajorAxis LCA	.193	0.713953
490	GrayLevelNonUniformityNormalised HLH RCA	.195	0.710253
491	DifferenceVariance HLH RCA	.197	0.706562
492	ZonePercentage LLL LCA	.198	0.7038
493	ZonePercentage HHL RCA	.198	0.70288
494	SumEntropy HHH RCA	.199	0.701042
495	LowGrayLevelEmphasis LCA	.199	0.700123
496	DifferenceEntropy HLH RCA	.200	0.699206
497	SmallDependenceEmphasis LLL LCA	.202	0.69554
498	SizeZoneNonUniformity HHL LCA	.202	0.69371
499	ShortRunEmphasis HHL LCA	.204	0.690969
500	ZoneEntropy HHL LCA	.204	0.690057
501	Skewness HHL RCA	.204	0.690057
502	RunLengthNonUniformityNormalised HHL LCA	.205	0.687322
503	LongRunEmphasis LCA	.206	0.686412
504	Contrast HLH RCA	.207	0.684592
505	ShortRunEmphasis RCA	.207	0.684592
506	X90Percentile HLH RCA	.208	0.682775
507	RunLengthNonUniformityNormalised RCA	.208	0.68096
508	DifferenceEntropy HHH RCA	.208	0.68096
509	Contrast HHH RCA.1	.209	0.679147
510	ClusterProminence HLH RCA	.209	0.679147
511	JointEntropy HLH RCA	.210	0.677336
512	DependenceEntropy HLH LCA	.210	0.677336
513	GrayLevelVariance HLH RCA	.210	0.677336
514	SumSquares HLH RCA	.212	0.67372
515	LongRunEmphasis LLL LCA	.212	0.672817
516	Uniformity HLH RCA	.214	0.670113
517	Correlation HHL LCA	.215	0.668312
518	Entropy HLH RCA	.216	0.666513
519	SmallDependenceEmphasis LCA	.216	0.665615
520	Imc2 HHL RCA	.217	0.662923
521	DependenceVariance RCA	.218	0.66113
522	Energy LLH RCA	.218	0.66113
523	LargeDependenceEmphasis HHH RCA	.219	0.65934
524	Variance HLH RCA	.220	0.657552
525	LongRunEmphasis HHH RCA	.220	0.657552
526	LargeAreaLowGrayLevelEmphasis HLL RCA	.220	0.657552
527	Imc1 LHL LCA	.220	0.656659
528	RootMeanSquared HLH RCA	.221	0.655766
529	SmallDependenceEmphasis HHL RCA	.221	0.655766
530	LongRunLowGrayLevelEmphasis LHH LCA	.221	0.655766
531	Imc2 LHL LCA	.223	0.6522
532	LargeAreaEmphasis LLL LCA	.223	0.6522
533	MeanAbsoluteDeviation HLH RCA	.225	0.646867
534	SmallDependenceEmphasis RCA	.226	0.645093
535	DependenceEntropy HLH RCA	.226	0.645093
536	Imc1 LHH LCA	.226	0.645093
537	TotalEnergy LLH LCA	.227	0.643322
538	ZonePercentage LCA	.228	0.641552
539	DependenceNonUniformityNormalised RCA	.229	0.639785
540	X10Percentile LHL RCA	.229	0.639785
541	Minimum HHH RCA	.230	0.63802
542	RunPercentage RCA	.231	0.636256
543	Skewness LHL RCA	.231	0.636256
544	RunVariance LCA	.231	0.636256
545	DependenceVariance LLL LCA	.232	0.634495
546	SumSquares HHH LCA	.232	0.633615
547	LargeDependenceLowGrayLevelEmphasis LHH LCA	.232	0.633615
548	RunPercentage HHL LCA	.233	0.631857
549	Volume LCA	.235	0.629224
550	Range HHH RCA	.236	0.627471
551	JointEnergy HLH RCA	.236	0.627471

Rank	Radiomic feature	P value	-log(P value)
552	SmallDependenceLowGrayLevelEmphasis HHL RCA	.237	0.62572
553	ClusterTendency HLH RCA	.238	0.623972
554	LowGrayLevelRunEmphasis LCA	.238	0.623972
555	LargeDependenceEmphasis RCA	.239	0.622225
556	ZoneVariance LLL LCA	.240	0.62048
557	LongRunEmphasis RCA	.242	0.616997
558	Range HLL LCA	.242	0.616997
559	SumEntropy HLH RCA	.243	0.615259
560	DifferenceVariance LLL LCA	.243	0.613522
561	DifferenceAverage HLH RCA	.244	0.611788
562	X10Percentile HLH RCA	.245	0.610056
563	RunVariance LLL LCA	.246	0.60919
564	Maximum3DDiameter LCA	.246	0.608326
565	RunPercentage HHH RCA	.248	0.604871
566	LargeDependenceEmphasis HHL LCA	.249	0.603147
567	Busyness LHH RCA	.252	0.597988
568	RunVariance RCA	.252	0.597988
569	Busyness LHH LCA	.252	0.597988
570	RobustMeanAbsoluteDeviation HLH RCA	.252	0.597988
571	Idm HLH RCA	.252	0.597988
572	MinorAxis LCA	.253	0.596272
573	X90Percentile HLH LCA	.254	0.594558
574	DependenceVariance LCA	.254	0.594558
575	GrayLevelNonUniformity HHL LCA.2	.255	0.592847
576	Energy HHH LCA	.256	0.591137
577	ClusterShade HHH RCA	.257	0.589429
578	Id HLH RCA	.259	0.58602
579	Complexity LHH LCA	.260	0.585169
580	SmallAreaEmphasis LLL RCA	.260	0.584319
581	SizeZoneNonUniformity LLH RCA	.260	0.584319
582	ShortRunLowGrayLevelEmphasis LCA	.261	0.583469
583	GrayLevelVariance HHH LCA.1	.261	0.583469
584	InterquartileRange HLH RCA	.261	0.58262
585	SizeZoneNonUniformity HHH LCA	.263	0.579227
586	GrayLevelNonUniformity HHH LCA.2	.263	0.579227
587	SizeZoneNonUniformityNormalised LLL LCA	.265	0.577534
588	SizeZoneNonUniformityNormalised LLL RCA	.265	0.577534
589	LongRunEmphasis HHL LCA	.265	0.577534
590	Minimum LHL RCA	.265	0.577534
591	GrayLevelVariance HHH LCA	.266	0.574998
592	SmallAreaEmphasis LLL LCA	.267	0.574154
593	Maximum HHH RCA	.268	0.572466
594	Maximum LLH RCA	.269	0.570781
595	Range HLH RCA	.269	0.570781
596	ClusterProminence LCA	.271	0.567418
597	ZonePercentage RCA	.271	0.567418
598	ShortRunHighGrayLevelEmphasis LCA	.271	0.567418
599	JointEntropy HHH LCA	.271	0.567418
600	Skewness LHL LCA	.272	0.5649
601	LargeDependenceHighGrayLevelEmphasis HHH RCA	.275	0.560714
602	LargeDependenceHighGrayLevelEmphasis HLL LCA	.277	0.557375
603	SmallDependenceEmphasis LLL RCA	.277	0.557375
604	DifferenceVariance HHH RCA	.278	0.555708
605	DependenceVariance LLL RCA	.279	0.554044
606	SurfaceArea LCA	.279	0.554044
607	GrayLevelVariance HLH LCA.1	.280	0.553212
608	MaximumProbability HLH RCA	.280	0.552381
609	ShortRunEmphasis LLL RCA	.285	0.545751
610	HighGrayLevelRunEmphasis HHH RCA	.286	0.544099
611	LargeAreaEmphasis HHL LCA	.286	0.544099
612	RootMeanSquared HLH LCA	.287	0.542449
613	Variance HLH LCA	.288	0.5408
614	SumEntropy HLH LCA	.288	0.5408

Rank	Radiomic feature	P value	-log(P value)
615	ClusterTendency HLH LCA	.288	0.539977
616	RunLengthNonUniformityNormalised LLL RCA	.289	0.539154
617	ZoneVariance HHL LCA	.290	0.53751
618	SmallAreaLowGrayLevelEmphasis LHH RCA	.291	0.535868
619	RobustMeanAbsoluteDeviation HLH LCA	.292	0.534227
620	Kurtosis HHH RCA	.294	0.530953
621	GrayLevelVariance HLH LCA	.296	0.529319
622	RunVariance HHL LCA	.296	0.529319
623	SumSquares HLH LCA	.296	0.528503
624	InterquartileRange HLH LCA	.296	0.528503
625	ZonePercentage LLL RCA	.297	0.527687
626	GrayLevelNonUniformityNormalised HHH LCA	.297	0.526872
627	JointEnergy HLH LCA	.298	0.525243
628	Entropy HHH LCA	.298	0.525243
629	MeanAbsoluteDeviation HLH LCA	.299	0.524429
630	LongRunHighGrayLevelEmphasis HHH RCA	.302	0.519557
631	LargeAreaHighGrayLevelEmphasis HHH LCA	.302	0.519557
632	Uniformity HLH LCA	.303	0.517937
633	Uniformity HHH LCA	.304	0.517128
634	RunPercentage LLL RCA	.305	0.516319
635	GrayLevelNonUniformityNormalised HLH LCA	.306	0.514704
636	ShortRunEmphasis HHL RCA	.308	0.511478
637	LongRunEmphasis LLL RCA	.308	0.511478
638	HighGrayLevelRunEmphasis HLH RCA	.309	0.509868
639	GrayLevelVariance LLH LCA.2	.309	0.509868
640	SizeZoneNonUniformityNormalised LHH LCA	.310	0.50826
641	DifferenceVariance HLH LCA	.311	0.507457
642	LargeDependenceEmphasis LLL RCA	.311	0.506655
643	DifferenceEntropy HHH LCA	.311	0.506655
644	Contrast HLH LCA	.313	0.505051
645	ShortRunEmphasis HHH RCA	.313	0.505051
646	DependenceNonUniformityNormalised LLL RCA	.315	0.50185
647	ShortRunHighGrayLevelEmphasis LHL RCA	.316	0.500252
648	ZoneEntropy LLH LCA	.316	0.500252
649	Entropy HLH LCA	.317	0.498656
650	JointEntropy HLH LCA	.319	0.496267
651	HighGrayLevelEmphasis HLH RCA	.320	0.495471
652	X10Percentile HLH LCA	.320	0.495471
653	ZonePercentage HHH LCA	.321	0.493881
654	TotalEnergy HHL LCA	.321	0.493881
655	RunLengthNonUniformityNormalised HHL RCA	.322	0.492294
656	Correlation HLH RCA	.322	0.492294
657	DifferenceVariance HHH LCA	.322	0.491501
658	MaximumProbability HLH LCA	.323	0.490708
659	RunVariance LLL RCA	.323	0.490708
660	SmallAreaEmphasis HLH RCA	.323	0.490708
661	ClusterProminence LHL LCA	.324	0.489125
662	LongRunHighGrayLevelEmphasis LLH LCA	.325	0.487543
663	GrayLevelVariance LLL LCA.2	.327	0.485964
664	ClusterShade HHL RCA	.330	0.481237
665	SmallAreaEmphasis LHH LCA	.331	0.480451
666	DifferenceEntropy HLH LCA	.333	0.477312
667	HighGrayLevelZoneEmphasis LHL RCA	.334	0.476529
668	Skewness HLL RCA	.335	0.474963
669	ClusterShade LLL LCA	.337	0.471838
670	ShortRunLowGrayLevelEmphasis LLH RCA	.339	0.470279
671	GrayLevelVariance HHH LCA.2	.340	0.468721
672	HighGrayLevelZoneEmphasis LLH LCA	.340	0.468721
673	HighGrayLevelEmphasis LHL RCA	.340	0.468721
674	HighGrayLevelRunEmphasis LHL RCA	.340	0.468721
675	Autocorrelation HLH RCA	.340	0.468721
676	DifferenceAverage HLH LCA	.341	0.467166
677	JointAverage LHL RCA	.342	0.465612

Rank	Radiomic feature	P value	-log(P value)
678	SumAverage LHL RCA	.342	0.465612
679	JointEnergy HHH RCA	.345	0.462511
680	ShortRunLowGrayLevelEmphasis LLH LCA	.345	0.461737
681	HighGrayLevelZoneEmphasis HLH RCA	.346	0.460964
682	LongRunLowGrayLevelEmphasis LCA	.346	0.460964
683	LargeAreaHighGrayLevelEmphasis LHL RCA	.346	0.460964
684	Idm HLH LCA	.347	0.459418
685	Skewness LHH LCA	.347	0.459418
686	Imc1 HLL RCA	.347	0.459418
687	Imc2 HHH RCA	.348	0.457875
688	GrayLevelNonUniformityNormalised HHH LCA.1	.348	0.457875
689	Autocorrelation LHL RCA	.348	0.457875
690	LargeAreaLowGrayLevelEmphasis LHH RCA	.351	0.454794
691	SmallAreaHighGrayLevelEmphasis LHL RCA	.351	0.454794
692	Correlation LHL LCA	.353	0.451721
693	GrayLevelNonUniformity HLL LCA	.353	0.451721
694	ZoneVariance LLL RCA	.355	0.450187
695	JointAverage HLH RCA	.355	0.450187
696	SumAverage HLH RCA	.355	0.450187
697	Id HLH LCA	.357	0.447126
698	LargeAreaLowGrayLevelEmphasis LCA	.360	0.444073
699	Kurtosis LHL RCA	.360	0.444073
700	Correlation LHL RCA	.361	0.44255
701	ZoneVariance LLH RCA	.362	0.441028
702	LowGrayLevelEmphasis LLH LCA	.362	0.441028
703	Idn LHL RCA	.362	0.441028
704	SmallDependenceHighGrayLevelEmphasis HHL LCA	.363	0.440268
705	LargeAreaEmphasis LLH RCA	.363	0.439509
706	LowGrayLevelRunEmphasis LLH LCA	.363	0.439509
707	Contrast HHH LCA.1	.363	0.439509
708	SmallAreaLowGrayLevelEmphasis LLH LCA	.365	0.437233
709	LargeAreaEmphasis LLL RCA	.366	0.436476
710	Imc2 HLL RCA	.366	0.436476
711	LargeDependenceLowGrayLevelEmphasis HHL LCA	.366	0.436476
712	LowGrayLevelZoneEmphasis LLH LCA	.367	0.434962
713	GrayLevelNonUniformityNormalised HHH RCA.1	.367	0.434962
714	RunEntropy LCA	.367	0.434962
715	ClusterProminence HHH LCA	.369	0.432695
716	LowGrayLevelEmphasis LLH RCA	.371	0.430433
717	LargeDependenceLowGrayLevelEmphasis LHL RCA	.372	0.428927
718	HighGrayLevelRunEmphasis LLH LCA	.372	0.428927
719	DependenceEntropy LLH RCA	.374	0.427424
720	MaximumProbability LHL RCA	.375	0.425922
721	HighGrayLevelEmphasis LLH LCA	.375	0.425922
722	GrayLevelNonUniformity HLL LCA.2	.378	0.422925
723	JointAverage LLH LCA	.378	0.422925
724	SumAverage LLH LCA	.378	0.422925
725	Autocorrelation LLH LCA	.378	0.422925
726	Mean HLH RCA	.378	0.422925
727	Range HHL LCA	.380	0.419935
728	LowGrayLevelZoneEmphasis HHH RCA	.380	0.419935
729	LowGrayLevelRunEmphasis LLH RCA	.383	0.416953
730	ClusterProminence LLL LCA	.383	0.416953
731	ClusterTendency HHH LCA	.383	0.416953
732	RunEntropy LHL RCA	.384	0.415466
733	LargeAreaLowGrayLevelEmphasis HHL RCA	.385	0.41398
734	LargeAreaLowGrayLevelEmphasis HHL LCA	.387	0.412496
735	Minimum LLH RCA	.387	0.412496
736	GrayLevelNonUniformityNormalised LHH RCA.1	.392	0.40658
737	ShortRunHighGrayLevelEmphasis LLH LCA	.393	0.405106
738	HighGrayLevelZoneEmphasis HHL LCA	.393	0.405106
739	LongRunLowGrayLevelEmphasis HHL LCA	.393	0.405106
740	SmallDependenceEmphasis HLH LCA	.394	0.40437

Rank	Radiomic feature	P value	-log(P value)
741	JointEnergy HHH LCA	.395	0.403634
742	SumEntropy HHH LCA	.397	0.400696
743	RunPercentage HHL RCA	.399	0.39923
744	SmallDependenceHighGrayLevelEmphasis LLL RCA	.399	0.39923
745	SmallDependenceEmphasis HHH LCA	.399	0.398497
746	Minimum LLH LCA	.400	0.397765
747	Maximum LLL LCA	.400	0.397765
748	Imc2 HHH LCA	.400	0.397765
749	LargeAreaHighGrayLevelEmphasis HLL LCA	.403	0.394843
750	GrayLevelNonUniformity HLL LCA.1	.404	0.393385
751	SizeZoneNonUniformity HLH LCA	.406	0.391928
752	HighGrayLevelZoneEmphasis HHH RCA	.406	0.391928
753	LargeDependenceEmphasis HHL RCA	.406	0.391928
754	GrayLevelNonUniformityNormalised LHL RCA.1	.407	0.390474
755	ClusterProminence HLH LCA	.410	0.387571
756	SmallDependenceHighGrayLevelEmphasis LCA	.410	0.386847
757	ZoneEntropy HLL LCA	.412	0.385399
758	SizeZoneNonUniformityNormalised HLH RCA	.414	0.383232
759	LowGrayLevelZoneEmphasis LHH RCA	.414	0.383232
760	LargeDependenceHighGrayLevelEmphasis HLH RCA	.415	0.381789
761	SmallAreaHighGrayLevelEmphasis LLH LCA	.415	0.381789
762	RunLengthNonUniformityNormalised HHH RCA	.415	0.381789
763	SmallDependenceHighGrayLevelEmphasis LLL LCA	.417	0.380348
764	ZoneEntropy LCA	.419	0.378191
765	LowGrayLevelRunEmphasis HLH LCA	.419	0.377473
766	ZonePercentage HLH LCA	.421	0.376038
767	Correlation HHL RCA	.421	0.376038
768	ClusterProminence LLH LCA	.421	0.376038
769	ZoneVariance LHH RCA	.422	0.374605
770	DependenceNonUniformity HLL LCA	.422	0.374605
771	JointEnergy LHL RCA	.423	0.373174
772	Minimum HLH RCA	.423	0.373174
773	LargeAreaEmphasis LHH RCA	.425	0.371745
774	HighGrayLevelRunEmphasis HHL LCA	.425	0.371745
775	Imc1 LCA	.426	0.370319
776	RunEntropy HLH LCA	.430	0.366049
777	LowGrayLevelZoneEmphasis LLH RCA	.432	0.36463
778	TotalEnergy LCA	.435	0.361798
779	Busyness HLL LCA	.435	0.361798
780	ShortRunLowGrayLevelEmphasis LHH RCA	.435	0.361798
781	LongRunHighGrayLevelEmphasis HLH RCA	.436	0.360384
782	RunEntropy LHH RCA	.436	0.360384
783	RunLengthNonUniformityNormalised HLH LCA	.436	0.360384
784	ShortRunHighGrayLevelEmphasis HHL LCA	.439	0.357564
785	Idm LHL RCA	.440	0.356156
786	Idmn HLL RCA	.440	0.356156
787	Range LLL LCA	.442	0.354751
788	GrayLevelNonUniformityNormalised LHH LCA.1	.442	0.354751
789	Id LHL RCA	.443	0.353347
790	LongRunEmphasis HHL RCA	.449	0.347752
791	SizeZoneNonUniformity LHH LCA	.450	0.346358
792	Contrast HHH LCA	.456	0.340802
793	ShortRunEmphasis HLH LCA	.456	0.340802
794	TotalEnergy LLL LCA	.456	0.340802
795	LowGrayLevelEmphasis HLH LCA	.457	0.340109
796	ZoneEntropy LHH LCA	.458	0.339418
797	SmallAreaLowGrayLevelEmphasis LLH RCA	.458	0.339418
798	LargeAreaEmphasis HLL RCA	.458	0.339418
799	Energy LLH LCA	.458	0.339418
800	LowGrayLevelRunEmphasis LHH RCA	.458	0.339418
801	SmallAreaHighGrayLevelEmphasis HLH RCA	.459	0.338035
802	LongRunLowGrayLevelEmphasis LLH LCA	.461	0.336655
803	SmallDependenceHighGrayLevelEmphasis LHL RCA	.462	0.335276

Rank	Radiomic feature	P value	-log(P value)
804	HighGrayLevelRunEmphasis LLH RCA	.462	0.335276
805	Busyness HHH RCA	.464	0.3339
806	Busyness LLH RCA	.464	0.3339
807	ZoneVariance HLL RCA	.464	0.3339
808	SmallAreaLowGrayLevelEmphasis HLH LCA	.464	0.333212
809	DifferenceAverage LHL RCA	.468	0.329782
810	GrayLevelNonUniformity HLH LCA	.468	0.329782
811	SmallAreaHighGrayLevelEmphasis LLH RCA	.468	0.329782
812	LowGrayLevelEmphasis LHH RCA	.468	0.329782
813	ZoneVariance HLH LCA	.468	0.329782
814	HighGrayLevelZoneEmphasis LLH RCA	.468	0.329782
815	LargeAreaEmphasis HLH LCA	.468	0.329782
816	JointEntropy LHL RCA	.469	0.328413
817	JointAverage LLH RCA	.469	0.328413
818	SumAverage LLH RCA	.469	0.328413
819	Id HHH LCA	.470	0.32773
820	HighGrayLevelEmphasis LLH RCA	.472	0.325681
821	ShortRunHighGrayLevelEmphasis HLH RCA	.474	0.324318
822	Uniformity LHL RCA	.474	0.324318
823	InterquartileRange LHL RCA	.475	0.322957
824	SmallAreaEmphasis HLH LCA	.476	0.322277
825	Idn HLL RCA	.477	0.321598
826	GrayLevelNonUniformityNormalised LHL RCA	.477	0.321598
827	DependenceEntropy LHL LCA	.478	0.320919
828	SmallDependenceHighGrayLevelEmphasis HLH RCA	.478	0.320241
829	GrayLevelVariance LHL RCA.2	.481	0.317532
830	DifferenceEntropy LHL RCA	.481	0.317532
831	ShortRunLowGrayLevelEmphasis HHH RCA	.481	0.317532
832	Autocorrelation LLH RCA	.481	0.317532
833	TotalEnergy LHL LCA	.481	0.317532
834	DependenceEntropy HHH RCA	.481	0.317532
835	X90Percentile LLL LCA	.481	0.317532
836	DependenceNonUniformityNormalised HHL LCA	.484	0.315506
837	Imc1 HHH LCA	.484	0.315506
838	LowGrayLevelZoneEmphasis HLH LCA	.484	0.314831
839	SizeZoneNonUniformityNormalised HLH LCA	.487	0.31281
840	InverseVariance LLH LCA	.488	0.311466
841	RobustMeanAbsoluteDeviation LHL RCA	.489	0.310794
842	LowGrayLevelEmphasis HHH LCA	.489	0.310794
843	LargeAreaEmphasis RCA	.490	0.309452
844	ZoneVariance RCA	.490	0.309452
845	Busyness HHL LCA	.492	0.308112
846	ClusterShade LHL LCA	.492	0.308112
847	Sphericity LCA	.493	0.306774
848	HighGrayLevelEmphasis HHL LCA	.496	0.304104
849	RunEntropy LLH RCA	.496	0.304104
850	Idmn LHL RCA	.496	0.304104
851	ShortRunHighGrayLevelEmphasis LLH RCA	.500	0.301441
852	ZonePercentage HLH RCA	.500	0.301441
853	GrayLevelVariance LHH LCA.2	.501	0.300112
854	SumAverage HHH LCA	.502	0.299449
855	Idm HHH LCA	.502	0.299449
856	SmallAreaEmphasis LHL RCA	.503	0.298786
857	Complexity LLH LCA	.505	0.296799
858	JointAverage HHH LCA	.505	0.296799
859	MaximumProbability HHH RCA	.506	0.296138
860	LongRunEmphasis HLH LCA	.506	0.296138
861	SmallDependenceHighGrayLevelEmphasis HHH LCA	.506	0.295477
862	SizeZoneNonUniformityNormalised LHL RCA	.507	0.294817
863	Imc2 LCA	.507	0.294817
864	Entropy LHL RCA	.507	0.294817
865	SumEntropy LHL RCA	.510	0.292181
866	ShortRunHighGrayLevelEmphasis LHH RCA	.510	0.292181

Rank	Radiomic feature	P value	-log(P value)
867	LargeDependenceLowGrayLevelEmphasis HLH RCA	.512	0.290866
868	SmallAreaHighGrayLevelEmphasis HHL LCA	.512	0.290866
869	ZonePercentage HHH RCA	.512	0.290866
870	Imc1 HHL LCA	.516	0.287586
871	LargeDependenceEmphasis HLH LCA	.516	0.286932
872	DifferenceAverage HHH LCA	.518	0.285624
873	SmallAreaHighGrayLevelEmphasis LLL RCA	.518	0.285624
874	GrayLevelNonUniformityNormalised HHL LCA.1	.522	0.282364
875	ShortRunLowGrayLevelEmphasis HLH RCA	.523	0.281713
876	SmallDependenceEmphasis HLH RCA	.524	0.280413
877	Contrast LHL RCA	.524	0.280413
878	Imc1 HLL LCA	.525	0.279764
879	ZoneVariance HHH LCA	.526	0.279115
880	LargeAreaEmphasis HHH LCA	.526	0.279115
881	Energy HLH LCA	.527	0.277819
882	HighGrayLevelEmphasis HHH RCA	.527	0.277819
883	Idn LLH RCA	.529	0.276524
884	SmallAreaEmphasis RCA	.529	0.276524
885	SizeZoneNonUniformity LCA	.531	0.275232
886	LongRunLowGrayLevelEmphasis LHH RCA	.532	0.273941
887	SumAverage HHL LCA	.532	0.273941
888	DependenceVariance LHL LCA	.532	0.273941
889	JointAverage HHL LCA	.533	0.273297
890	Imc1 LLL LCA	.534	0.272653
891	Autocorrelation HHL LCA	.537	0.270081
892	Kurtosis HLH RCA	.539	0.268798
893	Correlation LCA	.539	0.268798
894	Kurtosis LLH RCA	.539	0.268798
895	LargeAreaLowGrayLevelEmphasis HHH LCA	.540	0.267517
896	Median HLH RCA	.540	0.267517
897	Contrast HHH RCA	.542	0.266238
898	DependenceNonUniformityNormalised HHL RCA	.543	0.26496
899	DependenceVariance LHL RCA	.546	0.262411
900	LongRunLowGrayLevelEmphasis HLH RCA	.546	0.262411
901	InverseVariance HHH LCA	.547	0.261775
902	LongRunLowGrayLevelEmphasis LLH RCA	.548	0.26114
903	RunVariance LHL LCA	.548	0.26114
904	MaximumProbability LHL LCA	.549	0.260505
905	LargeDependenceLowGrayLevelEmphasis LHH RCA	.550	0.25987
906	RunVariance HHL RCA	.550	0.25987
907	TotalEnergy LHH LCA	.551	0.258602
908	LargeAreaLowGrayLevelEmphasis LLH RCA	.553	0.257336
909	GrayLevelNonUniformityNormalised LLH LCA.1	.555	0.256072
910	MeanAbsoluteDeviation LHL RCA	.556	0.25481
911	Minimum LHH RCA	.556	0.25481
912	TotalEnergy LLH RCA	.556	0.25481
913	RunPercentage HLH LCA	.558	0.253549
914	RunVariance HLH LCA	.559	0.252291
915	DifferenceVariance LHL RCA	.559	0.252291
916	LongRunEmphasis LHL LCA	.563	0.249779
917	LargeAreaLowGrayLevelEmphasis LLL RCA	.563	0.249779
918	Correlation LLL LCA	.564	0.248526
919	GrayLevelNonUniformity HHL LCA	.564	0.248526
920	Correlation HHH RCA	.564	0.248526
921	SizeZoneNonUniformityNormalised RCA	.566	0.247275
922	Median HHH RCA	.568	0.246026
923	Imc1 LHH RCA	.571	0.243533
924	DependenceNonUniformityNormalised LHL LCA	.571	0.243533
925	GrayLevelVariance LHL LCA.2	.571	0.243533
926	Idmn LLH RCA	.572	0.24229
927	DependenceVariance HHH LCA	.576	0.239808
928	Autocorrelation LHH RCA	.576	0.239808
929	HighGrayLevelZoneEmphasis LHH RCA	.576	0.239808

Rank	Radiomic feature	P value	-log(P value)
930	Idm LHL LCA	.576	0.239808
931	SmallAreaHighGrayLevelEmphasis LLL LCA	.577	0.23857
932	Id LHL LCA	.578	0.237952
933	LargeAreaEmphasis HHL RCA	.581	0.2361
934	ZoneEntropy LHH RCA	.582	0.234868
935	Idm HHH RCA	.586	0.232409
936	LowGrayLevelRunEmphasis HHH LCA	.586	0.232409
937	ZoneVariance HHL RCA	.586	0.232409
938	SmallDependenceHighGrayLevelEmphasis LHH RCA	.586	0.232409
939	Sphericity RCA	.592	0.227513
940	LowGrayLevelEmphasis HLH RCA	.592	0.227513
941	Autocorrelation HHH LCA	.593	0.226903
942	Id HHH RCA	.594	0.226293
943	JointAverage LHH RCA	.594	0.226293
944	SumAverage LHH RCA	.594	0.226293
945	Busyness LHL LCA	.596	0.225076
946	InverseVariance HHL RCA	.597	0.22386
947	InverseVariance LHH RCA	.599	0.222646
948	Skewness HHH LCA	.604	0.219016
949	GrayLevelVariance HLH LCA.2	.604	0.219016
950	LowGrayLevelRunEmphasis HLH RCA	.604	0.219016
951	RunLengthNonUniformity HHL LCA	.606	0.21781
952	JointEnergy LHL LCA	.607	0.216605
953	LargeDependenceEmphasis LHL LCA	.609	0.215402
954	Imc2 LLH LCA	.610	0.214802
955	Strength HLH LCA	.613	0.212404
956	LowGrayLevelRunEmphasis HHL LCA	.614	0.211805
957	HighGrayLevelRunEmphasis LHH RCA	.617	0.209416
958	Maximum LHH RCA	.617	0.209416
959	X10Percentile LHL LCA	.619	0.208225
960	RunPercentage LHL LCA	.619	0.208225
961	LargeAreaLowGrayLevelEmphasis LHH LCA	.623	0.205847
962	DifferenceAverage HHH RCA	.624	0.204661
963	DependenceNonUniformityNormalised LHL RCA	.624	0.204661
964	DependenceEntropy LLL LCA	.624	0.204661
965	LowGrayLevelZoneEmphasis HHL LCA	.626	0.203477
966	ShortRunEmphasis LHL LCA	.628	0.202294
967	DependenceVariance LHH RCA	.628	0.202294
968	ZoneEntropy HLH RCA	.629	0.201114
969	Maximum HHH LCA	.629	0.201114
970	Imc2 LLL LCA	.632	0.199346
971	SmallAreaLowGrayLevelEmphasis HHL LCA	.633	0.198758
972	InverseVariance LLH RCA	.633	0.198758
973	GrayLevelNonUniformity LCA	.634	0.197583
974	RunLengthNonUniformityNormalised LHL LCA	.634	0.197583
975	SumSquares LHL RCA	.636	0.196409
976	ClusterProminence LHH LCA	.636	0.196409
977	GrayLevelNonUniformity HHL LCA.1	.638	0.195238
978	LargeDependenceEmphasis LHH RCA	.638	0.195238
979	SmallDependenceEmphasis LHL LCA	.640	0.193484
980	ShortRunEmphasis HLH RCA	.643	0.191734
981	RunLengthNonUniformityNormalised HLH RCA	.643	0.191734
982	TotalEnergy HHH LCA	.645	0.19057
983	Imc1 RCA	.647	0.189408
984	ShortRunLowGrayLevelEmphasis HHL LCA	.647	0.189408
985	GrayLevelNonUniformity LHH LCA.1	.648	0.188247
986	ClusterShade LLL RCA	.650	0.187089
987	Imc2 LHH LCA	.651	0.18651
988	DependenceNonUniformity LLH LCA	.652	0.185932
989	Idn HLH RCA	.652	0.185932
990	SmallAreaEmphasis LLH RCA	.652	0.185932
991	SmallAreaHighGrayLevelEmphasis LHH RCA	.652	0.185932
992	GrayLevelVariance LHL RCA	.653	0.184777

Rank	Radiomic feature	P value	-log(P value)
993	InterquartileRange LHL LCA	.653	0.184777
994	RunLengthNonUniformity HLL LCA	.653	0.184777
995	RunVariance LHL RCA	.653	0.184777
996	RunPercentage LHH RCA	.653	0.184777
997	RootMeanSquared LLH LCA	.653	0.184777
998	Variance LHL RCA	.655	0.183624
999	SmallDependenceHighGrayLevelEmphasis LLH LCA	.655	0.183624
1000	GrayLevelNonUniformity LHL LCA	.657	0.182472
1001	ZonePercentage LHL LCA	.658	0.181897
1002	HighGrayLevelEmphasis LHH RCA	.659	0.181323
1003	SmallAreaLowGrayLevelEmphasis HLH RCA	.659	0.181323
1004	Median HHL LCA	.659	0.181323
1005	SizeZoneNonUniformity LLH LCA	.659	0.181323
1006	GrayLevelVariance LHL RCA.1	.660	0.180175
1007	Correlation LLH RCA	.660	0.180175
1008	HighGrayLevelZoneEmphasis LLL RCA	.660	0.180175
1009	GrayLevelVariance LLH LCA.1	.664	0.177885
1010	Maximum2DDiameterSlice RCA	.667	0.175602
1011	GrayLevelVariance LLH LCA	.667	0.175602
1012	Variance LLH LCA	.667	0.175602
1013	HighGrayLevelEmphasis HHH LCA	.668	0.175032
1014	DifferenceAverage LHL LCA	.671	0.173326
1015	LongRunEmphasis LHL RCA	.671	0.173326
1016	RobustMeanAbsoluteDeviation LHL LCA	.674	0.171058
1017	DependenceNonUniformityNormalised LHH LCA	.674	0.171058
1018	SurfaceVolumeRatio LCA	.676	0.169927
1019	RunEntropy LLH LCA	.677	0.169362
1020	RunVariance LHH RCA	.678	0.168797
1021	SizeZoneNonUniformityNormalised LLH RCA	.680	0.167669
1022	ClusterTendency LLH LCA	.683	0.165419
1023	LowGrayLevelEmphasis HHL LCA	.683	0.165419
1024	LargeDependenceEmphasis LHL RCA	.683	0.165419
1025	LongRunLowGrayLevelEmphasis HHH RCA	.685	0.164296
1026	GrayLevelVariance LHH RCA.2	.685	0.164296
1027	ShortRunEmphasis LHL RCA	.685	0.164296
1028	DifferenceEntropy LHL LCA	.686	0.163736
1029	ClusterTendency LHL RCA	.687	0.163176
1030	Idn HHH RCA	.687	0.163176
1031	GrayLevelNonUniformity LLH LCA	.687	0.163176
1032	X10Percentile LLH RCA	.689	0.162057
1033	Range HHH LCA	.689	0.162057
1034	ClusterShade LHL RCA	.692	0.159825
1035	JointEntropy LHL LCA	.693	0.159268
1036	Range LLH RCA	.694	0.158711
1037	LargeDependenceLowGrayLevelEmphasis LLH LCA	.695	0.158155
1038	RunPercentage LHL RCA	.696	0.1576
1039	SmallDependenceLowGrayLevelEmphasis HLH RCA	.696	0.1576
1040	Uniformity LHL LCA	.697	0.157044
1041	LargeAreaLowGrayLevelEmphasis HLH LCA	.697	0.15649
1042	Idmn HHH RCA	.699	0.155382
1043	GrayLevelNonUniformityNormalised HHL RCA.1	.699	0.155382
1044	RunEntropy LHH LCA	.701	0.154275
1045	LargeDependenceLowGrayLevelEmphasis HHH RCA	.701	0.154275
1046	SizeZoneNonUniformityNormalised LHH RCA	.701	0.154275
1047	GrayLevelNonUniformityNormalised LLH RCA.1	.701	0.154275
1048	RunLengthNonUniformityNormalised LHL RCA	.701	0.154275
1049	DependenceVariance HHL RCA	.706	0.150967
1050	Imc2 HLL LCA	.708	0.149868
1051	SmallAreaEmphasis LLH LCA	.712	0.147675
1052	Mean LHH RCA	.712	0.147675
1053	Imc1 HLH LCA	.714	0.146582
1054	RunLengthNonUniformityNormalised LHH RCA	.714	0.146582
1055	SmallDependenceHighGrayLevelEmphasis HHH RCA	.715	0.14549

Rank	Radiomic feature	P value	-log(P value)
1056	ZoneVariance LHL RCA	.715	0.14549
1057	LowGrayLevelZoneEmphasis HLH RCA	.715	0.14549
1058	Kurtosis HHL RCA	.717	0.144399
1059	InverseVariance LHL LCA	.718	0.143855
1060	LargeAreaEmphasis LHL RCA	.721	0.142224
1061	Idn HHH LCA	.721	0.142224
1062	GrayLevelVariance LLH RCA.2	.723	0.14114
1063	MeanAbsoluteDeviation LLH LCA	.723	0.14114
1064	GrayLevelNonUniformityNormalised LHL LCA	.723	0.140598
1065	InverseVariance HLH RCA	.724	0.140056
1066	SmallDependenceEmphasis LHL RCA	.724	0.140056
1067	SizeZoneNonUniformity LLL LCA	.726	0.138975
1068	SumSquares LLH LCA	.726	0.138975
1069	SmallAreaEmphasis LHL LCA	.727	0.138435
1070	SmallAreaEmphasis LHH RCA	.730	0.136818
1071	Idmn HHH LCA	.733	0.134668
1072	LowGrayLevelRunEmphasis HHH RCA	.735	0.133595
1073	Mean LHH LCA	.735	0.133595
1074	RootMeanSquared LHL RCA	.737	0.132525
1075	RunPercentage HLH RCA	.737	0.132525
1076	SmallDependenceEmphasis LHH LCA	.737	0.132525
1077	Minimum HHL LCA	.739	0.131456
1078	ZonePercentage LLH RCA	.739	0.131456
1079	Imc2 LLL RCA	.739	0.131456
1080	SizeZoneNonUniformityNormalised LLH LCA	.742	0.129856
1081	Autocorrelation HHH RCA	.742	0.129324
1082	LongRunEmphasis LHH RCA	.742	0.129324
1083	SizeZoneNonUniformityNormalised LHL LCA	.743	0.128792
1084	LargeAreaEmphasis LHL LCA	.744	0.12826
1085	ZoneVariance LHL LCA	.744	0.12826
1086	LargeDependenceEmphasis HLH RCA	.746	0.127198
1087	Energy LCA	.748	0.126138
1088	ClusterShade RCA	.750	0.12508
1089	Imc1 HHH RCA	.750	0.12508
1090	Idmn HLH RCA	.750	0.12508
1091	LargeAreaLowGrayLevelEmphasis RCA	.753	0.122969
1092	Contrast LHL LCA	.755	0.121916
1093	Entropy LLH LCA	.755	0.121916
1094	ZoneVariance LHH LCA	.757	0.120864
1095	Range LHL RCA	.759	0.119815
1096	Correlation LHH LCA	.759	0.119815
1097	LargeAreaEmphasis LHH LCA	.759	0.119815
1098	LowGrayLevelEmphasis HHH RCA	.759	0.119815
1099	DependenceVariance HHL LCA	.761	0.118767
1100	DependenceVariance HHH RCA	.763	0.117721
1101	LargeDependenceLowGrayLevelEmphasis LCA	.764	0.116677
1102	ClusterProminence LLH RCA	.766	0.115635
1103	DependenceEntropy LHH RCA	.766	0.115635
1104	HighGrayLevelZoneEmphasis LLL LCA	.768	0.114594
1105	Minimum HHH LCA	.770	0.113555
1106	SumEntropy LHL LCA	.772	0.112518
1107	ShortRunEmphasis LHH RCA	.772	0.112518
1108	DependenceEntropy HHH LCA	.773	0.112
1109	SmallDependenceEmphasis LLH RCA	.774	0.111482
1110	RunLengthNonUniformityNormalised HHH LCA	.775	0.110965
1111	HighGrayLevelRunEmphasis HHH LCA	.775	0.110449
1112	ZonePercentage LHH LCA	.776	0.109932
1113	GrayLevelNonUniformity LHL LCA.1	.779	0.108387
1114	RunEntropy LHL LCA	.781	0.107358
1115	LargeDependenceHighGrayLevelEmphasis HHL LCA	.781	0.107358
1116	ShortRunLowGrayLevelEmphasis HHH LCA	.782	0.106844
1117	Correlation LHH RCA	.783	0.106331
1118	Minimum HLH LCA	.783	0.106331

Rank	Radiomic feature	P value	-log(P value)
1119	LongRunEmphasis HLH RCA	.785	0.105306
1120	X90Percentile LLH LCA	.785	0.105306
1121	MaximumProbability LHH LCA	.786	0.104795
1122	Entropy LHL LCA	.786	0.104795
1123	Range HLH LCA	.787	0.104283
1124	MeanAbsoluteDeviation LHL LCA	.787	0.104283
1125	Energy LHL LCA	.788	0.103262
1126	LargeDependenceLowGrayLevelEmphasis LLL RCA	.788	0.103262
1127	Energy LLL LCA	.788	0.103262
1128	DependenceNonUniformityNormalised HHH LCA	.788	0.103262
1129	RunLengthNonUniformity LLH LCA	.788	0.103262
1130	DependenceNonUniformityNormalised HLH RCA	.788	0.103262
1131	Median LHH LCA	.789	0.102752
1132	RunEntropy HHH LCA	.791	0.101733
1133	InverseVariance LHL RCA	.792	0.101224
1134	ShortRunHighGrayLevelEmphasis HHH RCA	.792	0.101224
1135	X90Percentile LHL LCA	.792	0.101224
1136	Imc1 LLH RCA	.794	0.100208
1137	LargeDependenceEmphasis LLH RCA	.794	0.100208
1138	RunLengthNonUniformityNormalised LLH RCA	.794	0.100208
1139	SumEntropy LLH LCA	.794	0.100208
1140	DifferenceVariance LLH LCA	.796	0.099193
1141	InverseVariance HLH LCA	.797	0.098686
1142	DependenceEntropy LHL RCA	.798	0.09818
1143	LargeAreaHighGrayLevelEmphasis HHL RCA	.798	0.09818
1144	LargeAreaHighGrayLevelEmphasis HLH RCA	.800	0.097169
1145	RunVariance LLH RCA	.801	0.09616
1146	Correlation LLH LCA	.802	0.095656
1147	HighGrayLevelZoneEmphasis HHH LCA	.803	0.095152
1148	LongRunHighGrayLevelEmphasis HHL LCA	.803	0.095152
1149	RunPercentage LLH RCA	.803	0.095152
1150	Median LHH RCA	.807	0.093142
1151	Busyness HLH LCA	.809	0.09214
1152	ZonePercentage LHL RCA	.813	0.09014
1153	DependenceVariance HLH LCA	.815	0.088645
1154	LargeDependenceLowGrayLevelEmphasis LLH RCA	.816	0.088147
1155	LongRunEmphasis LHH LCA	.816	0.088147
1156	DependenceNonUniformityNormalised LLH RCA	.818	0.087154
1157	InverseVariance HHH RCA	.818	0.087154
1158	LongRunEmphasis LLH RCA	.818	0.087154
1159	LargeDependenceLowGrayLevelEmphasis LHL LCA	.818	0.087154
1160	DifferenceEntropy LLH LCA	.818	0.087154
1161	DependenceEntropy LHH LCA	.819	0.086657
1162	Maximum HLH LCA	.820	0.086162
1163	ShortRunEmphasis LLH RCA	.822	0.085171
1164	GrayLevelNonUniformityNormalised HLH RCA.1	.824	0.084183
1165	JointAverage HHH RCA	.824	0.084183
1166	SumAverage HHH RCA	.824	0.084183
1167	X90Percentile LLH RCA	.826	0.083196
1168	LargeAreaLowGrayLevelEmphasis LHL LCA	.826	0.083196
1169	DependenceVariance LLH RCA	.829	0.081227
1170	X90Percentile LHL RCA	.829	0.081227
1171	SmallDependenceHighGrayLevelEmphasis RCA	.829	0.081227
1172	ShortRunEmphasis HHH LCA	.829	0.081227
1173	GrayLevelNonUniformityNormalised LLH LCA	.830	0.080736
1174	GrayLevelNonUniformityNormalised HLH LCA.1	.832	0.079755
1175	LargeAreaHighGrayLevelEmphasis LHH RCA	.833	0.079265
1176	ShortRunHighGrayLevelEmphasis LLL RCA	.833	0.079265
1177	SizeZoneNonUniformity LHL LCA	.833	0.079265
1178	Mean HLL RCA	.835	0.078287
1179	JointEntropy LLH LCA	.836	0.077798
1180	ClusterProminence LHH RCA	.837	0.07731
1181	Imc1 LLL RCA	.837	0.07731

Rank	Radiomic feature	P value	-log(P value)
1182	Idn LHH RCA	.843	0.07439
1183	RunLengthNonUniformity HHH LCA	.843	0.07439
1184	RunPercentage HHH LCA	.845	0.072936
1185	RunVariance LHH LCA	.845	0.072936
1186	SmallDependenceHighGrayLevelEmphasis LLH RCA	.846	0.072452
1187	Busyness LCA	.846	0.072452
1188	JointEnergy LHH RCA	.846	0.072452
1189	DependenceVariance LHH LCA	.848	0.071486
1190	JointAverage LLL RCA	.848	0.071486
1191	SumAverage LLL RCA	.848	0.071486
1192	RunVariance HHH LCA	.849	0.071003
1193	DifferenceAverage LLH LCA	.852	0.069558
1194	Imc1 LLH LCA	.853	0.069077
1195	Imc2 LHH RCA	.854	0.068597
1196	DependenceVariance HLH RCA	.854	0.068597
1197	X90Percentile LHH RCA	.856	0.067637
1198	DependenceEntropy LLH LCA	.857	0.067158
1199	ClusterShade HLH RCA	.860	0.065723
1200	Contrast LLH LCA	.860	0.065723
1201	DependenceNonUniformity HHH LCA	.860	0.065723
1202	InverseVariance LHH LCA	.861	0.065246
1203	LongRunHighGrayLevelEmphasis LLL LCA	.861	0.064769
1204	VoxelNum LCA	.861	0.064769
1205	X90Percentile LHH LCA	.861	0.064769
1206	Maximum HLL LCA	.863	0.063816
1207	LargeAreaHighGrayLevelEmphasis HHH RCA	.863	0.063816
1208	Uniformity LLH LCA	.864	0.06334
1209	Idm LHH LCA	.864	0.06334
1210	DependenceNonUniformityNormalised HLH LCA	.865	0.062865
1211	JointEnergy LHH LCA	.867	0.061915
1212	DependenceNonUniformity LLL LCA	.869	0.060968
1213	DifferenceVariance LHL LCA	.870	0.060494
1214	DependenceNonUniformityNormalised LHH RCA	.873	0.059077
1215	LongRunEmphasis HHH LCA	.873	0.059077
1216	Mean HHL LCA	.874	0.058606
1217	RobustMeanAbsoluteDeviation LLH LCA	.875	0.058134
1218	ZonePercentage LLH LCA	.875	0.058134
1219	TotalEnergy HLH LCA	.877	0.057193
1220	GrayLevelNonUniformity HHH LCA	.877	0.057193
1221	Idmn LHH RCA	.877	0.057193
1222	MaximumProbability LHH RCA	.879	0.056254
1223	DifferenceEntropy LHH RCA	.880	0.055316
1224	Id LHH RCA	.882	0.05438
1225	Maximum2DDiameterRow LCA	.884	0.053446
1226	DependenceNonUniformity LHH LCA	.884	0.053446
1227	GrayLevelVariance LHL LCA.1	.887	0.052048
1228	RunLengthNonUniformity LHH LCA	.888	0.051583
1229	Uniformity LHH RCA	.888	0.051583
1230	Id LHH LCA	.889	0.051118
1231	DependenceNonUniformity LCA	.890	0.050653
1232	LargeDependenceEmphasis HHH LCA	.890	0.050653
1233	GrayLevelNonUniformity HHH LCA.1	.890	0.050653
1234	GrayLevelNonUniformityNormalised LHH RCA	.890	0.050653
1235	LongRunHighGrayLevelEmphasis HHH LCA	.890	0.050653
1236	GrayLevelNonUniformity LHH LCA	.890	0.050653
1237	Idm LHH RCA	.892	0.049726
1238	Correlation HLH LCA	.893	0.049263
1239	Id LLH LCA	.896	0.047876
1240	ShortRunEmphasis LLH LCA	.898	0.046953
1241	InterquartileRange LHH LCA	.898	0.046953
1242	ZoneVariance HHH RCA	.899	0.046032
1243	HighGrayLevelRunEmphasis LLL RCA	.899	0.046032
1244	SmallDependenceEmphasis LLH LCA	.899	0.046032

Rank	Radiomic feature	P value	-log(P value)
1245	RunVariance HLH RCA	.899	0.046032
1246	RunLengthNonUniformityNormalised LLH LCA	.900	0.045573
1247	RunPercentage LLH LCA	.901	0.045113
1248	SmallDependenceHighGrayLevelEmphasis LHL LCA	.901	0.045113
1249	Contrast LHH RCA	.901	0.045113
1250	Idm LLH LCA	.902	0.044654
1251	RobustMeanAbsoluteDeviation LHH LCA	.903	0.044196
1252	SumEntropy LLH RCA	.903	0.044196
1253	Correlation RCA	.905	0.04328
1254	SmallDependenceEmphasis HHH RCA	.905	0.04328
1255	DifferenceAverage LHH RCA	.905	0.04328
1256	HighGrayLevelEmphasis LLL RCA	.907	0.042365
1257	GrayLevelNonUniformityNormalised LLH RCA	.907	0.042365
1258	DifferenceAverage LHH LCA	.909	0.041453
1259	ShortRunEmphasis LHH LCA	.912	0.040087
1260	Contrast LHH LCA	.913	0.039633
1261	ClusterTendency LHL LCA	.917	0.037819
1262	LargeDependenceEmphasis LLH LCA	.917	0.037819
1263	LongRunEmphasis LLH LCA	.917	0.037819
1264	Kurtosis HLL RCA	.917	0.037819
1265	InterquartileRange LLH LCA	.918	0.037367
1266	X10Percentile LLH LCA	.919	0.036915
1267	LargeAreaEmphasis HHH RCA	.919	0.036915
1268	Range LHH RCA	.919	0.036915
1269	DependenceNonUniformity HLH LCA	.919	0.036915
1270	LongRunHighGrayLevelEmphasis LLL RCA	.920	0.036013
1271	JointEntropy LHH RCA	.920	0.036013
1272	Imc2 LLH RCA	.924	0.034212
1273	DependenceNonUniformity HHL LCA	.924	0.034212
1274	GrayLevelNonUniformity LHL LCA.2	.926	0.033315
1275	DependenceNonUniformityNormalised LLH LCA	.926	0.033315
1276	MaximumProbability HHH LCA	.926	0.033315
1277	LargeAreaLowGrayLevelEmphasis HLH RCA	.928	0.032419
1278	ShortRunHighGrayLevelEmphasis LLL LCA	.928	0.032419
1279	GrayLevelNonUniformityNormalised LHL LCA.1	.929	0.031971
1280	RunPercentage LHH LCA	.930	0.031524
1281	ClusterTendency LLH RCA	.930	0.031524
1282	Elongation RCA	.930	0.031524
1283	InverseVariance HHL LCA	.930	0.031524
1284	ClusterTendency LHH LCA	.931	0.031078
1285	JointEntropy LLH RCA	.932	0.030632
1286	RunLengthNonUniformity LLL LCA	.932	0.030632
1287	VolumeNum RCA	.933	0.030186
1288	GrayLevelVariance LHH RCA.1	.934	0.029741
1289	DependenceVariance LLH LCA	.936	0.028851
1290	SizeZoneNonUniformityNormalised LCA	.936	0.028851
1291	DifferenceEntropy LHH LCA	.936	0.028851
1292	JointEnergy LLH LCA	.938	0.027964
1293	DifferenceVariance LHH RCA	.938	0.027964
1294	SumSquares LHH RCA	.938	0.027964
1295	Median HLL RCA	.940	0.027077
1296	ShortRunHighGrayLevelEmphasis HHH LCA	.940	0.027077
1297	GrayLevelVariance LHH LCA.1	.940	0.027077
1298	ZoneEntropy HLH LCA	.941	0.026635
1299	Correlation HHH LCA	.941	0.026635
1300	RunVariance LLH LCA	.941	0.026635
1301	SmallDependenceEmphasis LHH RCA	.941	0.026193
1302	RobustMeanAbsoluteDeviation LHH RCA	.941	0.026193
1303	Imc2 HHL LCA	.942	0.025751
1304	ClusterProminence LHL RCA	.943	0.02531
1305	SmallAreaHighGrayLevelEmphasis LHL LCA	.943	0.02531
1306	Entropy LLH RCA	.943	0.02531
1307	ClusterShade LCA	.943	0.02531

Rank	Radiomic feature	P value	-log(P value)
1308	Entropy LHH RCA	.943	0.02531
1309	LargeDependenceHighGrayLevelEmphasis HHH LCA	.945	0.024429
1310	GrayLevelVariance LHH RCA	.945	0.024429
1311	SmallAreaEmphasis LCA	.947	0.02355
1312	Maximum LHL RCA	.947	0.02355
1313	Imc2 RCA	.947	0.02355
1314	Variance LHH RCA	.947	0.02355
1315	MeanAbsoluteDeviation LLH RCA	.947	0.02355
1316	MeanAbsoluteDeviation LHH RCA	.947	0.02355
1317	Uniformity LHH LCA	.949	0.022672
1318	Uniformity LLH RCA	.949	0.022672
1319	InterquartileRange LHH RCA	.949	0.022672
1320	RootMeanSquared LLH RCA	.953	0.020921
1321	SumSquares LLH RCA	.953	0.020921
1322	RootMeanSquared LHH RCA	.955	0.020048
1323	LargeDependenceEmphasis LHH LCA	.955	0.020048
1324	DependenceEntropy LCA	.956	0.019612
1325	ZonePercentage LHH RCA	.959	0.018307
1326	Energy LHH LCA	.959	0.018307
1327	LargeAreaLowGrayLevelEmphasis LLH LCA	.959	0.018307
1328	GrayLevelVariance LHL LCA	.959	0.018307
1329	RootMeanSquared LHL LCA	.959	0.018307
1330	Variance LHL LCA	.961	0.017439
1331	LargeDependenceLowGrayLevelEmphasis HLH LCA	.962	0.017005
1332	MaximumProbability LLH RCA	.963	0.016572
1333	JointEntropy LHH LCA	.963	0.016572
1334	Busyness HLH RCA	.964	0.015707
1335	Complexity HLH LCA	.966	0.014844
1336	RunLengthNonUniformityNormalised LHH LCA	.967	0.014413
1337	LargeAreaHighGrayLevelEmphasis LLH LCA	.968	0.013983
1338	Correlation LLL RCA	.968	0.013983
1339	LongRunLowGrayLevelEmphasis HLH LCA	.970	0.013123
1340	Autocorrelation LLL LCA	.970	0.013123
1341	Strength HLH RCA	.972	0.012264
1342	Autocorrelation LLL RCA	.972	0.012264
1343	Busyness HHH LCA	.972	0.012264
1344	ZoneEntropy LLL LCA	.973	0.011836
1345	MaximumProbability LLH LCA	.973	0.011836
1346	GrayLevelVariance LLH RCA.1	.974	0.011408
1347	DifferenceVariance LLH RCA	.974	0.011408
1348	X10Percentile LHH LCA	.974	0.011408
1349	GrayLevelVariance LHH LCA	.974	0.011408
1350	LargeDependenceLowGrayLevelEmphasis HHH LCA	.974	0.011408
1351	LongRunLowGrayLevelEmphasis HHH LCA	.974	0.011408
1352	ZoneEntropy LHL RCA	.974	0.011408
1353	Strength HHH LCA	.975	0.01098
1354	SumSquares LHH LCA	.975	0.01098
1355	ClusterTendency LHH RCA	.976	0.010553
1356	LargeAreaLowGrayLevelEmphasis HHH RCA	.976	0.010553
1357	ZoneEntropy LLH RCA	.976	0.010553
1358	DifferenceVariance LHH LCA	.977	0.010126
1359	HighGrayLevelRunEmphasis LLL LCA	.978	0.009699
1360	RobustMeanAbsoluteDeviation LLH RCA	.978	0.009699
1361	JointEnergy LLH RCA	.978	0.009699
1362	LargeAreaEmphasis LLH LCA	.980	0.008847
1363	ZoneVariance LLH LCA	.980	0.008847
1364	InterquartileRange LLH RCA	.982	0.007997
1365	GrayLevelNonUniformityNormalised LHH LCA	.983	0.007572
1366	MeanAbsoluteDeviation LHH LCA	.984	0.007148
1367	DifferenceEntropy LLH RCA	.984	0.007148
1368	SmallAreaHighGrayLevelEmphasis HHH LCA	.984	0.007148
1369	SmallDependenceLowGrayLevelEmphasis HHH RCA	.986	0.006301
1370	LargeAreaLowGrayLevelEmphasis LHL RCA	.986	0.006301

Rank	Radiomic feature	P value	-log(P value)
1371	VolumeNum LCA	.986	0.006301
1372	DependenceNonUniformity LHL LCA	.988	0.005456
1373	Complexity HLH RCA	.988	0.005034
1374	HighGrayLevelEmphasis LLL LCA	.989	0.004612
1375	RunLengthNonUniformity LCA	.989	0.004612
1376	GrayLevelVariance LLH RCA	.989	0.004612
1377	RootMeanSquared LHH LCA	.991	0.00377
1378	Variance LHH LCA	.991	0.00377
1379	ZoneVariance HLH RCA	.991	0.00377
1380	Idm LLH RCA	.991	0.00377
1381	SumEntropy LHH RCA	.991	0.00377
1382	Entropy LHH LCA	.993	0.002929
1383	Id LLH RCA	.993	0.002929
1384	SumSquares LHL LCA	.993	0.002929
1385	DifferenceAverage LLH RCA	.995	0.00209
1386	Variance LLH RCA	.995	0.00209
1387	X10Percentile LHH RCA	.995	0.00209
1388	SumEntropy LHH LCA	.998	0.000835
1389	Contrast LLH RCA	.999	0.000417
1390	LargeAreaEmphasis HLH RCA	.999	0.000417
1391	RunLengthNonUniformity HLH LCA	.999	0.000417